Alma Mater Studiorum · Università di Bologna

Settore Concorsuale: 02/C1 - Astronomia, Astrofisica, Fisica della Terra e dei Pianeti
Settore Scientifico Disciplinare: FIS/05 - Astronomia e Astrofisica

NON-THERMAL PHENOMENA IN GALAXY CLUSTERS: THE *LOFAR* REVOLUTION

Dottorato di Ricerca in Astrofisica

Candidato:
Luca Bruno

Supervisore:
Dr. **Gianfranco Brunetti**

Coordinatore Dottorato:
Prof. **Andrea Miglio**

Co-Supervisore:
Prof. **Daniele Dallacasa**
Dr. **Fabio Gastaldello**

Ciclo XXXV
Esame finale Anno 2023

This Thesis work was done as part of the research activity of the Istituto di Radioastronomia - Istituto Nazionale di Astrofisica (Bologna)

Thesis outline

Cosmic structures form and grow in mass and size hierarchically through mergers with smaller objects. Mergers between galaxy clusters are the most energetic events in the Universe, and a fraction of their energy can be channelled by shocks and turbulence into non-thermal components that are mixed with the thermal particles of the intra-cluster medium (ICM). As a consequence of these events, diffuse synchrotron radio emission can be triggered on cluster-scales.

The diffuse radio sources in galaxy clusters are primarily classified on the basis of their morphology, size, and location. Among the various diffuse radio sources, radio halos (RHs) are thought to trace particle re-acceleration driven by turbulence induced in the ICM by a cluster merger. RHs are characterised by steep ($\alpha \sim 1.3$) synchrotron spectral indices, which challenge the detection of these targets at high ($\sim$ 1 GHz) frequencies. In the last decades, observations in the range $\sim$ 300 – 1000 MHz allowed to perform the first statistical studies of these objects. Milestone works demonstrated that RHs are not ubiquitous, but are mainly found in the most massive and disturbed galaxy clusters. By computing upper limits to the radio power of possible undetected halos, it was discovered that a bimodal distribution exists between clusters hosting and lacking RHs, and that this behaviour likely reflects their dynamical state. In this respect, the radio power of RHs correlates with the host mass, thus suggesting a connection between the non-thermal emission and energy budget available during mergers.

Even though important steps forward have been made in the field of diffuse sources, many questions are still open. It has become evident that low frequency ($<$ 200 MHz) observations can shed light on the origin, properties, and occurrence of RHs, by allowing to test theoretical models in an uncharted frequency regime, where diffuse sources are much brighter because of their steep spectra.

The LOw Frequency ARray (LOFAR) is a new generation interferometer with antennas spread over 10 European countries, operating in the frequency range $\sim$ 10 – 250 MHz. Thanks to its unprecedented combination of high resolution and sensitivity at low frequency, LOFAR is rapidly revolutionising our knowledge in many fields of galactic and extragalactic radio astronomy. Indeed, LOFAR is not only detecting a remarkable increasing number of RHs, especially those with very steep spectra that are elusive at higher frequency, but it is also revealing RHs with peculiar morphological and spectral properties that challenge the current standard classification. Furthermore, LOFAR has recently allowed the striking detection of diffuse radio emission extending beyond the canonical cluster boundaries and even between pairs of merging clusters. These results have important implications on the cosmic magnetism, and the physics of cosmic rays and energy

transfer in the large structures of the Universe.

In this Thesis we focus on the study of diffuse radio sources, especially on RHs, by analysing both large samples of clusters and specific interesting targets observed by LOFAR. To these aims, we make use of complementary radio (GMRT, uGMRT, VLA, JVLA) and X-ray (Chandra, XMM-Newton) data.

The first part of this Thesis is devoted to the analysis of the largest-ever sample of galaxy clusters observed at radio frequencies, which I have been firsthand involved in as a member of the LOFAR survey Key Science Project. In this large program, named 'The *Planck* clusters in the LOFAR sky', we built a complete mass-selected sample of 309 *Planck* clusters in the footprint of the Second Data Release of the LOFAR Two Metre Sky Survey (LoTSS-DR2), which span previously unexplored ranges of mass and redshift. My main contribution to this project was the development of new techniques to derive solid upper limits in the 140 out of 309 cases of non-detection of RHs. By comparing the radio power of detected RHs and upper limits in our sample, we carried out the first statistical analysis of the properties and occurrence of RHs in clusters at low frequencies, and we were able to test the predictions of the turbulent re-acceleration scenario in uncharted regimes.

In the last part of this Thesis we analyse deep LOFAR and multifrequency observations of two interesting galaxy clusters, namely MACS J1149.5+2223 (MACS J1149) and Abell 2142 (A2142), both hosting a very steep spectrum radio halo. MACS J1149 is a massive merging system at high ($z \sim 0.5$) redshift. By combining its thermal and non-thermal properties, we ruled out a pure hadronic origin of the RH, and constrained the contribution of secondary electrons produced by proton-proton collisions in the ICM. A2142 is a nearby and massive cluster, exhibiting extremely atypical thermal and non-thermal properties. Previous radio observations at higher frequencies revealed the presence of a peculiar RH consisting of two distinct radio components. By means of new deep LOFAR observations we detected a third, very-steep spectrum, component extending over the entire volume of the cluster, thus making A2142 a unique science-case to be investigated.

The structure of this Thesis is described below.

- **Chapter 1**. We provide a general overview on the formation of cosmic structures and the populations of galaxies in clusters. We then focus on the phenomena involving the ICM, and the consequences of cluster mergers.

- **Chapter 2**. We introduce the properties of radio galaxies in clusters and the non-thermal components of the ICM. We then review the different diffuse radio sources, by emphasising the essential role of low frequency observations in this field.

- **Chapter 3**. We describe the infrastructures of LOFAR, its ongoing surveys, and the advanced data reduction algorithms that have been developed by the LOFAR collaboration.

- **Chapter 4**. We present the largest-ever sample of 309 *Planck* clusters observed at radio frequencies in the context of LoTSS-DR2. We describe the complex methods adopted to reduce, image, and analyse these data, and we finally classify the

detected diffuse sources. We claim the detection of 83 RHs (including candidates), about half of which being new discoveries.

- **Chapter 5**. We consider a sub-sample of 140 *Planck* clusters which lack a detected RH. By simulating mock RHs with different sizes and flux densities in the observed *uv*-datasets (injection technique), we first test the capabilities of LOFAR to recover extended emission in the sky. Thanks to the extremely dense *uv*-coverage of a standard (8 hour long) LoTSS pointing, we find few percents of flux density losses for targets of size $\sim 15'$. We then determine a relation to quickly derive firm upper limits, showing its potentialities and limitations. By means of injections and this relation, we compute solid upper limits for 75 clusters.

- **Chapter 6**. We present the results of the statistical analysis carried out on the LoTSS-DR2 sample. By comparing the radio power of detected RHs and upper limits in mass-complete sub-samples, we study the bimodal distribution of clusters in LoTSS-DR2. Furthermore, we determine the occurrence of RHs and test the predictions of the turbulent re-acceleration model.

- **Chapter 7**. We analyse the ultra-steep spectrum radio halo in the high-z galaxy cluster MACS J1149 by means of LOFAR, GMRT, JVLA, and Chandra data. We study the spatial correlation between the thermal and non-thermal emission. We test a pure hadronic origin of the halo, which is possible in this target thanks to its combination of steep spectral index and high redshift. We find an unrealistically high non-thermal energy budget that rules out a pure hadronic model.

- **Chapter 8**. We investigate the multi-component RH in A2142 with LOFAR, GMRT, VLA, Chandra, and XMM-Newton data. In addition to the previously known two-components of diffuse emission, we discovered a third radio component on scales $\gtrsim 2$ Mpc, which is characterised by a very steep spectral index. We perform an accurate spectral analysis of the three components and investigate the connection with their thermal counterparts. Furthermore, we search for a megahalo in A2142, and derive upper limits to its emission. We finally discuss possible formation scenarios for this extremely complex target.

- **Chapter 9**. We summarise the works of this Thesis and discuss future prospects.

This Thesis in based on the following publications and ongoing works.

1. **L. Bruno**, G. Brunetti, A. Botteon, V. Cuciti, D. Dallacasa, R. Cassano, R. J. van Weeren, T. Shimwell, G. Taffoni, S. A. Russo, A. Bonafede, M. Brüggen, D. N. Hoang, H. J. A. Röttgering, C. Tasse; *The Planck clusters in the LOFAR sky. II. LoTSS-DR2: Recovering diffuse extended emission with LOFAR*. Published in 2023 by A&A, 672, A41.

2. **L. Bruno**, K. Rajpurohit, G. Brunetti, F. Gastaldello, A. Botteon, A. Bonafede, D. Dallacasa, R. Cassano, R. J. van Weeren, V. Cuciti, G. Di Gennaro, T. Shimwell, M. Brüggen; *The LOFAR and JVLA view of the distant steep spectrum radio halo in MACS J1149.5+2223*. Published in 2021 by A&A, 650, A44.

3. **L. Bruno** et al., in prep.; *The puzzling giant, multi-component, ultra-steep spectrum radio halo in Abell 2142*

4. A. Botteon, T. Shimwell, R. Cassano, V. Cuciti, X. Zhang, **L. Bruno**, L. Camillini, R. Natale, A. Jones, F. Gastaldello, A. Simionescu, M. Rossetti, H. Akamatsu, R. J. van Weeren, G. Brunetti, M. Brüggen, C. Groeneveld, D. N. Hoang, M. J. Hardcastle, A. Ignesti, G. Di Gennaro, A. Bonafede, A. Drabent, H. J. A. Röttgering, M. Hoeft, F. de Gasperin; *The Planck clusters in the LOFAR sky. I. LoTSS-DR2: New detections and sample overview*. Published in 2022 by A&A, 660, A78.

5. X. Zhang, A. Simionescu, F. Gastaldello, D. Eckert, L. Camillini, R. Natale, M. Rossetti, G. Brunetti, H. Akamatsu, A. Botteon, R. Cassano, V. Cuciti, **L. Bruno**, T. Shimwell, A. Jones, J.S. Kaastra, S. Ettori, M. Brüggen, F. de Gasperin, A. Drabent; *The Planck clusters in the LOFAR sky. III. LoTSS-DR2: Dynamic states and density fluctuations of the intracluster medium*. Published in 2023 by A&A, 672, A42.

6. R. Cassano, V. Cuciti, G. Brunetti, A. Botteon, M. Rossetti, **L. Bruno**, A. Simionescu, F. Gastaldello, R. J. van Weeren, M. Brüggen, D. Dallacasa, X. Zhang, H. Akamatsu, A. Bonafede, G. Di Gennaro, T. Shimwell, F. de Gasperin, H. J. A. Röttgering, A. Jones.; *The Planck clusters in the LOFAR sky. IV. LoTSS-DR2: statistics of radio halos and re-acceleration models*. Published in 2023 by A&A, 672, A43.

7. V. Cuciti, R. Cassano, M. Sereno, G. Brunetti, A. Botteon, T. Shimwell, **L. Bruno**, F. Gastaldello, M. Rossetti, X. Zhang, A. Simionescu, M. Brüggen, R. J. van Weeren, A. Jones, H. Akamatsu, A. Bonafede, F. De Gasperin, G. Di Gennaro, T. Pasini, H. J. A. Röttgering; *The Planck clusters in the LOFAR sky. V. LoTSS-DR2: mass - radio halo power correlation at low frequency*. Submitted to A&A.

Contents

List of acronyms

Radio facilities

GBT Green Bank Telescope
GMRT, **uGMRT** Giant Metrewave Radio Telescope, upgraded Giant Metrewave Radio Telescope
LOFAR LOw Frequency ARray
MWA Murchison Widefield Array
SKA Square Kilometer Array
VLA, **JVLA** Very Large Array, Karl G. Jansky Very Large Array
WSRT Westerbork Synthesis Radio Telescope

Nomenclature

AGN Active Galactic Nucleus
BCG Brightest Cluster Galaxy
CC Cool Core (cluster)
cD Central Dominant (galaxy)
CMB Cosmic Microwave Background
CR, **CRe**, **CRp** Cosmic Ray, Cosmic Ray electron, Cosmic Ray proton
DM Dark Matter
GReET Gently Re-Energised Tail
FR Fanaroff-Riley (radio galaxy)
HT Head-Tail (radio galaxy)
ICM Intra-Cluster Medium
MH (radio) Mini-Halo
NCC Non-Cool Core (cluster)
RH Radio Halo
RP Radio Phoenix
RR Radio Relic
USSRH Ultra-Steep Spectrum Radio Halo
WAT Wide Angle Tail (radio galaxy)
XRG X-shaped Radio Galaxy
ZRG Z-shaped Radio Galaxy

Chapter 1

Galaxy clusters

Galaxy clusters are the largest structures in the Universe bounded by the gravitational force. They have masses $M \sim 10^{14} - 10^{15}$ $M_{\odot}$ and host $\sim 100 - 1000$ galaxy members within radii of $R \sim 1 - 3$ Mpc. The baryonic matter in the form of galaxies represents only a small fraction ($\sim 5\%$) of the total mass, whereas dark matter (DM) is the main component ($\sim 80\%$). The rest ($\sim 15\%$) of the mass is in the form of the intra-cluster medium (ICM), which is a hot ($T \sim 10^7 - 10^8$ K) and rarefied ($n_e \sim 10^{-2} - 10^{-4}$ cm^{-3}) plasma that occupies the bulk of the volume of the cluster, filling the space in-between the galaxies (e.g. Sarazin 1986b).

Galaxy clusters are fundamental subjects for cosmology and astrophysics studies at all wavelengths. For example, by analysing the evolution of count numbers of clusters in redshift and mass we can constrain the cosmological parameters, test theoretical models, and thus reconstruct the history of the Universe. Moreover, clusters allow to probe the properties of galaxies and active galactic nuclei (AGN) in unique environmental conditions. Finally, and mostly important for the aims of Thesis, in galaxy clusters we can investigate the connection between the thermal and non-thermal components in the ICM, and topics of fundamental physics such as magneto-hydrodynamics and energy transfer mechanisms over a wide range of scales.

In this Chapter, we provide an overview on the origin and evolution of galaxy clusters, the properties of their members, and the thermal phenomena associated with the ICM.

1.1 Formation and evolution

According to standard cosmologies, including the ΛCDM[1] (Λ - Cold Dark Matter) model (e.g. Spergel et al. 2007; Allen et al. 2011), structures in the Universe originate and grow hierarchically through merging of smaller substructures (e.g. Voit 2005; Kravtsov & Borgani 2012). The observed small temperature anisotropies ($\Delta T/T \sim 10^{-5}$) of the Cosmic Microwave Background (CMB) (Bennett et al. 1996; Planck Collaboration et al. 2011) are the footprints of primordial, randomly distributed, density fluctuations. Among these primordial fluctuations, overdensities have been naturally enhanced over time because of

[1]Throughout this Thesis, we assume cosmological parameters $\Omega_M = 0.30$ and $\Omega_\Lambda = 0.70$ for the matter and dark energy content, respectively, and Hubble constant $H_0 = 70$ km s^{-1} Mpc^{-1}.

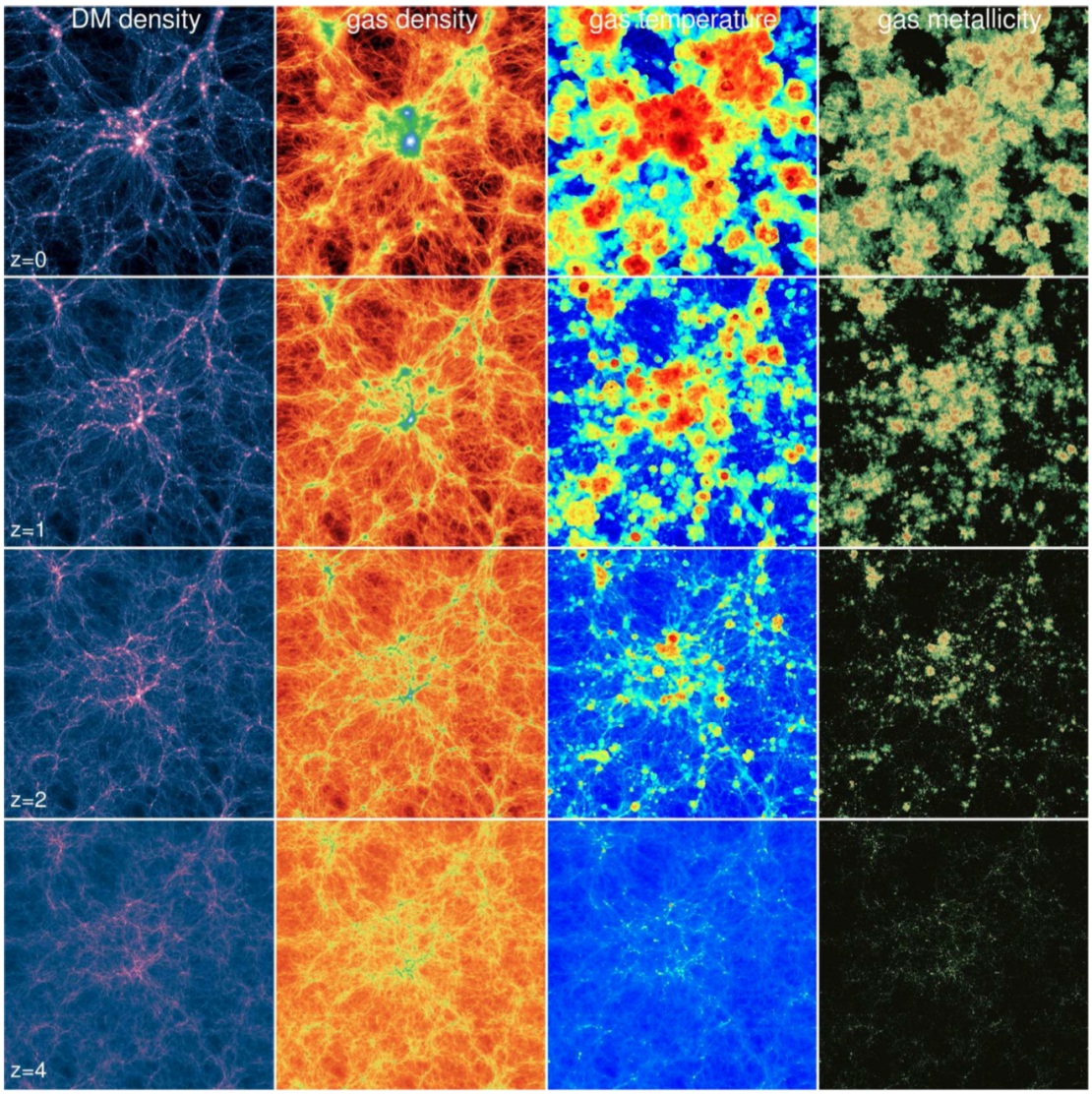

Figure 1.1: Evolution of dark matter density, gas density, gas temperature, and gas metallicity with increasing redshift (from upper to lower panels) in a volume of $\sim 100^3$ Mpc^3 as obtained from the *Illustris* simulation (Vogelsberger et al. 2014).

their own higher gravitational field than that of the mean density, which delayed their expansion caused by the Hubble flow. Once reached the conditions for the gravitational instability (i.e. $M > M_J$, being $M_J \propto T^{\frac{3}{2}}\rho^{-\frac{1}{2}}$ the Jeans mass), the overdensities have collapsed into the first halos of dark matter, which then have grown hierarchically through accretion of smaller halos, and, after a number of such events, finally evolved into the present day galaxy clusters (e.g. Coles & Lucchin 2002).

Initially, density fluctuations are $\Delta\rho/\rho \ll 1$ and can be treated analytically as linear perturbations of the continuity, momentum conservation, and Poisson equations. However, they rapidly evolve, reaching non-linear phases that require computing-intensive numerical simulations; recent prominent examples of cosmological simulations are the *Millenium* (Springel 2005) and *Illustris* (Vogelsberger et al. 2014, see Fig. 1.1) simulations. Simulations show that, on cosmological scales, the Universe is organised in a network of filaments of dark matter that constitute the so-called 'Cosmic Web'; the cosmic filaments intersect at the nodes of the Web, which are the densest regions where DM halos grow pulling additional matter via the filaments themselves. In this scenario, baryons that have infallen into the gravitational potential well of the DM can cool down and condense to form stars and galaxies.

1.2 Member galaxies

Optical, infrared, and UV emission of galaxy clusters includes stellar black body radiation and line emission processes associated with its member galaxies. Spectroscopic and photometric surveys of clusters, such as SDSS (York et al. 2000), 2MASS (Skrutskie et al. 2006), WINGS (Fasano et al. 2006), COSMOS-Web (Casey et al. 2022), are fundamental tools, as they provide redshifts z, colours, star formation rates, velocities, and AGN activity of their members, as well as hints on the global dynamical state of the cluster.

Galaxy clusters were historically classified based on the number ('richness' classification; Abell 1958) and distribution ('morphological' classification; Zwicky et al. 1961) of their members, as inferred from optical observations. Roughly, clusters can be distinguished as regular and irregular (see examples in Fig. 1.2). Regular clusters are more compact, denser in the central regions, and dominated by early-type (elliptical and lenticular) galaxies, whereas irregular clusters are less compact, have substructures, and show a larger number of late-type (spiral and irregular) galaxies. Moreover, regular clusters hosts a central dominant (cD) galaxy in their centre, typically coinciding with the brightest cluster galaxy (BCG): this is a giant ($M \sim 10^{12}\ M_\odot$) elliptical galaxy that exhibits (at least) one bright optical core and it is surrounded by a diffuse stellar halo (e.g. Matthews et al. 1964). Overall, these properties suggest that regular clusters are dynamically relaxed systems, whereas irregular clusters are unrelaxed and still in an evolutionary phase.

1.2.1 Luminosity and colour distributions

The luminosity distribution of the galaxies in clusters is fundamental for both astrophysical and cosmological studies. The first analytical expression of the luminosity function

Figure 1.2: Images of A2029 (left, credits: SDSS) and Hercules (right, credits: Trottier, https://apod.nasa.gov) as examples of regular and irregular clusters, respectively.

was proposed by Schechter (1976) as:

$$N(L)\mathrm{d}L = N^* \left(\frac{L}{L^*}\right)^{-\alpha} e^{-\frac{L}{L^*}} \mathrm{d}\left(\frac{L}{L^*}\right) \quad , \tag{1.1}$$

where N^* is the normalisation and L^* is the characteristic luminosity (for $L \gg L^*$ the exponential law becomes dominant with respect to the power-law of slope α). Eq. 1.1 provides the number of galaxies with luminosity in the range $[L, L + \mathrm{d}L]$ per unit volume (Mpc^3), and is typically a good representation of the actual observed distributions, as shown in Fig. 1.3, despite not being physically motivated. Discrepancies between Eq. 1.1 and the observed distributions are found at high luminosities for the BCGs, whose properties are different from classical galaxies, and their formation may be possibly connected with multiple minor mergers and cannibalism of small galaxy groups (e.g. Dressler 1980; De Lucia & Blaizot 2007; Lauer et al. 2014).

Galaxies in clusters are known to show a bimodal distribution in the colour-magnitude (or analogously colour-stellar mass, by using the mass to luminosity ratio) diagram (e.g. Schawinski et al. 2014). Indeed, late-type galaxies have lower stellar masses, but are highly star-forming, and populate the bluer region of the diagram known as 'blue cloud', whereas early-type galaxies have higher stellar masses, but almost absent star formation, and populate the redder region of the diagram known as 'red sequence'; galaxies with intermediate properties are instead found in the 'green valley' (see Fig. 1.4, left panel). This bimodal distribution is peculiar of galaxy clusters, whose members are intrinsically different from isolated field galaxies, which instead mostly consist of younger stellar populations and star-forming late-type galaxies (e.g. Sampaio et al. 2022). As shown in Fig. 1.4 (right panel), for regular clusters and for the inner regions of irregular clusters, the number of early-type galaxies increases with the density of galaxies, whereas the number of late-type galaxies decreases (e.g. Dressler 1980; Fasano et al. 2015; Cava et al.

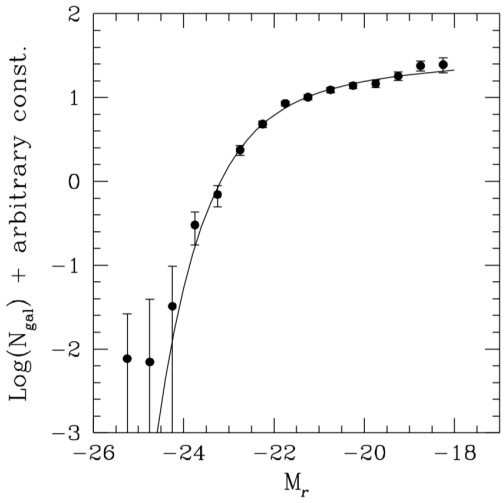

Figure 1.3: Fit of the observed distribution (in terms of absolute magnitude in *r*-filter) of galaxies with the luminosity function in Eq. 1.1 by Paolillo et al. (2001).

2017). Overall, these results suggest that the environmental conditions play a major role in the formation and evolution of galaxies. In dense cluster environments, overdensities are larger and allowed star-formation phases earlier than in isolated galaxies; on the other hand, many (hydro-)dynamical processes (such as tidal stripping, ram-pressure stripping, galaxy-galaxy encounters; e.g. van de Voort et al. 2017) occurring in galaxy clusters can contribute to the quenching of their members by directly removing the cold gas or indirectly triggering star-bursts that rapidly exhaust the gas reservoirs.

1.3 The intra-cluster medium (ICM)

The ICM is the most abundant baryonic component of galaxy clusters. It permeates the volume of the cluster, filling the space in-between galaxies. Owing to its high temperature ($T \sim 10^7 - 10^8$ K), the ICM is a plasma mainly consisting of thermal electrons ($n_e \sim 10^{-2} - 10^{-4}$ cm^{-3}), protons ($n_p \sim 0.8 n_e$), and ionised helium and heavier elements (e.g. Peterson et al. 2001; Matsushita et al. 2002). On average, typical values of the metallicity are $Z \sim 0.2 - 0.3\ Z_\odot$; such an high metallicity indicates that the composition of the ICM is the result of galactic enrichment rather than being primordial (Mernier et al. 2018, for a review).

Given the high temperatures, low densities, and weak magnetic fields, the ICM is considered as a weakly collisional plasma. In this condition, wave-particle interactions are much more important than Coulomb particle-particle collisions in driving the micro-physical properties of the ICM; more specifically, plasma instabilities and collisionless processes allow the transfer of energy and momentum from large-scale ICM motions down to microscopical scales, thus resulting in particle acceleration and electromagnetic fluctuations (e.g. Brunetti & Lazarian 2011b; Santos-Lima et al. 2014).

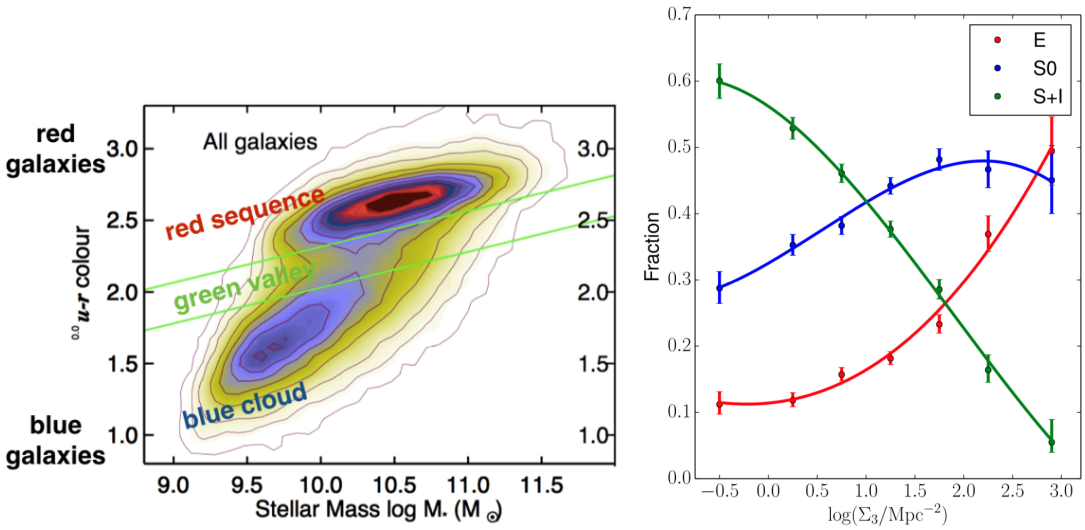

Figure 1.4: *Left*: Colour-stellar mass diagram (Schawinski et al. 2014). Early-type galaxies are redder and more massive (red sequence), late-type galaxies are bluer and less massive (blue cloud); galaxies with intermediate colours and masses are located in the green valley. *Right*: Fraction of cluster galaxy members as a function of projected galaxy number density (Houghton 2015). Early-type and late-type galaxies increase and decrease with the galaxy density, respectively.

1.3.1 X-ray emission

The ICM emits in the X-ray band due to thermal bremsstrahlung (see Fig. 1.5), with typical bolometric luminosities $L_X \sim 10^{43} - 10^{45}$ erg s^{-1} (Sarazin 1986b). The monochromatic emissivity for a plasma of electron density n_e and ion density n_i in thermal equilibrium is given by (Rybicki & Lightman 1979):

$$J_{br}(\nu, T) \propto n_e n_i T^{-\frac{1}{2}} e^{-\frac{h\nu}{kT}} \quad , \tag{1.2}$$

where h and k are the Planck and Boltzmann constants, respectively. The density and exponential cut-off in Eq. 1.2 provide the average density and temperature of the ICM within a given volume, respectively.

By integrating Eq. 1.2 over the frequencies, we obtain the bolometric emissivity as:

$$J_{br}(T) = \int J_{br}(\nu, T) d\nu \propto T^{\frac{1}{2}} n_e n_i q^2 = \Lambda(T) n_e n_i \quad , \tag{1.3}$$

where constants and temperature dependencies have been included in the cooling function $\Lambda(T)$ (Sutherland & Dopita 1993; Katz et al. 1996). At temperatures $T > 2 \times 10^7$ K (i.e. $kT > 2$ keV), the main cooling channel is thermal bremsstrahlung and the cooling function can be estimated as $\Lambda(T) \sim 2.5 \times 10^{-27} \sqrt{T}$ erg cm^3 s^{-1} (e.g. Gitti et al. 2012a); at temperatures $T \lesssim 2 \times 10^7$ K, line emission from ions largely contributes to the cooling as well. From Eq. 1.3 it is possible to derive the cooling time of bremsstrahlung as:

$$t_{cool} = \frac{\Gamma}{\Gamma - 1} \frac{kT}{\mu X n_e \Lambda(T)} \sim 100 \times \left(\frac{T}{10^8 \text{ K}}\right)^{\frac{1}{2}} \left(\frac{n_e}{10^{-3} \text{ cm}^{-3}}\right)^{-1} \text{ Gyr} \quad , \tag{1.4}$$

Figure 1.5: Composite optical (white; credits: NASA/STScI, ESO/VLT, SDSS) and X-ray (purple; credits: NASA/CXC/Caltech/Newman et al./Tel Aviv/Morandi & Limousin) image of A383.

where $\Gamma = 5/3$ is the adiabatic index for a non-relativistic monoatomic gas, $\mu \sim 0.6$ is the mean molecular weight, and $X \sim 0.7$ is the hydrogen mass fraction. For typical values of density and temperature, Eq. 1.4 provides $t_{\rm cool} \sim 100$ Gyr $\gg t_{\rm H}$ (Hubble time), thus indicating that in general the ICM will not efficiently cool down; as further discussed in Sect. 1.3.3, cooling may be relevant only in the central and densest regions of the cluster.

X-ray observations are nowadays the standard and most accurate tool to determine the dynamical state of galaxy clusters. Indeed, clusters are classified as 'cool core' (CC) and 'non-cool core' (NCC) based on the presence or absence of a prominent X-ray peak of emission in their centre, respectively (see examples in Fig. 1.6). The term 'cool core' refers to the fact that a drop in temperature is observed in correspondence of the X-ray peak. While CC are relaxed (more similar to regular) clusters that have not undergone a recent major merger (within the last $\sim$ 3 Gyr), NCC are disturbed (more similar to irregular) merging systems. In the next sections we provide a better description of the dichotomy between CC and NCC clusters.

1.3.2 Galaxy and gas density profiles

Galaxy clusters are virialised systems (except for their outskirts, which are subject to continuous accretion from the Cosmic Web). The thermodynamic equilibrium is reached on time-scales of the order of the crossing time $t_{\rm cross} \sim 1-2$ Gyr through 'violent relaxation' Lynden-Bell (1967); this is a collective gravitational phenomenon which efficiently allows the scattering and mixing of galaxies that infall towards the potential well of the DM. As a result of this process, the spatial distribution of galaxies will become isothermal, and the velocity distribution will be Gaussian, with a fairly uniform velocity dispersion σ_v.

In the framework of virialised systems, a galaxy cluster can be treated as a set of concentric isothermal spheres where galaxies are distributed according to local Maxwell-Boltzmann distributions. Under this assumption, at first approximation, the radial profile

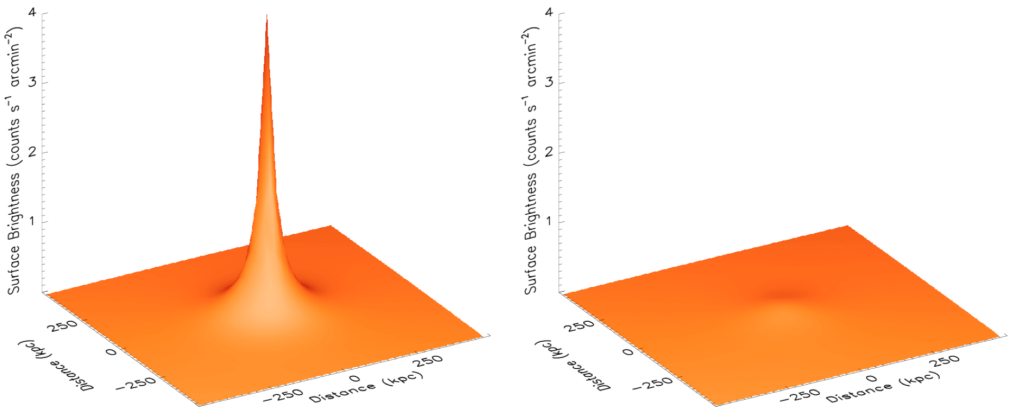

Figure 1.6: 3D representation of the projected X-ray surface brightness profile of A2029 (left) and A2319 (right) as examples of a CC and a NCC cluster, respectively (Million & Allen 2009). CC clusters exhibit a prominent peak, whereas NCC clusters have shallower profiles.

of the numeric density of galaxies can be described by a King (1962) model:

$$n_{\rm gal}(r) = n_{\rm gal,0}\left[1+\left(\frac{r}{r_{\rm c}}\right)^2\right]^{-\frac{3}{2}} \quad , \tag{1.5}$$

where $r_{\rm c}$ is the core radius and $n_{\rm gal,0}$ is the central numeric density.

Since galaxies and gas are subject to the same gravitational potential of the DM, their density profiles are reasonably correlated as $n_{\rm gas} \propto n_{\rm gal}^{\beta}$, where the slope β represents the ratio of the specific kinetic energy of the galaxies and the specific thermal energy of the gas. By considering the King model in Eq. 1.5 for the numeric galaxy density profile, the corresponding numeric gas density profile is known as 'β-model' (Cavaliere & Fusco-Femiano 1976):

$$n_{\rm gas}(r) = n_{\rm gas,0}\left[1+\left(\frac{r}{r_{\rm c}}\right)^2\right]^{-\frac{3}{2}\beta} \quad . \tag{1.6}$$

As a standard method, in practice, the density profile is computed from the observed projected surface brightness profile $I_{\rm X}$, being:

$$I_{\rm X}(r) = \sqrt{\pi} r_{\rm c} n_{\rm gas,0}^2 \frac{\Gamma(3\beta-0.5)}{\Gamma(3\beta)}\left[1+\left(\frac{r}{r_{\rm c}}\right)^2\right]^{\frac{1}{2}-3\beta} \quad , \tag{1.7}$$

where $\Gamma(z) = \int_0^\infty t^{z-1}e^{-t}{\rm d}t$ is the Gamma function.

The β-model is commonly used to fit the radial profile of NCC clusters (e.g. Forman et al. 1984; Arnaud et al. 2002; Arnaud 2009), with typical fitted parameters $\beta \sim 0.6-0.7$ and $r_{\rm c} \sim 200-300$ kpc. On the other hand, it should be noticed that this is only a rough representation that does not take into account possible sub-structures and fluctuations in the real density profiles. In this respect, a simple β-model cannot properly reproduce the

observed profiles of CC clusters, which exhibit a peaked inner distribution and a shallower outer distribution more similar to NCC clusters (e.g. Eckert et al. 2011). The density profile of CC clusters can be fitted with alternative functions, such as a double β-model or a cuspy β-model (e.g. Pratt & Arnaud 2002), or even much more complex, but flexible expressions (e.g. Vikhlinin et al. 2006).

1.3.3 Cooling in CC clusters

In Sect. 1.3.1 we demonstrated that the radiative cooling of the ICM is not efficient (Eq. 1.4). On the other hand, Eq. 1.6 indicates that the density is not constant, but increases towards the centre. For NCC clusters this increase is moderate due to a shallower profile and cooling is still negligible, whereas for CC clusters the central density is much higher and cooling plays an important role. In this respect, for CC clusters a cooling radius $r_{\rm cool}$ can be defined as the radial distance for which $t_{\rm cool} = t_{\rm H}$; for $r \ll r_{\rm cool}$, $t_{\rm cool} \ll t_{\rm H}$ and the ICM can more efficiently cool down.

Within $r_{\rm cool}$, the temperature of the ICM decreases due to the radiative cooling. To maintain the pressure equilibrium between the cooler and hotter gas at $r_{\rm cool}$, an increase in density is required, being $P = \frac{\rho kT}{\mu m_{\rm p}}$ for ideal gas. Therefore, the hotter gas inflows from outer regions towards the centre, where it 'rapidly' cools according to Eq. 1.3; further gas then moves inwards and cools down, thus establishing a natural and continuous self-induced process called 'cooling flow' (Fabian et al. 1994). In this scenario, CC clusters are relaxed systems with a cuspy central density profile, which enhances the X-ray luminosity (Eq. 1.3), and favours the radiative cooling through a stable cooling flow.

In spite of its predictions, the cooling flow scenario cannot explain some observational evidences of CC clusters. First, when the temperature drops below ~ 2 keV, line emission from heavy ions further increases the efficiency of the cooling; moreover, the model predicts a mass rate of cooling gas within $r_{\rm cool}$ which can be inferred from the observed X-ray luminosity as:

$$\dot{M}_{\rm cool} = \frac{2}{5}\frac{\mu m_{\rm p}}{kT} L_{\rm X} \sim 458 \times \left(\frac{L_{\rm X}}{10^{44}\ {\rm erg\ s^{-1}}}\right)\left(\frac{T}{10^{7}\ {\rm K}}\right)^{-1} \quad {\rm M_{\odot}\ yr^{-1}} \quad . \tag{1.8}$$

Observations do not confirm neither the predicted emission lines, nor such an high mass rate of dense and cold gas that would give rise to an extremely intense star formation, thus raising the 'cooling flow problem' (e.g. Fabian et al. 1994; Peterson & Fabian 2006; Hudson et al. 2010).

X-ray spectra of CC clusters show that the temperature never drops below $\sim 1/3$ of the virial temperature $T_{\rm vir}$ (e.g. Molendi & Pizzolato 2001; Peterson et al. 2001; Kaastra et al. 2004). This suggests that an heating source partially inhibits the radiative cooling of the ICM. Among the various sources of heating that have been proposed, the most plausible are AGN (Fabian 2012, for a review). Only a fraction of cold gas becomes fuel for the star formation, whereas the rest feeds the (quiescent) super massive black hole (SMBH) at the centre of the BCG, thus triggering its activity. The mechanical work done by its jets while expanding through the ICM is able to heat the surrounding medium. Observational evidences supporting the hypothesis of AGN as source of heating have come with the

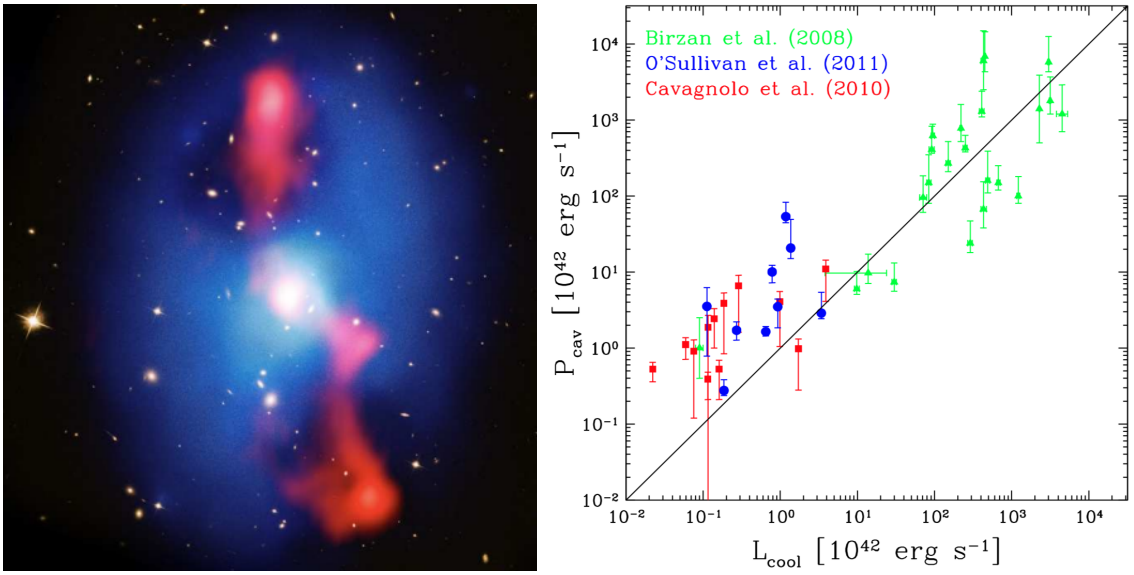

Figure 1.7: *Left*: Composite optical (HST in yellow), X-ray (Chandra in blue), and radio (VLA in red) image of MS 0735+7421, showing the X-ray cavities filled by the radio lobes of the central radio galaxy (Gitti et al. 2012a). *Right*: Mechanical power of the jets ($P_{\rm cav}$) vs X-ray luminosity ($L_{\rm cool}$) within the cooling radius. As $P_{\rm cav} \gtrsim L_{\rm cool}$, the AGN heating can balance the ICM cooling (Gitti et al. 2012a).

discovery of the X-ray cavities (see Fig. 1.7). Cavities are regions in the ICM exhibiting a deficit of thermal gas and hence detected as depressions of the X-ray surface brightness, which are filled by the radio lobes of the central AGN (e.g. Blanton et al. 2001; Bîrzan et al. 2004; McNamara et al. 2005; McDonald et al. 2015; Bîrzan et al. 2020). The work $P_{\rm cav}$ done by the jets to excavate the ICM and form the cavity is found to be $\gtrsim L_{\rm X}$, thus indicating that the AGN mechanical heating may balance the ICM radiative cooling (e.g. O'Sullivan et al. 2011; Gitti et al. 2012a). Further heating mechanisms associated with the central AGN may be weak shocks or dissipation of sound waves in the ICM induced by the expansion of the radio jets (e.g. Fabian et al. 2006; Forman et al. 2007).

The balance between cooling and heating may also explain the life cycles of AGN, under the 'self-regulated AGN feedback loop' scenario (e.g. McNamara & Nulsen 2012). The own work of the jets reduces the available cold gas for the AGN, which thus progressively quenches. After this process, a quiescent phase is established, until further gas inflows towards the centre, cools, and re-activates the AGN in a new cycle.

1.3.4 Thermal Sunyaev-Zel'dovich effect

The CMB consists of thermal radiation emitted in the early Universe ($\sim$ 380 Myr after the Big Bang), which is observed today as a black body Planck distribution peaking at $\lambda \sim 2$ mm ($\nu \sim 150$ GHz) and temperature $T \sim 2.7$ K. In addition to primary anisotropies, which are the signatures of the primordial density fluctuations (see Sect. 1.1), secondary

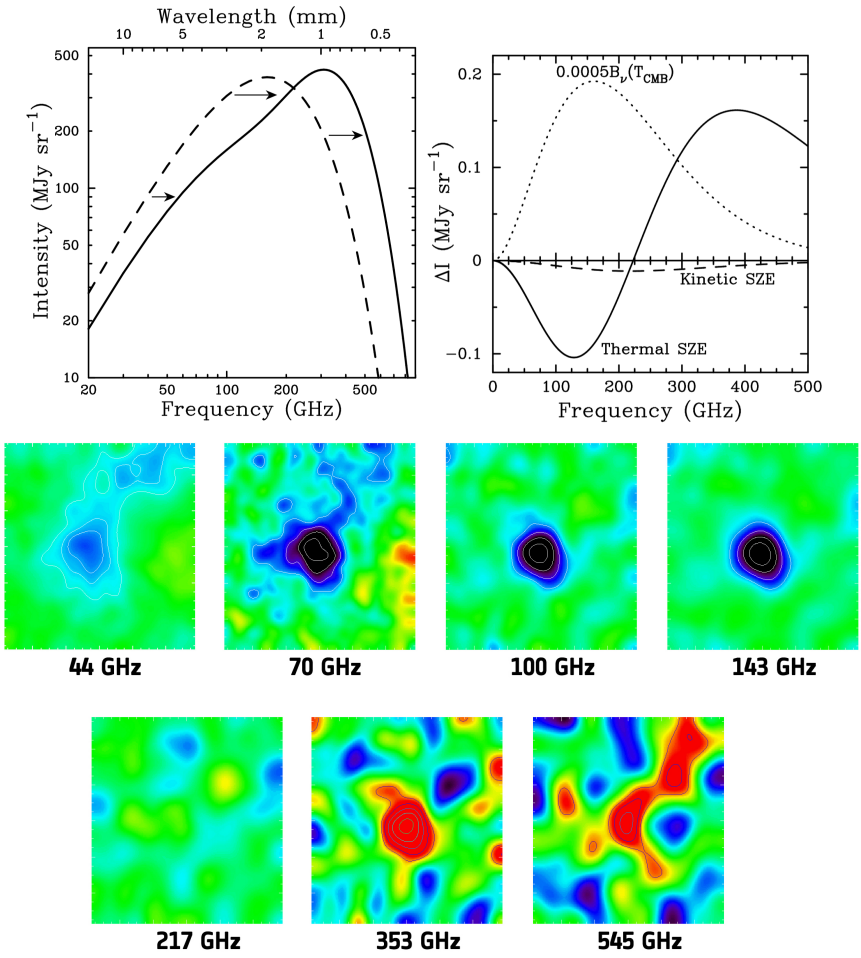

Figure 1.8: *Top*: Deformation and shifting of the initial CMB distribution due to the SZ effect (left) and absolute brightness fluctuations (right) as a function of the frequency (Carlstrom et al. 2002). *Bottom*: Multifrequency Planck observations of A2319, showing negative ($\nu < 218$ GHz), null ($\nu = 217$ GHz), and positive ($\nu > 218$ GHz) SZ signal (credits: ESA / HFI & LFI Consortia)

anisotropies are caused by the interaction with the matter on the path to the observer.

Among the secondary anisotropies, the thermal Sunyaev-Zel'dovich (SZ) effect (Sunyaev & Zeldovich 1972) involves thermal particles in the ICM and is a powerful tool for galaxy cluster studies (Carlstrom et al. 2002; Aghanim et al. 2008, for reviews). The cooler CMB photons can be scattered by the hotter thermal electrons of the ICM ($T_{\rm CMB} \ll T_{\rm e}$) through inverse Compton. The initial Planck distribution is thus shifted and re-shaped, showing fluctuations in amplitude and/or temperature as

$$\frac{\Delta I}{I} \propto \frac{\Delta T}{T} \propto \int_L n_{\rm e} T_{\rm e} {\rm d}l = y_{\rm SZ} \quad , \tag{1.9}$$

and described by the Compton y-parameter ($y_{\rm SZ}$), which is a measure of the thermal pressure of the ICM along the line of sight. As shown by the example in Fig. 1.8, the SZ signal from a galaxy cluster is frequency-dependent because fluctuations are negative for $\nu < 218$ GHz, null for $\nu = 218$ GHz, and positive for $\nu > 218$ GHz.

The SZ effect is a powerful tool to detect galaxy clusters (Hasselfield et al. 2013; Reichardt et al. 2013; Planck Collaboration et al. 2014). Owing to the cosmological dimming, the X-ray surface brightness of the ICM rapidly drops with redshift ($I_{\rm X} \propto (1+z)^{-4}$); on the other hand, $y_{\rm SZ}$ does not depend on z for unresolved targets, thus allowing us to detect high-redshift galaxy clusters. Moreover, $I_{\rm X} \propto n_{\rm e}^2$, while $y_{\rm SZ} \propto n_{\rm e}$, allowing us to constrain the density profile of the ICM in the rarefied outskirts of the cluster. Finally, the Compton y-parameter is a proxy for the mass of the cluster, as described in Sect. 1.5.

1.4 Overview on cluster mergers

Galaxy clusters experience various mergers that allow them to grow and evolve. Mergers of clusters are the most energetic events in the Universe after the Big Bang, releasing energies $E \sim 10^{63} - 10^{64}$ erg in a time scale of $t_{\rm cross} \sim 1-2$ Gyr. These mergers have extreme consequences on the ICM, which can be observed in the X-rays to infer information on the dynamical state of the cluster.

1.4.1 Dynamics of mergers

Let us consider two galaxy clusters of masses M_1 and M_2. Due to the expansion of the Universe, they initially move apart one another and have null radial velocities. The two clusters start to gravitationally interact at a certain $t_{\rm merge}$ (i.e. the age of the Universe at the merger time), when they reach the turn-around distance d_0; from this moment on, they can be treated in the framework of a binary system, as depicted in Fig. 1.9. The third Kepler law provides an estimate of typical turn-around distances (Sarazin 2002):

$$d_0 \sim 4.5 \times \left(\frac{M_1 + M_2}{10^{15}\ {\rm M}_\odot}\right)^{\frac{1}{3}} \left(\frac{t_{\rm merge}}{10\ {\rm Gyr}}\right)^{\frac{2}{3}} \quad {\rm Mpc} \quad . \tag{1.10}$$

By using the conservation laws of orbital energy and angular momentum, it is possible to compute the relative impact velocity $v_{\rm imp}$ as a function of the distance d separating the

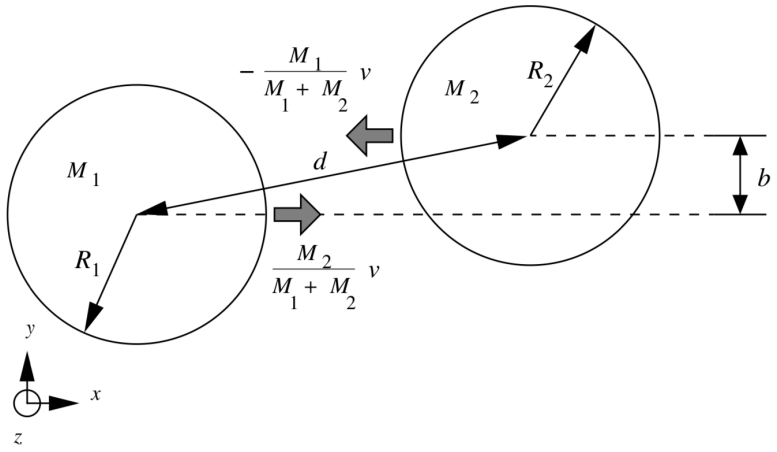

Figure 1.9: Schematic view of the dynamics of a cluster merger (Ricker & Sarazin 2001). The two clusters of masses M_1 and M_2, separated by a distance d, collide with a relative velocity $v_{\rm imp}$ and an impact parameter b.

two clusters as (Ricker & Sarazin 2001):

$$v_{\rm imp} \sim 2930 \times \left(\frac{M_1+M_2}{10^{15}\ {\rm M}_\odot}\right)^{\frac{1}{2}} \left(\frac{d}{1\ {\rm Mpc}}\right)^{\frac{1}{2}} \left[\frac{1-\frac{d}{d_0}}{1-\left(\frac{b}{d_0}\right)^2}\right]^{\frac{1}{2}} \quad {\rm km\ s^{-1}} \quad , \tag{1.11}$$

where $b \sim 150$ kpc $\ll d_0$ is a typical value of the impact parameter (Sarazin 2002), indicating that the merger involves the innermost regions of the clusters as well, with important consequences on their cores. For advanced stages of the merger, when $d \ll d_0$, the last term in Eq. 1.11 is ~ 1, therefore typical impact velocities are $v_{\rm imp} \sim 3000$ km s^{-1}.

1.4.2 Shocks and cold fronts

The sound velocity $c_{\rm s}$ in the ICM is:

$$c_{\rm s} = \sqrt{\frac{\Gamma kT}{\mu m_{\rm p}}} \sim 1520 \times \sqrt{\frac{T}{10^8\ {\rm K}}} \quad {\rm km\ s^{-1}} \tag{1.12}$$

By comparing Eqs. 1.11 and 1.12, the impact velocity is higher than the sound velocity in the ICM, meaning that cluster mergers are (weakly) super-sonic, with typical Mach-numbers $\mathcal{M} \sim 2$ (e.g. Gabici & Blasi 2003).

As a consequence, mergers generate weak shocks that affect the thermal properties of the ICM and can be detected in the X-rays as surface brightness discontinuities. The Hugoniot-Rankine jump conditions can be used to derive the ratios of temperature, density, and pressure in the downstream (perturbed) and upstream (unperturbed) regions of the ICM (Landau & Lifshitz 1959):

$$\frac{T_{\rm down}}{T_{\rm up}} = \frac{5\mathcal{M}^4 + 14\mathcal{M}^2 - 3}{16\mathcal{M}^2}$$

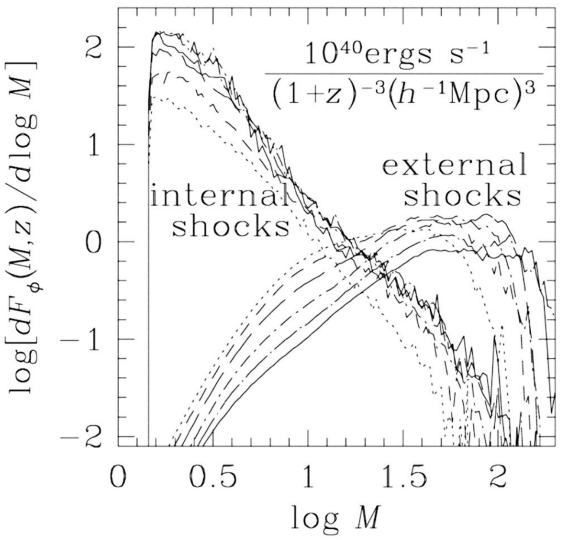

Figure 1.10: Energy flux of the shock as a function of the Mach-number, obtained from cosmological simulations (Ryu et al. 2003). Internal shocks have lower $\mathcal{M}$, but higher energy flux than external shocks, owing to the denser environments where the former propagate.

$$\frac{\rho_{\rm down}}{\rho_{\rm up}} = \frac{4\mathcal{M}^2}{\mathcal{M}^2+3} \qquad . \tag{1.13}$$

$$\frac{P_{\rm down}}{P_{\rm up}} = \frac{5\mathcal{M}^2-1}{4}$$

Part of the kinetic energy of the merger is dissipated through these shocks, which contribute to the heating of the ICM (e.g. Schindler & Muller 1993). Moreover, merger shocks can transfer energy to non-thermal components in the ICM, possibly triggering the formation of radio relics (see details in Sect. 2.4 in Chapter 2).

Merger shocks are also known as internal shocks, in contrast to external shocks. The continuous infall of matter from the cosmic filaments occurring in the unvirialised cluster outskirts generate external strong shocks (e.g. Miniati et al. 2001; Ryu et al. 2003). Despite much higher $\mathcal{M} \sim 10-100$ than that of mergers, external shocks propagate in regions of lower temperature and density and therefore the energy dissipation is inefficient (see Fig. 1.10).

In addition to shocks, X-ray surface brightness discontinuities can be associated also with cold fronts. These are contact discontinuities (i.e. $P_{\rm down} = P_{\rm up}$) between cooler and hotter gas phases, which exhibit opposite temperature gradients ($T_{\rm down} < T_{\rm up}$) with respect to shocks (Markevitch & Vikhlinin 2007, for a review). 'Merging' and 'sloshing' cold fronts are found in NCC and CC clusters, respectively (see examples in Fig. 1.11). In NCC clusters, merging cold fronts are signatures of the remnants of the cool core of a sub-cluster, which is in pressure equilibrium with the shocked and hotter surrounding gas (e.g. Vikhlinin et al. 2001; Markevitch et al. 2002). Despite CC clusters have not experienced a recent major merger, minor mergers can occur in these systems as well,

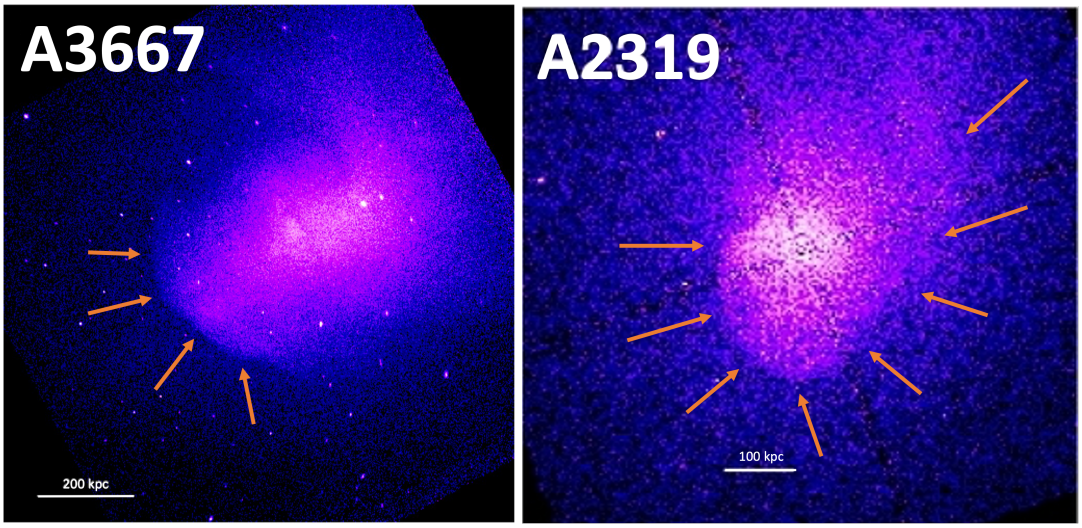

Figure 1.11: Examples of merging and sloshing cold fronts (indicated by arrows). *Left*: Merging cold front in A3667 (adapted from Zuhone & Roediger 2016). The edge at SE is associated with the remnant cool core a sub-cluster, in pressure equilibrium with the hotter ICM. *Right*: Sloshing cold front in A2319 (adapted from ZuHone et al. 2013). The spiral-like cold front is associated with sloshing of cold gas in the core of the cluster, after it has been perturbed by a minor merger.

and gently perturb their central regions without completely disrupt the cool core. As a result of a minor merger, a fraction of cold gas can be displaced from the centre of the potential well, thus acquiring angular momentum and triggering oscillating (sloshing) motions, which produce a spiral-shaped cold front typically confined within the innermost regions of the cluster (e.g. Clarke et al. 2004; Simionescu et al. 2010; Ehlert et al. 2015).

Cold fronts are not only important probes of the dynamics of mergers, but also of the microphysics of the ICM. Indeed, they allow us to investigate the suppression of thermal conduction across the front, the redistribution of metallicity due to sloshing on larger scales, and the viscosity and magnetic field through the possible development of Kelvin-Helmholtz instabilities (Zuhone & Roediger 2016, for a review). In addition, sloshing might be connected with the formation of radio mini-halos in relaxed clusters (see details in Sect. 2.6 in Chapter 2).

1.4.3 Turbulence

In addition to weak shocks, mergers can induce turbulence in the ICM on large scales, which can be studied through numerical simulations (e.g. Dolag et al. 2005; Vazza et al. 2009; Iapichino et al. 2011; Miniati 2014; Wittor et al. 2017; Vazza et al. 2018; Angelinelli et al. 2020; Vallés-Pérez et al. 2021). Turbulence can transfer energy and momentum to non-thermal components and originate giant radio halos (see details in Sect. 2.5 in Chapter 2).

The direct observation of turbulence can be achieved through high resolution X-ray

spectroscopy, which can provide the measure of the turbulent velocity responsible for the Doppler broadening of ion emission lines. At present, this method has been applied only once (in the Perseus cluster) thanks to the Hitomi satellite (Hitomi Collaboration et al. 2016), which however was lost after just few weeks of activity. Hitomi measured a turbulent velocity dispersion of $\sigma_{\rm turb} \sim 150$ km s^{-1} within the inner ~ 50 kpc from the core of Perseus. Accurate measures of $\sigma_{\rm turb}$ are essential to constrain the turbulent power per unit volume $P_{\rm turb} \propto \sigma^3_{\rm turb} n_{\rm therm} L^{-1}_{\rm turb}$ injected in the ICM on typical scales $L_{\rm turb} \sim 500$ kpc (e.g. Eckert et al. 2017).

Indirect constraints on the turbulent motions are currently inferred from X-ray observations, by computing the power spectrum of the fluctuations in pressure, temperature, density, entropy, and surface brightness of the ICM (e.g. Schuecker et al. 2004; Churazov et al. 2012; Gaspari et al. 2014; Zhuravleva et al. 2014, 2015).

1.4.4 X-ray morphological parameters

The ICM distribution is particularly sensitive to the dynamical history of the cluster. Therefore, important information on the dynamical state of a cluster can be inferred through morphological parameters of the ICM derived from X-ray observations (e.g. Buote 2001; Santos et al. 2008; Cassano et al. 2010; Rasia et al. 2013; Parekh et al. 2015; Rossetti et al. 2017; Lovisari et al. 2017). Two solid morphological parameters are the concentration parameter (c), which is more sensitive to the core properties, and the centroid shift (w), which is sensitive to the presence of substructures.

The concentration parameter (Santos et al. 2008) is defined as the ratio of the X-ray flux F within two circular apertures centred on the peak of the X-ray emission. To the aims of this Thesis (see also Chapters 4 and 6), following Cassano et al. (2010), we consider inner and outer apertures of physical radii 100 and 500 kpc, respectively, thus yielding:

$$c = \frac{F(r < 100 \text{ kpc})}{F(r < 500 \text{ kpc})} \quad . \tag{1.14}$$

The centroid shift parameter (Mohr et al. 1993; Poole et al. 2006) is defined as the variance of the separation between the X-ray peak and the centroid of the emission obtained within a number N of apertures of increasing radius out to a certain aperture radius, which we assume 500 kpc as in Cassano et al. (2010):

$$w = \left[\frac{1}{N-1} \sum_i (\Delta_i - \overline{\Delta})^2 \right]^{\frac{1}{2}} \frac{1}{500 \text{ kpc}} \quad , \tag{1.15}$$

where Δ_i is the centroid for the i-th aperture and $\overline{\Delta}$ is the average centroid.

By definition, more relaxed (CC) clusters are characterised by higher values of c and lower values of w; conversely, more disturbed (NCC) clusters are characterised by lower values of c and higher values of w.

1.5 Cluster mass

The mass is a fundamental quantity to understand the properties, formation, and evolution of galaxy clusters. In this Section we review the various methods used to derive the cluster mass, bearing in mind that each method is based on underlying (physical and/or technical) assumptions which may be not representative of a specific target, thus leading to discrepant measures (we refer to Ettori et al. 2013; Limousin et al. 2013; Sereno et al. 2017, for recent reviews).

Virial mass

As mentioned in Sect. 1.3.2, the inner regions of the cluster reach the virial equilibrium through violent relaxation in $\sim t_{\rm cross}$, whereas the outer regions are unrelaxed. The boundary between the relaxed and unrelaxed regions is determined by the virial radius $R_{\rm vir}$; in the literature, it is usually considered $R_{\rm vir} \sim R_{200}$ (e.g. Walker et al. 2019), being in general R_Δ the radius enclosing $\Delta \times \rho_{\rm c}(z)$, where $\rho_{\rm c}(z) \propto H^2(z)$ is the critical density of the Universe at a given redshift ($H(z)$ is the Hubble parameter).

Through the virial theorem, the (virial) mass is obtained from the velocity dispersion of the member galaxies σ_v as:

$$M_{200} = 1.73 \times 10^{15} \left(\frac{\sigma_v}{1000 \text{ km s}^{-1}} \right)^3 \left(\frac{H(z)}{70 \text{ km s}^{-1} \text{ Mpc}^{-1}} \right)^{-1} \quad M_\odot \quad . \tag{1.16}$$

Hydrostatic mass

Let us assume that galaxy clusters have a spherical symmetry, and that the ICM is in hydrostatic equilibrium within the gravitational potential generated by the total (baryonic and dark matter) mass $\phi = -\frac{GM(r)}{r}$. Through the equation of state for an ideal gas $P = \frac{\rho(r) k T(r)}{\mu m_{\rm p}}$ and the hydrostatic equilibrium equation, it is possible to derive the (hydrostatic) mass as:

$$M(r) = -\frac{r k T_{\rm gas}}{G \mu m_{\rm p}} \left[\frac{{\rm d}\log(\rho_{\rm gas})}{{\rm d}\log(r)} + \frac{{\rm d}\log(T_{\rm gas})}{{\rm d}\log(r)} \right] \quad , \tag{1.17}$$

Eq. 1.17 provides an estimate of the total mass within r as a function of the temperature and density profiles of the ICM, which can be inferred from X-ray spectra and SZ observations (e.g. Ettori et al. 2013).

Mass from gravitational lensing

The gravitational lensing is an effect of General Relativity occurring when the trajectories of photons from a background source along the line of sight are bent when passing close by a massive object such as a galaxy cluster. A schematic sketch and a spectacular example of this phenomenon observed by Hubble Space Telescope (HST) are shown in Fig. 1.12. As gravitational lensing amplifies the light of a source, the most distant and faintest objects in the Universe can be detected through this effect (e.g. Coe et al. 2013).

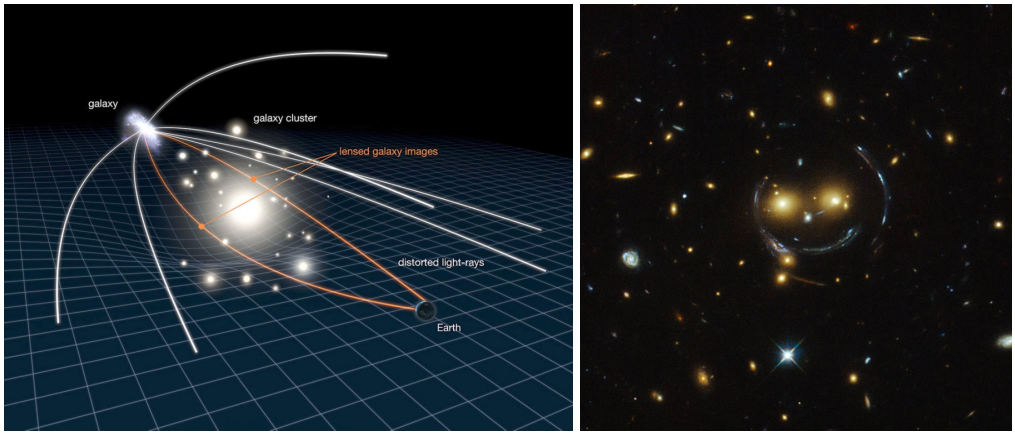

Figure 1.12: *Left*: Schematic sketch of the gravitational lensing effect. The gravitational field of the lens galaxy cluster deflects and amplifies the photons coming from the background source. *Right*: Example of a lensed background galaxy observed by HST. The light of the galaxy is bent by the strong gravitational field of the galaxy cluster SDSS J1038+4849, thus producing a system of arcs (credits: NASA/ESA).

The geometrical distortion of the lensed background source can be exploited to infer the DM distribution of the lens cluster (e.g. Hoekstra et al. 2013). In the case of strong lensing, the background photons are deflected along circular trajectories, which produce arcs and possible multiple images of the same source. From the geometry of the lensed source, the mass of the lens cluster can be inferred as (Bartelmann et al. 2003):

$$M \sim \pi r^2 \Sigma_{\rm crit} \quad , \tag{1.18}$$

where $\Sigma_{\rm crit}$ is the critical surface mass density for lensing, defined as:

$$\Sigma_{\rm crit} = \frac{c^2}{4\pi G} \frac{D_{\rm S}}{D_{\rm LS} D_{\rm L}} \quad , \tag{1.19}$$

being $D_{\rm L}$, $D_{\rm LS}$, $D_{\rm S}$ the distances from the observer to the lens, from the lens to the source, and from the observer to the source, respectively.

Mass from intrinsic Compton parameter

In Sect. 1.3.4 we described the thermal SZ effect. This phenomenon can be exploited to provide accurate measures of the cluster mass (e.g. Metzler 1998; White et al. 2002). More specifically, by integrating $y_{\rm SZ}$ over the solid angle Ω, we obtain the integrated Compton y-parameter $Y_{\rm SZ}$:

$$Y_{\rm SZ} = \int_{\Omega} y_{\rm SZ} {\rm d}\Omega \quad . \tag{1.20}$$

The $Y_{\rm SZ}$ parameter has the meaning of a flux, and can thus be related to the analogous of a luminosity (by multiplying by the squared angular distance $D_{\rm A}$), expressed by the

intrinsic Compton y-parameter $\Upsilon_{\rm SZ}$ as:

$$\Upsilon_{\rm SZ} = D_{\rm A}^2 Y_{\rm SZ} = D_{\rm A}^2 \int_\Omega y_{\rm SZ} {\rm d}\Omega = \int_L \int_S y_{\rm SZ} {\rm d}L {\rm d}S \propto \int_V n_{\rm e} T_{\rm e} {\rm d}V \quad . \tag{1.21}$$

As shown from Eq. 1.21, the $\Upsilon_{\rm SZ}$ parameter is the integral measure of the gas pressure over the volume of the cluster. Therefore, $\Upsilon_{\rm SZ} \propto M_{\rm gas} T_{\rm gas}$ provides an estimate of the mass of the ICM.

Chapter 2

Non-thermal phenomena in galaxy clusters

Observations in the radio band allow the detection of synchrotron radiation in galaxy clusters. This radio emission implies the presence of non-thermal components, namely relativistic particles and magnetic fields, that are either associated with radio galaxies or are mixed with the thermal particles of the ICM.

In this Chapter we briefly review some formulas derived for the synchrotron emission, summarise the properties of radio galaxies in clusters, and describe the non-thermal components of the ICM. We then focus on the various forms of diffuse radio sources in clusters and the fundamental role of low frequency observations to probe their origin, which are the main topics of this Thesis.

2.1 Radio emission

A relativistic particle moving at velocity $\vec{v}$ in a magnetic field $\vec{B}$ emits synchrotron radiation with power given by (Rybicki & Lightman 1979):

$$P_{\rm synch} \propto \beta^2 \gamma^2 B^2 \sin^2\theta \quad , \tag{2.1}$$

where $\beta = \frac{v}{c}$, $\gamma = \left(1-\beta^2\right)^{-\frac{1}{2}}$ is the Lorentz factor, and θ is the pitch angle between $\vec{v}$ and $\vec{B}$.

A non-thermal population of electrons can be described with a power-law distribution in terms of momentum as $N(p) \propto p^{-\delta}$, being δ the injection index. These electrons emit by synchrotron emission in the radio band for typical electron momenta and magnetic fields in galaxy clusters (see Sects. 2.3.1, 2.3.2), with a flux density $S(\nu) \propto \nu^{-\alpha}$, where $\alpha = (\delta - 1)/2$ is the spectral index. By measuring the flux density $S_1 = S(\nu_1)$ and $S_2 = S(\nu_2)$ at two different frequencies, it is possible to compute α as

$$\alpha = -\frac{\log\left(\frac{S_1}{S_2}\right)}{\log\left(\frac{\nu_1}{\nu_2}\right)} \quad , \tag{2.2}$$

which is used to obtain the k-corrected monochromatic radio power as

$$P_\nu = 4\pi S_\nu D_{\rm L}^2 (1+z)^{\alpha-1} \quad , \tag{2.3}$$

where $D_{\rm L}$ is the luminosity distance to the source.

Eq. 2.1 points out that more energetic electrons loose their energy faster by emitting synchrotron radiation. This causes a progressive steepening of the original spectrum above a 'break' frequency $\nu_{\rm break}$ during the lifetime of a radio source. In addition to the synchrotron emission, electrons further cool due to non-thermal inverse Compton interaction with the CMB photons; radiative losses by inverse Compton can be parametrised by introducing an equivalent, redshift-dependent, magnetic field of the CMB, being $B_{\rm CMB} = 3.25(1+z)^2$ μG. This is used to estimate the radiative age of a radio source cooling through synchrotron and inverse Compton emission as (e.g. Murgia et al. 1999):

$$t_{\rm rad} = 1590 \times \frac{\sqrt{B}}{B^2 + B_{\rm CMB}^2} \frac{1}{\sqrt{(1+z)\nu_{\rm break}}} \quad {\rm Myr} \quad , \tag{2.4}$$

where magnetic fields are in units of μG and the break frequency is in units of GHz.

2.2 Radio galaxies in clusters

Radio galaxies were first classified by Fanaroff & Riley (1974) into the morphological FRI and FRII classes. The radio power of FRIs is dominated by the core, whereas their jets are decelerated and weakened on scales $\ll$ kpc by the dense environment in which they expand; on the other hand, the jets of FRIIs maintain relativistic and supersonic velocities on scales $\gtrsim$ kpc, exhibit hotspots at their tips, and produce powerful radio lobes when they impact on the environment gas (e.g. Saripalli 2012; Mingo et al. 2019; Hardcastle & Croston 2020).

Radio galaxies in clusters are mainly FRIs, but their jets can interact with the surrounding ICM and give rise to spectacular morphologies (e.g. O'Dea & Owen 1985). If the host galaxy moves at high ($v \sim 1000$ km s^{-1}) relative velocities, it is subject to a strong ram pressure $P_{\rm RAM} = \rho_{\rm ICM} v^2$, which is able to extremely deflect the radio jets by $\sim 90^{\rm o}$ and form an head-tail (HT) galaxy (e.g. Miley et al. 1972), whereas moderate deflections by $\ll 90^{\rm o}$, possibly associated with merging subclusters, form a wide-angle tail (WAT) galaxy (e.g. Owen et al. 1978; Pinkney et al. 1993). The radio galaxies hosted by the BCG can show complex morphologies as well, such as X-shaped (XRG) and Z-shaped (ZRG) galaxies (e.g. Wirth et al. 1982; Bruno et al. 2019; Hardcastle et al. 2019; Ignesti et al. 2020b); their origin is still unclear, but may be associated with re-orientation of jets, hydro-dynamical interaction between the jets and the host galaxy gas, or presence of multiple AGN (Gopal-Krishna et al. 2012, for a review). In Fig. 2.1 we report some examples of the large variety of morphologies of radio galaxies.

2.3 Non-thermal components in the ICM

In this section we review the properties of magnetic fields and relativistic particles in the ICM, which produce cluster-scale diffuse synchrotron radio emission.

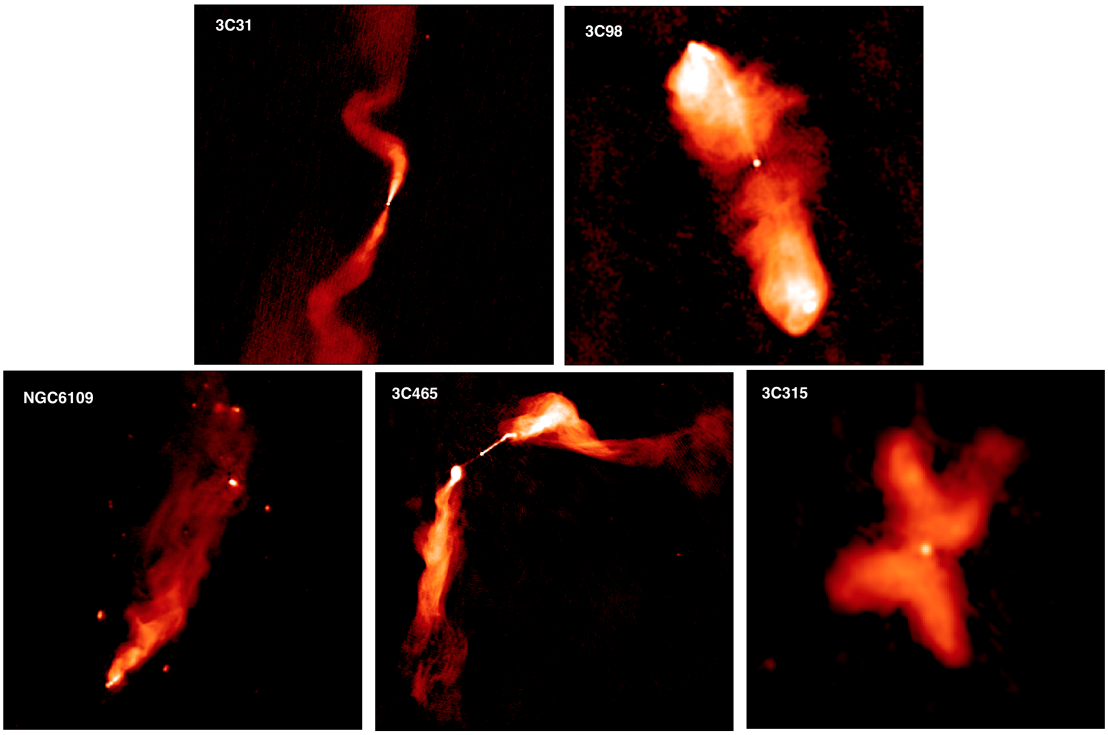

Figure 2.1: Examples of radio galaxies showing different morphologies (Hardcastle & Croston 2020): 3C31 is an FRI (top left), 3C98 is an FRII (top right), NGC6109 is an HT (bottom left), 3C465 is a WAT (bottom middle), 3C315 (bottom right) is an XRG.

2.3.1 Magnetic fields

The existence of large scale diffuse synchrotron sources such as radio halos and relics demonstrates that the ICM is a magnetised plasma consisting of both thermal and non-thermal particles.

Accurate measures on the ICM magnetic field strength are routinely derived by exploiting the Faraday rotation phenomenon (e.g. Feretti et al. 2012). When a synchrotron radio wave emitted by a background radio galaxy passes through a magnetised plasma, its linear polarisation vector is rotated by an angle $\Delta\Psi$, which depends on the (squared) wavelength itself and on the properties of the plasma as:

$$\Delta\Psi = \lambda^2 RM = 812 \cdot \lambda^2 \int_0^L \left(\frac{n_\mathrm{e}}{\mathrm{cm}^{-3}}\right)\left(\frac{B_\parallel}{\mu\mathrm{G}}\right)\left(\frac{\mathrm{dl}}{\mathrm{kpc}}\right) \quad \mathrm{rad\ m}^{-2} \quad , \tag{2.5}$$

where RM is the rotation measure, which is the integral over the crossed plasma layer L of the magnetic field component along the line of sight weighted by the thermal electron density. By measuring $\Delta\Psi$ at different radio frequencies and deriving n_e from X-ray observations, it is possible to constrain $B_\parallel$.

The Faraday rotation phenomenon has allowed to estimate average magnetic fields at levels of $B \sim 1 - 10\ \mu$G in the ICM (e.g. Vogt & Enßlin 2005; Govoni & Feretti 2004). Numerical simulations and observations show that the magnetic field is not constant over the ICM, but decreases outwards (Dolag et al. 2001; Murgia et al. 2004; Bonafede et al. 2010); the magnetic field is thought to scale as a power-law of the thermal particle density profile as:

$$B(r) = B_0 \left(\frac{n_\mathrm{e}(r)}{n_{\mathrm{e},0}}\right)^\eta \quad , \tag{2.6}$$

where likely slopes are in the range $\eta = 0.4 - 0.7$, as found for the Coma cluster by Bonafede et al. (2010). Notable slopes in this range are $\eta = 0.5$, which would indicate a proportionality of the magnetic and thermal energy densities, and $\eta \sim \beta$, which would instead suggest a magnetic field frozen in the ICM.

The origin of cosmic magnetic fields on large scales is still debated. They possibly arise from very weak ($\ll$ nG) primordial fields, which then have been amplified by turbulent dynamos induced by the structure formation (Dolag et al. 2008; Ryu et al. 2012; Subramanian 2016; Donnert et al. 2018, for reviews). At lower redshifts ($z \sim 2 - 3$), outflows from AGN, supernovae, and galactic winds can contribute to inject and further amplify the magnetic fields (e.g. Bertone et al. 2006; Donnert et al. 2009; Xu et al. 2009; Beck et al. 2013; Samui et al. 2018).

2.3.2 Relativistic particles

Shock waves and large-scale turbulence generated during the formation of cosmic structures are thought to be the main accelerators of relativistic particles. In addition, various sources (AGN, supernovae, galactic winds) are able to inject relativistic particles in the ICM. Depending on their energy, cosmic ray electrons (CRe) and protons (CRp) are subject to different processes that determine their lifetimes (Brunetti & Jones 2014, for a review), as shown in Fig. 2.2.

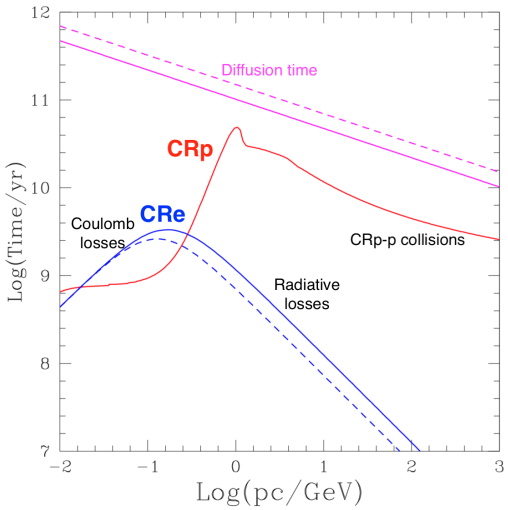

Figure 2.2: Lifetime of CRp (in red) and CRe (in blue) in the ICM as a function of energy and different processes, compared to the diffusion time (in magenta) required for CRp to reach Mpc-distances (adapted from Blasi et al. 2007). Solid and dashed lines refer to magnetic fields $B = 1$ μG and $B = 3$ μG, respectively.

Below energies $E \sim 100-300$ MeV, both CRp and CRe interact through Coulomb collisions. At higher energies, CRe emit synchrotron and inverse Compton radiation; these are the dominant cooling processes for CRe at $E \sim 5$ GeV, which are those responsible for the diffuse radio emission in clusters, and their corresponding maximum lifetime from Eq. 2.4 is $t_{\rm life} \sim 100$ Myr.

High-energy CRp are subject to inelastic hadronic collisions with the thermal protons of the ICM. Their lifetime is given by:

$$\tau_{\rm pp} \sim \frac{1}{c n_{\rm th} \sigma_{\rm pp}} \quad , \tag{2.7}$$

where $n_{\rm th}$ is the number density of thermal protons and $\sigma_{\rm pp}$ is the proton-proton inclusive cross section (Dermer 1986). Eq. 2.7 provides lifetimes of several Gyr for CRp.

Cosmic rays propagate throughout the ICM by diffusion. The short lifetimes of CRe do not allow them to reach scales $\gtrsim 100$ kpc by such process (e.g. Brunetti & Jones 2014). CRp have instead much longer lifetimes (e.g. Blasi et al. 2007), which allow them to diffuse over larger distances. Therefore, CRp are expected to be efficiently stored over the whole volume of the cluster; this favours the hadronic collisions, which are responsible for the generation of a cascade of by-products (pions, muons, electrons, positrons, neutrinos, gamma-ray photons), being:

$$p + p \longrightarrow \pi^0 + \pi^- + \pi^+$$

$$\pi^0 \longrightarrow \gamma\gamma$$

$$\pi^\pm \longrightarrow \mu^\pm + \nu_\mu$$

$$\mu^{\pm} \longrightarrow e^{\pm} + \nu_{\mu} + \nu_{e}$$

Non-thermal components in the ICM can generate different kinds of diffuse radio sources on scales $\gg$ 100 kpc, which are characterised by steep ($\alpha \gtrsim 1$) synchrotron spectral indices (Ferrari et al. 2008; Feretti et al. 2012; Brunetti & Jones 2014; van Weeren et al. 2019, for reviews). These sources are primarily classified on the basis of their morphology and location, but additional information such as optical images, dynamical state of the host cluster, local properties of the ICM, polarisation, and spectral index are important as well to unambiguously claim their nature. As mentioned above, $t_{\rm life} \ll t_{\rm diff}$ for CRe, meaning that the observed emission on large scales can only be explained by assuming that the emitting particles are produced in-situ (hadronic scenario) and/or are (re)-accelerated by some mechanisms occurring in the ICM (leptonic scenario). In the next sections, we review the properties of the diffuse sources, the proposed formation scenarios to solve the so-called 'slow diffusion problem', and the currently open questions. We then focus on the crucial role of low frequency observations, especially with LOFAR, to probe the origin of the diffuse sources.

2.4 Radio relics

Radio relics (RRs) are elongated and arc-shaped, Mpc-scale, diffuse sources mostly found in the peripheral regions of massive and disturbed clusters. In a number of cases, two RRs are detected at opposite sides with respect to the cluster centre, as in the prototypical example of CIZA J2242.8+5301 (e.g. van Weeren et al. 2010; Stroe et al. 2013; Hoang et al. 2017; Loi et al. 2017; Di Gennaro et al. 2018), also known as the 'Sausage' cluster (see Fig. 2.3). Other notable and well studied examples of RRs are those in the Coma (e.g. Thierbach et al. 2003; Bonafede et al. 2022a), Bullet (Shimwell et al. 2015), Toothbrush (e.g. van Weeren et al. 2012a; Rajpurohit et al. 2020), El Gordo (Lindner et al. 2014; Botteon et al. 2016b), A2255 (e.g. Pizzo et al. 2011; Botteon et al. 2020b), A2256 (e.g. van Weeren et al. 2012b; Rajpurohit et al. 2022c), A2744 (e.g. Pearce et al. 2017; Rajpurohit et al. 2021b), and A3667 (e.g. Hindson et al. 2014; de Gasperin et al. 2022) clusters.

2.4.1 Properties of RRs

There are many observational evidences indicating that the origin of RRs is associated with merger shocks (see also Sect. 1.4.2 in Chapter 1). X-ray images have allowed the detection of ICM shocks that are spatially coincident with RRs (e.g. Bourdin et al. 2013; Botteon et al. 2016b; Eckert et al. 2016; Akamatsu et al. 2017; Urdampilleta et al. 2018); spectroscopy and lensing studies have demonstrated that the orientation of the RR is generally perpendicular to the merger axis (e.g. Barrena et al. 2007; Boschin et al. 2013; Golovich et al. 2017), implying that shock propagates parallel to the major axis of the relic.

Multi-frequency radio observations have shown that the spectral index is steep ($\alpha \sim 1$) on average, with indications of radial steepening (see middle panel of Fig. 2.3) towards

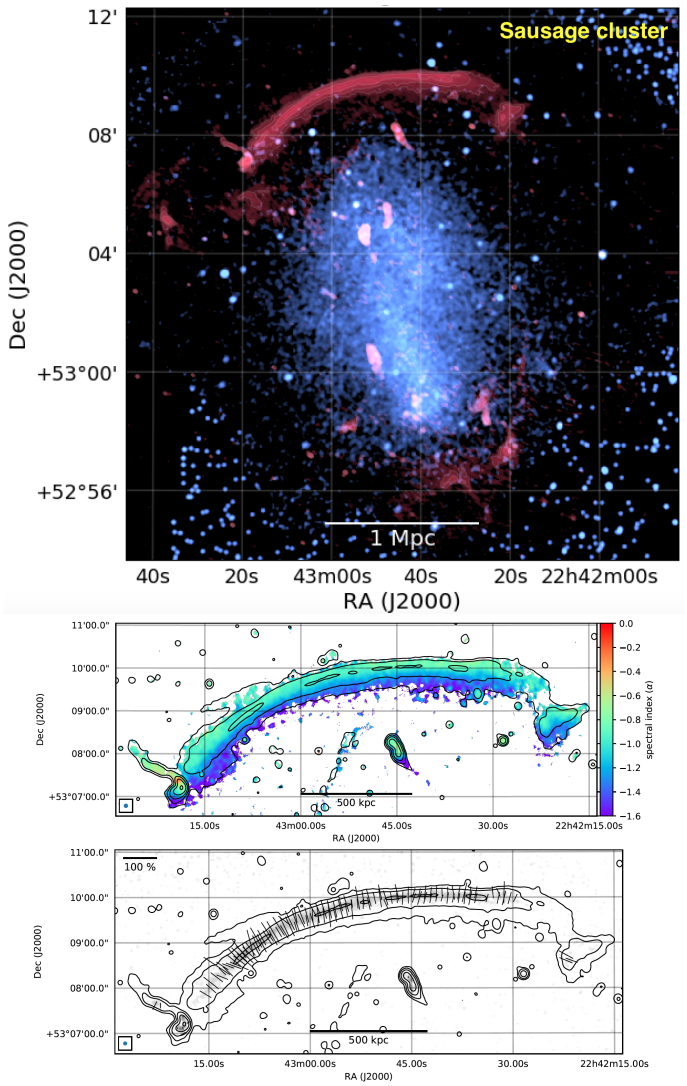

Figure 2.3: *Top*: Radio (red) and X-ray (blue) composite image of the Sausage cluster, which hosts two radio relics (van Weeren et al. 2019). *Middle*: Spectral index map of the northern relic between 150 and 3000 MHz. The spectral index steepens from the shock front towards the cluster centre (Di Gennaro et al. 2018). *Bottom*: Polarised intensity map of the northern relic at 3 GHz, showing the electric field vectors (van Weeren et al. 2019).

the cluster centre (e.g. Pearce et al. 2017; Di Gennaro et al. 2018; Rajpurohit et al. 2018), i.e. in the downstream region of the associated shock.

Finally, because of the high degree of polarisation ($\gg 20\%$) of RRs, it has been possible to find out that the magnetic field is aligned with the length (major axis) of the RR (e.g. Ensslin et al. 1998; van Weeren et al. 2010; Bonafede et al. 2012; Pearce et al. 2017), as shown in the bottom panel of Fig. 2.3).

2.4.2 Diffusive shock acceleration scenario

The observed radio properties and information at other wavelengths indicate that RRs trace particle acceleration and compression of the magnetic field associated with merger shocks via Fermi I-type mechanisms (Brunetti & Jones 2014, for a review). Particles are continuously scattered upstream and downstream the shock front, thus systematically gaining energy; this process is treated in the framework of the diffusive shock acceleration (DSA) theory (Krymskii 1977; Bell 1978a,b; Drury 1983), first developed for supernovae.

The momentum distribution of particles accelerated by DSA is $N_{\rm inj}(p) \propto p^{-\delta_{\rm inj}}$, where the injection index is related to the shock Mach-number as:

$$\delta_{\rm inj} = \frac{2\mathcal{M}^2 + 2}{\mathcal{M}^2 - 1} \quad . \tag{2.8}$$

Since merger shocks are associated with low $\mathcal{M} \sim 2 - 4$, the resulting injection index is notably steep ($\delta_{\rm inj} > 2$), meaning that the shock energy is primarily transferred to the low-energy particles, whereas high-energy particles are not efficiently accelerated. Afterwards, synchrotron and IC radiative losses cause a radial steepening of the spectrum integrated over the downstream region, being $\delta = \delta_{\rm inj} + 1$ the corresponding slope.

In the framework of the DSA theory, the high radio power and steep spectra of RRs cannot be reproduced if particles are accelerated to relativistic velocities from the thermal pool (e.g. Botteon et al. 2016a; Eckert et al. 2016; Hoang et al. 2017; Botteon et al. 2020a). These problems can be partly overcome by assuming that a population of pre-existing mildly-relativistic electrons are re-accelerated by the shock wave (e.g. Markevitch et al. 2005; Kang et al. 2012; Pinzke et al. 2013; Vazza & Brüggen 2014). Seed relativistic particles can be injected by AGN; indeed, tails of radio galaxies have been found to provide seed CRe that can be then more efficiently re-accelerated by shocks (e.g. Bonafede et al. 2014a; van Weeren et al. 2017).

Even though the diffusive shock re-acceleration scenario is robust in explaining the spectrum and power of RRs, many questions are still open. First, the direct connection between AGN as source of seed CRe and RR is not always observed, and moreover it is necessary for CRe to be uniformly distributed across Mpc-scale lengths to reproduce the regular morphology of some RRs (such as that of the Sausage cluster). Another issue is related to the Mach-number derived from the measured radio spectral index, which is:

$$\mathcal{M}_{\rm radio} = \sqrt{\frac{2\alpha_{\rm inj} + 3}{2\alpha_{\rm inj} - 1}} \quad . \tag{2.9}$$

In order to obtain $\alpha_{\rm inj}$, high-resolution multi-frequency images are necessary to measure the spectral index at the shock front, where particles are re-accelerated and have just started radiative losses. In practice, this is an hard task, and the volume-averaged integrated spectral index (assumed to be $\alpha = \alpha_{\rm inj} + 0.5$) from the front to the downstream region is the only available measure that can be performed in most of the cases; this procedure likely biases $\mathcal{M}_{\rm radio}$, which was found to be typically higher than $\mathcal{M}$ derived from X-ray spectra. Further biases (for example associated with projection effects, unfavourable viewing angles, models of particle ageing, non-uniform distribution of the Mach-number across the downstream region) may affect the measure of $\mathcal{M}_{\rm radio}$ and/or $\mathcal{M}$, and can be investigated through numerical simulations (e.g. Skillman et al. 2013; Wittor et al. 2021).

To systematically investigate the limitations of the DSA theory, large samples of RRs having available spectral, polarisation, and X-ray information are necessary. However, RRs are fairly rare sources, with typical detection fractions of $\sim 5 - 10\%$ (Kale et al. 2015; Cuciti et al. 2021b) in high-mass ($M_{500} \gtrsim 5\ M_{\odot}$) samples obtained from GMRT and JVLA observations.

2.5 Radio halos

Radio halos (RHs) are centrally-located diffuse sources which extend up to Mpc-scales, roughly following the ICM distribution. They are mainly found in massive and disturbed clusters. The prototypical example is the RH in the Coma cluster (Large et al. 1959; Giovannini et al. 1993; Thierbach et al. 2003; Brown & Rudnick 2011; Bonafede et al. 2021a). Many clusters hosting RRs (see examples in Sect. 2.4) host a RH as well, but clusters with RHs only are more common (van Weeren et al. 2019, for a recent catalogue of known RHs). As an example, the RH in A2744 is shown in Fig. 2.4.

Unlike RRs, RHs are unpolarised sources; the detection of polarised emission from RHs in a handful of clusters (Govoni et al. 2005; Bonafede et al. 2009; Girardi et al. 2016) has been found to be actually associated with shocks and radio galaxies (Pizzo 2011; Rajpurohit et al. 2022a).

2.5.1 Spectral index of RHs

A crucial information to probe the origin and evolutionary stage of RHs is their spectral index (e.g. Brunetti & Jones 2014). Measuring the spectral index of extended sources is never a trivial task. In general, the uncertainty on the flux density of a radio source takes into account systematic calibration errors and noise of the image; in addition, flux density measurements of extended targets may be remarkably biased by the contamination from embedded discrete sources and bad sampling of the *uv*-coverage at short spacings. For RHs, the inaccuracy of α can further increase when employing two flux density measurements only, which are often obtained from different instruments that may not necessarily have a similar *uv*-coverage. The relative roles of all these effects need to be deeply understood; in this respect, in Chapter 5 we investigate if the flux density of RHs detected by

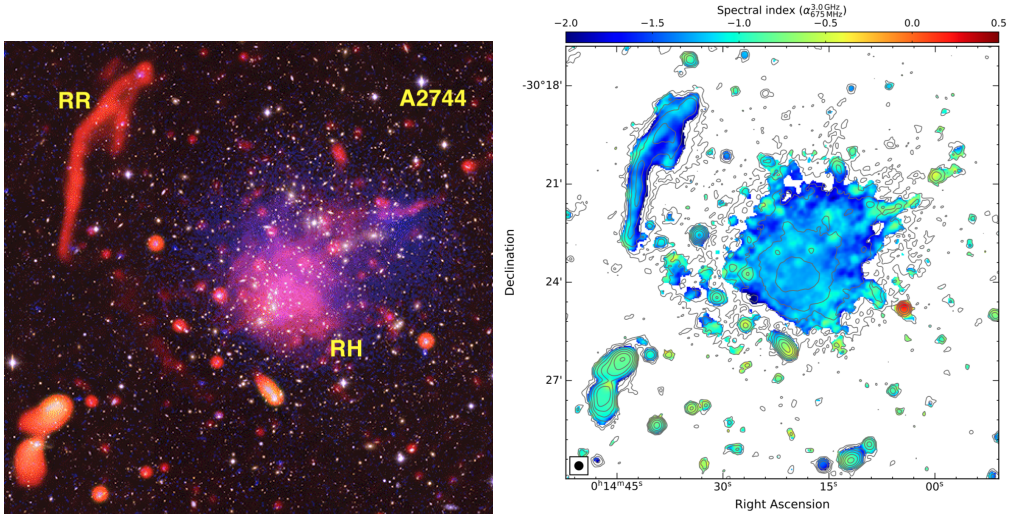

Figure 2.4: *Left*: Radio (red), X-ray (blue), and optical (white) composite image of A2744 as an example of a RH (Pearce et al. 2017). *Right*: Spectral index map between 675 and 3000 MHz, showing a roughly uniform $\alpha \sim 1.3$ across the RH (Rajpurohit et al. 2021b).

different interferometers (LOFAR, uGMRT, JVLA) is affected by losses associated with under-sampling of short baselines.

Despite the high number of possible biases associated with the estimate of α for RHs, a single power-law is typically employed to fit the flux density measurements over a broad range of frequencies (from tens of MHz to few GHz). The corresponding fitted spectral index is steep, being $\alpha \sim 1-1.3$ (see also an example of a spectral index map in Fig. 2.4). The integrated spectrum of Coma significantly deviates from a single power-law, thus confirming a spectral curvature at GHz frequencies (Thierbach et al. 2003). This is likely a more common feature (see also Rajpurohit et al. 2021a; Xie et al. 2020), but it is difficult to observe in other targets due to the limited number of flux density measurements.

The spectral index of RHs likely spans fairly wider ranges than those mentioned above. Indeed, in the past, the study of RHs was limited to the GHz-regime only, thus potentially biasing their spectrum. More recently, radio observations at low frequencies (carried out with uGMRT and LOFAR) have become more common, leading to the discovery of an increasing number of RHs with very steep ($\alpha \gtrsim 1.5$) spectral indices (also referred as ultra-steep spectrum radio halos, USSRHs; Brunetti et al. 2008; Dallacasa et al. 2009; Macario et al. 2010; Bonafede et al. 2012; Venturi et al. 2017; Wilber et al. 2018; Di Gennaro et al. 2021b). The study of USSRHs is crucial to test the proposed formation scenarios and investigate the occurrence of RHs in galaxy clusters; these sources are one of the main topics of this Thesis and two of them are described in Chapters 7, 8.

2.5.2 The role of cluster dynamics

Radio surveys from many facilities, such as VLA, WSRT, GMRT, have enabled the detection of an increasing number of RHs in the last decades, allowing to investigate the

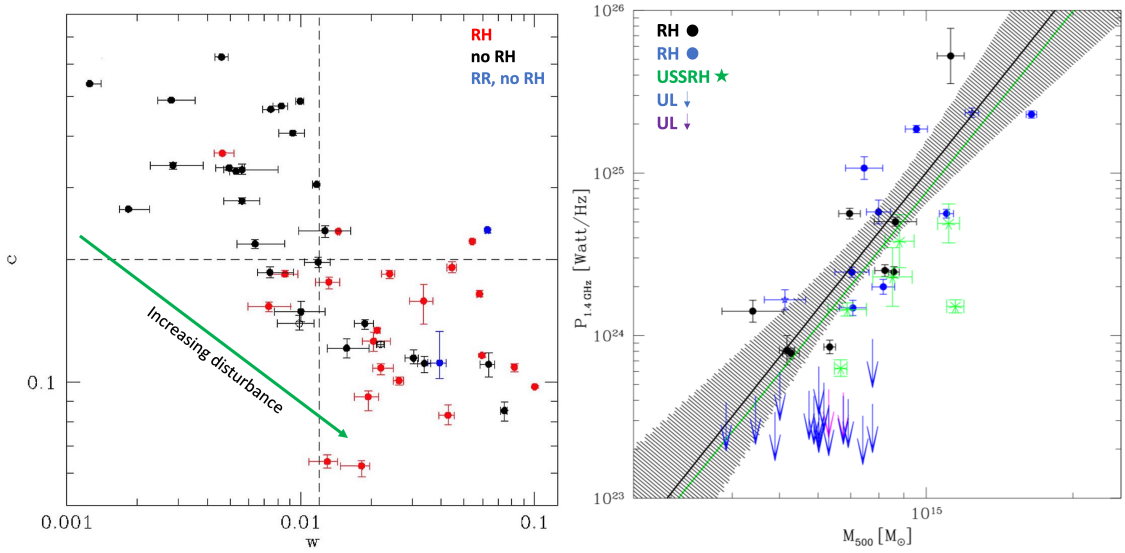

Figure 2.5: *Left*: Cluster distribution in the $c - w$ plane (adapted from Cuciti et al. 2015). Clusters hosting RHs mainly have low c and high w. *Right*: Cluster distribution in the $P_{1.4\,GHz} - M_{500}$ plane (adapted from Cassano et al. 2013). The radio power at 1.4 GHz of RHs (marked with dots) correlates with the mass of the host cluster. USSRHs (marked with stars) are underluminous with respect to the correlation. Upper limits (marked with arrows) are typically well below the correlation.

tight connection with their host cluster (Giovannini et al. 1999; Giovannini & Feretti 2000; Kempner & Sarazin 2001; Giovannini et al. 2006; Venturi et al. 2007, 2008; Rudnick & Lemmerman 2009; van Weeren et al. 2009, 2011; Kale et al. 2013, 2015; Cuciti et al. 2021b,a; George et al. 2021a). It is now well established that RHs are not ubiquitous in clusters, with average detection fractions of $\sim 30\%$ (Venturi et al. 2007, 2008; Cassano et al. 2013; Kale et al. 2015); the detection rate is lower in clusters of masses $M_{500} < 6 \times 10^{14}\ M_\odot$, and increases in systems of higher masses (Cuciti et al. 2015). Moreover, RHs are predominantly found in merging clusters (e.g. Cassano et al. 2010b, 2013; Kale et al. 2013; Cuciti et al. 2015; Eckert et al. 2017; Bîrzan et al. 2019), as shown in the left panel of Fig. 2.5 that reports the distribution of clusters with and without RHs in the $c - w$ plane (see Sect. 1.4.4 in Chapter 1). Clusters hosting RHs are predominantly located in the region of low c and high w, which are associated with disturbed systems.

An additional key finding is that the most powerful RHs are hosted by the most massive (or X-ray luminous) clusters. In this respect, a power-law correlation in the form $P_{1.4} \propto M_{500}^k$ (with $k \sim 3 - 4$) exists between the radio power at 1.4 GHz and the host cluster mass (e.g. Basu 2012; Cassano et al. 2013; Cuciti et al. 2021a), as shown in the right panel of Fig. 2.5. For clusters where RHs are not detected, owing to an intrinsic absence of radio emission or insufficient sensitivity of the observation, it is possible to derive upper limits (ULs) to the power of a possible halo. In the power-mass plane, ULs are typically located well below the correlation. This suggests a bimodal distribution of galaxy clusters with and without RHs, which depends on their dynamical state. One of

the main aims of this Thesis is the derivation of solid ULs to be compared with the radio power of RHs detected by LOFAR, as detailed in Chapter 5.

2.5.3 Origin and life cycle of RHs

RHs are thought to trace re-acceleration of particles and amplification of magnetic fields associated with turbulence induced in the ICM by a cluster merger (e.g. Brunetti et al. 2001; Petrosian 2001; Brunetti & Lazarian 2007; Beresnyak et al. 2013; Miniati 2015; Brunetti & Lazarian 2016). Indeed, as mentioned in Sect. 1.4.3 (Chapter 1), a fraction of the kinetic energy of the merger can be dissipated through a cascade of turbulence, which is able to transfer energy to non-thermal components in the ICM from Mpc-scales down to smaller scales via Fermi II-type mechanisms (Brunetti & Jones 2014, for a review of the complex processes). In the framework of the turbulent re-acceleration scenario, the higher the mass of the merging clusters, the higher the amount of energy that can be channeled into non-thermal components, thus explaining the power-mass relation. On the other hand, relaxed clusters which have not undergone a recent ($\sim$ 1 Gyr) merger will be more radio quiet.

As an alternative formation scenario, RHs may trace the emission of secondary CRe produced by hadronic proton-proton collisions (see details in Sect. 2.3.2; Dennison 1980; Blasi & Colafrancesco 1999; Dolag & Enßlin 2000; Pfrommer et al. 2008), but this is not supported by observations. As CRp are ubiquitously stored in clusters for several Gyr, the hadronic model predicts the potential presence of RHs in all clusters. Moreover, we would expect a roughly uniform distribution of the radio spectra of RHs, and no spectral breaks due to the extremely high energies ($E \sim 100$ GeV) that can be in principle reached by CRp; these are in contrast with typical measures of $\alpha \sim 1-1.3$ and the spectral break of Coma. Two further observational evidences definitely exclude a major contribution from the hadronic hypothesis. First, the emission of USSRHs requires an unacceptably high non-thermal energy budget to be reproduced by pure hadronic models (Brunetti et al. 2008; Bruno et al. 2021). Finally, among the byproducts of the hadronic decays there is also γ-ray radiation; however, a decade of observations from the Fermi-LAT satellite has not allowed a firm detection of γ-rays in galaxy clusters (Brunetti 2009; Brunetti et al. 2012; Ackermann et al. 2014; Zandanel & Ando 2014; Ackermann et al. 2016). Nevertheless, it is not excluded that secondary CRe provide a (minor) contribution to the emission of some RHs, or that secondary CRe can be re-accelerated by turbulence. Indeed, in this latter case, it was shown that turbulent re-acceleration models are still in agreement with the current data (e.g. Brunetti & Blasi 2005; Brunetti & Lazarian 2011a; Brunetti et al. 2017; Pinzke et al. 2017).

In the power-mass diagram, RHs are significantly scattered around the fitted power-law. This behaviour can be explained in light of the leptonic formation scenario, and is supported by simulations about the evolution of the radio and X-ray brightness as a consequence of a cluster merger (Donnert et al. 2013), as reported in Fig. 2.6. These simulations show that during infall ($t < 1.25$ Gyr), the X-ray brightness moderately increases, whereas radio emission is highly enhanced due to the passage of the merger shock. After the core passage ($1.25 < t < 1.7$ Gyr), the cool core is disrupted, thus causing a

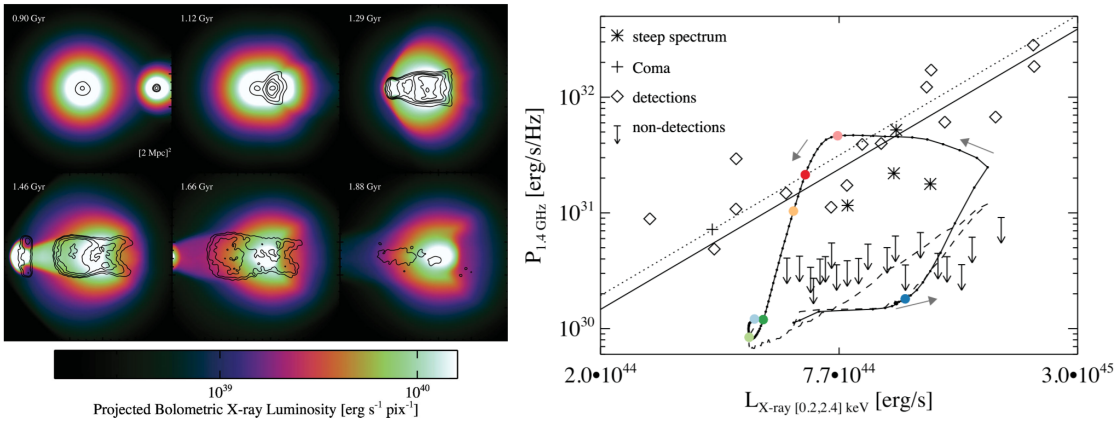

Figure 2.6: Life cycle of RHs from simulations of a cluster merger (Donnert et al. 2013). *Left*: Evolution over time of the X-ray emission of the ICM, with overlaid radio contours at 1.4 GHz of the RH. *Right*: Expected evolutionary path of a RH during its lifetime in the radio power vs X-ray power diagram (see Donnert et al. 2013, and references therein for further details).

rapid decline of the X-ray brightness. Nevertheless, turbulence is induced in a large fraction of the cluster volume, which further increases the radio emission. Due to radiative losses ($t > 1.7$ Gyr), the radio emission gradually turns-off. This life cycle reflects in the power-mass plane. Initially, off-state clusters lie in the region of the ULs, well below the correlation. The merger then triggers the formation of the RH, thus moving the cluster towards or above the correlation. During its radiative lifetime, the RH scatters around near the correlation, and gradually moves towards the region of the USSRHs, which are notably under-luminous with respect to the correlation (see Fig. 2.5, right). After $t \sim 1.5-2$ Gyr, the radio emission finally fades away, and the cluster comes back to the UL region. This scenario can therefore account for the intrinsic scatter around the scaling relation, as RHs are caught at different evolutionary stages; moreover, this scenario well explains the remarkable under-luminosity of USSRHs with respect to the correlation and RHs with typical spectral indices.

2.6 Radio mini-halos

Diffuse radio emission can be found in relaxed systems in the form of mini-halos (MHs). These are diffuse, roundish sources extending within the cool core on scales $\sim 100-500$ kpc. The prototypical example is the MH in the Perseus cluster (Miley & Perola 1975; Pedlar et al. 1990; Burns et al. 1992; Gendron-Marsolais et al. 2017, 2021), which is shown in Fig. 2.7

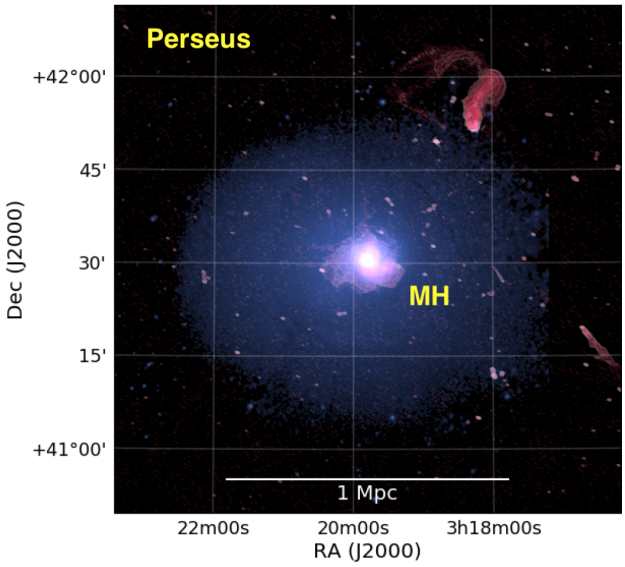

Figure 2.7: Composite radio (red) and X-ray (blue) image of the Perseus cluster, hosting the prototypical MH (van Weeren et al. 2019).

2.6.1 Properties of MHs

Owing to the relatively small sizes of MHs, an unambiguous classification strongly requires solid information from the X-ray thermal counterpart of the cluster. Measuring the flux density and length is also difficult since the fainter emission of the MH has to be disentangled from that of the powerful central jetted radio galaxy generally found in the cool core (see Sect. 1.3.3 in Chapter 1).

Similarly to RHs, the spectral index of MHs is steep ($\alpha \sim 1 - 1.3$) (e.g. Murgia et al. 2010; Giacintucci et al. 2014; Riseley et al. 2022). In few cases, the detection of a spectral break has been claimed (e.g. Govoni et al. 2009; Giacintucci et al. 2014), which would crucially constrain the origin of MHs, but this is still controversial.

In massive ($M > 6 \times 10^{14}\ M_{\odot}$) relaxed clusters, the detection rate of MHs is notably high, being $\sim 50 - 80\%$ (Kale et al. 2013; Giacintucci et al. 2017). However, only ~ 30 MHs are known to date (see Giacintucci et al. 2017; van Weeren et al. 2019, for recent censuses).

2.6.2 Origin of MHs

Typically, MHs are found to be confined by cold fronts (Mazzotta & Giacintucci 2008). This suggests that MHs trace the region of particle re-acceleration from turbulence caused by gas sloshing in the core induced by a minor merger (e.g. ZuHone et al. 2011, 2013). In this scenario, the radio galaxy in the BCG is the most likely candidate to supply seed CRe to be re-accelerated (e.g. Fujita et al. 2007). Numerical simulations support the turbulent re-acceleration model for MHs (e.g. Fujita & Ohira 2013; ZuHone et al. 2013).

As for RHs, the hadronic scenario has been also proposed for MHs (Pfrommer & Enßlin 2004). In contrast with RHs, current upper limits to the γ-ray emission are not

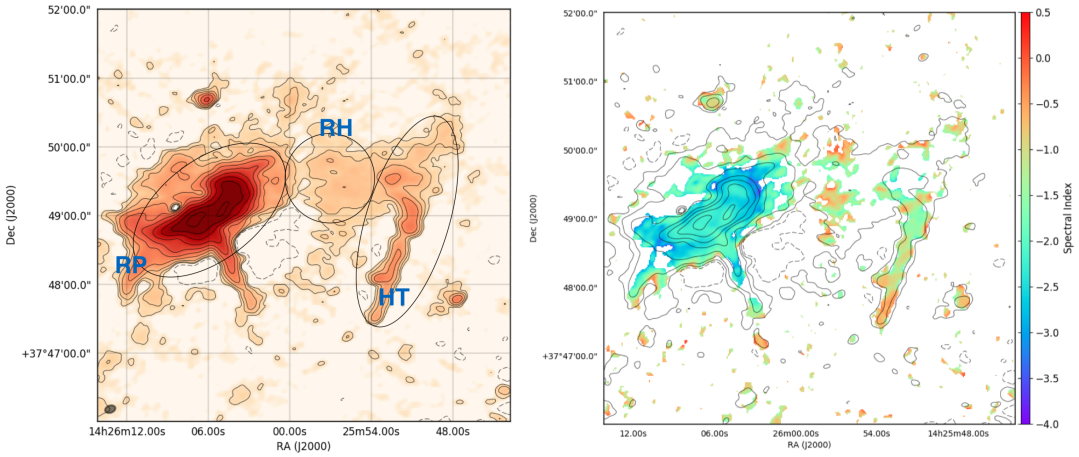

Figure 2.8: *Left*: Example of radio phoenix (labelled as 'RP'; 'RH' and 'HT' indicate a radio halo and a head-tail galaxy) in A1914 observed by LOFAR at 150 MHz (Mandal et al. 2019). *Right*: Spectral index map between 150 and 610 MHz.

deep enough to rule out the hadronic origin. Indeed, the high brightness of MHs makes the γ-ray to radio luminosity ratio to be much lower than that of RHs, thus not allowing to derive stringent constraints (Perkins et al. 2006; Ackermann et al. 2010; Aleksić et al. 2012). Therefore, even though the leptonic origin is more plausible, the hadronic origin is still possible for MHs (Ignesti et al. 2020a), and new data are necessary to further constrain these scenarios.

2.7 The need for low frequency observations

Owing to their steep synchrotron spectra, diffuse sources in galaxy clusters are much brighter at low frequencies (hundreds of MHz). Therefore, facilities operating in these regimes are expected to favour the detection of new objects. By increasing the number of known diffuse sources, statistical analyses of their properties can be performed, thus allowing us to probe their occurrence and test the theoretical formation scenarios. These have implications on the re-acceleration processes, the cosmic magnetic fields, the physics of cosmic rays, and the cluster merger rate. In this Section we briefly review some important discoveries obtained with observations at low frequencies, especially with LOFAR.

2.7.1 Radio phoenixes and GReETs

When very old populations of electrons associated with extended radio galaxies are re-accelerated, their synchrotron emission can be revived, thus originating diffuse radio emission in the form of a radio phoenix or a Gently Re-Energised Tail (GReET). These sources are primarily classified based on their morphology and spectral properties. Their study is important to both probe the interplay between the ICM and radio galaxies and the origin and re-acceleration of seed electrons. Phoenixes and GReETs have very steep spec-

tra (even much steeper than RHs), thus being extremely faint at $\sim$ 1 GHz, and requiring low frequency observations to be properly detected.

Radio phoenixes are mostly irregular sources with roughly uniform very steep spectral indices $\alpha \sim 1.5 - 2$ on scales $\sim$ 100 kpc (Kempner et al. 2004); they are thought to trace re-acceleration of old radio lobes from adiabatic compression after the passage of a shock wave (Enßlin & Gopal-Krishna 2001; Enßlin & Brüggen 2002; Nolting et al. 2019). In this scenario, the high sound speed associated with a relativistic radio lobe prevents the particles to be shocked; on the other hand, particles can gain momentum and the magnetic field strength can increase via adiabatic compression, thus causing the expansion of the lobe perpendicularly to the direction of the shock motion. Therefore, radio phoenixes trace the interplay between shocks and pre-existing radio sources. It is worth to notice that the morphology of phoenixes is similar to that of RRs, but their orientation is parallel to the merger axis. Examples of radio phoenixes are those in A85 (Giovannini & Feretti 2000; Kempner et al. 2004; Rahaman et al. 2022), A1550 (Pasini et al. 2022), A1914 (Mandal et al. 2019, see Fig. 2.8), A2048 (Mandal et al. 2020), A2443 (Cohen & Clarke 2011), A2593 (Mandal et al. 2020), A4038 (Kale et al. 2018).

Typical HT and WAT galaxies show a gradual spectral index steepening starting from the core due to the natural spectral ageing along the tail. However, GReETs are characterised by a sudden change of this trend, with α becoming constant or even flatter in regions of the tail where also the brightness either increases or does not progressively decrease. This spectral behaviour is thought to arise from a gentle re-energising of fossil electrons operated by ICM turbulence, which may be induced by the tail itself, but the exact mechanism is still unclear. The prototype of these sources is the GReET in A1033 (de Gasperin et al. 2017; Edler et al. 2022), which is shown in Fig. 2.9. Additional few cases have been claimed as candidate GReETs in the literature (Cuciti et al. 2018; Wilber et al. 2018; Ignesti et al. 2022; Pasini et al. 2022).

2.7.2 Ultra-steep spectrum radio halos

The existence of USSRHs having $\alpha \gtrsim 1.5$ rules out a pure hadronic origin, owing to the unrealistically high non-thermal to thermal energy density ratio that would be necessary to reproduce the observed radio emission (e.g. Brunetti et al. 2008; Bruno et al. 2021).

The turbulent re-acceleration model can instead account for the properties of USSRHs (e.g. Cassano et al. 2010a, 2012). These can originate from aged RHs and/or minor mergers. In the former case, the bulk of turbulence has been already dissipated and the electrons of an old RH have emitted a large amount of energy, especially at high redshift ($z \gtrsim 0.5$), where radiative losses by inverse Compton are prominent; in the latter case, minor mergers provide a lower energy budget to be transferred to non-thermal components. In both these scenarios, a very steep radio spectrum can be produced above the break frequency $\nu_{\rm break}$. As a consequence, the properties of RHs significantly depend on the observing frequency $\nu_{\rm obs}$ (e.g. Cassano et al. 2006), and USSRHs will be hardly detected if $\nu_{\rm obs} \gtrsim \nu_{\rm break}$.

Having that said, according to the hierarchical structure formation, minor mergers are much more frequent than major mergers. This suggests that a large population of

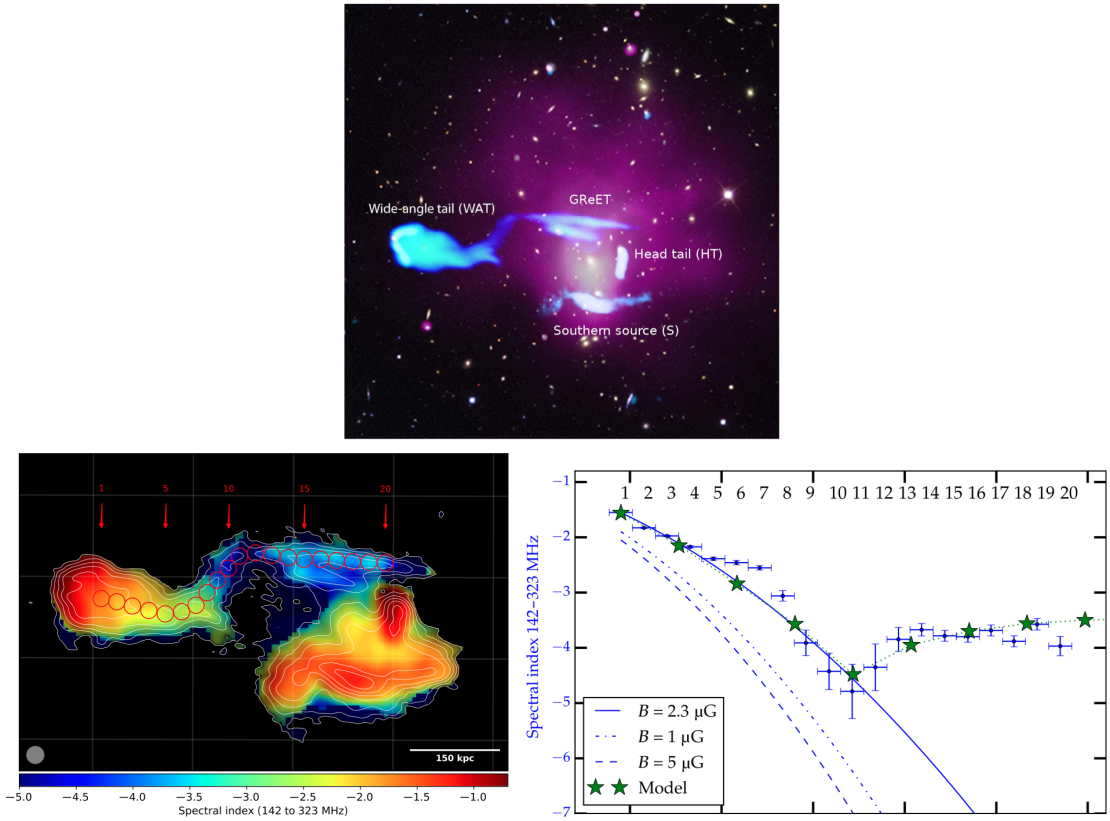

Figure 2.9: *Top*: Composite radio (blue), X-ray (purple), and optical (yellow) image of the GReET in A1033 (de Gasperin et al. 2017). *Bottom*: Spectral index map of A1033 between 142 and 323 MHz (left) and corresponding spectral index profile (right). The spectral index suddenly becomes constant along the re-energised tail.

USSRHs is undetected by past observations mainly led at high frequencies (e.g. Cassano et al. 2010a), but they are expected to be more easily revealed by the present and next generations of sensitive inteferometers, such as uGMRT, LOFAR, MWA, MeerKAT, and SKA. In this respect, LOFAR is allowing us the clear detection of USSRHs below $\sim$ 150 MHz (e.g. Wilber et al. 2018; Bruno et al. 2021; Di Gennaro et al. 2021b; Pasini et al. 2022; Rajpurohit et al. 2022b), thus supporting the hypothesis that these are not as rare as they are at higher (GHz) frequencies (see also Duchesne et al. 2021, for an example of USSRH detected by MWA.).

Since USSRHs are likely the most representative population of RHs in the Universe, their detection is crucial to test theoretical models in large samples of clusters. Indeed, present and future sensitive surveys at low frequencies offer the unique chance to constrain the luminosity function of RHs, their distribution in mass and redshift, the radio bimodality, and the life cycle of low-energy CRe, which is still poorly explored.

2.7.3 Multi-component radio halos

As reviewed in the previous Sections, RHs and MHs are associated with remarkably different dynamical states of their host clusters, and therefore, they have always been considered as distinct classes of objects from an observational point of view. Nevertheless, this firm belief is being hardly challenged by the discovery of RHs in relaxed systems and hybrid[1] diffuse sources that exhibit an inner MH-like component and an outer RH-like component. Examples of these objects have been found in A2142 (Fig. 2.10, Farnsworth et al. 2013; Venturi et al. 2017), A2261 (Sommer et al. 2017), CL1821+643 (Bonafede et al. 2014b), PSZ1G139.61+24.20 (Savini et al. 2018, 2019), RXC J0232.2-4420 (Kale et al. 2019), RX J1720.1+2638 (Fig. 2.10, Savini et al. 2019; Biava et al. 2021), SPT-CL J2031-4037 (Raja et al. 2020). In Chapter 8 we present new LOFAR observations of the striking hybrid halo in A2142.

An evolutionary connection between MHs and RHs may be physically motivated. For example, turbulent motions induced by a cluster merger may reasonably transport CRe from the (completely or partly) destroyed cool core towards larger scales, where then they are re-accelerated. In this scenario, a previous on-state MH switches off, and the formation of a RH is triggered, thus opening to the possibility of observing an intermediate evolutionary stage in which both components co-exist (e.g. Brunetti & Jones 2014).

Furthermore, Zandanel et al. (2014) proposed that the inner MH-like and outer RH-like components may be produced by secondary CRe (hadronic origin) and turbulent re-accelerated CRe (leptonic origin), respectively.

To understand the origin of the hybrid sources, observations at low frequencies are required because the outer RH-like component is often found to be very steep. Complementary data from X-rays, lensing, and spectroscopy are crucial as well to probe the merger dynamics. Indeed, hybrid sources may be tightly linked to the geometry and mass-ratio of the merger. Future observations might possibly lead to the unification of the MH

[1]Differently from the hybrid hadronic plus leptonic model described in Zandanel et al. (2014), in this Thesis we consider as 'hybrid' a diffuse cluster source showing multiple radio components, without referring to a specific formation scenario.

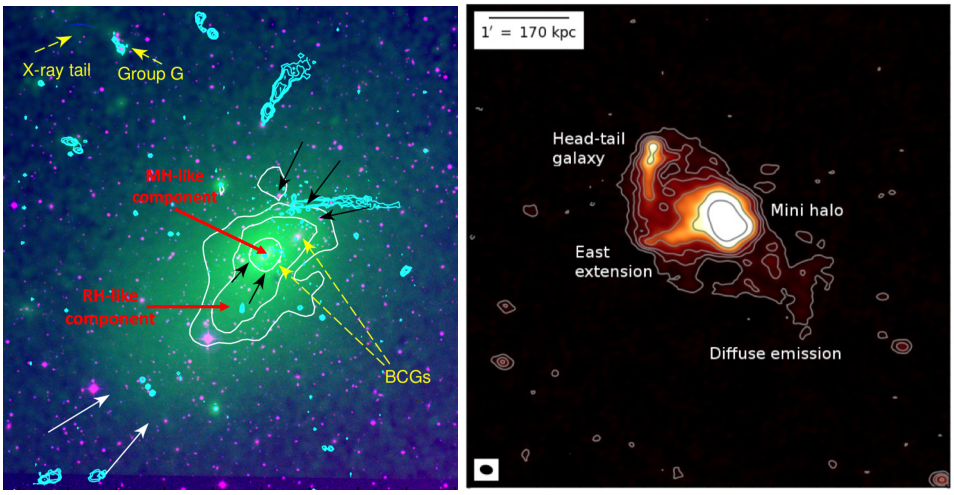

Figure 2.10: Examples of hybrid diffuse sources showing an inner MH-like component and an outer RH-like component: A2142 (left, adapted from Venturi et al. 2017) and RX J1720.1+2638 (right, Biava et al. 2021).

and RH classes.

2.7.4 Radio emission in cluster outskirts and beyond

Sensitive LOFAR observations have recently allowed the discovery of new families of diffuse sources on larger scales than those of classical RHs.

Cuciti et al. (2022) have reported the detection of diffuse emission in four disturbed clusters (ZwCl 0634.1+4750, A665, A697, A2218) surrounding classical RHs, which has been called megahalo (see Fig. 2.11, top panel). Megahalos are diffuse sources extending up to scales $\sim R_{500}$, which embed a RH and have a very steep spectrum ($\alpha \gtrsim 1.6$ between $\sim 50 - 150$ MHz); they are characterised by a shallower radio surface brightness profile than that of RHs, thus suggesting different mechanisms producing the two emitting components. Megahalos might trace particle re-acceleration from turbulence associated with accretion of matter in the outskirts of the cluster, where the conditions of the ICM are fairly unconstrained. Even though the known megahalos discovered so far are hosted in merging clusters, simulations suggest that turbulence induced by accretion should be present in massive and relaxed systems as well.

Botteon et al. (2022c) have discovered radio emission extending beyond the virial radius ($\sim R_{200}$) of A2255 (see Fig. 2.11, bottom left panel). Even though the bulk of the emission is thought to trace large-scale turbulence, the presence of the external relics suggests that accretion shocks are likely responsible for part of the radio emission, by re-accelerating relativistic particles and amplifying magnetic fields.

On larger scales, beyond the conventional cluster boundaries, radio emission has been detected in-between the pairs of clusters A1758 N and A1758 S (Botteon et al. 2018, 2020c), and A399 and A401 (Govoni et al. 2019; de Jong et al. 2022), in the form of radio bridges (see Fig. 2.11, bottom right panel). Simulations (Brunetti & Vazza 2020)

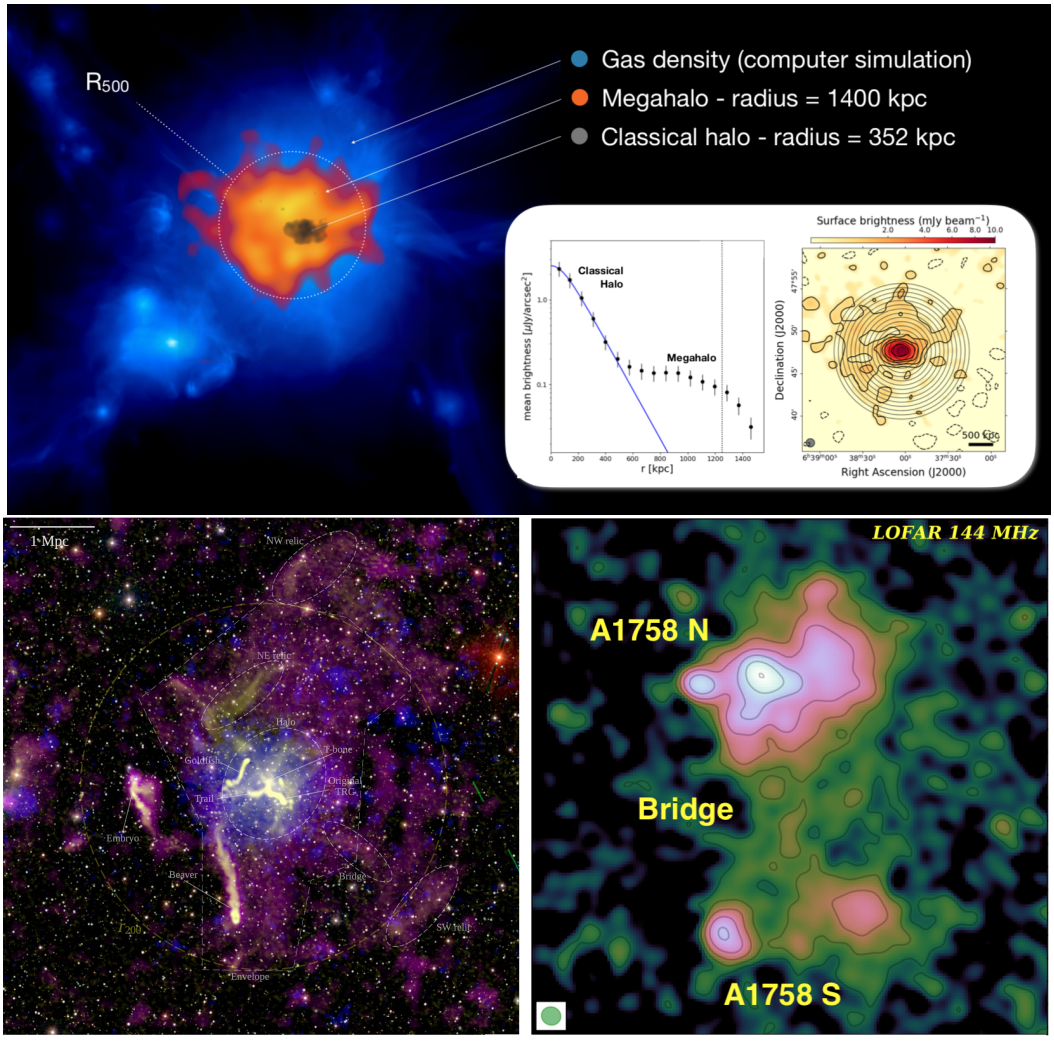

Figure 2.11: Diffuse radio emission on scales $\sim R_{500}$ and beyond discovered by LOFAR. *Top*: Megahalo (orange) embedding the inner RH (black) in ZwCl 0634.1+4750 on scales $\sim R_{500}$ (Cuciti et al. 2022). The thermal ICM counterpart (blue) is obtained from a numerical simulation. The inset shows the surface brightness profiles of the RH and megahalo. *Bottom left*: Radio emission in A2255 extending beyond the virial radius (indicated by the yellow circle; Botteon et al. 2022c). *Bottom right*: Radio bridge in the pre-merger cluster pair A1758 N and A1758 S, at a projected distance of $\sim$ 2 Mpc (adapted from Botteon et al. 2020c).

show that in the early phases of a cluster merger, turbulence is induced, which is able to re-accelerate particles and generate a radio bridge. At present, the spectral index of radio bridges is not firmly constrained, but it is likely very steep.

The existence of diffuse radio emission on scales $\sim R_{500}$ and beyond the classical boundaries of single clusters challenges our current knowledge of relativistic particles and magnetic fields in the Universe. These radio sources allow to explore environments and conditions that could not be probed in any other band of the electromagnetic spectrum, with important implications for the understanding of cosmology, magnetogenesis, and energy transfer mechanisms. These results again confirm the extreme potential of low frequency observations, especially with LOFAR, which is entering into previously uncharted territories, and showing that classical diffuse sources (RHs, MHs, RRs) are just the tip of the iceberg of the non-thermal content of the Universe on large scales.

Chapter 3

The LOFAR era

The LOw Frequency ARray (LOFAR; van Haarlem et al. 2013) is a next-generation radio inteferometer extending across 10 European countries, with most of its antennas concentrated in the Netherlands. LOFAR covers the frequency range 10-240 MHz, thus reaching the lowest end of the radio band observable from Earth, with an unprecedented sensitivity and angular resolution in this poorly explored regime. Owing to the extremely complex systems of hardware and software which are necessary to acquire, transport, store, and analyse the huge amount of data, LOFAR is one of the most important pathfinders of SKA.

The main objectives of LOFAR are described in six Key Science Projects (KSPs), which cover wide fields of radio astronomy. They are summarised below.

1. **Solar physics and space weather**: The radio emission of the Sun associated with periodical flares and coronal mass ejections have a huge impact on Earth and the space environment. Most of the activity has strong signatures in the frequency range explored by LOFAR, which can be used for monitoring programs.

2. **Epoch of Reionization**: The 21 cm line from neutral hydrogen at the Epoch of Reionization is red-shifted to the frequency regime of LOFAR. The detection of this signal provides valuable information on the first stars and galaxies in the early Universe.

3. **Ultra High Energy Cosmic Rays** (UHECRs): The collisions between UHECRs and atoms in our atmosphere generate a cascade of secondary particles that emit radio flashes, and can thus be studied by LOFAR.

4. **Transient events**: Long-period monitoring of wide areas of the sky can reveal transient phenomena, such as variable AGN, novae, supernovae, pulsars, X-ray binaries, fast radio bursts, and gamma-ray burst afterglows.

5. **Cosmic magnetism**: LOFAR can provide new insights on the magnetic fields of the Universe, by observing synchrotron radiation from CRe in both the Milky Way and distant galaxies, as well as by exploiting the Faraday rotation of the emitted signals.

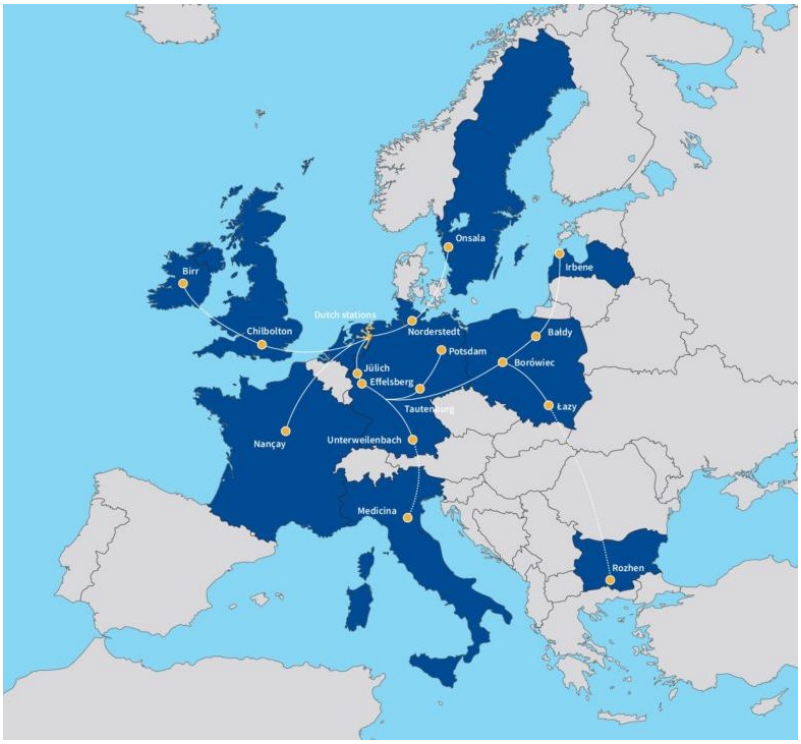

Figure 3.1: Distribution of the LOFAR stations over Europe.

6. **Deep extragalactic surveys**: LOFAR is scanning the whole Northern Sky through different ongoing surveys. These are providing unprecedentedly large catalogues of radio sources thanks to the excellent sensitivity of LOFAR.

The KSPs have guided the design and development of LOFAR antennas to maximise their performances and minimise the building costs. LOFAR started its routine observing campaigns in 2012. In Chapter 2 we have already introduced some of the astonishing results reached by LOFAR in its first 10 years of activity in the context of the diffuse radio sources, and the crucial role that ongoing observations at low frequencies will have to test the theoretical models. In this Chapter we provide a technical description of LOFAR stations and antennas, surveys, and the algorithms that were employed to reduce the data presented in this Thesis.

3.1 Array configuration

At present, LOFAR consists of a network of 52 stations spread all over Europe, as depicted in Fig. 3.1. The Netherlands host 38 stations, whereas 14 stations are distributed in France (1), Germany (6), Ireland (1), Latvia (1), Poland (3), Sweden (1), and United Kingdom (1); two additional stations are going to be built in Italy at the Medicina Radio Observatory site (Bologna) and in Bulgaria as part of the LOFAR 2.0 upgrade.

The Dutch stations are organised in ‘core’ (CS) and ‘remote’ (RS) stations, while the other European stations are referred to as ‘international’ (IS) stations. Near the village

Figure 3.2: Aerial view of the LOFAR Superterp (van Haarlem et al. 2013).

of Exloo (∼ 50 km from ASTRON), the 24 core stations are distributed across an area of radius 2 km; among them, 6 stations are located in a small central island of 320 m of diameter, and constitute the so-called 'Superterp' (see Fig. 3.2). The 14 remote stations are spread within a radius of 90 km. The distribution of the core and remote stations optimises the density of the *uv*-coverage, especially at the shortest baselines. The 14 international stations are located in sites of pre-existing facilities, and provide the longest baselines that allow to reach sub-arcsec resolution.

Each LOFAR station includes a large number of antennas sensitive to two orthogonal linear polarisations. In total, more than 20000 antennas are spread over Europe. These do not have moving parts, therefore pointing and tracking are carried out by combining the signals acquired by each antenna to form a phased-array.

To match the necessity of covering a broad frequency range sensitive to Radio Frequency Interference (RFI) of various origins, as well as minimising the construction costs, two different designs have been developed for the antennas of LOFAR, namely the High Band Antenna (HBA) and the Low Band Antenna (LBA). These have different instrumental specifics, observing strategies, and calibration algorithms of the corresponding data.

3.1.1 High Band Antenna and Low Band Antenna

The High Band Antennas operate in the frequency range 110-250 MHz. Due to the instrumental RFI, which largely increase at the highest frequencies, the actual usable bandwidth is typically limited to 110-240 MHz (see Fig. 3.3, top right). Each HBA element (shown in Fig. 3.3, top left) is a tile hosting 16 dipoles. The tiles are protected from the weather conditions by a foil layer. Signals acquired by each antenna are first amplified and combined in phase to obtain a single 'tile beam'.

The Low Band Antennas operate in the frequency range 10-90 MHz. Due to the high levels of RFI at the lowest frequencies, primarily associated with the ionospheric reflection of long wavelengths, and the commercial FM radio band at the highest frequencies (where the response of the instrument is also very low), the actual usable bandwidth is

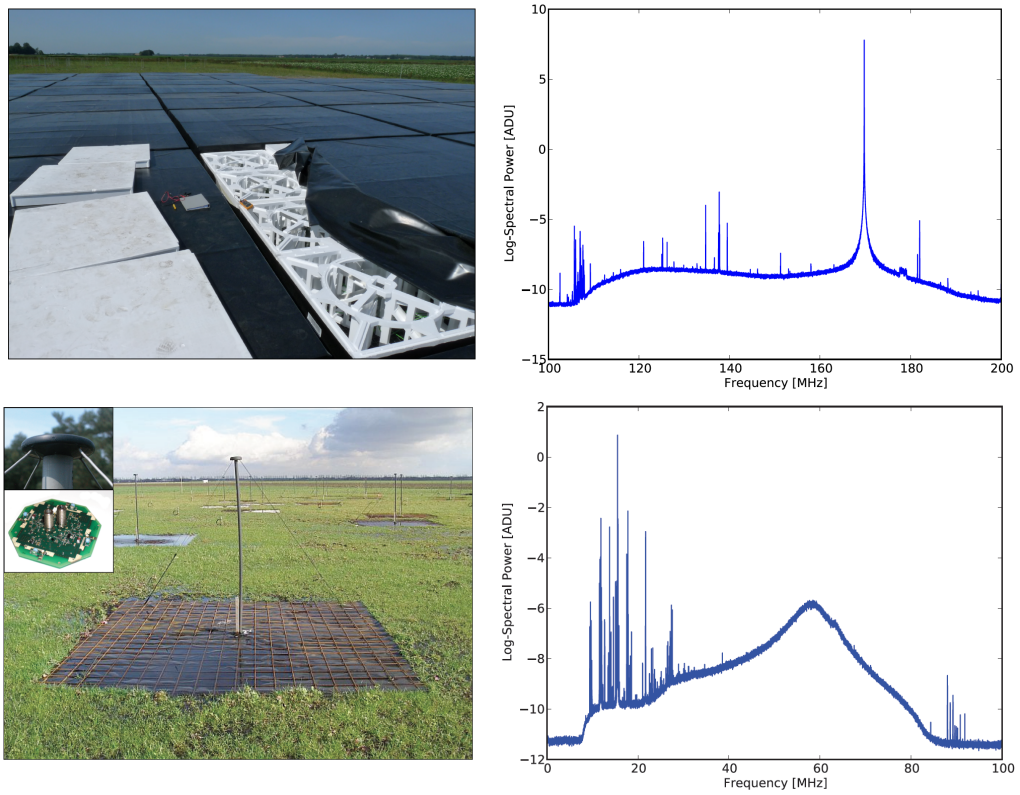

Figure 3.3: Designs and responses of LOFAR HBA and LBA (van Haarlem et al. 2013). *Top left*: LOFAR HBA element. *Top right*: Median averaged spectrum for all HBA tiles of a single station. The RFI are mainly due to instrumental noise, and largely increase above 240 MHz (not shown). *Bottom left*: LOFAR LBA element. *Bottom right*: Median averaged spectrum for all LBA dipoles of a single station. The RFI below 30 MHz are mainly due to ionospheric reflection, whereas RFI above 80 MHz (where the response of the instrument is also very low) are associated with the FM band.

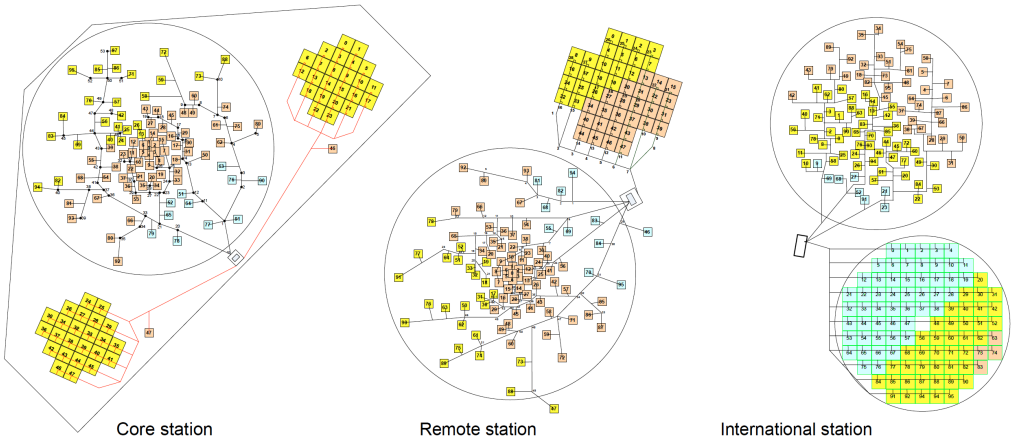

Figure 3.4: Distribution of HBAs and LBAs within each core, remote, and international station (van Haarlem et al. 2013).

typically limited to 30-80 MHz (see Fig. 3.3, bottom right). Each LBA element (shown in Fig. 3.3, bottom left) is a dipole made by two copper wires. At one end, the wires are connected to a vertical shaft that contains a low-noise amplifier on the top; at the other end, they are anchored to the ground plane, which consists of a metal mesh placed above a foil sheet that avoids the growth of the vegetation underneath the antenna.

3.1.2 Antenna distributions and observing modes

Each Dutch station includes 48 HBAs and 96 LBAs, whereas each international station includes 96 HBAs and 96 LBAs to grant extra sensitivity to the longest interferometric spacings. The distribution of the antennas within a station is shown in Fig. 3.4.

In a core station, the LBAs are gathered within a field of 87 m diameter, while the HBAs are arranged in two sub-stations of 30.8 m diameter. In a remote station, two fields of 87 m and 41 m host the LBAs and HBAs, respectively. In an international station, the LBAs and HBAs are distributed in two fields of 70 m and 56.5 m, respectively.

Depending on the scientific aims, different combinations of the antennas can be employed, thus resulting in varying instrumental specifics (see Table 3.1 for details). The two HBA core sub-stations can be used together as a single station, or can be used simultaneously as two independent stations (‘HBA inner dual’ mode) to increase the number of short baselines. Even though the Dutch stations have 96 LBAs, only 48 digital Receiver Units (RCUs) are available to filter, amplify, and digitise the input signals, meaning that only half dipoles can be employed during an observation at present (this issue will be solved by the LOFAR 2.0 upgrade); the 48 LBAs can be all selected from an inner circle (‘LBA inner’ mode) or an outer annulus (‘LBA outer’ mode), or alternatively 24 plus 24 LBAs can be selected from both these regions (‘LBA sparse’ mode) for the best instrumental response on the basis of the scientific target.

Table 3.1: LOFAR station diameter (D), effective area ($A_{\rm eff}$), FWHM, and FOV, for different frequencies and station configurations (van Haarlem et al. 2013).

Freq. (MHz)	λ (m)	D (m)	$A_{\rm eff}$ (m^2)	$FWHM$ (deg)	FOV (deg^2)	D (m)	$A_{\rm eff}$ (m^2)	$FWHM$ (deg)	FOV (deg^2)	D (m)	$A_{\rm eff}$ (m^2)	$FWHM$ (deg)	FOV (deg^2)
		NL Inner				NL Outer				EU			
15	20.0	32.25	1284.0	39.08	1199.83	81.34	4488.0	15.49	188.62	65.00	3974.0	19.39	295.36
30	10.0	32.25	848.9	19.55	299.96	81.34	1559.0	7.75	47.15	65.00	2516.0	9.70	73.84
45	6.67	32.25	590.2	13.02	133.31	81.34	708.3	5.16	20.96	65.00	1378.0	6.46	32.82
60	5.00	32.25	368.5	9.77	74.99	81.34	399.9	3.88	11.78	65.00	800.0	4.85	18.46
75	4.00	32.25	243.6	7.82	47.99	81.34	256.0	3.10	7.55	65.00	512.0	3.88	11.81
		NL core				NL Remote				EU			
120	2.50	30.75	600.0	4.75	17.73	41.05	1200.0	3.56	9.95	56.50	2400.0	2.59	5.25
150	2.00	30.75	512.0	3.80	11.35	41.05	1024.0	2.85	6.37	56.50	2048.0	2.07	3.36
180	1.67	30.75	355.6	3.17	7.88	41.05	711.1	2.37	4.42	56.50	1422.0	1.73	2.33
200	1.50	30.75	288.0	2.85	6.38	41.05	576.0	2.13	3.58	56.50	1152.0	1.55	1.89
210	1.43	30.75	261.2	2.71	5.79	41.05	522.5	2.03	3.25	56.50	1045.0	1.48	1.72
240	1.25	30.75	200.0	2.38	4.43	41.05	400.0	1.78	2.49	56.50	800.0	1.29	1.31

3.2 LOFAR surveys

One of the KSP of LOFAR is the surveying of the whole Northern Sky with unprecedented sensitivities and resolutions at low radio frequencies. A brief overview of the ongoing campaigns is provided in the following Sections.

3.2.1 LOFAR Two Metre Sky Survey (LoTSS)

LoTSS (Shimwell et al. 2017, 2019, 2022a) is observing the Northern Sky in the frequency range 120-168 MHz with the HBA inner dual configuration mode. A total of 3170 pointings of 8-hours each have been planned. As shown in Fig. 3.5, the typical resolution and noise are $\sim 6''$ and ~ 0.1 mJy beam^{-1} at the nominal frequency of 144 MHz, thus making LoTSS the most sensitive and highest-resolution survey in this frequency regime so far. For a comparison, the TIFR GMRT Sky Survey (TGSS; Intema et al. 2017) at 150 MHz has a resolution of $\sim 25''$ and a median noise of ~ 3 mJy beam^{-1}.

The first data release (LoTSS-DR1; Shimwell et al. 2019) has covered an area of 424 deg^2 (2% of the Northern Sky) in the direction of the Hobby-Eberly Dark Energy Experiment (HETDEX; Hill et al. 2008) field. The second data release (LoTSS-DR2; Shimwell et al. 2022a) includes two areas (embedding the HETDEX field as well) for a total of 5635 deg^2 (27% of the Northern Sky), as shown in Fig. 3.6. LoTSS-DR2 has improved the quality of the data products[1] due to a development of the calibration techniques, and has provided the largest catalogue of radio sources ($\sim$ 4.4 million) to date. An important part of this Thesis (Chapters 4, 5, 6) is devoted to the exploitation of LoTSS-DR2 observations of galaxy clusters.

[1] https://lofar-surveys.org

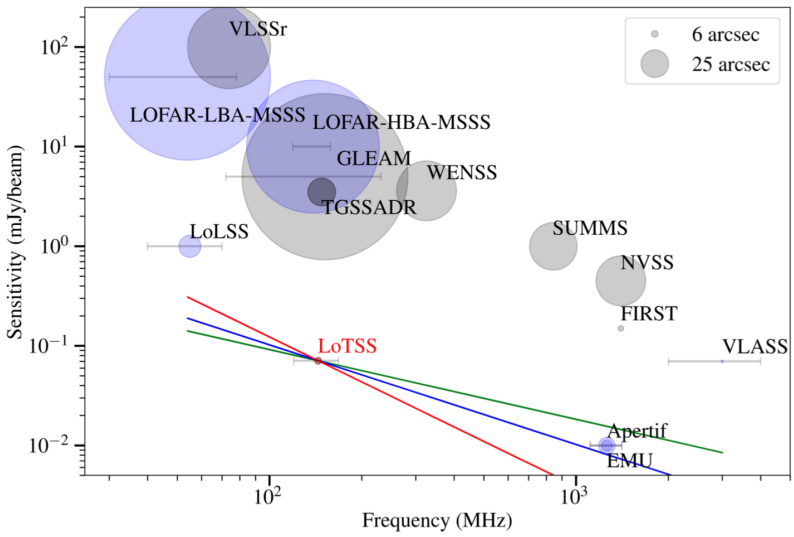

Figure 3.5: Sensitivity as a function of the observing frequency for various radio surveys (Shimwell et al. 2019). The size of the circles is proportional to the resolution. LoTSS and LoLSS are the most sensitive and highest-resolution surveys in their operative frequencies.

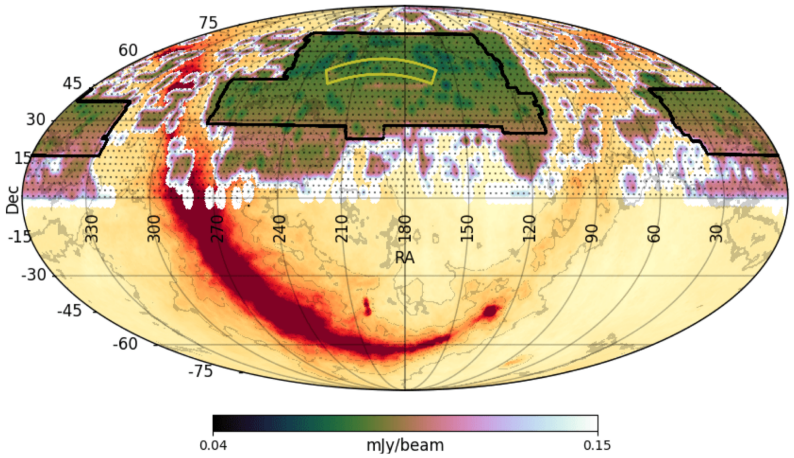

Figure 3.6: Areas (delimited in black) covered by LoTSS-DR2, representing the 27% of the Northern Sky (Shimwell et al. 2022a). Within one these areas, the region delimited in yellow indicates the HETDEX field covered by LoTSS-DR1. The colour scale refers to the reached noise level.

3.2.2 LOFAR LBA Sky Survey (LoLSS)

LoLSS (de Gasperin et al. 2021) is currently scanning the Northern Sky in the frequency range 42-66 MHz with the LBA outer configuration mode. As for LoTSS, 3170 pointings of 8-hours each are being carried out. As reported in Fig. 3.5, the typical resolution and noise are $\sim 15''$ and ~ 1 mJy beam^{-1} at the nominal frequency of 54 MHz. Before LoLSS, the very low frequency regime was only explored by the Very Large Array Low-Frequency Sky Survey Redux (Lane et al. 2014) at 74 MHz, with a resolution of $\sim 75''$ and a noise level of ~ 100 mJy beam^{-1}, and no other surveys below ~ 100 MHz have been planned with other instruments to date. Therefore, LoLSS will provide exclusive information in its operative frequency range for many years in the future.

The first data release (LoLSS-DR1; de Gasperin et al. 2021) has covered an area of 740 deg^2 (4% of the Northern Sky) in the direction of the HETDEX field. The reached resolution and noise are $\sim 47''$ and ~ 5 mJy beam^{-1}, but the planned values of $\sim 15''$ and ~ 1 mJy beam^{-1} are expected to be achieved once that direction-dependent effects are properly corrected (the final version of the data reduction pipeline is still under testing).

3.2.3 LOFAR deep fields

In the context of LoTSS, some fields have been selected for deep (~ 100 hours) observations that aim to reach final noise levels of ~ 10 μJy beam^{-1} at their completion. The first data release of the LoTSS deep fields includes the Boötes (80 h, 30 μJy beam^{-1}; Tasse et al. 2021), Lockman Hole (100 h, 23 μJy beam^{-1}; Tasse et al. 2021), and Elais-N1 (164 h, 20 μJy beam^{-1}; Sabater et al. 2021) fields.

In the context of LoLSS, deep observations of the Boötes field have been carried out as well (56 h, 0.7 mJy beam^{-1}; Williams et al. 2021).

Further deep fields are being carried out with both HBA and LBA.

3.3 LOFAR data processing

Radio observations at $\sim$ GHz frequencies, such as those of VLA, include a primary and a secondary calibrator. The primary calibrator is a non-variable source of known brightness distribution that is pointed during the observation, and it is used to correct for the bandpass and determine the absolute flux density of the target; the secondary calibrator is a bright and unresolved source, which is alternately observed with the target to track and correct the time variations of the phases. Furthermore, steps of self-calibration can be performed by exploiting the phase and amplitude solutions of the target itself (as inferred from the calibrators) to obtain more accurate solutions.

Radio observations at low frequencies require notably different calibration approaches. In this regime, the ionosphere introduces strong time and direction-dependent errors (especially for the phases) that need specific strategies to be properly corrected. In the following Sections we describe the procedures developed for HBA and LBA data that we employed in this Thesis.

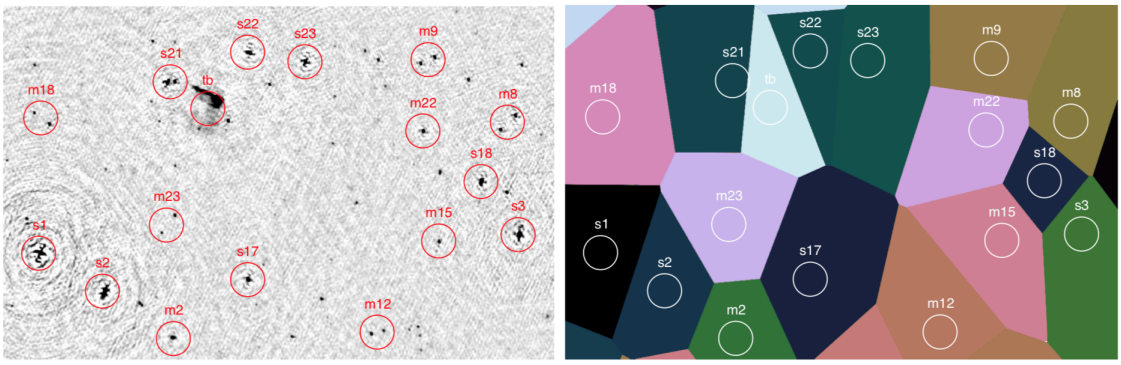

Figure 3.7: Example of facets each containing a bright source (marked by a red circle) to be used as direction-dependent calibrator (van Weeren et al. 2016). Only a portion of the whole field of view is shown.

3.3.1 HBA data reduction

The HBA data reduction is carried out by means of KSP pipelines, which perform the direction-independent (DI) and direction-dependent (DD) calibrations. The imaging process is performed by means of `WSClean`[2] (Offringa et al. 2014; Offringa & Smirnov 2017), which can properly account for wide-field, multifrequency, and multiscale synthesis; these algorithms are strongly recommended for data having large FOV, wide bandwidths, and extended sources in the field, therefore `WSClean` is now routinely used for many other facilities in addition to LOFAR.

After acquisition and pre-processing, the raw LOFAR data are stored in the long term archive (LTA). Owing to their extremely large size (~ 10 TB for an 8-hour pointing), the DI-calibration is performed on computer clusters locally connected to the LTA by executing `PREFACTOR`[3] (van Weeren et al. 2016; Williams et al. 2016; de Gasperin et al. 2019). First, RFI from the flux density calibrator are removed by means of `AOFlagger`[4] (Offringa et al. 2012), and direction-independent corrections (for clock offsets between the stations, ionospheric Faraday rotation, and offsets between the polarisation components) are determined. The flux density scale is set according to Scaife & Heald (2012), and the solutions are transferred from the calibrator to the target. The DI-calibrated dataset is finally averaged in time and frequency to reduce its size, thus allowing the users to download it on their own computer clusters and perform the direction-dependent calibration.

The DD-calibration is carried out through `ddf-pipeline`[5], which makes use of `DDFacet`[6] (Tasse et al. 2018) and `KillMS`[7] (Tasse 2014a,b; Smirnov & Tasse 2015). First, the data are self-calibrated to obtain a preliminary model of the sky. This model is exploited to split the FOV into 45 'facets', each having a bright source to be used as direction-dependent

[2] https://gitlab.com/aroffringa/wsclean/
[3] https://github.com/lofar-astron/prefactor
[4] https://gitlab.com/aroffringa/aoflagger
[5] https://github.com/mhardcastle/ddf-pipeline
[6] https://github.com/saopicc/DDFacet
[7] https://github.com/saopicc/killMS

calibrator (see an example in Fig. 3.7). Afterwards, phase and amplitude solutions are obtained for each calibrator and then transferred to the other sources within the corresponding facet. In these steps, astrometric offsets are corrected by aligning the radio sources with their optical counterparts in the The Panoramic Survey Telescope & Rapid Response System (Pan-STARRS) catalogue (Flewelling et al. 2020). The final DD-calibrated image of the whole FOV is output at 6″ resolution.

Typically, users can be interested in a specific object in the large FOV. To this aim, the 'extraction & re-calibration' process (van Weeren et al. 2020) has been developed to further reduce the size of the dataset to $\sim$ 10 GB and improve the calibration towards the target. First, sources outside an extraction region (with typical sizes of $\sim 20-30$ arcmin) centred on the target are subtracted out from the *uv*-data; then, cycles of phase and amplitude self-calibration are performed within the extraction region, thus refining the solutions.

Uncertainties in the beam model of LOFAR HBA can introduce offsets in the flux density scale when the amplitude solutions are transferred from the primary calibrator to the target. To overcome this issue, the flux density scale needs to be set a posteriori based on different radio surveys and following a statistical approach. In this respect, the ratio $S_{6C}/S_{NVSS} = 5.9124$ of the median flux densities at 150 MHz from the 6C (Hales et al. 1988, 1990) and at 1.4 GHz from the NRAO VLA Sky Survey (NVSS; Condon et al. 1998) catalogues is assumed. Being S_{LOFAR}/S_{6C} the ratio of the median flux densities of the considered LOFAR field and the 6C catalogue, LOFAR HBA images need to be multiplied by a correcting factor $f = 5.9124 \times S_{LOFAR}/S_{6C}$.

3.3.2 LBA data reduction

The LBA data reduction is carried out by means of the Library for Low-Frequencies (LiLF[8]) pipelines.

Following the process described in de Gasperin et al. (2019), corrections for polarisation offsets, bandpass, and clock drifts, are determined for the flux density calibrator, and then transferred to the target. An initial DI-calibration of the target corrects for the direction-averaged ionospheric delay, the Faraday rotation, and beam variations in time and frequency (de Gasperin et al. 2020a).

Afterwards, the FOV is divided into facets by means of `DDFacet` to search for adequate calibrators of the direction-dependent ionospheric distortions. A final DD-calibrated image of the whole FOV is output at a resolution of 15″.

Similarly to the LOFAR HBA data, the 'extraction & re-calibration' procedure can be employed to reduce the size of the dataset and improve the calibration in a small portion of the FOV.

Differently from LOFAR HBA, the beam model of LOFAR LBA is typically accurate and the flux density scale does not require further corrections a posteriori.

[8] https://github.com/revoltek/LiLF

Chapter 4

The Planck clusters in the LOFAR sky

As introduced in Sect. 3.2.1 (Chapter 3), LoTSS-DR2 has recently provided the largest catalogue of radio sources to date, including an unprecedentedly high number of galaxy clusters. As it is currently believed that the cluster mass is a key parameter for the formation of RHs (see Sect. 2.5 in Chapter 2), catalogues of clusters detected via the SZ effect (Sect. 1.3.4 in Chapter 1) are particularly interesting as they provide unbiased samples that are almost mass-selected.

By cross-matching the PSZ2 and LoTSS-DR2 catalogues, we built a sample of 309 Planck galaxy clusters that span previously uncharted ranges in mass and redshift. To date, this is the largest sample of clusters observed at radio frequencies. As a member of the LOFAR survey KSP, I was involved in the exploitation of this sample to perform the first statistical analysis of radio halos at low ($\sim$ 150 MHz) frequencies. The milestone results of this large program are being published in a series of works, which we outline below:

- **Paper I** (Botteon et al. 2022a). A. Botteon, T. Shimwell, R. Cassano, V. Cuciti, X. Zhang, **L. Bruno**, L. Camillini, R. Natale, A. Jones, F. Gastaldello, A. Simionescu, M. Rossetti, H. Akamatsu, R. J. van Weeren, G. Brunetti, M. Brüggen, C. Groeneveld, D. N. Hoang, M. J. Hardcastle, A. Ignesti, G. Di Gennaro, A. Bonafede, A. Drabent, H. J. A. Röttgering, M. Hoeft, F. de Gasperin; *The Planck clusters in the LOFAR sky. I. LoTSS-DR2: New detections and sample overview*. 2022, A&A, 660, A78.

- **Paper II** (Bruno et al. 2023). **L. Bruno**, G. Brunetti, A. Botteon, V. Cuciti, D. Dallacasa, R. Cassano, R. J. van Weeren, T. Shimwell, G. Taffoni, S. A. Russo, A. Bonafede, M. Brüggen, D. N. Hoang, H. J. A. Röttgering, C. Tasse; *The Planck clusters in the LOFAR sky. II. LoTSS-DR2: Recovering diffuse extended emission with LOFAR*. 2023, A&A, 672, A41.

- **Paper III** (Zhang et al. 2023). X. Zhang, A. Simionescu, F. Gastaldello, D. Eckert, L. Camillini, R. Natale, M. Rossetti, G. Brunetti, H. Akamatsu, A. Botteon, R. Cassano, V. Cuciti, **L. Bruno**, T. Shimwell, A. Jones, J.S. Kaastra, S. Ettori, M. Brüggen, F. de Gasperin, A. Drabent; *The Planck clusters in the LOFAR sky. III.*

LoTSS-DR2: Dynamic states and density fluctuations of the intracluster medium. 2023, A&A, 672, A42.

- **Paper IV** (Cassano et al. 2023). R. Cassano, V. Cuciti, G. Brunetti, A. Botteon, M. Rossetti, **L. Bruno**, A. Simionescu, F. Gastaldello, R. J. van Weeren, M. Brüggen, D. Dallacasa, X. Zhang, H. Akamatsu, A. Bonafede, G. Di Gennaro, T. Shimwell, F. de Gasperin, H. J. A. Röttgering, A. Jones.; *The Planck clusters in the LOFAR sky. IV. LoTSS-DR2: statistics of radio halos and re-acceleration models*. 2023, A&A, 672, A43.

- **Paper V**. V. Cuciti, R. Cassano, M. Sereno, G. Brunetti, A. Botteon, T. Shimwell, **L. Bruno**, F. Gastaldello, M. Rossetti, X. Zhang, A. Simionescu, M. Brüggen, R. J. van Weeren, A. Jones, H. Akamatsu, A. Bonafede, F. De Gasperin, G. Di Gennaro, T. Pasini, H. J. A. Röttgering; *The Planck clusters in the LOFAR sky. V. LoTSS-DR2: mass - radio halo power correlation at low frequency*. Submitted to A&A.

This Chapter is based on Paper I and Paper III. We present our cluster sample and report on the challenging classification of the diffuse sources; we then derive flux density and radio power measurements for radio halos, as well as X-ray morphological parameters to characterise the dynamical state of our targets. Chapter 5 is based on Paper II, where we exploit the sub-sample of clusters that lack the detection of diffuse emission to provide solid upper limits to the radio power of a possible radio halo. Finally, Chapter 6 is based on Paper IV and Paper V, where we make use of both radio powers and upper limits to study the radio power-mass relation and the occurrence of radio halos in our sample, thus allowing us to test the theoretical predictions of the turbulent re-acceleration model.

4.1 Cluster sample

The PSZ2 catalogue (Planck Collaboration XXVII 2016) contains 1653 SZ-sources detected over the entire sky. Among them, 309 entries lie in the LoTSS-DR2 footprint, as listed in Table B.1. This comprises two regions covering 5634 deg^2 that are centred at approximately (12h45m00s; +44°30′00″) and (01h00m00s; +28°00′00″). Optical follow-ups provided missing redshift for 63 out of 309 PSZ2 detections, whereas 28 targets still lack redshift confirmation. In the end, our sample consists of galaxy clusters that are known to span at least the redshift and mass ranges of $0.016 < z < 0.9$ (median of 0.280) and $1.1\times10^{14} < M_{\odot}\,/M_{500} < 11.7\times10^{14}$ (median of $4.9\times10^{14}\ M_{\odot}$). The mass and redshift distribution of the full PSZ2 clusters is shown in Fig. 4.1, whereas the sky distribution of the PSZ2 clusters within the LoTSS-DR2 area is reported in Fig. 4.2.

4.2 Radio and X-ray data

In this Section we present the LoTSS-DR2 data processing, and the Chandra and XMM-Newton X-ray archival observations of our sample.

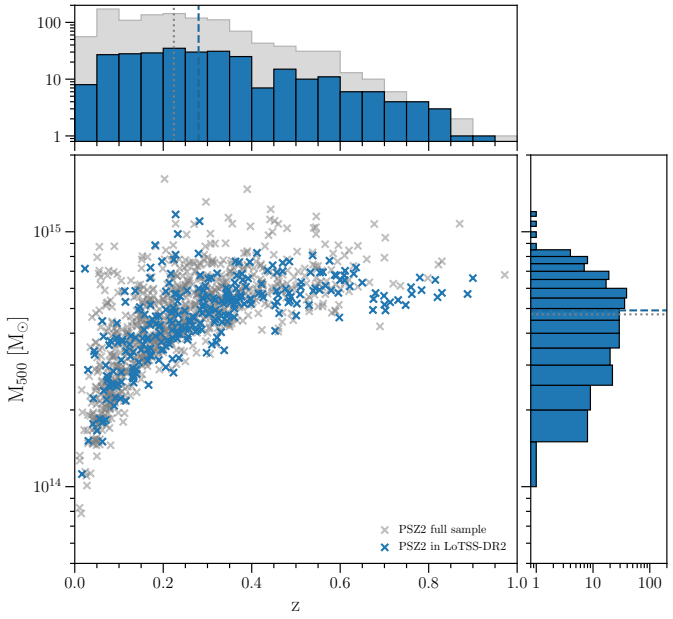

Figure 4.1: The redshift-mass distribution of all PSZ2 sources (grey) and those in the LoTSS-DR2 area (blue). The histograms show the number of clusters at various z and M_{500}, where the dashed and dotted lines mark the median values of the LoTSS-DR2 sample and full PSZ2 sample, respectively.

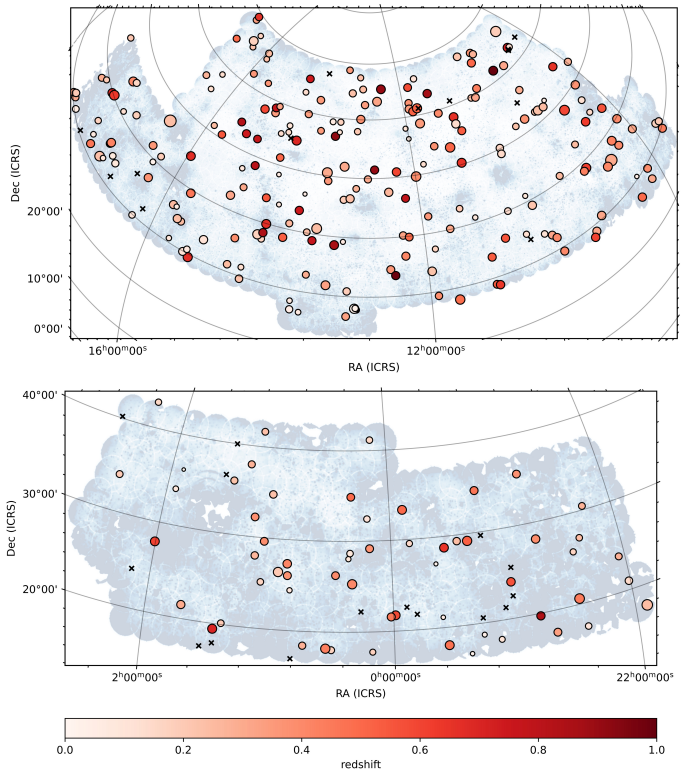

Figure 4.2: Position of the PSZ2 clusters in the regions covered by LoTSS-DR2. Color code represents the redshift of the cluster. The radius of the circle is proportional to M_{500}. Clusters without redshift/mass are reported as black crosses. The background image represents the noise variations in LoTSS-DR2 (darker colors denotes higher noise values) and is reproduced from Shimwell et al. (2022a).

4.2.1 LOFAR data reduction and imaging

LoTSS-DR2 data (Shimwell et al. 2022a) were processed with the KSP pipelines described in Sect. 3.3.1 (Chapter 3). Overlapping pointings of the same target were combined and analysed together. The extraction and re-calibration steps could not be performed for 5 targets, namely PSZ2 G057.80+88.00 (i.e. Coma, which requires special treatment owing to its large extension; see Bonafede et al. 2021a), PSZ2 G056.62+88.42 and PSZ2 G061.75+88.11 (both embedded within the RH of Coma), PSZ2 G060.10+15.59 and PSZ2 G075.08+19.83 (for which the DD-calibration failed likely due to very poor ionospheric conditions). These 5 targets were excluded from the analysis. A collection of the LOFAR images of the 304 remaining targets in our PSZ2 sample is shown in Fig. B.1.

For each cluster, we produced images at different resolutions to search for diffuse radio emission in the ICM and perform the subsequent analysis. The imaging was done by means of WSClean v2.8 (Offringa et al. 2014) with the multiscale (`-multiscale-scales 0,4,8,16,32,64`, being the scales expressed in pixel units) and multifrequency (by subdividing the bandwidth into 6 chunks) deconvolution options (Offringa & Smirnov 2017); we adopted the Briggs (1995) weighting scheme with `robust=-0.5`, and applied Gaussian *uv*-tapers in arcsec equivalent approximately to 25, 50, and 100 kpc at the cluster redshift. For the PSZ2 entries without redshift, the Gaussian *uv*-taper was set to 15, 30, and 60 arcsec to span a wide range of resolutions. For each cluster we also produced a high resolution ($5.0'' \times 3.5''$) image by using `robust=-1.25`.

We used the images obtained with `robust=-0.5` and no *uv*-taper as reference images to assess the quality of the datasets, which were visually inspected and graded according to: 1 for high quality images; 2 for images that are partially affected by calibration artifacts or rms levels higher than nominal values; and 3 for low quality images where the scientific analysis is not possible due to strong calibration artifacts or very high rms noise levels (i.e. >0.3 mJy beam^{-1}). Such image quality is reported in Table B.1. Radio contours from the reference images were overlaid on optical Pan-STARRS (Chambers et al. 2016) mosaics using the *g,r,i* filters to verify the presence of optical counterparts.

To better study the diffuse emission, we removed the contribution of discrete sources by imaging the datasets with an *uv*-cut corresponding to a physical scale of 250 kpc at the cluster redshift (for PSZ2 entries without redshift we arbitrarily adopted an *uv*-cut of 2722λ, corresponding to 2.82 arcmin or 250 kpc at $z = 0.2$) and subtracting their clean components from the visibility data. The new visibility data were then imaged with the same values of *uv*-taper adopted for the images obtained before discrete source subtraction. The low-resolution radio contours with discrete sources subtracted were overlaid onto the Chandra and/or XMM-Newton X-ray images (when available, see Sect. 4.2.2) smoothed to 30 kpc by a Gaussian function.

All images that we produced are available for download in PNG and FITS format on the project website `https://lofar-surveys.org/planck_dr2.html`.

4.2.2 X-ray data

As we will describe in Section 4.3, for the purpose of classifying the detected cluster diffuse radio sources, it is crucial to compare the position of the extended radio emission

with the other cluster components and especially the ICM, which can be traced by its X-ray emission and by the SZ effect. Since all clusters in our sample have been detected by *Planck*, maps of the SZ signal are available for all of them (Planck Collaboration XXII 2016), but their use is hampered by their 10 arcmin resolution, which does not allow us to spatially resolve most of the targets of the sample. We thus decided to map the ICM distribution with the X-ray images obtained by the current generation X-ray telescopes (Chandra and XMM-Newton), whose spatial resolution is higher or comparable to that of our radio images.

We retrieved archival Chandra and XMM-Newton data for 115 and 100[1] galaxy clusters, respectively; 72 targets have been observed both by Chandra and XMM-Newton. The procedures adopted to prepare the X-ray images for each instrument are described in Sects. A.0.1 and A.0.2.

As in Eqs. 1.14 and 1.15 (Chapter 1), we derived the concentration (c) and centroid shift (w) morphological parameters to characterise the dynamical state of our targets by assuming maximum apertures of $R_{\rm ap} = 500$ kpc centred on the X-ray peak (see details in Zhang et al. 2023) as in Cuciti et al. (2015, 2021b). The error on c is obtained by taking into account the Poisson noise in both the source and background images. For w, we considered a fixed number of $N = 20$ apertures in the case of XMM-Newton images, whereas in the case of Chandra images N is given by the number of annuli of fixed 5 arcsec width within 500 kpc. The error on w is obtained by using a Monte Carlo approach: for the Chandra analysis we simulated 100 realizations of the X-ray images obtained by resampling the counts per pixel according to their Poisson error, performed the measurement on the simulated image and estimated the standard deviation of the distribution of w thus obtained; for the XMM-Newton analysis we simulated 10000 realizations of the centroids of the 20 apertures, sampled within their statistical errors.

We measured the concentration and centroid shift parameters for a sub-sample of 140 clusters respecting a selection in redshift to accommodate the aperture of 500 kpc within the FOV of each respective detector ($z > 0.065$ for ACIS-I, $z > 0.072$ for ACIS-S, $z > 0.035$ for XMM-Newton). With these criteria, we obtained 105 and 98 clusters having c and w measurements from Chandra and XMM-Newton data, respectively. Among these targets, 63 have c and w measurements from both Chandra and XMM-Newton, therefore we computed combined morphological parameters according to the following equation:

$$\mathcal{P}_{\rm combined} = \frac{\mathcal{P}_{\rm xmm} + \mathcal{P}_{\rm chandra}}{2} \quad , \tag{4.1}$$

where $\mathcal{P}$ is either c or w and the error $\sigma_{\mathcal{P}}$ on this combined parameter is given by the sum of the statistical $\sigma_{\mathcal{P},\rm stat}$ and systematic $\sigma_{\mathcal{P},\rm sys}$ error as:

$$\sigma^2_{\mathcal{P}} = \sigma^2_{\mathcal{P},\rm stat} + \sigma^2_{\mathcal{P},\rm sys} = \frac{(\sigma_{\mathcal{P},xmm} + \sigma_{\mathcal{P},chandra})^2 + (\mathcal{P}_{\rm xmm} - \mathcal{P}_{\rm chandra})^2}{4} \quad . \tag{4.2}$$

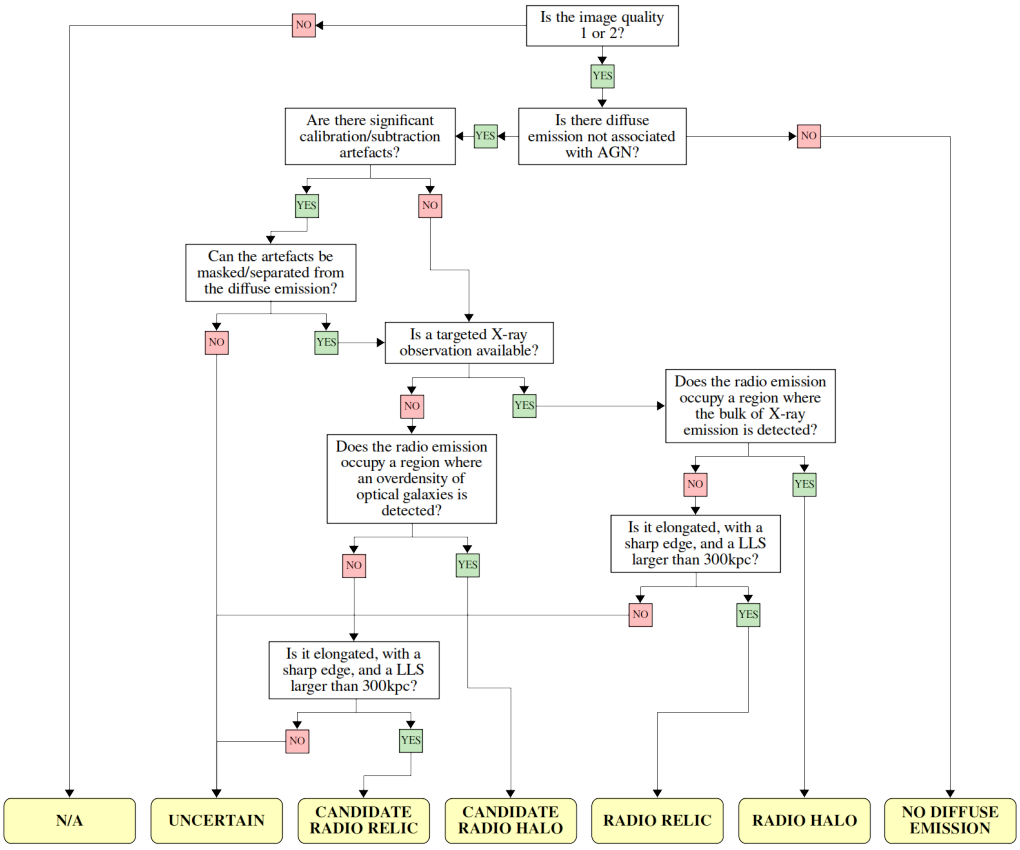

Figure 4.3: Decision tree used to classify the diffuse radio sources in the ICM. The classes of objects forming the end points of the decision tree are described in Section 4.3.

4.3 Classification of radio sources

For each cluster listed in Table B.1 we searched for diffuse radio sources in the ICM that are not clearly associated with any AGN by visually inspecting the set of LOFAR images at different resolutions (with and without source subtraction) together with the optical/X-ray overlay images. To make the classification of the radio emission as objective as practical at present and easily reproducible, we created a decision tree (Fig. 4.3) which we followed during the inspection of the images and classified each cluster. Below we define the classes of objects that form the end points of our decision tree.

- *Radio halos (RH)*: extended sources that occupy the region where the bulk of the X-ray emission from the ICM is detected. Historically, they were divided according to their sizes: giant halos extended on cluster-scale and mini-halos covering the cluster central region. Since in this work we are dealing with a large sample of clusters with masses spanning over one order of magnitude of difference, we prefer to not divide mini-halos from giant-radio halos based on the size of the radio emission, and refer generically to radio halos.

- *Radio relics (RR)*: elongated sources whose position is offset from the bulk of the X-ray emission from the ICM and consistent with lying in cluster outskirts. We also checked for a sharp edge in the radio emission and a largest-linear size (LLS) $\gtrsim$ 300 kpc.

- *Candidate radio halos/relics (cRH/cRR)*: if Chandra or XMM-Newton X-ray observations are not available, the presence of a halo or relic cannot be firmly claimed because we are uncertain if the emission is in the central or outer region of the ICM. However, it is possible to make an assessment based on the position of the radio emission with respect to the apparent overdensity of galaxies in the optical image. We thus classify the emission as being a candidate radio halo or radio relic if it is consistent with the other properties of these types of sources but co-located with or offset from the overdensity of galaxies rather than the X-ray emission from the ICM.

- *Uncertain (U)*: objects were classified as uncertain if the emission was either significantly affected by calibration/subtraction artifacts or if it did not show the morphology, size, and/or position consistent with the categories of radio halos and relics.

- *No diffuse emission (NDE)*: these objects do not show the presence of diffuse emission that could be attributed to the ICM (although they may show the presence of lobes/tails from AGN in the field).

- *Not applicable (N/A)*: if the image quality is 3 (see Section 4.2.1) the object cannot be adequately classified because of the poor data quality.

[1]The actual number of XMM-Newton observations is 110 because we considered as separate targets those clusters in double (interacting) systems.

If a target showed more than one diffuse source not related with any AGN, we repeated the decision tree for each source separately. All the answers to the questions of the decision tree are available on the project website. A gallery highlighting the wide variety of different types of emission is shown in Fig. 4.4.

4.4 Flux density measurements

In this Section we describe the procedures that we followed to measure the flux density S_{144} at 144 MHz. By assuming $\alpha = 1.3$ as a typical spectral index for radio halos (e.g. van Weeren et al. 2019), we derived S_{150} at 150 MHz, and computed the corresponding k-corrected radio power as $P_{150} = 4\pi S_{150} D_{\rm L}^2 (1+z)^{\alpha-1}$. It is worth to notice that the value of P_{150} is always biased by the arbitrary choice of α, which affects the k-correction term. For low-z clusters, the k-correction term is negligible, thus not significantly affecting P_{150}; on the other hand, this may have a large impact on high-z clusters, and their P_{150} should be taken with more caution.

The quantities derived for RHs in our sample are reported in Table B.3. Uncertainties on the flux densities of the diffuse sources are obtained as:

$$\Delta S_{\rm diffuse} = \sqrt{(\xi_{\rm cal} S_{\rm diffuse})^2 + \left(\sigma \sqrt{N_{\rm beam}}\right)^2 + (\xi_{\rm res} S_{\rm discrete})^2}\,, \tag{4.3}$$

where the first term ($\xi_{\rm cal} S_{\rm diffuse}$) represents the systematic calibration error, the second term ($\sigma \sqrt{N_{\rm beam}}$) represents the statistical error related to the noise image and the integration area, and the last term ($\xi_{\rm res} S_{\rm discrete}$) represents the subtraction error related to the residual discrete sources. We assumed $\xi_{\rm cal} = 10\%$ for LoTSS-DR2 (Shimwell et al. 2022a). To assess what is the fraction of residual contaminating emission, we visually inspected the images used for the subtraction for a subsample of clusters characterised by different values of flux density in discrete sources, and found that the following percentages

$$\xi_{\rm res} = \begin{cases} 16\% & \text{if } S_{\rm discrete} < 10 \text{ mJy} \\ 8\% & \text{if } 10 \text{ mJy} < S_{\rm discrete} < 100 \text{ mJy} \\ 4\% & \text{if } 100 \text{ mJy} < S_{\rm discrete} < 1000 \text{ mJy} \\ 2\% & \text{if } S_{\rm discrete} > 1000 \text{ mJy} \end{cases} \tag{4.4}$$

provide a good approximation to quantify the level of contamination in our measurements.

4.4.1 The Halo-FDCA algorithm

We employed the Halo-Flux Density CAlculator[2] (Halo-FDCA; Boxelaar et al. 2021) to measure the integrated flux density from the observed radio halos. This code fits the 2D surface brightness profile with a Markov chain Monte Carlo (MCMC) method that

[2] https://github.com/JortBox/Halo-FDCA

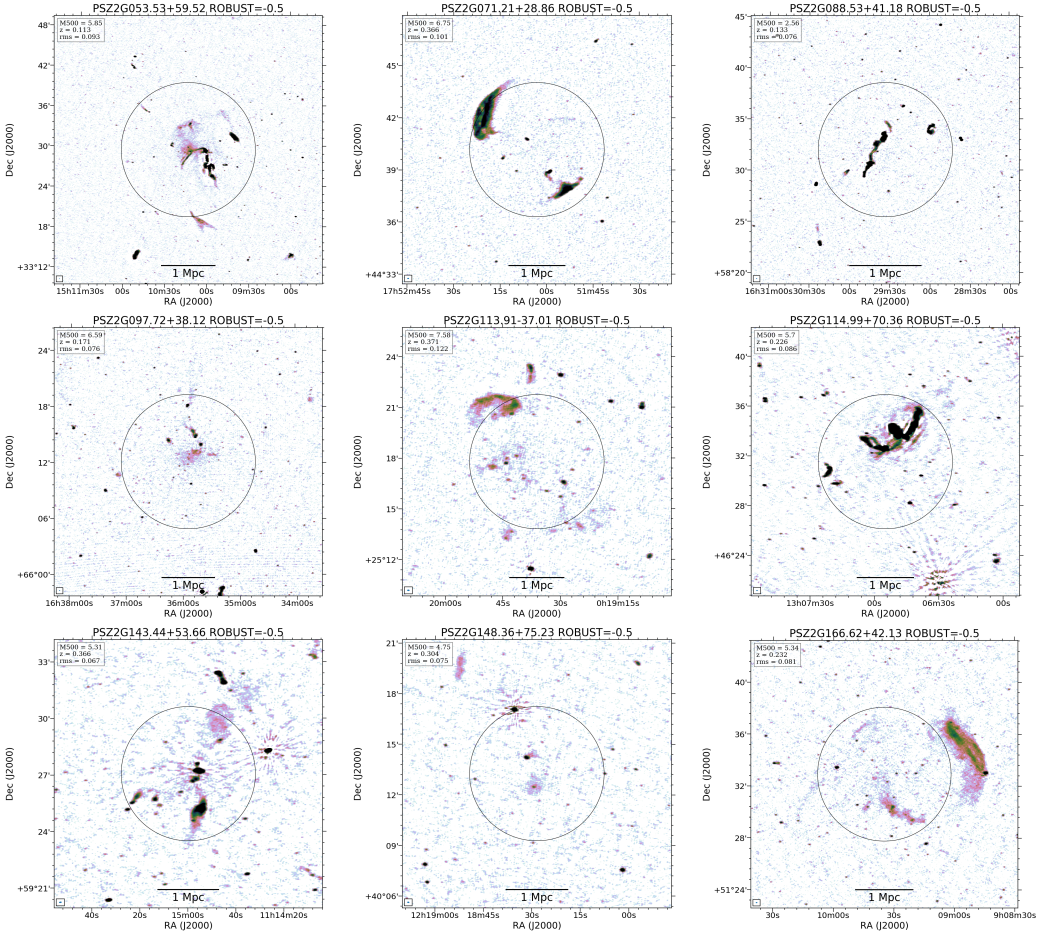

Figure 4.4: Collection of clusters showing several types of radio emission. PSZ2 G053.53+59.52: a central radio halo and a number of sources with uncertain origin. PSZ2G071.21+28.86: a double radio relic. PSZ2 G088.53+41.18: a cluster without diffuse emission, as the emission detected is associated a to an optical galaxy. PSZ2 G097.72+38.12: a radio halo. PSZ2 G113.91-37.01: a radio halo and two relics. PSZ2 G114.99+70.36: emission with uncertain origin. PSZ2 G143.44+53.66: emission with uncertain origin. PSZ2 G148.36+75.23: a radio halo. PSZ2 G166.62+42.13: a radio halo and multiple relics.

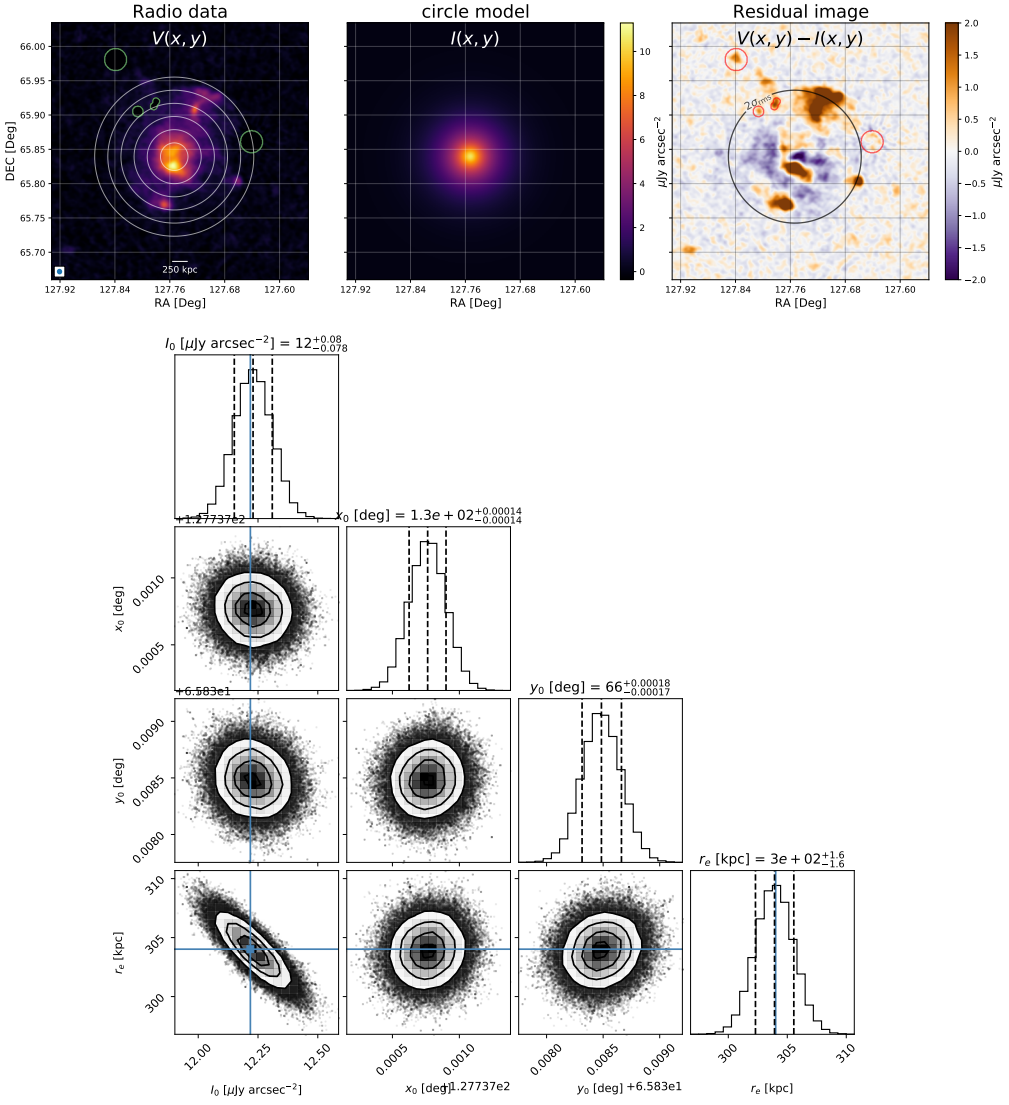

Figure 4.5: Results obtained by fitting the radio halo in PSZ2 G149.75+34.68 with HALO-FDCA (Boxelaar et al. 2021). *Top figures*: image used for the fit with overlaid the contours (white circles) of the best-fit circular model drawn at $[1, 2, 4, 8, \dots] \times \sigma$ (*left* panel), image of the best-fit model (*central* panel), and residual image of the fit with the 2σ model contour denoted by the black circle (*right* panel). Contaminating sources are masked out and are highlighted by the green and red regions (*left* and *right* panels, respectively). *Bottom figure*: MCMC corner plot presenting the distribution of the posteriors of each fitted parameter (Foreman-Mackey et al. 2013).

estimates the best-fit parameters and associated uncertainties. As proposed by Murgia et al. (2009), for the fitting we assume an exponential profile in the form

$$I(r) = I_0 e^{-G(r)}\,, \tag{4.5}$$

where the fitted parameters are the central brightness I_0 and the function that determines the model morphology $G(r)$ (i.e. circular, elliptical or skewed; see Boxelaar et al. 2021 for more details). As done for the LoTSS-DR1 cluster sample (van Weeren et al. 2021), we primarily used a simple circular exponential model to fit the discrete source subtracted images that were obtained with a Gaussian *uv*-taper corresponding to 50 kpc at the cluster redshift. If the signal to noise in these images was low or the emission was clearly non circular, we instead used the discrete source subtracted images with *uv*-taper of 100 kpc or the elliptical exponential model. In total, the circular model has four free parameters: I_0, the coordinates of the centre (x_0 and y_0), and a single *e*-folding radius (r_1). The elliptical model has two additional free parameters: a second *e*-folding radius (r_2) and a position angle (ϕ).

Prior to fitting the radio halos we carefully examined the images for contaminating extended sources that had been poorly subtracted and identified regions affected by residual calibration errors. These problematic regions were manually masked during the fitting. We integrated the best-fit models up to a radius of three times the *e*-folding radius. This choice leads to a flux density which is ∼80% of the one that would be obtained by integrating the model up to infinity and is motivated by the fact that halos do not extend indefinitely. The quantities derived for the radio halos and candidate radio halo in our sample are reported in Table B.3.

A qualitative assessment of the fit quality can be done by inspecting the residual images and corner plots produced by Halo-FDCA, which are publicly available for each cluster on the project website. An example of these plots for the prominent radio halo that is hosted in the cluster PSZ2 G149.75+34.68 is reported in Fig. 4.5. We note that Halo-FDCA returns the signal-to-noise ratio (SNR) and the $\chi^2_{\rm red}$ of the fit which can also be used to assess the fit quality. However, we urge caution in interpreting these values. The SNR in Halo-FDCA is defined as the integrated flux density value divided by the uncertainty introduced by the fit (which is based on the image noise and the number of data points related to the area of the halo), hence it is not a parameter that determines the significance of the detection. The $\chi^2_{\rm red}$ instead is calculated from the difference between the fitted exponential model and the data, and high $\chi^2_{\rm red}$ values may suggest that a halo has substructures (which are not included in the model). For example, this is the case of the halo shown in Fig. 4.5, where $\chi^2_{\rm red} = 7.23$. We note a positive trend between SNR and $\chi^2_{\rm red}$ for the radio halos and candidate radio halos in our sample (Fig. 4.6), indicating that the exponential model, whilst being a reasonable description of the data, may be affected by the presence of asymmetries and substructures that become evident only when the data are of sufficient statistical quality.

4.4.2 Comparison between flux density measurements

To demonstrate the performance of Halo-FDCA, we compared the flux density obtained by manually integrating the flux density within a circle (or ellipse, depending on the

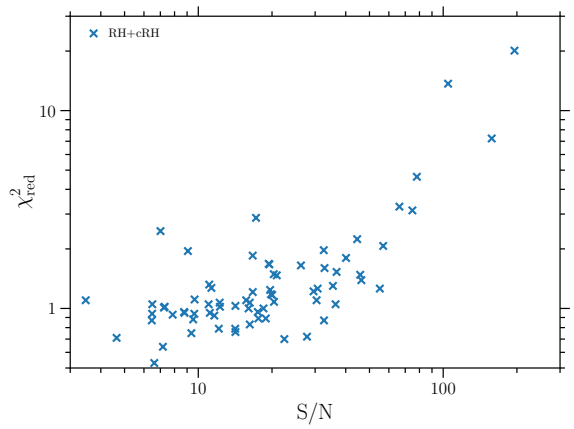

Figure 4.6: $\chi^2_{\rm red}$ vs. SNR (i.e. the ratio between the integrated flux density and its fitting uncertainty) for the radio halos and candidate radio halos in our sample. The positive trend indicates that deviations from the exponential model become evident only for the halos that are detected with sufficient significance.

model used in Halo-FDCA) that roughly encompasses the 2σ contour of the radio halo ($S_{2\sigma}$) with that obtained with Halo-FDCA ($S_{\rm fit}$). As shown in Fig. 4.7 there is generally good agreement between the two quantities, although a few outliers are present.

We inspected the radio images and results of the fitting for all clusters and found that the outliers may indicate cases in which Halo-FDCA provides a unreliable fit because of the low-significance of the radio halo. To verify this, we produce the plot shown in the right panel of Fig. 4.7, which shows the ratio between the best-fit value of the central surface brightness I_0 and the 3σ noise of the map as a function of the $S_{\rm fit}/S_{2\sigma}$ ratio. We observe a trend between the plotted quantities, noting indeed that the halos where the two flux density measurements are in most disagreement (large $S_{\rm fit}/S_{2\sigma}$ values) are typically those with the lowest $I_0/3\sigma$. Our interpretation is that when the radio halo is observed with low-significance, Halo-FDCA does not converge on the diffuse emission but it provides a non-physical best-fit with low-I_0 and large-r_1, basically fitting the image noise. Important, these non-physical best-fit models have still good SNR and $\chi^2_{\rm red}$ values and corner plots as the fit reached convergence, thus they cannot be simply rejected by using these tools. We therefore used the right panel of Fig. 4.7 as diagnostic plot, adopting the arbitrary thresholds of $S_{\rm fit}/S_{2\sigma} > 1.5$ and $I_0/3\sigma < 2$ to identify the bad cases. These radio halos and candidate radio halos are marked with an asterisk in Table B.1 (i.e. RH*/cRH*) and represent 10 out of the 83 fitted halos. They are collected in Table B.4. Deeper LOFAR observations are required to reliably determine the integrated flux density of the halo emission in these clusters.

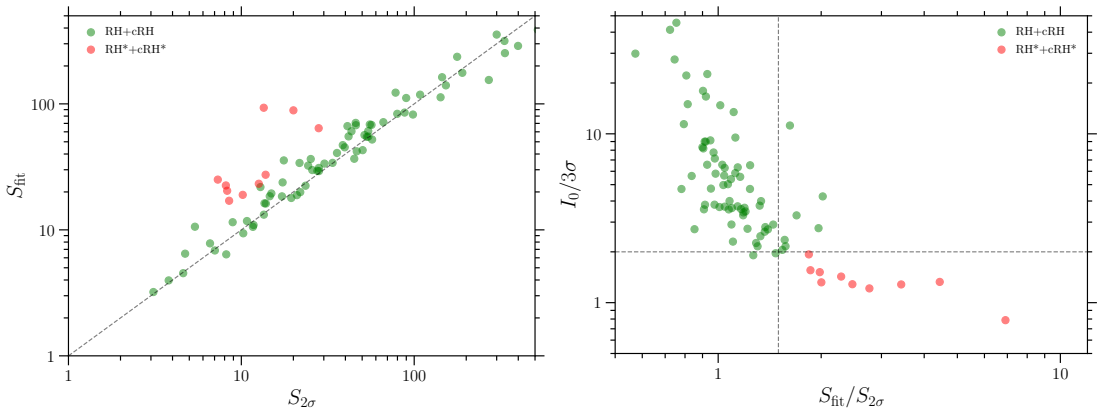

Figure 4.7: *Left*: comparison between the flux density derived with HALO-FDCA ($S_{\rm fit}$) and that obtained manually within the 2σ contour ($S_{2\sigma}$). The dashed line indicates the linear correlation as a reference. *Right*: diagnostic plot used to determine when HALO-FDCA does not provide a reliable flux density measurement due to the low-significance of the radio halo. The dashed lines indicate the thresholds of $S_{\rm fit}/S_{2\sigma} > 1.5$ and $I_0/3\sigma < 2$ that were used to identify the sources that were classified as radio halos or candidate radio halos with the decision tree of Fig. 4.3, but whose flux density was not considered reliable. These sources are reported in red and in the manuscript are referred to as RH* and cRH*.

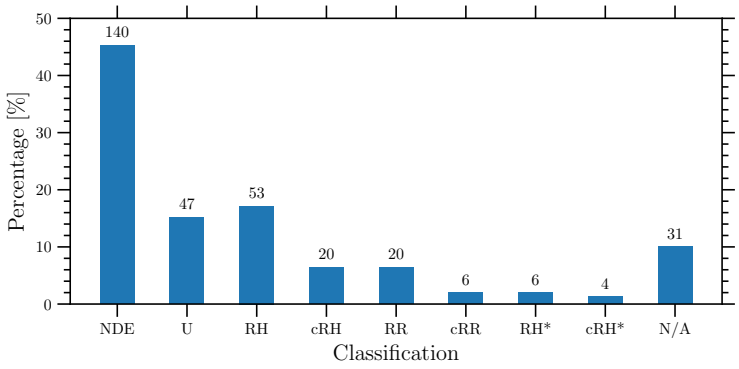

Figure 4.8: Summary of the number of clusters classified in our sample divided per category (NDE=No Diffuse Emission; U=Uncertain; RH=Radio Halo; RR=Radio Relic; c=candidate; *=flux density measurement not reliable; N/A=Not Applicable). We note that a cluster can be classified under multiple categories, such as both RH and RR. The percentage on the *y*-axis is referred with respect to the total number of PSZ2 in LoTSS-DR2 (309 targets).

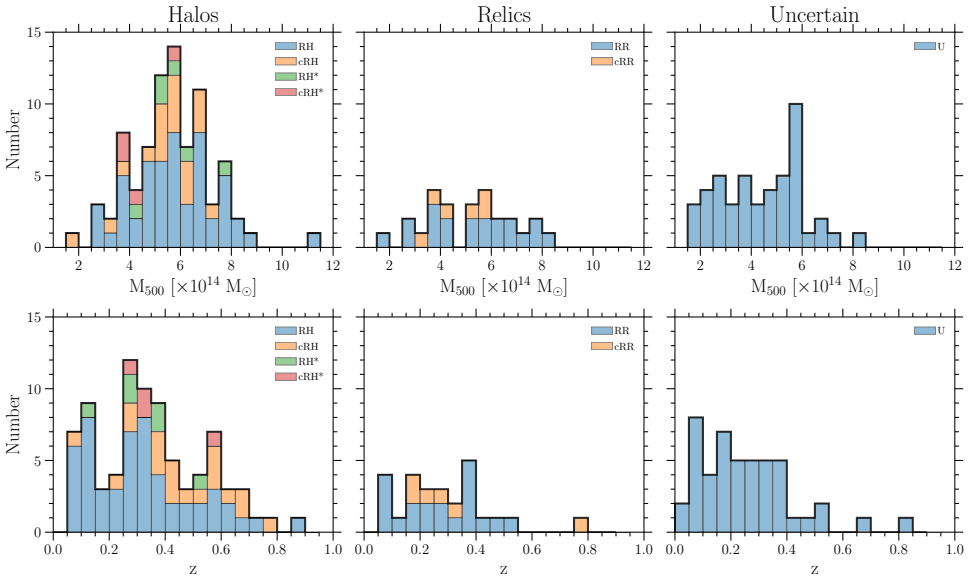

Figure 4.9: Histograms of the mass (*top* panels) and redshift (*bottom* panels) distribution for the main categories of objects classified in this work.

4.5 Results and discussion

4.5.1 Number and distribution of sources

With 309 objects, the LoTSS-DR2/PSZ2 sample represents the largest statistical sample of galaxy clusters observed with highly sensitive low frequency observations that has been ever used to search for and study diffuse synchrotron emission in the ICM. The number of clusters divided per category as defined in Section 4.3 is summarised in Fig. 4.8. We found 73 clusters hosting a radio halo (i.e. 53 RH and 20 cRH), 26 clusters hosting one or more relics (i.e. 20 RR and 6 cRR), and 47 clusters with diffuse emission of uncertain origin. Additional 10 clusters are found to host a radio halo from visual inspection but since the surface brightness profile fittings were of poor quality they were reported with an asterisk in Fig. 4.8 and Table B.1. No diffuse radio emission from the ICM was found for 140 targets, while for 36 objects it was not possible to investigate the presence of diffuse emission either due to the impossibility of applying the 'extraction + re-calibration' method (5 out of 36) or due to the bad image quality (31 out of 36).

The number of clusters with newly discovered radio halos and relics in our sample is 50 (i.e. 50% of the total number of halo and relic detections) and these clusters are highlighted in Table B.1. These new discoveries consist of 35 clusters hosting a radio halo (i.e. 21 RH and 14 cRH, namely 48% of the number of halo detections) and 15 clusters hosting one or more radio relics (i.e. 9 RR and 6 cRR, namely 58% of the number of relic detections). In addition, 6 RH* and 3 cRH* are reported in this work for the first time. In Fig. 4.9 we show the mass and redshift distribution for the clusters hosting halos, (one or more) relics, and uncertain sources in our sample.

We have detected radio halos over the entire M_{500} range of the PSZ2 sample we have

studied, which spans nearly one order of magnitude. The bulk of detections occur in the mass range $M_{500} \sim [5-7] \times 10^{14}\ M_{\odot}$. Of particular interest is the large number of detections of halos in clusters with a mass $M_{500} < 5 \times 10^{14}\ M_{\odot}$ (i.e. 17 RH, 4 cRH, 3 cRH*, and 1 cRH*). This mass regime is poorly studied and it has been disclosed only very recently thanks to sensitive observations with new generation instruments (e.g. Hlavacek-Larrondo et al. 2018; Hoang et al. 2019; van Weeren et al. 2021; Botteon et al. 2019, 2021a,b; Duchesne et al. 2021, for recent works). We note that the candidate radio halo in PSZ2 G192.77+33.14 ($M_{500} = (1.66 \pm 0.20) \times 10^{14}\ M_{\odot}$), if confirmed, would be the least massive system presently known to host a radio halo. Radio halos in our sample cover also a wide redshift range ($0.05 \leq z \leq 0.888$), with the bulk located at $0.25 \lesssim z \lesssim 0.4$. The discovery of a significant number of bright radio halos in systems (partially overlapping with our sample) with $z > 0.6$ has been recently made possible thanks to LoTSS observations (Cassano et al. 2019; Di Gennaro et al. 2021a).

The radio relic sample has a broad distribution both in terms of M_{500} and z (despite being more limited in size with respect to that of halos). Unlike halos, we find only one radio relic in clusters at $z > 0.6$ (PSZ2 G069.39+68.05, $z = 0.762$, new discovery). The least massive cluster with a RR in our sample is also that with the lowest redshift: PSZ2 G089.52+62.34 ($M_{500} = (1.83 \pm 0.19) \times 10^{14}\ M_{\odot}$ at $z = 0.07$), which was already reported in van Weeren et al. (2021). The total number of relic sources is 35, and the number of clusters hosting more than one relic in the ICM is 8.

Clusters with uncertain diffuse emission are mainly observed for $z < 0.4$ and $M_{500} < 6 \times 10^{14}\ M_{\odot}$. From visual inspection, we expect that a large fraction of these systems may host a radio halo (which however cannot be firmly claimed at the moment), while a smaller fraction may contain different kinds of sources in the ICM. Follow-up observations are required to confirm the nature of the observed emission.

4.5.2 Classification

Diffuse sources in our sample were classified by visually inspecting LOFAR 120−168 MHz images at different resolutions, before and after the subtraction of the discrete sources. We also made use of overlays of our radio data with optical and X-ray data when available. The most challenging aspect of the inspections was to disentangle the sources of interest (halos and relics) from other contaminating sources such as AGN and phoenixes and also from calibration artifacts. This separation relied upon the high resolution of LOFAR and availability and high quality of the auxiliary datasets. However, in some cases it still remained very challenging to conclusively classify the emission.

Although we found the application of the decision tree (Fig. 4.3) useful to make the classification less biased and more reproducible, we acknowledge that the visual inspection of the 309 objects in our sample is a painstaking procedure. It is clear that the strategy used in this work needs further development to properly assess significantly larger cluster samples and to eventually conduct a blind search and classification for cluster emission. In this respect, machine-learning based techniques represent an appealing solution to classify the emission in large object samples (e.g. Aniyan & Thorat 2017; Alhassan et al. 2018; Domínguez Sánchez et al. 2018; Lukic et al. 2018, 2019; Sadeghi et al. 2021; Vavilova

et al. 2021). As part of this work we have made all our images and the detailed results of our decision tree based classification public, which we hope can provide a good training set for algorithms that attempt either the full classification or to aid the automation at specific intersections in a decision tree type approach.

4.5.3 Prospects

The fraction of identifications in each of our classifications with respect to the full LoTSS-DR2 sample is shown Fig. 4.8. In the following, reported fractions were computed excluding the 36 targets of the sample for which we could not verify the presence of diffuse emission in the radio images (i.e. 5 not extracted and 31 N/A). The reported uncertainties are computed based on Poisson statistics.

The fractions of PSZ2 clusters in which a RH or one or more RRs is claimed in this work are 19 ± 9% and 7 ± 5%, respectively, and increase to 27 ± 10% and 10 ± 6% if candidates are also included. If the 10 RH*/cRH* are also taken into account, the fraction of clusters with a detected radio halo further raises to 30 ± 11%. The fraction of clusters hosting sources with uncertain origin is 17 ± 8%, while that of targets that do not show the presence of diffuse synchrotron emission in the ICM is 51 ± 14%.

The area covered by LoTSS-DR2 is ideal to study the extragalactic sky as it avoids regions at low Galactic latitude and low-declination fields (i.e. between declination 0° and +15°), where the sensitivity of LoTSS is generally a factor of 2−3 lower than the nominal survey noise. van Weeren et al. (2021) presented the first statistical analysis of galaxy clusters observed with LoTSS and studied the 26 PSZ2 clusters residing in the area covered by LoTSS-DR1, which is contained within LoTSS-DR2. LoTSS-DR2 has a sky coverage ∼13 times larger (5634 deg^2 vs. 424 deg^2) than LoTSS-DR1 and it samples a broader declination and right ascension range. This makes the new data release more representative of the quality of LoTSS for extragalactic studies. We thus use our findings to estimate the number of PSZ2 sources that will be found to host radio halos at the completion of LoTSS. We consider that there are 835 detections in the PSZ2 catalogue above a declination of 0° and assume a uniform sensitivity for LoTSS for simplicity. We note that the presence of the Galactic plane is taken into account in the PSZ2 selection due to the lack of *Planck* detections in the zone of avoidance. By considering a detection fraction of 30 ± 11% (which includes RH*/cRH*) of halos in our sample, we predict that we will find 251 ± 92 clusters hosting a halo (including candidates), and, as in our study, approximately half of them should be new discoveries. If we assume that also all uncertain sources trace a halo, we obtain a conservative upper limit of < 401 ± 117. In Chapter 6 we will refine these estimates by taking into account the sensitivity of present observations, the PSZ2 selection functions, and the new $P_{150} - M_{500}$ correlation.

4.6 Summary and conclusions

We have presented the largest statistical sample of galaxy clusters used to date to search and study diffuse synchrotron sources in the ICM. We examined the 120−168 MHz radio emission from 309 galaxy clusters selected from PSZ2 that span a redshift and mass

range of $0.016 < z < 0.9$ and $1.1 \times 10^{14}\ M_{\odot} < M_{500} < 11.7 \times 10^{14}\ M_{\odot}$, that have been covered by LoTSS-DR2. We produced radio images with different resolutions and with or without discrete source subtracted, and overlays with Pan-STARRS optical images for all the targets in our sample. When available, we also used targeted Chandra and XMM-Newton observations to compare the radio emission with that of the X-rays and derive morphological parameters of the ICM. All these images are publicly available on the project website https://lofar-surveys.org/planck_dr2.html.

We divided the diffuse synchrotron emission into the classes of halos, relics, and uncertain sources. The physical properties of halos have been collected into tables (also available on the website) and are used in Chapter 6 to discuss their statistical properties, such as occurrence and scaling relations. Overall, we found 83 clusters hosting a radio halo and 26 clusters hosting one or more radio relics (including candidates), of which about half are new discoveries. These numbers correspond to a detection fraction in our sample of $30 \pm 11\%$ and $10 \pm 6\%$, respectively. Based on these results, we expect to find 251 ± 92 cluster hosting a halo in the PSZ2 catalogue at the completion of LoTSS.

In the future, LoTSS will benefit from the synergy of complementary radio surveys, which will be fundamental to study the spectral properties of the observed sources. Moreover, new X-ray observations for clusters in our sample that at present lack Chandra and XMM-Newton pointings will be crucial to confirm the candidate halos and relics, and derive morphological parameters (especially for NDE targets, as discussed in Chapter 6). Finally, we note that there are opportunities to further improve the image quality with respect to that presented in this work (e.g. by fine-tuning the parameters adopted for the self-calibration and subtraction of discrete sources), which is primarily important to investigate the nature of the uncertain sources.

Chapter 5

Recovering diffuse extended emission with LOFAR

In Chapter 4 we presented the sample of 309 Planck clusters in LoTSS-DR2. Among them there are 140 NDE clusters that lack a detected radio halo, and are the focus of this Chapter. As part of my main contribution in the analysis of LoTSS-DR2 clusters, this large sample of non-detections offered us the opportunity to systematically test the capabilities of LOFAR to recover extended targets in the sky, and develop new methods to derive upper limits to the radio power of a possible RH. In this respect, obtaining solid upper limits is primarily crucial to interpret the evolution of RHs and the statistical radio properties of clusters.

This Chapter is based on the results presented in Paper II (Bruno et al. 2023). By simulating mock RHs in the observed *uv*-dataset of the field of NDE clusters, we first demonstrate the extremely high performance of LOFAR for the study of any extended source. We then present the new methods that we developed to derive upper limits in large samples of objects, such as those that will be provided by the next generations of interferometers (e.g. SKA). Finally, for a proper sub-sample of 75 NDE clusters, we determine the deepest upper limits obtained so far in the literature, which will be used in the analysis outlined in Chapter 6.

5.1 Introduction

Radio sources with large extents in the sky may be not properly recovered by radio interferometers with an insufficient number of short baselines. A poorly sampled *uv*-coverage at short spacings will thus cause unavoidable flux density losses (e.g. Wilner & Welch 1994; Deo & Kale 2017). This problem arises in many fields of radio astronomy, such as the study of extended radio galaxies, supernova remnants, and diffuse emission in galaxy clusters.

Among the various diffuse synchrotron sources found in galaxy clusters, RHs are the most extended ones. RHs are not ubiquitous in galaxy clusters. The non-detections of RHs may be intrinsically due to absence of radio emission (off-state clusters), or result

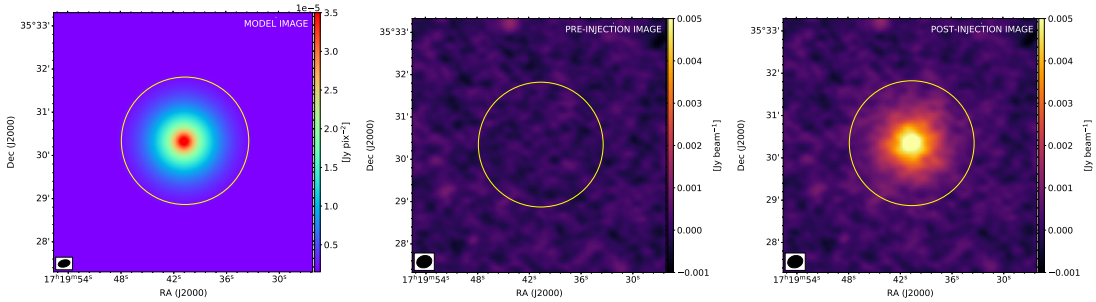

Figure 5.1: Example of the injection process. The yellow circle is centred on (RA_{inj}, DEC_{inj}) and has a radius $r = 3r_e$. *Left*: model image at 144 MHz of the mock halo following the exponential surface brightness profile of Eq. 5.1. *Middle*: pre-injection image. *Right*: post-injection image.

from instrumental and/or observational limits, namely a combination of insufficient sensitivity and poor sampling of short baselines.

In galaxy clusters where no radio emission is detected, upper limits on the radio power of a possible halo can be determined. Upper limits are important in statistical studies to constrain theoretical models of formation and evolution of the diffuse sources (e.g. Brunetti et al. 2007). In this respect, upper limits are necessary to understand whether off-state and on-state clusters belong to two distinct populations (i.e. relaxed and disturbed, respectively), and thus obtain constraints on the origin of the non-thermal emission. To this aim, it is necessary to compare the radio powers of detected halos and limits as a function of the mass of the host cluster (e.g. Cassano et al. 2013; Cuciti et al. 2021a). Moreover, deep upper limits can be exploited to test the level at which purely hadronic (Dennison 1980; Blasi & Colafrancesco 1999; Dolag & Enßlin 2000) RHs may be detected or test models of dark matter interactions (Storm et al. 2017). Various methods have been adopted to determine upper limits. The most widely used method follows the 'injection' technique first exploited for RHs by Brunetti et al. (2007) and Venturi et al. (2008). It consists of modelling simulated RHs, whose predicted visibilities are added to the observed ones, and then regularly processed to obtain images to check for possible detections at a given flux density threshold. Since then, this technique has been commonly adopted on data of galaxy clusters from different facilities (e.g. Kale et al. 2013; Bonafede et al. 2017; Johnston-Hollitt & Pratley 2017; Cuciti et al. 2021b; George et al. 2021a; Osinga et al. 2021; Duchesne et al. 2022).

In this work, we focus on the sub-sample of 140 non-detections ('NDE') of diffuse emission from the ICM in *Planck* clusters belonging to LoTSS-DR2 (Chapter 4). We exploit these datasets to test the capabilities of LOFAR to recover extended emission and obtain upper limits to the presence of possible RHs.

5.2 Injection algorithm

To test the capabilities of LOFAR and determine upper limits for the NDE clusters, we followed the injection technique. We first derived the visibilities from the Fourier inver-

sion of a set of models of mock halos ('prediction' step) sampling a range of flux densities and angular sizes, and then added these mock visibilities to the dataset of each observation ('injection' step). Imaging and Fourier transforms were carried out by means of `WSClean` v. 2.10 (Offringa et al. 2014; Offringa & Smirnov 2017). The main steps of the procedure can be summarised as below:

1. The coordinates (RA_{inj}; DEC_{inj}) of the centre of the injection and the total injected flux density at 144 MHz ($S_{inj,tot}$) are required as inputs.

2. Frequency-dependent model images of the mock halo that follow an exponential surface brightness profile are built (see Sect. 5.2.1). We assumed a spectral index $\alpha = 1.3$ in the frequency range 120-168 MHz, as typical of RHs. This is computed through the `channels-out 6` parameter in `WSClean`, which produces model images at 6 sub-bands spaced by 8 MHz each.

3. The model images are Fourier transformed by means of the `predict` function in `WSClean` to obtain the corresponding mock visibilities, which are then added to the real *uv*-data.

4. The updated (real plus mock visibilities) datasets are imaged by adopting the multi-scale (fixed scales of [0, 4, 8, 16, 32, 64] pixels) and multi-frequency (`channels-out 6`) cleaning algorithm. To enhance the diffuse emission, the baselines are tapered by a Gaussian function (`taper-gaussian`) to lower resolutions.

An example of this process is shown in Fig. 5.1, where we injected a bright ($S_{inj,tot} = 100$ mJy) mock halo into a source-free region in the field of PSZ2 G059.18+32.91.

To investigate the capabilities of LOFAR to recover extended emission and derive upper limits, we need to repeat the steps 2-4 by gradually decreasing $S_{inj,tot}$ in step 1 until some given detection criteria (e.g. recovered flux density or sizes, signal-to-noise ratio, inspection by eye) are not fulfilled anymore, as further discussed in Sect. 5.4.2.

5.2.1 Modelling of the surface brightness profile

Murgia et al. (2009) showed that a simple exponential law provides a good representation of the observed surface brightness distribution of a number of RHs, with few free parameters. Following a common approach adopted for both real and mock halos (e.g. Murgia et al. 2009; Bonafede et al. 2017; Boxelaar et al. 2021; Osinga et al. 2021; Botteon et al. 2022a; Hoang et al. 2022), we assumed an exponential, spherically-symmetric, exponential law to model the surface brightness profiles of our mock halos:

$$I(r) = I_0 e^{-\frac{r}{r_e}} , \tag{5.1}$$

where I_0 is the central surface brightness and r_e is the e-folding radius.

The flux density is obtained by integrating Eq. 5.1 in circular annuli up to a certain radius $\hat{r}$:

$$S_\nu = 2\pi \int_0^{\hat{r}} I(r) r dr = 2\pi I_0 [r_e^2 - (\hat{r} r_e + r_e^2) e^{-\frac{\hat{r}}{r_e}}] . \tag{5.2}$$

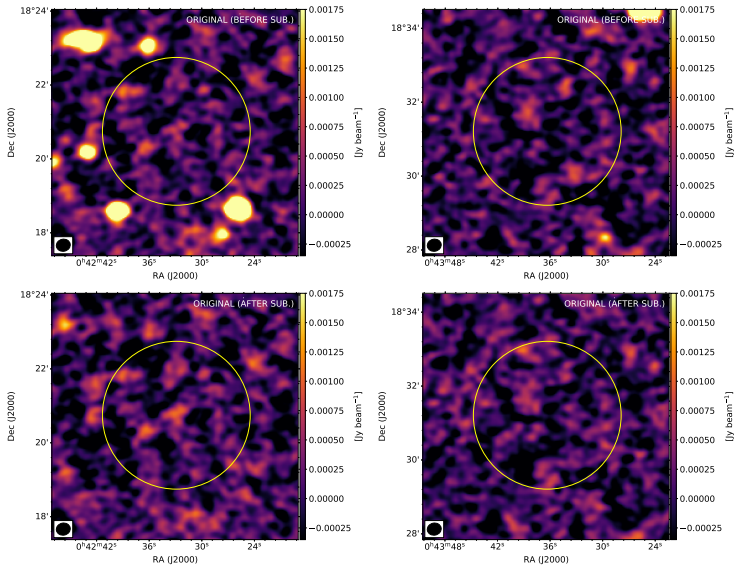

Figure 5.2: Restored images before injections in the centre (left panels) and periphery (right panels) of PSZ2 G120.08-44.41 before (upper panels) and after (lower panels) subtraction of discrete sources.

Eq. 5.2 can be simply expressed as $S_\nu = 2\pi f(\hat{r}) I_0 r_e^2$, where $f(\hat{r}) = [r_e^2 - (\hat{r}r_e + r_e^2)e^{-\frac{\hat{r}}{r_e}}]$ is the fraction of flux density within the integration radius $\hat{r}$ to the total one ($f(\hat{r}) = 1$ when $\hat{r} = +\infty$). RHs do not extend indefinitely, thus their emission is typically measured up to $\hat{r} = 3r_e$, which provides a fraction $f(\hat{r}) = 0.8$ of the total flux density.

For the injection process, we derive the central brightness from the total injected flux density as $I_0 = S_{\rm inj,tot}/2\pi r_e^2$. In the following, we will refer to the injected diameter of the mock halo as being $D = 6r_e$ (i.e. we assume a radius $R = 3r_e$).

5.2.2 Schemes of injection

As examples, in Fig. 5.3 we show the injections of mock halos with $r_e = 40.7''$ and $S_{\rm inj,tot} = 20$, 50, 100 mJy that we performed both close to the pointing centre of PSZ2 G120.08-44.41 and far from it (at a distance of $\sim 19'$), by using the extracted & re-calibrated datasets ('Inj.' scheme); images of this field before the injections are shown in Fig. 5.2 with the same color scale for a comparison. As preliminary checks of our procedure, we fitted the surface brightness of the mock halos (discrete sources close to the mock emission were masked) by means of the `Halo-FDCA` code (Boxelaar et al. 2021), which was used for RHs in LoTSS as well (van Weeren et al. 2021; Botteon et al. 2022a; Hoang et al. 2022), and measured the flux density in circles of radius $\hat{r} = 3r_e$, where a fraction $f(\hat{r}) = 0.80$ of the total injected flux density is expected according to Eq. 5.2. The images in Fig. 5.3 show that injecting the same flux density in different locations generally provides visually-different mock halos, because of the presence of discrete sources and local fluctuations of the noise, contaminating the morphology of the mock emission. Nevertheless, as reported in Table 5.1, the flux densities measured by hand ($S_{\rm meas}$) are in good agreement for all the corresponding injections in the centre and far from it. The flux

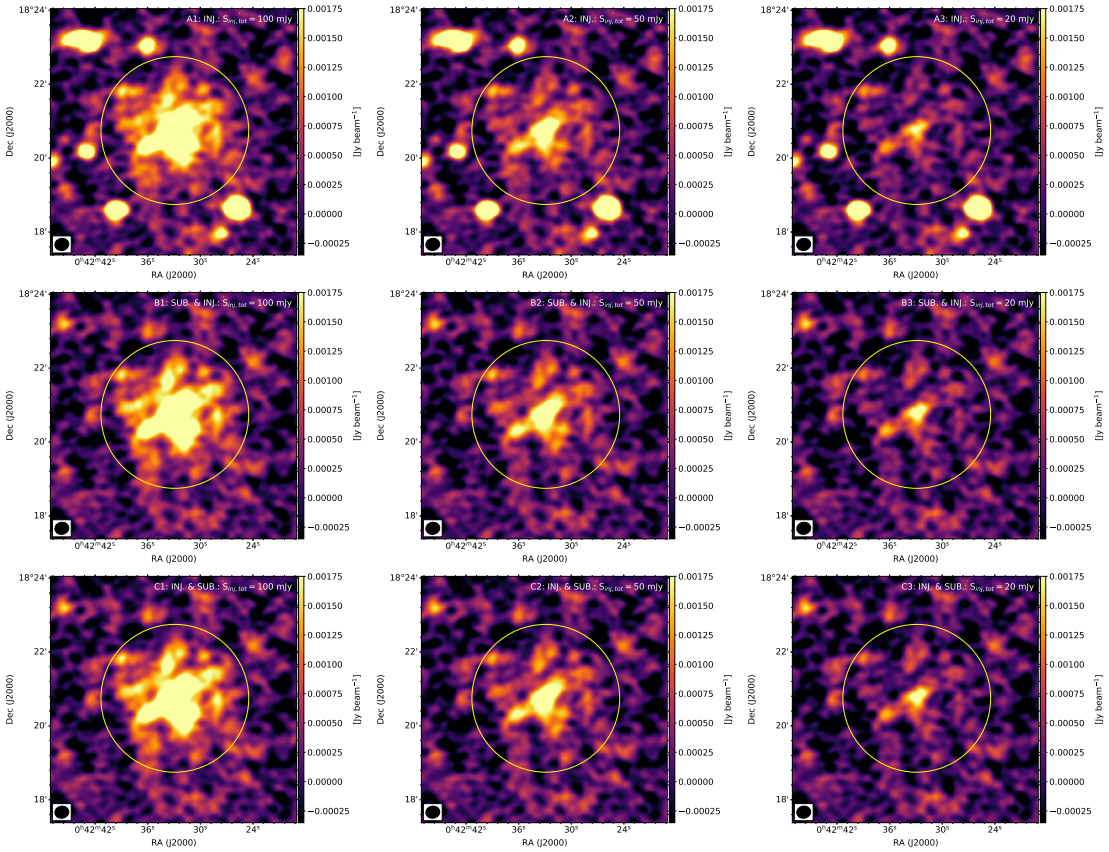

Figure 5.3: Restored images after injections in the centre (panels A, B, C) and periphery (panels D, E, F) of PSZ2 G120.08-44.41 with different schemes: injection in the original dataset ('INJ.', panels A, D), injection in the discrete source-subtracted dataset ('SUB. & INJ.', panels B, E), and injection in the original dataset and subsequent subtraction of the discrete sources ('INJ. & SUB.', panels C, F). The yellow circle (centred on $\mathrm{RA_{inj}}$, $\mathrm{DEC_{inj}}$) has a radius of $3r_\mathrm{e}$ and contains $S_\mathrm{inj} = 0.8S_\mathrm{inj,tot}$, where $S_\mathrm{inj,tot} = 100,\ 50,\ 20$ mJy, for panels in columns 1, 2, 3, respectively.

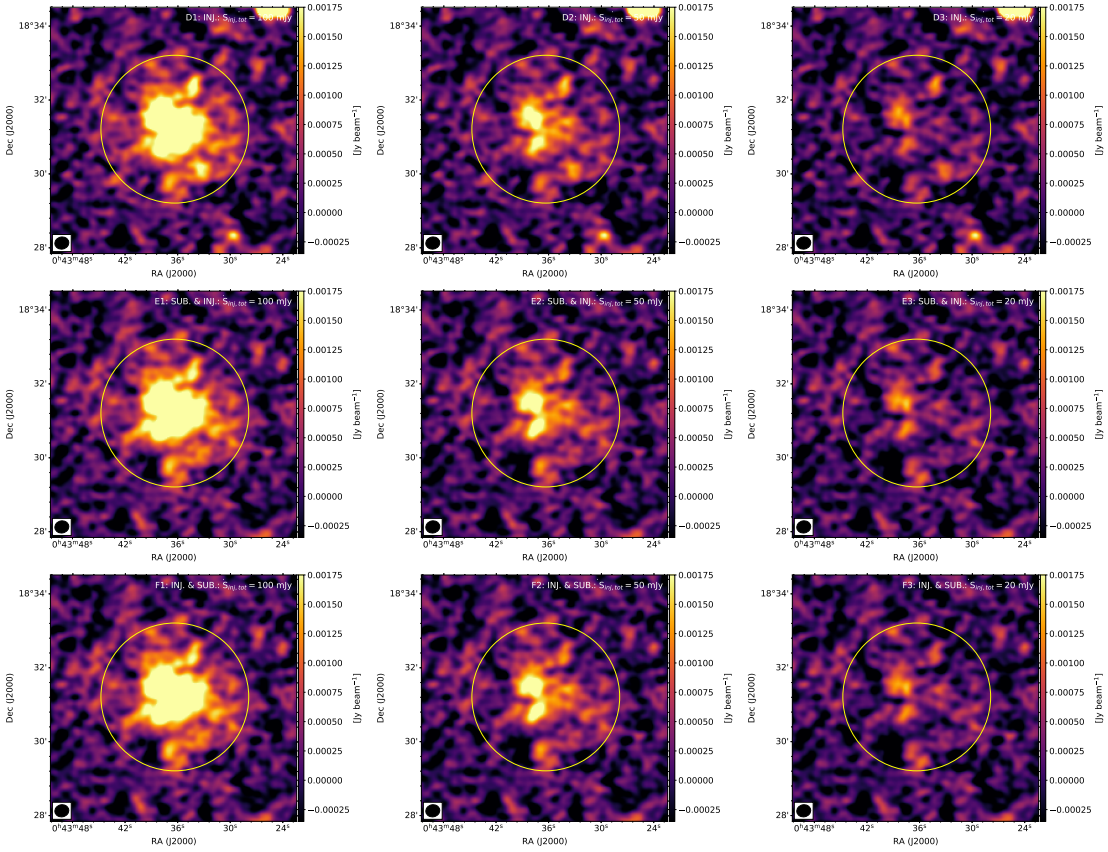

Figure 5.3: continued.

density obtained through Halo-FDCA is computed as $S_{\rm fit} \propto I_{0,\rm fit} r^2_{\rm e,fit}$, thus it is strongly dependent on the fitted e-folding radius and its associated error; in particular, the less the significance of the emission of mock or real halos, the higher the errors on $r_{\rm e,fit}$. Despite this, all the corresponding injected and fitted parameters are consistent within the fitting errors. These tests indicate that our simulations are barely dependent on the position of the injection, meaning that the response of the instrument can be considered uniform, at least across the extraction regions.

Background, foreground, and embedded sources contaminate the faint diffuse emission of RHs. A model of the discrete sources can be obtained by selecting only the longest baselines, depending on the angular scales that need to be filtered out, and their contribution can be then directly subtracted from the *uv*-data. We compared the results of the 'Inj.' scheme with the injection in source-subtracted datasets ('Sub. & Inj.' scheme) and the effects of subtraction after injecting in the original datasets ('Inj. & Sub.' scheme). To this aim, following the approach described in Botteon et al. (2022a), we selected the baselines corresponding to projected sizes < 250 kpc at the cluster redshift, and removed discrete sources in our targets. As reported in Table 5.1, the measured and fitted flux densities are consistent for all the three schemes. We notice, however, differences in $I_{0,\rm fit}$ and $r_{\rm e,fit}$ in case of the injection with the lowest flux density, i.e. $S_{\rm inj,tot} = 20$ mJy. As previously mentioned, this is due to the low significance of the diffuse emission with respect to the background, and in these cases, residuals from the source subtraction process that were not masked during the fit could have a non-negligible impact on the fit with Halo-FDCA. By comparing the 'Sub. & Inj.' and 'Inj. & Sub.' schemes, we find an almost perfect agreement in both the measures and fitting of the corresponding cases, meaning that the mock diffuse emission is not included in the subtraction model. This latter result has a major practical utility for our work; indeed, the subtraction can be performed only once, thus allowing us to save a huge amount of computing time, and different injections can be carried out in the same source-subtracted dataset, with no need to subtract sources after each injection (see also Sect. 5.4.2).

We conclude this section by commenting on the recovered morphology of mock halos. For very bright mock halos, the spherical and smooth profile is typically recovered. On the other hand, in the case of less bright mock halos, the roundish and smooth shape can be easily perturbed depending on the local noise pattern and effective sensitivity of the observations. By gradually decreasing the injected flux density, the symmetry is progressively broken, and the mock halo will appear as patches of emission around the peak. This behaviour can be seen in Fig. 5.3. Even though the recovered morphology depends on the specific dataset and injection position, we can quantify the relative deviations as a function of radius and injected flux density through a point-to-point comparison. To this aim, we considered our brightest injections at 100 mJy (with the 'Sub. & Inj.' scheme), and sampled the corresponding mock halos with a grid of beam-size square boxes down to the 2σ contour level. The same grid was used to sample the mock halos of $S_{\rm inj,tot} = 50$ and 20 mJy as well. The surface brightness at 20 and 50 mJy were normalised to match the injection at 100 mJy (i.e. they are multiplied by factor of 5 and 2, respectively), and the corresponding measures were reported in Fig. 5.4 as a function of the brightness at 100 mJy. These plots show that progressively increasing deviations from the one-to-one

Table 5.1: Comparison between injected and recovered parameters within $3r_e$ of the mock halos in Fig. 5.3. Column 1 reports the adopted algorithm scheme discussed in the text. Columns 2, 3 report the location of the injection and the flux density measured in the halo area before the injection (S_{pre}). Columns 4, 5, 6 report the injected ($S_{inj} = 0.8S_{inj,tot}$), the measured by hand (S_{meas}), and the fitted (S_{fit}) flux density. Columns 7, 8, 9, 10 report the injected and fitted I_0 and r_e.

Scheme	Location	S_{pre} (mJy)	S_{inj} (mJy)	S_{meas} (mJy)	S_{fit} (mJy)	$I_{0,inj}$ (μJy arcsec^{-2})	$I_{0,fit}$ (μJy arcsec^{-2})	$r_{e,inj}$ (arcsec)	$r_{e,fit}$ (arcsec)
Inj.	Centre	0.4	80.0	81.1 ± 8.8	84.0 ± 5.3	9.6	$10.1^{+0.7}_{-0.7}$	40.7	$40.7^{+2.4}_{-2.2}$
			40.0	40.6 ± 5.3	42.9 ± 4.4	4.8	$5.2^{+0.6}_{-0.5}$		$40.7^{+3.9}_{-3.4}$
			16.0	16.6 ± 3.8	18.8 ± 4.1	1.9	$2.3^{+0.6}_{-0.5}$		$40.5^{+9.3}_{-7.8}$
Inj.	Off-centre	−0.8	80.0	79.8 ± 8.7	80.0 ± 4.4	9.6	$9.5^{+0.6}_{-0.6}$	40.7	$40.7^{+2.0}_{-2.0}$
			40.0	39.7 ± 5.2	39.6 ± 3.3	4.8	$4.6^{+0.4}_{-0.4}$		$41.2^{+3.2}_{-2.9}$
			16.0	15.7 ± 3.7	13.0 ± 3.0	1.9	$2.1^{+0.6}_{-0.5}$		$35.1^{+8.0}_{-7.1}$
Sub. & Inj.	Centre	0.7	80.0	81.7 ± 8.8	82.6 ± 4.9	9.6	$10.5^{+0.7}_{-0.7}$	40.7	$39.5^{+2.2}_{-2.0}$
			40.0	41.0 ± 5.2	41.3 ± 3.8	4.8	$5.8^{+0.6}_{-0.6}$		$37.5^{+3.2}_{-2.9}$
			16.0	16.8 ± 3.7	15.2 ± 3.1	1.9	$3.5^{+1.0}_{-0.7}$		$29.5^{+6.3}_{-5.6}$
Sub. & Inj.	Off-centre	−0.8	80.0	79.9 ± 8.6	81.0 ± 3.9	9.6	$9.8^{+0.5}_{-0.5}$	40.7	$40.5^{+1.7}_{-1.7}$
			40.0	39.6 ± 5.1	39.8 ± 3.4	4.8	$5.0^{+0.5}_{-0.5}$		$40.0^{+2.9}_{-2.9}$
			16.0	15.9 ± 3.6	13.7 ± 2.7	1.9	$2.6^{+0.6}_{-0.5}$		$32.7^{+6.1}_{-5.6}$
Inj. & Sub.	Centre	0.4	80.0	81.9 ± 8.8	82.9 ± 4.9	9.6	$10.5^{+0.7}_{-0.6}$	40.7	$39.7^{+2.2}_{-2.0}$
			40.0	40.8 ± 5.2	41.0 ± 3.9	4.8	$5.8^{+0.6}_{-0.6}$		$37.3^{+3.4}_{-3.2}$
			16.0	16.5 ± 3.7	15.1 ± 3.1	1.9	$3.5^{+1.0}_{-0.7}$		$29.3^{+6.6}_{-5.6}$
Inj. & Sub.	Off-centre	−0.8	80.0	79.9 ± 8.6	80.7 ± 4.0	9.6	$9.9^{+0.5}_{-0.5}$	40.7	$40.2^{+1.7}_{-1.7}$
			40.0	39.7 ± 5.1	40.0 ± 3.5	4.8	$4.9^{+0.5}_{-0.5}$		$40.2^{+3.2}_{-2.9}$
			16.0	15.9 ± 3.6	14.4 ± 2.8	1.9	$2.4^{+0.6}_{-0.5}$		$34.6^{+6.6}_{-5.9}$

Notes. Errors on S_{meas} are calculated as $\Delta S_{meas} = \sqrt{(\sigma^2 \cdot N_{beam}) + (\xi_{cal} \cdot S_{meas})^2}$, where σ is the noise of the restored image, N_{beam} is the number of beams within the considered region, and ξ_{cal} is the flux density scale uncertainty; we adopted $\xi_{cal} = 10\%$ (Shimwell et al. 2022a). Errors on S_{fit} take into account the fitting uncertainties only, which depend on $\Delta r_{e,fit}$ and $\Delta I_{0,fit}$.

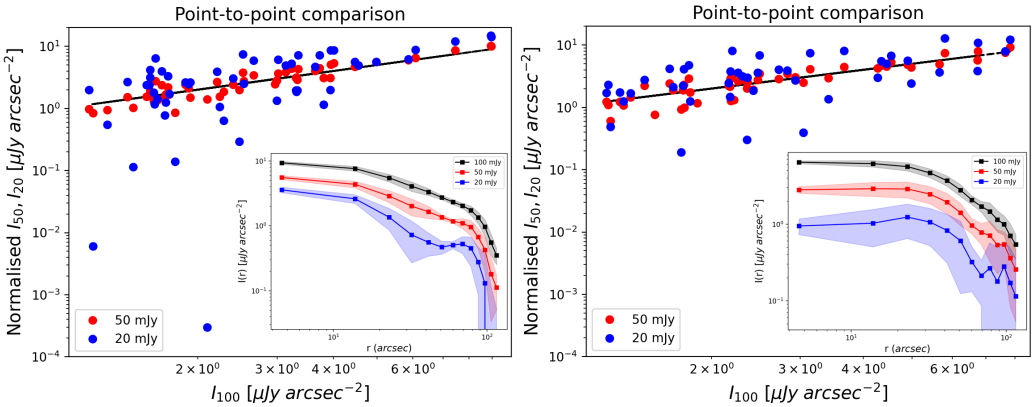

Figure 5.4: Point-to-point comparison of the surface brightness of mock halos in PSZ2 G120.08-44.41 ('Sub. & Inj.' scheme; central and peripheral injections are shown in the left and right panel, respectively). Values at 20 and 50 mJy are multiplied by a factor 5 and 2, respectively, to match the injection at 100 mJy. The one-to-one line is plotted in black. Insets show the corresponding (non-normalised) radial profiles, whose data points are obtained as the average brightness of four 90°-wide sectors, whereas the shaded region represents their standard deviation. The point-to-point plots show that the lower the brightness and the injected flux density, the higher the scatter around the one-to-one line, indicating the progressive arise of patches of emission. Analogously, the radial profiles indicate that the scatter increases at larger radii and lower brightness.

line are found from higher to lower brightness (i.e. outwards from the peak), and that the scatter is larger for the injections at 20 mJy than at 50 mJy. This can be also observed in the insets of Fig. 5.4: the reported radial profiles are obtained by averaging profiles extracted in four 90°-wide sectors for each mock halo. Both the point-to-point plot and radial profiles show that the scatter of the brightness is larger in the outermost regions of the mock halos, where the faint emission consists of asymmetric patches and less flux density is recovered. Moreover, the differences between the injections in the centre and periphery are associated with the local noise conditions, which notably contribute to the recovered morphology of the mock halo. By decreasing $S_{\rm inj,tot}$ and approaching the noise level, the scatter will further increase.

5.3 LOFAR performances

In this section, we explore in detail the capabilities of LOFAR to recover extended emission, by simulating mock RHs with a wide range of flux densities and angular sizes in some clusters of our reference sample. By adopting the standard *uv*-cut for LOFAR HBA, baselines $< 80\lambda$ will be not employed in our analysis[1].

[1]Baselines shorter than 80λ are typically more challenging to calibrate and sample possible emission on angular scales larger than $40'$ from our Galaxy that needs to be filtered.

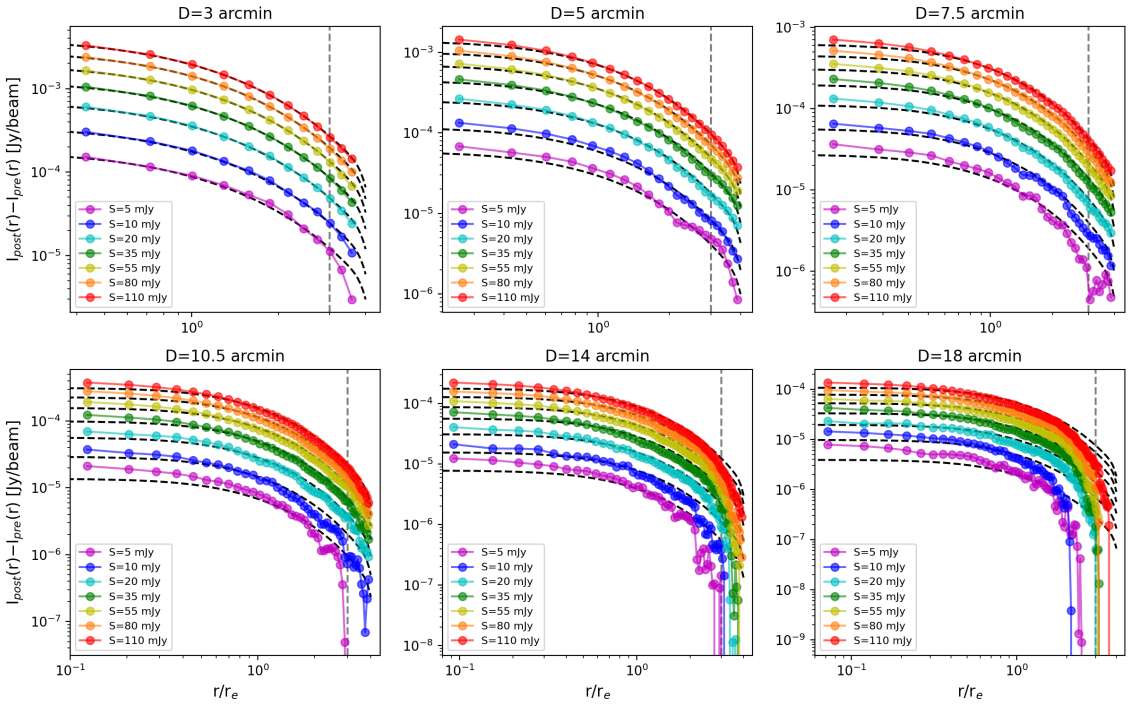

Figure 5.5: Net azimuthally-averaged surface brightness profiles of the images shown in Section C for PSZ2 G098.62+51.76. The dashed black lines represent the theoretical injected profiles. The sampled profiles ($S_{\mathrm{inj,tot}}$ is reported in the legend) are obtained by subtracting the pre-injection from the post-injection contribution. The grey vertical line indicates $r = 3r_e$.

5.3.1 The role of the *uv*-coverage

When dealing with extended radio emission, the role played by the *uv*-coverage needs to be carefully taken into account. Indeed, interferometers lacking short baselines will not be able to fully recover extended sources in the sky. As a consequence, non-detections might arise from insufficient sampling of the *uv*-coverage at short spacings. In previous works, LOFAR *uv*-coverage was tested on the basis of injections on specific observations (Hoang et al. 2018; Botteon et al. 2020b). Here we aim to systematically investigate the associated flux density losses by performing $\sim$ 500 injections in $\sim$ 10 cluster fields characterised by different data quality and noise. In each of these clusters, we injected mock halos with various flux densities (ranging from 5 to 145 mJy) and angular diameters (3, 5, 7.5, 10.5, 14, 18 arcmin, corresponding to baseline lengths of $\sim$ 1150kλ, 690λ, 460λ, 330λ, 250λ, 190λ, respectively). As a representative example of one of these clusters, in Section C we show a collection of mock halos injected in the field of PSZ2 G098.62+51.76, which was used to produce the plots discussed throughout this and next section. For each mock halo, we obtained the corresponding azimuthally-averaged surface brightness profile $I_{\mathrm{post}}(r)$ by adopting sampling annuli of width equal to half of the FWHM of the restoring beam of the images. The same analysis was performed on the pre-injection images, whose profiles $I_{\mathrm{pre}}(r)$ include the contribution of both radio

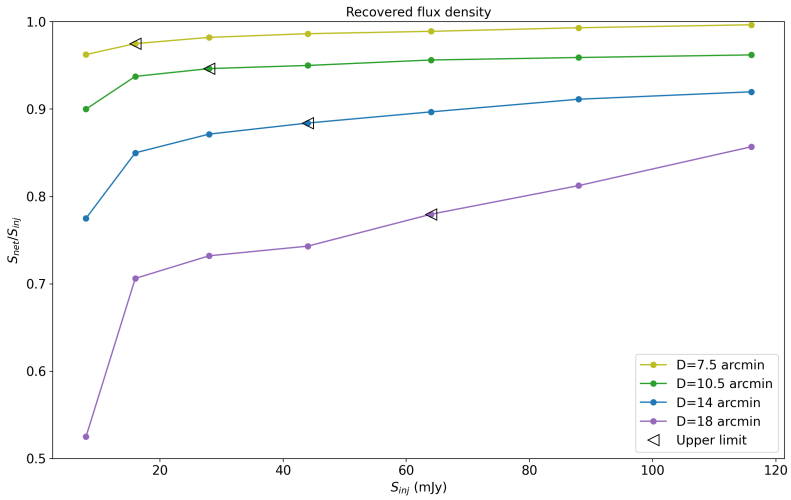

Figure 5.6: Fraction of recovered net flux density as a function of the injected flux density (within $3r_e$) at various angular scales. Triangular markers indicate the flux density threshold at which the mock emission is not visible based on images in Section C. Non-negligible flux density losses (> 15%) are expected for sources with angular sizes $D \gtrsim 15'$ only.

sources and noise.

In Fig. 5.5 we show the net profiles computed as the difference in each bin between $I_{\rm post}$ and $I_{\rm pre}$, overlaid on the injected profiles after being convolved with the restoring beam; since the peak of the profiles is always recovered, the first sampling annulus is not reported. The recovered net profiles are in agreement with the injected profiles for mock halos with sizes up to $D = 10.5'$; this result is a consequence of the dense *uv*-coverage of LOFAR on short spacings. On the other hand, deviations are visible in the cases of $D = 14'$ and $D = 18'$.

To estimate the losses in case of extended sources, in Fig. 5.6 we report the fraction of recovered flux density as a function of the injected flux density for each angular scale $D \geq 7.5'$. Overall, the recovered fractions are approximately constant over a wide range of injected flux densities up to $D = 14'$. To further constrain the effective losses, we inspected the images shown in Section C and determined the threshold among the injected flux densities $S_{\rm inj}$ at which the mock emission cannot be distinguished anymore from the local noise. Based on these flux density levels (indicated by triangular markers in Fig. 5.6), on average flux density losses associated with the *uv*-coverage are $\lesssim 5\%$ up to $D = 10.5'$, $\sim 10\%$ for $D = 14'$, and $\gtrsim 20\%$ for sources with $D = 18'$. In summary, we conclude that flux density measurements of sources observed by LOFAR are weakly dependent on the *uv*-coverage up to $D \sim 15'$, meaning that the instrument is still well sampled at spacings $\sim 250\lambda$, whereas non-negligible losses should be taken into account for sources with larger angular sizes. In the latter case, the use of baselines $< 80\lambda$ should be considered to mitigate the flux density losses.

It is worth to mention that more flux density than that injected might be recovered. This effect is described in detail in Shimwell et al. (2022a) and is due to uncleaned com-

ponents during the imaging step: when the peak of a cleaning component is lower than the cleaning threshold, it will be not correctly deconvolved and will be enhanced in the restored image. As seen in Fig. 5.5, this cleaning bias increases for wider (large r_e) and fainter (low I_0) profiles. In the worst cases, i.e. $S_{\rm inj,tot} = 5$ mJy, the recovered peaks are biased by factors of ∼1.2, 1.4, 1.6, 1.6, and 2, for $D = 5'$, $7.5'$, $10.5'$, $14'$, $18'$, respectively, in agreement with Shimwell et al. (2022a) who found maximum factors of 2 as well through injections of Gaussian profiles. For a comparison, with $S_{\rm inj,tot} = 10$ mJy and $D = 18'$, the maximum cleaning bias factor is ∼1.5, and further decreases for higher injected flux densities. Therefore, even if this systematic effect is present, the global results we drawn in this section still hold.

This work focuses on exponential profiles as they can reproduce the observed brightness of RHs, but losses with different injected models can be derived with the same approach. Shimwell et al. (2022a) probed the fraction of recovered flux density in LoTSS-DR2 by injecting Gaussian profiles, and found that this is of the order of $\sim$ 95% for standard deviations $\leq 2'$. Gaussian profiles are narrower than exponential profiles of the same width. Therefore, higher flux density fractions are expected to be recovered because of the increasing contribution of longer baselines. A systematic comparison between exponential and Gaussian profiles is beyond the aim of the present work. However, as a sanity check, we injected bi-dimensional Gaussian profiles in the form of $I(r) = I_0 e^{-\frac{r^2}{2r_e^2}}$ (where r_e now represents the standard deviation of the Gaussian and $S_{\rm inj,tot} = 2\pi I_0 r_e^2$) in PSZ2 G098.62+51.76. We found losses $\lesssim 10\%$ up to $D = 18'$ (i.e. $r_e = 3'$), in agreement with results of Shimwell et al. (2022a).

5.3.2 Dependencies of the upper limits

Through our simulations, limited to baselines $> 80\lambda$ only, we found that flux density losses are negligible and we can consider both detections and non-detections of extended emission independent on the *uv*-coverage of LOFAR up to $D \sim 15'$ (see also Sect. 5.5 for a comparison with other facilities). Therefore, we expect that non-detections of RHs in clusters are intrinsic or depend only on the sensitivity due to the depth of a specific observation. As a consequence, this suggests that our upper limits should rely on stringent parameters, that we aim to determine.

In Fig. 5.7 we both show the post-injection ($I_{\rm post}(r)$) and pre-injection ($I_{\rm pre}(r)$) surface brightness profiles (bright discrete sources were masked for this step). Uncertainties on the flux density of each sampling annulus are:

$$\Delta S_{\rm bin} = \sigma \sqrt{N_{\rm beam,bin}}\,, \tag{5.3}$$

where σ is the noise (in beam area units) of the radio image and $N_{\rm beam,bin}$ is the number of beams within each annulus. Therefore, the reported errors in Fig. 5.7 are computed as:

$$\Delta I_{\rm bin} = \frac{\Delta S_{\rm bin}}{N_{\rm beam,bin}} = \frac{\sigma}{\sqrt{N_{\rm beam,bin}}}\,. \tag{5.4}$$

We inspected our images and, as a rule of thumb, we found that the mock halos are still visible if at least 2-3 bins (as mentioned, the peak is excluded) are above the local noise

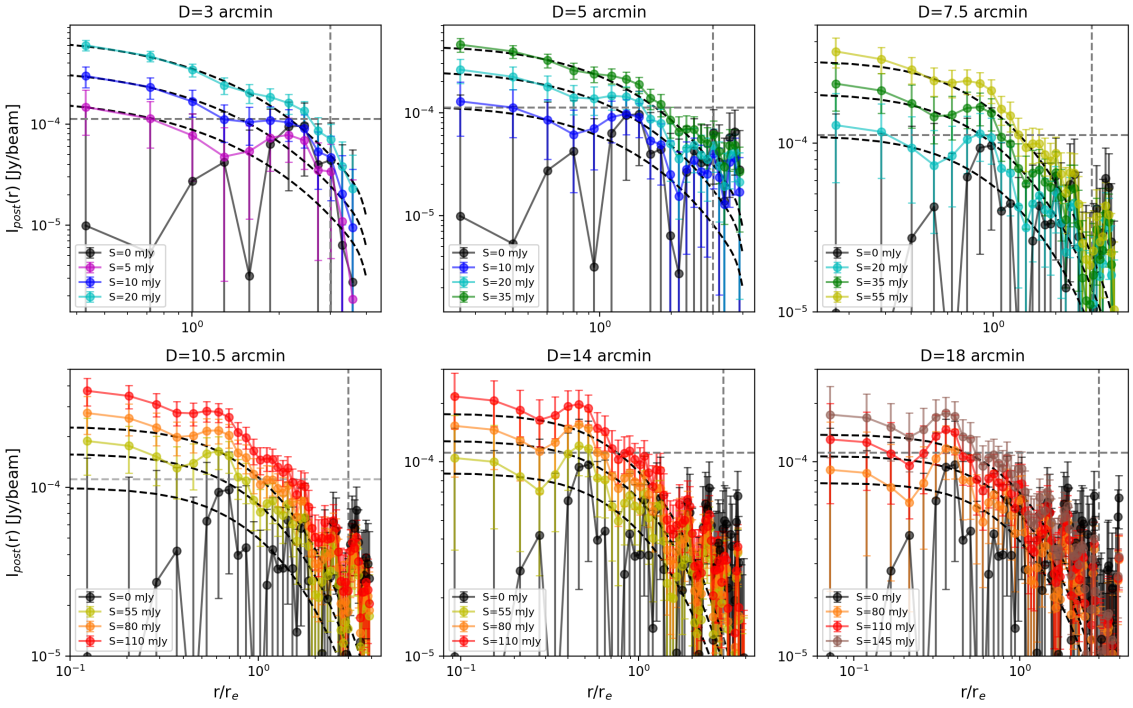

Figure 5.7: Azimuthally-averaged profiles of the images shown in Section C for PSZ2 G098.62+51.76. The dashed black lines represent the theoretical injected profiles. The sampled pre-injection and post-injection profiles are shown with black and coloured dots (see the total injected flux density in the legend), respectively. The grey vertical line indicates $r = 3r_e$. The grey horizontal line indicates the global 1σ noise level.

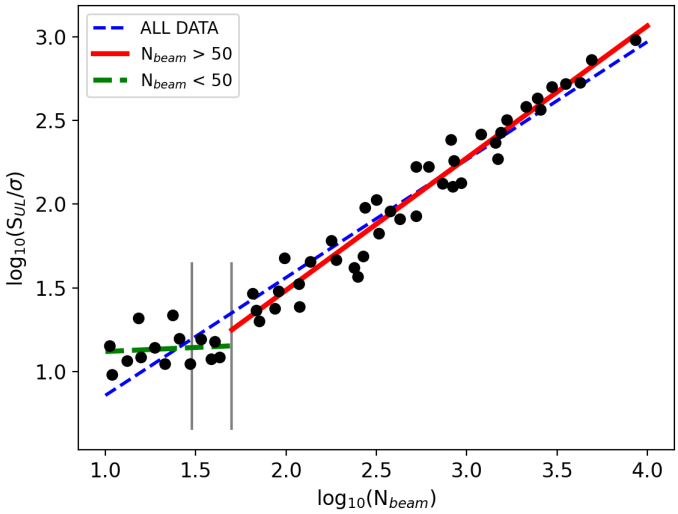

Figure 5.8: Logarithmic plot of the ratio of the upper limit flux density against the noise of the map ($S_{\rm UL}/\sigma$) as a function of the number of beams ($N_{\rm beam}$) within the injected halo. The blue, red, and green lines are the fitted linear regressions (see Tab. 5.2) obtained with no cut in $N_{\rm beam}$, with $N_{\rm beam} > 50$, and with $N_{\rm beam} < 50$, respectively. The grey vertical lines are drawn at $N_{\rm beam} = 30$ and $N_{\rm beam} = 50$.

level (i.e. $I_{\rm post} > I_{\rm pre}$) in our plots. Otherwise, the mock emission cannot be distinguished from the noise, allowing us to define the upper limit in combination with visual inspection.

For each set of injections, we determined the upper limit through visual inspection, guided by the azimuthally-averaged surface brightness profiles. We found that limits depend on a combination of the noise (σ) and resolution (θ) of the restored image, and on the angular size of the mock halo. In particular, the flux density of the upper limit correlates with the noise and the number of beams $N_{\rm beam} \sim D^2/\theta^2$ within the injected mock halo. As shown in Fig. 5.8, we performed a simple linear regression of the data points (~ 50 upper limits among our injections) in a logarithmic plane as:

$$\log\left(\frac{S_{\rm UL}}{\sigma}\right) = m \log\left(N_{\rm beam}\right) + q \ , \tag{5.5}$$

where m and q are the fitted slope and intercept, respectively.

Possible faint diffuse emission can be more easily identified by visual inspection if it is spread over larger areas, i.e. when $N_{\rm beam}$ is large, upper limits are guided by a surface brightness criterion; conversely, they follow a flux density criterion for smaller $N_{\rm beam}$. If our limits were determined based on a surface brightness criterion only, the flux density would scale with the area of the source as $S \propto r_{\rm e}^2 \propto N_{\rm beam}$, and thus we would expect a slope $m = 1$ in Eq. 5.5, whereas a flatter slope $m = 0.5$ is expected if limits were exclusively driven by a flux density criterion (see also Fig. 3 in Brunetti et al. 2007).

These two regimes can be observed in Fig. 5.8, with a flattening that roughly occurs for $N_{\rm beam} < 50$. We performed different linear regressions by using all the data points (blue line), points with $N_{\rm beam} > 50$ (red line), and points with $N_{\rm beam} < 50$ (green line); the results of these fits are reported in Table 5.2. The average slope $m = 0.703$ that we

Table 5.2: Slope (m) and intercept (q) of the linear regressions shown in Fig. 5.8 and discussed in the text.

Data	m	q
All data	0.703 ± 0.023	0.155 ± 0.057
$N_{\rm beam} > 50$	0.789 ± 0.029	-0.091 ± 0.081
$N_{\rm beam} > 30$	0.794 ± 0.024	-0.109 ± 0.066
$N_{\rm beam} < 50$	0.048 ± 0.141	1.072 ± 0.192

obtained by fitting all the data points is in line with the competing trends predicted by the two criteria. By considering only data points with larger $N_{\rm beam}$, the fitted slope $m = 0.789$ steepens, in agreement with the behaviour predicted by the surface brightness criterion. We notice that the same (red) line can interpolate data points down to $N_{\rm beam} \sim 30$ as well. Indeed, by considering data points with $N_{\rm beam} > 30$ we obtained a similar slope $m = 0.794$, which is consistent with that obtained with $N_{\rm beam} > 50$ within the fitting errors.

For fixed σ and D, this positive correlation shows that deeper upper limits can be obtained for injections of lower $N_{\rm beam}$, which are achievable by decreasing the resolution of the restored image. Even though worse σ are obtained by tapering the baselines, we found that images tapered to resolutions of 90″ have typical rms which are factors $\lesssim 2.5$ only with respect to those of images tapered to resolutions of 30″. According to these results, the depth of the limit is primarily driven by $N_{\rm beam} \propto \theta^{-2}$ and it generally benefits from the decrease of the resolution.

5.4 Upper limits for PSZ2 clusters in LoTSS-DR2

In this section we describe the procedures adopted to obtain the upper limits for the NDE clusters of our sample, and compare them with the flux densities of the detected RHs in LoTSS-DR2.

5.4.1 NDE cluster sample

From our initial sample of 140 NDE *Planck* clusters, we first excluded 26 objects whose redshift is unknown, thus not allowing us to make assumptions on the angular size and limits to the radio power of a possible halo. For 11 additional galaxy clusters, upper limits would not be reliable due to the presence of contaminating AGN with extended emission and/or calibration artifacts in their central regions. Finally, we did not consider the lowest-redshift NDE cluster (PSZ2 G136.64-25.03, $z = 0.016$) because a possible RH of ∼1 Mpc would have an angular size of $\sim 1^{\rm o}$ at the cluster redshift; sources of such large angular sizes require more specific calibration procedures than those adopted in LoTSS, making use of all the baselines instead of restricting to those $> 80\lambda$ (see e.g. the case of the Coma cluster in Bonafede et al. 2021a). Therefore, we will focus on a sample of 102

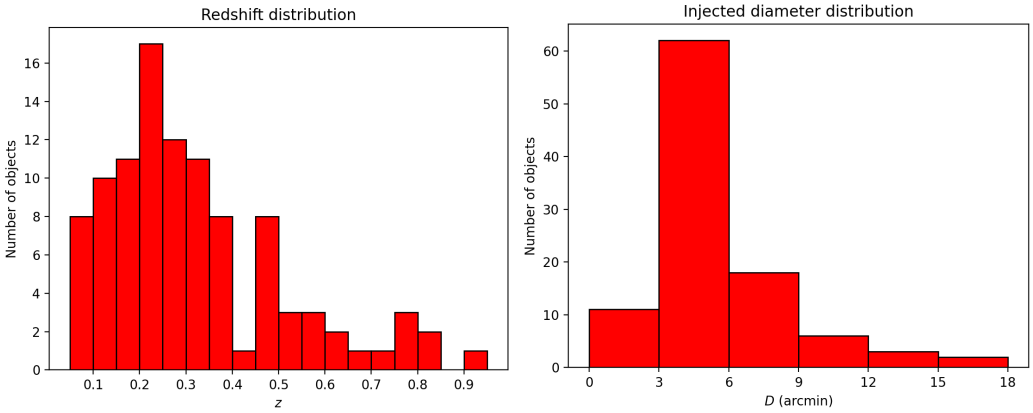

Figure 5.9: *Left*: Distribution of redshifts of the 102 NDE galaxy clusters in our final sample. *Right*: Distribution of the injected angular diameters under the assumption of $r_{\rm e,inj} = 200$ kpc.

NDE galaxy clusters. As shown in the upper panel of Fig. 5.9, these clusters lie in the redshift range $[0.062 - 0.9]$, where the mean and median are $\bar{z} = 0.318$ and $\tilde{z} = 0.267$, respectively.

5.4.2 Upper limit calculation

The injection technique requires input values of I_0 and $r_{\rm e}$. As mentioned, the central brightness is obtained as $I_0 = S_{\rm inj,tot}/2\pi r_{\rm e}^2$. In past works, the e-folding radius was derived from scaling relations with the host cluster mass, but these are still poorly constrained and should be used with caution, as discussed in Bonafede et al. (2017). To avoid the use of scaling relations, we consider mass-independent e-folding radii.

As discussed in Sections 5.3.1 and 5.3.2, our upper limits depend on the extent (in terms of number of beams) of the mock halo and the noise of the image, while the role of the uv-coverage is negligible for the extension of halos in our LoTSS sample. Therefore, in principle, by means of Eq. 5.5, we are able to immediately calculate the upper limits for the 102 NDE galaxy clusters of our sample as $S_{\rm UL} = 10^q \sigma N_{\rm beam}^m$ (with $m = 0.789$ and $q = -0.091$) without performing any additional injection. To this aim, values of σ and $N_{\rm beam}$ are required, which can be obtained from images of the original datasets and with a choice of $r_{\rm e}$. Bearing in mind that the mean and median e-folding radius of the PSZ2 radio halos in LoTSS-DR2 are $\bar{r}_{\rm e} = 194$ kpc (with a standard deviation of 94 kpc) and $\tilde{r}_{\rm e} = 186$ kpc, respectively, we assumed a nominal $r_{\rm e} = 200$ kpc for all the NDE objects to derive the corresponding angular diameter ($D = 6r_{\rm e}$). With this choice, the sizes of our mock halos are in the range [2.6′-16.7′]. The distribution of the angular diameters is shown in the lower panel of Fig. 5.9, where the mean and median are $\bar{D} = 5.7'$ and $\tilde{D} = 4.9'$, respectively; the 82% of our clusters have $D < 7.5'$, whereas only 2 clusters have $D > 14'$. We then produced images by tapering the baselines to different convenient low resolutions to find the deepest $S_{\rm UL}$ from Eq. 5.5 among the various combinations of σ and $N_{\rm beam}$, under the condition of avoiding $N_{\rm beam} \ll 30$, where the slope of our correlation

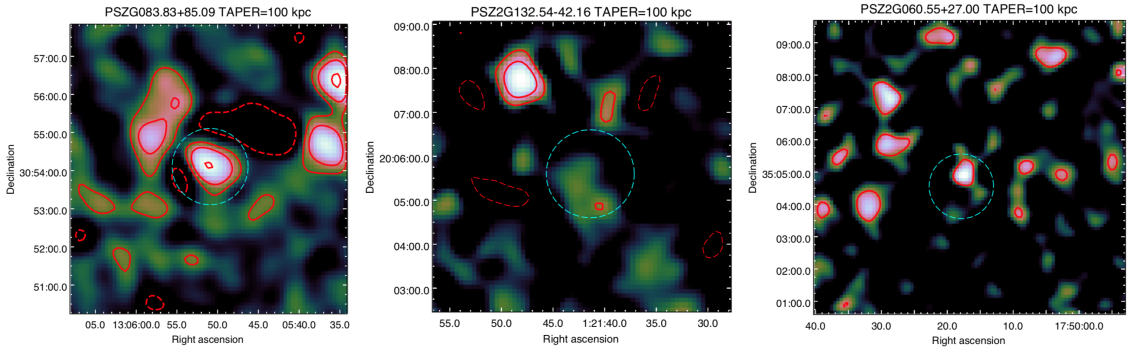

Figure 5.10: Representative examples of NDE clusters showing artifacts introduced by the subtraction of discrete sources near the cluster centre. The radio contours are drawn at $\pm 2\sigma$ and spaced by factors of 2. In all the panels, the dashed cyan circle indicates the cluster centre and has a fixed diameter of 2′. *Left*: NDE cluster excluded from our analysis due to severe (positive and/or negative) artifacts. *Middle*: NDE cluster with SQ = 1 due to the absence of artifacts. *Right*: NDE cluster with SQ = 2 due to the presence of moderate residuals.

significantly flattens.

Having said that, since RHs are centrally-located sources, physically-meaningful upper limits cannot ignore the local environment close to the cluster centre, which is usually dense of contaminating discrete sources. Therefore, at this stage it is also necessary to take into account the quality of the subtraction of the discrete sources close to the cluster centre, before blindly adopting Eq. 5.5. The subtraction process (particularly that obtained by means of semi-automatic pipelines) is typically not perfect for many reasons; it assumes that the model of discrete sources obtained from the long baselines adequately describes their emission for the short baselines as well, but extended sources are primarily sampled by the short spacings, and calibration may not be homogeneous for all baselines, thus providing unequal levels of subtraction. These effects may introduce subtraction artifacts in the form of positive residual blobs and negative holes, which are enhanced at low resolution and contaminate the faint diffuse emission; in these cases, upper limits are not driven by the instrumental capabilities (i.e. the reached rms noise), but by the level of imaging artifacts, thus making the $S_{\rm UL}$ provided by Eq. 5.5 not fully trustworthy.

For these reasons, we inspected our non-subtracted and source-subtracted images at various resolutions, and excluded from our analysis 27 out of 102 objects which are affected by severe subtraction artifacts that prevent us to provide meaningful upper limits[2] (see an example in Fig. 5.10). We then assigned a subtraction-quality (SQ) parameter to each remaining NDE cluster, based on the presence and impact of subtraction artifacts close to the cluster centre[3]; we assigned SQ = 1 if subtraction artifacts are absent or negligible (a sub-sample of these targets was used to derive Eq. 5.5), and SQ = 2 if subtraction

[2]Re-observations and/or more refined calibration and subtraction processes would be necessary to derive solid upper limits for these targets.

[3]SQ is a qualitative and subjective parameter, but is rather reproducible by following the examples in Fig. 5.11, and allows to easily find the best strategy to obtain upper limits.

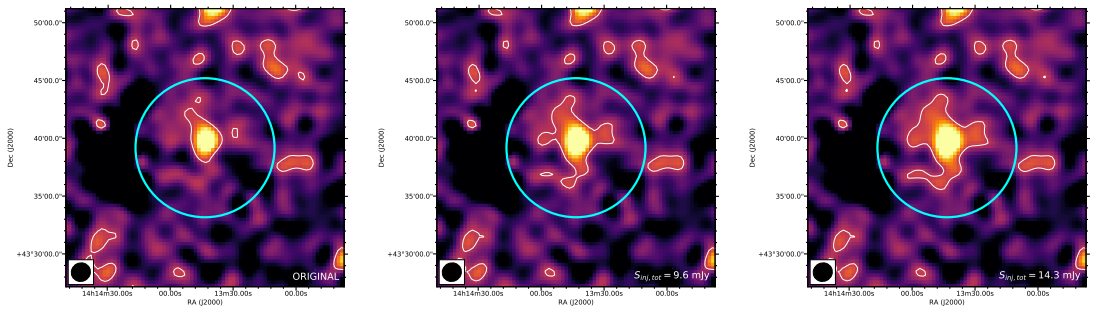

Figure 5.11: Examples of injections for a SQ = 2 cluster. Contours are drawn at 2σ of the pre-injection (left) image, and the cyan circle has a radius of $3r_{\rm e,inj}$. Two cycles of injections are performed with $S_{\rm UL}$ derived from Eq. 5.5 and $1.5 \times S_{\rm UL}$. The upper limit is obtained with the second cycle, which leaves extended excess ~ 2 times brighter with respect to the pre-injection image.

artifacts are not negligible (see examples in Fig. 5.10) . We directly derived upper limits through Eq. 5.5 only if SQ = 1 (15 out of 102). If SQ = 2 (60 out of 102), the presence of artifacts is not dominant and more reliable limits can be determined through the injection process in the source-subtracted data (i.e. through the 'Sub. & Inj.' scheme). In these cases, we performed a first cycle of injection by using the flux density provided by Eq. 5.5 with tapers corresponding to $N_{\rm beam} \sim 30 - 50$, and then increased/decreased $S_{\rm inj,tot}$ in few additional cycles to further constrain the limit level. Pre-injection and post-injection images were then inspected and, guided by the 2σ contour levels, we considered as effective limits those cases where the mock emission leaves extended excess ~ 2 times brighter than the previous injection cycle (see an example in Fig. 5.11).

Based on the scatter around the fit of Eq. 5.5 in the region $N_{\rm beam} \sim 30 - 50$, and the grid of values adopted to vary $S_{\rm inj,tot}$ in each cycle of injections, we claim conservative uncertainties of $\sim 10 - 15\%$ on the upper limits derived with the presented methods. As discussed in Sect. 5.3.1, the surface brightness is overestimated if emission is not fully deconvolved during imaging. This cleaning bias is expected to be higher for injections at the level of the upper limit and large angular size. Nevertheless, even in the case we were systematically biased by this cleaning effect, uncleaned excess would appear brighter, thus making the upper limits to be even more conservative.

We now aim to evaluate the efficacy of our strategies based on Eq. 5.5. For each of the 60 NDE clusters with SQ = 2, we obtained an estimate of the expected upper limit from Eq. 5.5 by assuming $N_{\rm beam} = 30$ and the noise corresponding to the adopted tapering. In Fig. 5.12 we report the distribution of the ratio between the effective and expected upper limits; the mean and median ratios are 1.59 and 1.44, respectively. Most of the targets (51 out of 60) have ratios ≤ 2, with maximum ratios of ~ 3.3. The 9 clusters with ratios > 2 have slightly higher levels of artifacts than those typical of SQ = 2, therefore they require higher injected flux densities to constrain the upper limit. This confirms that Eq. 5.5 remains a good starting point even in the presence of moderate artifacts, thus allowing to perform fewer additional cycles of injections in order to constrain the final level of the limit. Moreover, even though the required time to obtain upper limits

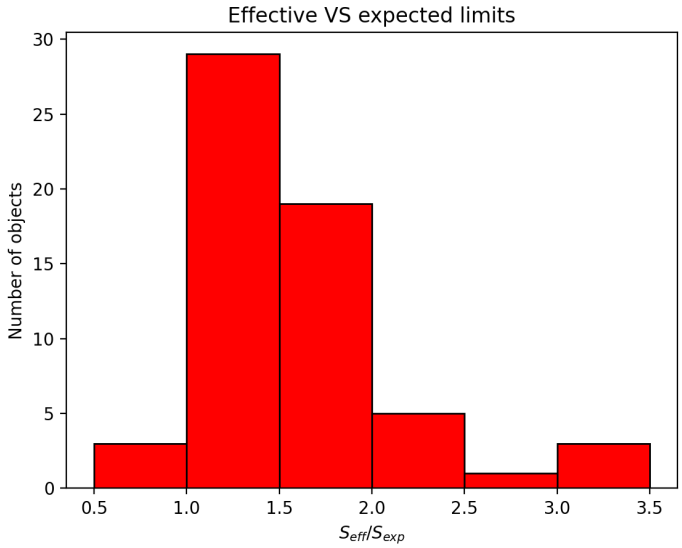

Figure 5.12: Distribution of the ratio between the effective upper limit and the expected upper limit inferred from Eq. 5.5 for the SQ = 2 clusters.

naturally depends on the available computing resources, we estimate that our strategies allowed us to remarkably reduce the computing time by factors ∼3-4[4] with respect to standards methods in the literature.

5.4.3 Upper limits and radio halos

Uncertainties in the beam model of LOFAR HBA can introduce offsets in the flux density scale when amplitude solutions are transferred from the primary calibrator to the target (e.g. Hardcastle et al. 2016). Therefore, all images need to be multiplied by a factor $f_{\rm LoTSS}$ (of order of unity), which is derived for each pointing after the data calibration (see Botteon et al. 2022a; Shimwell et al. 2022a) to align the flux density scale of LoTSS with that of Roger et al. (1973). As our injections are performed in the *uv*-data, we have to take into account the flux density scale correction by multiplying $S_{\rm UL}$ at 144 MHz by $f_{\rm LoTSS}$.

Our upper limits will be exploited in statistical analysis described in Chapter 6, where the radio power of the detected halos is reported at 150 MHz, within radii of $3r_{\rm e}$ (as done in Botteon et al. 2022a). To compare detections and upper limits, we therefore scaled $S_{\rm UL}$ from 144 to 150 MHz ($S_{\rm UL,150} = S_{\rm UL,144}(150/144)^{-\alpha}$, where $\alpha = 1.3$), calculated the corresponding radio power, and finally considered the 80% of this value which is expected within $3r_{\rm e,inj}$. In summary, the k-corrected radio powers of the upper limits are obtained as:

$$P_{\rm UL,150} = 0.8 \times f_{\rm LoTSS} \times 4\pi D_{\rm L}^2 S_{\rm UL,150}(1+z)^{\alpha-1} \ . \quad (5.6)$$

[4]A single run of injection plus imaging takes ∼ 2.0 + 0.5 h of computing time for a single LoTSS pointing. With our methods, SQ = 1 objects only require imaging to obtain σ and θ, whereas 2-3 cycles of the full process are necessary for SQ = 2 clusters. With methods in the literature, at least 6 cycles of injections plus imaging are instead necessary.

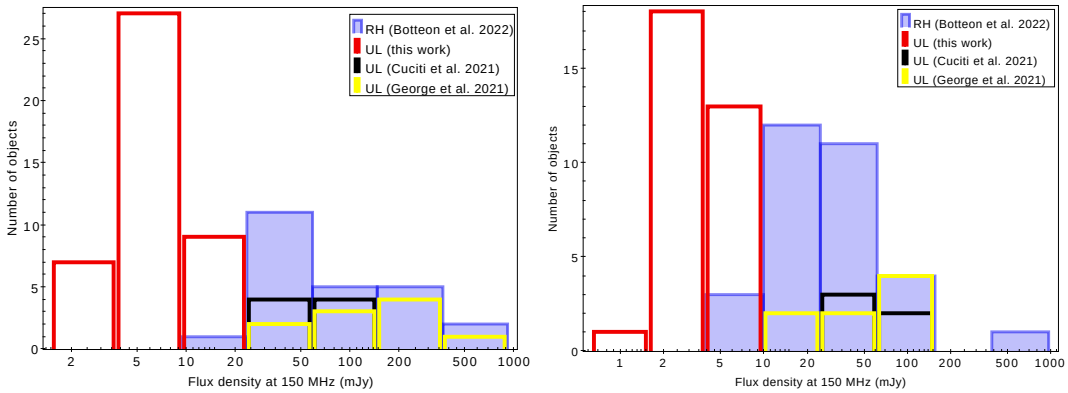

Figure 5.13: Distributions of the flux density of confirmed and candidate RHs (in blue) with $100 \leq r_e \leq 400$ kpc from Botteon et al. (2022a), our upper limits (in red), and upper limits from Cuciti et al. (2021b) (in black) and George et al. (2021b) (in yellow). Upper limits from the literature are re-scaled to 150 MHz by assuming $\alpha = 1.3$. The samples are split in redshift bins as $z < 0.3$ (left panel) and $z > 0.3$ (right panel).

The main host properties (*Planck* coordinates, redshift, mass), injection parameters (centre of injection, central brightness, *e*-folding radius), flux density, and radio power at 150 MHz for the final sample of 75 NDE clusters are reported in Table D.1.

A comparison of the distributions of flux densities for our upper limits and the 56 (confirmed and candidate) RHs detected in LoTSS-DR2 having $100 \leq r_e \leq 400$ kpc (Botteon et al. 2022a) is shown in Fig. 5.13, where we also reported upper limits from the literature (Cuciti et al. 2021b; George et al. 2021b) that we re-scaled to 150 MHz. For a clearer inspection, we split the samples in two redshift bins at $z < 0.3$ (left panel) and $z > 0.3$ (right panel). Our limits range in $1.5 - 17$ mJy, whereas RHs have flux densities in the range $\sim 3 - 700$ mJy. Except for few objects, the distributions of our limits are well separated from the RHs in the lower redshift bin, whereas more overlapping is found in the higher redshift bin. Our limits are deeper than those from the literature obtained with other interferometers (JVLA and GMRT), thanks to the higher sensitivity of LOFAR (see also Sect. 5.5). The deepest limits at 150 MHz are 36.5 mJy (at $z = 0.320$) and 11.3 mJy (at $z = 0.396$) in samples from Cuciti et al. (2021a) and George et al. (2021b), respectively, which are factors 24.3 and 7.5 higher than our deepest limit of 1.5 mJy (at $z = 0.830$), and factors 2.8 and 6.5 higher than our limits for objects at similar redshift ($z = 0.397$ and $z = 0.318$).

5.5 Comparison with uGMRT and JVLA capabilities

To date, studies of RHs have been mainly based on observations carried out with uGMRT and JVLA. To quantitatively compare the capabilities of these instruments with LOFAR, we injected mock halos with $S_{\rm inj,tot}$ ranging from 20 to 300 mJy in LOFAR (8 hr observation), uGMRT (band-3 at 400 MHz, 6 and 10 hr observations), uGMRT (band-4 at 700 MHz, 9 hr observation), and JVLA (L-band in combined DnC and BnC array configura-

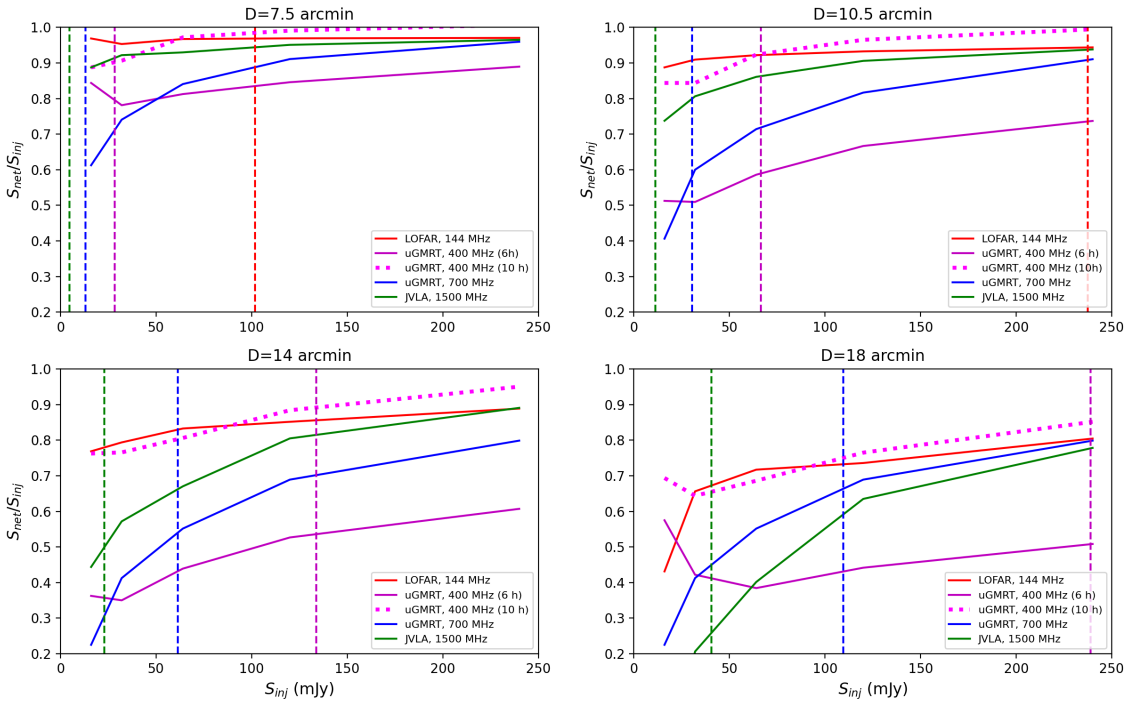

Figure 5.14: Recovered net flux density as a function of the injected flux density for various angular diameters and instruments. Red, magenta, blue, and green curves are injections in LOFAR (HBA at 144 MHz), uGMRT (band-3 at 400 MHz, 6 and 10 h on-source are shown with solid and dotted lines, respectively), uGMRT (band-4 at 700 MHz), and JVLA (DnC+BnC array, L-band at 1.5 GHz) datasets, respectively. The expected flux density integrated up to $3r_e$ of a representative radio halo with $M_{500} = 5 \times 10^{14}\ M_\odot$ is indicated by a dashed vertical line and can be exploited to estimate effective losses (see Table 5.3 and discussion in Sect. 5.5).

Table 5.3: Estimates of the percentage of recovered flux density for LOFAR (144 MHz), uGMRT (400 MHz), uGMRT (700 MHz), and JVLA (DnC+BnC-array, 1.5 GHz) based on our simulations. A representative RH with $M_{500} = 5 \times 10^{14}$ $M_{\odot}$, $D = 1.2$ Mpc, and $\alpha = 1.3$ is considered as a general reference for flux densities at each frequency.

D (arcmin)	$S_{\rm halo,144}$ (mJy)	LOFAR (%)	$S_{\rm halo,400}$ (mJy)	uGMRT^{400} (%)	$S_{\rm halo,700}$ (mJy)	uGMRT^{700} (%)	$S_{\rm halo,1500}$ (mJy)	JVLA (%)
7.5	101.8	95	28.4	80-90	13.0	60	4.8	90
10.5	237.5	95	66.4	60-90	30.4	60	11.3	70
14	479.1	90	133.8	55-90	61.4	55	22.8	50
18	855.0	80	238.9	50-85	109.4	65	40.6	25

tions at 1.5 GHz, 8 hr on-source in total) datasets. Even though the minimum baseline lengths of uGMRT and JVLA are similar to the inner *uv*-cut considered for LOFAR at 80λ, the density of the *uv*-coverage at short spacings is notably different for each dataset.

As in Fig. 5.6, we obtained the recovered flux density by considering the difference between $S_{\rm post}$ and $S_{\rm pre}$. Sources were not subtracted to avoid the introduction of heterogeneous artifacts of subtraction at the various frequencies. In Fig. 5.14 we show the fraction of the recovered flux density as a function of the injected flux density for the three considered instruments. Losses are negligible for all the three facilities up to $D = 5'$ (and thus $D = 3'$ and $D = 5'$ are not shown), but different behaviours are seen for larger angular sizes. To roughly determine the effective losses, we consider a representative radio halo of $D = 1.2$ Mpc, host mass of $M_{500} = 5 \times 10^{14}$ $M_{\odot}$, and spectral index $\alpha = 1.3$; we infer its radio power at 150 MHz from the mass-power relation (with fitted slope and intercept reported in Chaper 6), and re-scale its flux density based on the required angular diameters and frequency; the corresponding flux density is indicated by a vertical dashed line in Fig. 5.14. Our estimates on the effective recovered fractions are listed in Tab. 5.3 (due to large differences, for uGMRT band-3 we both reported the minimum and maximum values, obtained with 6 and 10 hr observations, respectively).

Obtaining more accurate assessment of the performances for uGMRT and JVLA requires systematic injections in many datasets, as done for LOFAR, but this is beyond the scope of this work. However, important conclusions can be drawn through our simulations. Owing to the high number of short baselines of LOFAR, the 8-hr LoTSS pointings ensure similar densities of the *uv*-coverage, independently on the specific observation. We found that uGMRT can provide very high performances in recovering extended emission, but the recovered trends are remarkably different for the uGMRT datasets that we considered. Indeed, Figs. 5.14, 5.15 indicate that the density of uGMRT *uv*-coverage is more dependent on the specific observation (e.g. total observing time, bandwidth, declination of the target, level of interference, flagging); in our tests, the lowest performances were obtained with the 6-hr band-3 dataset, which has not only the shortest duration, but also the highest number of flagged antennas, which largely contribute to compromise the recovery of the mock halos. Our simulations also suggest that losses for JVLA are high at $D \geq 10.5'$. In summary, for uGMRT and JVLA data, the inspection of the *uv*-coverage

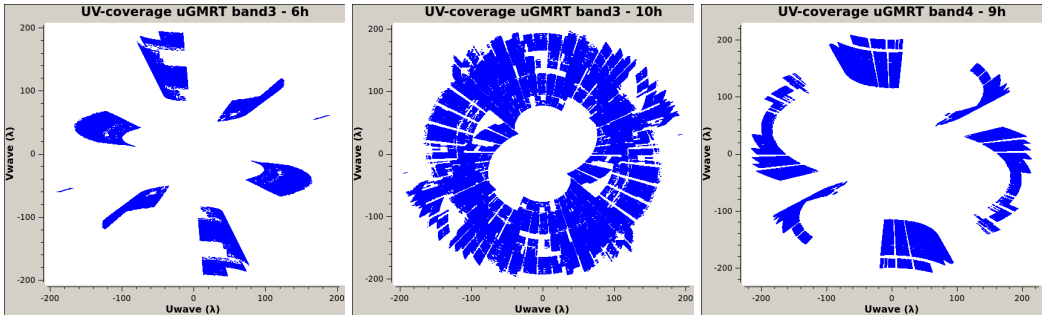

Figure 5.15: ($\leq 200\lambda$) *uv*-coverage of the uGMRT observations used for injections: 6 hr in band-3 (Dec $\sim -13^{o}$, top panel), 10 hr in band-3 (Dec $\sim +64^{o}$, middle panel), 9 hr in band-4 (Dec $\sim -29^{o}$, lower panel).

and classical derivation of upper limits through injection are recommended rather than the usage of scaling relations similar to ours in Eq. 5.5.

5.6 Summary and conclusions

LoTSS-DR2 includes 140 non-detections of RHs in *Planck* clusters. We exploited these data to test the instrumental capabilities of LOFAR to recover diffuse extended emission and determine upper limits to the radio power of a possible halo.

Through the injection of mock visibilities simulating RHs into the observed datasets, we estimated the flux density losses due to insufficient short baselines. We find that they are negligible ($\lesssim$ 5-10%) for sources of sizes up to $D = 14'$, and reach fractions of $\sim$ 20% at $D = 18'$. As common for LOFAR HBA data, our simulations were limited to baselines $> 80\lambda$ as well, meaning that more flux density can be recovered by including shorter baselines. For the first time, we systematically carried out tests on a large sample of datasets of different quality, demonstrating that LOFAR is one of the facilities with the densest *uv*-coverage in its inner part. It is thus able to recover large scale emission with lower flux density losses with respect to other instruments. Moreover, the low frequency range of LOFAR allows to explore host mass regimes that could be barely probed by facilities operating at higher frequencies.

We showed that non-detections of diffuse emission can be considered approximately independent on the *uv*-coverage of LOFAR in LoTSS observations. We therefore explored the parameters which determine the flux density of the upper limits, and found a relation with the noise of the image and the number of beams within the injected mock halo (depending on the resolution of the image and angular size of the mock emission). Our relation can be safely adopted to infer the upper limit if the subtraction of the discrete sources close to the cluster centre does not leave contaminating artifacts, which are enhanced at low resolution. Otherwise, subtraction artifacts typically drive the level of the limit, thus making the injection procedure and visual inspection still necessary to provide more reliable limits.

After excluding objects lacking redshift information, with extended radio galaxies,

and with severe subtraction artifacts, we obtained upper limits for 75 targets. Our limits will be exploited in Chapter 6 and compared to the detected RHs in LoTSS-DR2 (Chapter 4) to provide information on the populations, origin, and evolution of these sources.

Chapter 6

Radio halos in LoTSS-DR2: properties and occurrence

This is the last Chapter devoted to the analysis of the Planck clusters in LoTSS-DR2, and it is based on Paper IV (Cassano et al. 2023) and Paper V (Cuciti et al., submitted) of the series. For the first time, our sample allows to carry out a statistically complete analysis of clusters observed at low radio frequencies.

By employing the quantities derived in Chapter 4 and Chapter 5, we first study the radio power vs host mass correlation at 150 MHz, and the bimodal distribution of radio halos and upper limits. Afterwards, we derive the expected occurrence of clusters hosting radio halos in the framework of the turbulent re-acceleration scenario, and compare it to our observations.

6.1 Cluster sub-samples

The proper study of the scaling relation and occurrence of radio halos requires statistically complete samples, and any possible systematical bias needs to be carefully taken into account. In this respect, it is necessary to identify well-defined sub-samples of Planck clusters in LoTSS-DR2 to be used in our analysis. In this Section we describe the selection criteria adopted to define the two main sub-samples that we will consider in this Chapter.

We first considered the Planck completeness, by converting the selection function (available in the Planck archive, for the full survey region and for a signal-to-noise threshold of 4.5), originally defined in the SZ signal - cluster size plane, into the $M - z$ plane

Table 6.1: Number of clusters per category in the main sub-samples.

	RH	cRH	NDE	U	RR
Scaling relation sample	52	13	85	30	13[a]
Occurrence sample	47	8	71	25	13[a]

Notes. [a]: these include both RR and cRR objects which do not have a RH/cRH as well.

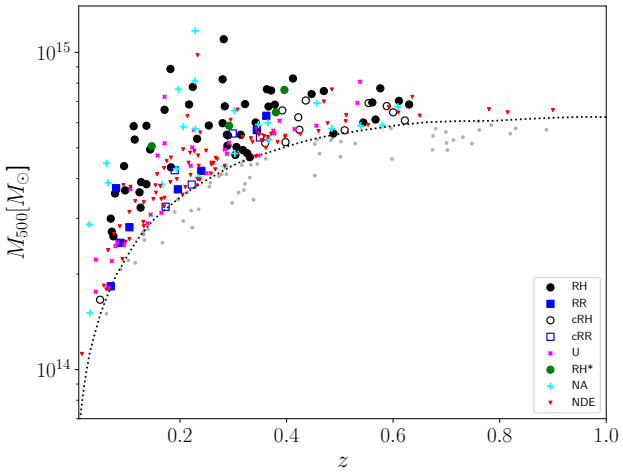

Figure 6.1: Mass–redshift distribution of the Planck clusters in LoTSS-DR2. In this Chapter we consider only clusters above the 50% Planck completeness line (dotted line).

as described in Planck Collaboration XXVII (2016), and found the boundary line above which the detection probability is larger than a given percentage. As reference, we used the 50% Planck completeness line in (M_{500}, z). This means that we may have missed 50% of clusters with mass close to the 50% completeness line. However, as soon as we move towards higher masses, the completeness increases so that we have, for instance, an 80% completeness for clusters with $M_{500} \sim 5 \times 10^{14}\, M_\odot$ at $z \sim 0.3$. We do not expect this choice to introduce significant biases in our results since there are no significant differences between the completeness functions for regular and disturbed clusters (Planck Collaboration XXVII 2016). The distribution in mass and redshift of LoTSS-DR2 clusters above the 50% Planck completeness line is reported in Fig. 6.1. Objects classified as N/A will be not considered. Moreover, we do not distinguish between radio halos and mini-halos, as discussed in Chapter 4. By means of this selection criterion, we identified the two sub-samples described below.

6.1.1 Sub-sample for the scaling relation

To study the scaling relation between the radio power of RHs and host mass we considered the 221 clusters above the 50% Planck completeness line. Among them, we excluded (i.) the three targets within the Coma cluster region, which requires special data reduction schemes given its large angular extent (Bonafede et al. 2021a), (ii.) PSZ2 G060.10+15.59, for which the ionospheric conditions did not allow a proper direction-dependent calibration, and (iii.) PSZ2 G166.62+42.13, whose radio halo is contaminated by multiple radio relics and its radio power was not computed (see also Chapter 4).

The number of clusters per category belonging to this sub-sample is listed in Table 6.1. For this analysis: (i.) we do not treat RR/cRR objects; (ii.) we consider cRH and RH as different categories; (iii.) we do not consider U objects. This sub-sample is employed

in Sect. 6.2.

6.1.2 Sub-sample for the occurrence

To study the occurrence of clusters hosting radio halos, we considered a total of 164 targets above the 50% Planck completeness line and in the redshift range of $0.07 < z < 0.5$. The low-z cut has been made to exclude the very nearby Universe where the cluster statistics is low because of the limited volume. The high-z cut has been imposed because the Planck selection is such as to detect only the most massive clusters which are rare at these redshifts, especially in the relatively small LoTSS-DR2 area (see also a discussion on the incompleteness of the redshift information in Planck Collaboration XXVII 2016).

The number of clusters per category belonging to this sub-sample is listed in Table 6.1. For this analysis: (i.) we do not treat RR/cRR objects; (ii.) we consider cRH objects as RH objects; (iii.) when specified, U objects will be considered either as RH or NDE objects. This sub-sample is used in Sects. 6.3, 6.5.

6.2 Radio power at 150 MHz vs host mass

By considering the sample described in Sect. 6.1.1, here we present the scaling relation between the radio power of RHs at 150 MHz and their host mass. The distribution of RHs in the radio power vs mass diagram is shown in Fig. 6.2 (left).

6.2.1 Fitting procedure

To derive the parameters of the correlation, we follow the fitting procedure outlined in Cassano et al. (2013) and Cuciti et al. (2021a). Specifically, we adopt the Bivariate Correlated Errors and intrinsic Scatter (BCES) linear regression algorithms (Akritas & Bershady 1996) to fit the observed data points with a power-law in the form:

$$\log\left(\frac{P_{150}}{10^{24.5}\ \mathrm{W\ Hz^{-1}}}\right) = B\log\left(\frac{M_{500}}{10^{14.9}\ M_{\odot}}\right) + A \quad , \tag{6.1}$$

where A and B are the intercept and slope of the correlation, respectively.

By defining $Y = \log(P_{150}) - 24.5$ and $X = \log(M_{500}) - 14.9$, and having N data points (X_i, Y_i) with errors $(\sigma_{X_i}, \sigma_{Y_i})$, we estimate the raw scatter as:

$$\sigma^2_{\mathrm{raw}} = \frac{1}{N-2}\sum_{i=0}^{N} w_i (Y_i - BX_i - A)^2 \quad , \tag{6.2}$$

where

$$w_i = \frac{\sigma_i^{-2}}{N^{-1}\sum_{i=0}^{N}\sigma_i^{-2}} \quad \text{and} \quad \sigma_i^2 = \sigma^2_{Y_i} + B^2\sigma^2_{X_i} \quad . \tag{6.3}$$

Table 6.2: Fitting parameters of the radio power vs host mass relation with BCES Y|X for different sub-samples. Cols. 2-3: slope and associated uncertainty. Cols. 4-5: intercept and associated uncertainty. Col. 6: raw scatter.

Method	B	err B	A	err A	$\sigma_{\rm raw}$
RHs					
BCES Y|X	3.59	0.48	1.1	0.09	0.39
RHs plus cRHs					
BCES Y|X	3.45	0.44	1.1	0.09	0.39
RHs in ranges $0.06 < z < 0.4$ and $100 < r_{\rm e}/{\rm kpc} < 400$					
BCES Y|X	3.55	0.60	1.1	0.1	0.35

To evaluate the 95% confidence region of the correlation, we calculated the 95% confidence interval of the mean value of Y, $\langle Y \rangle$. For a given X, this is $\langle Y \rangle \pm \Delta Y$, where:

$$\Delta Y = \pm 1.96 \sqrt{\left[\sum_{i=0}^{N} \frac{(Y_i - Y_m)^2}{N-2}\right]\left[\frac{1}{N} + \frac{(X - X_m)^2}{\sum_{i=0}^{N}(X_i - X_m)^2}\right]} \quad , \tag{6.4}$$

where $Y_m = BX_i + A$ and $X_m = \sum_{i=0}^{N} X_i/N$ for each observed X_i.

6.2.2 Scaling relation

The parameters of the correlation were both derived by considering only RHs and RHs plus cRHs, as reported in Table 6.2. The fitted slopes ($B \sim 3.5$) are consistent within the errors in the two considered cases. We refer to Cuciti et al. (submitted) for details and discussion on additional fitting algorithms that were employed. In Fig. 6.2 we show both the Y|X and bisector methods, for a comparison. In the following, we will consider the correlation derived with the Y|X method for RHs ($B = 3.59 \pm 0.48$, $A = 1.1 \pm 0.09$) as the reference correlation.

In Table 6.2 we also report the raw scatter, which is relatively large $\sigma_{\rm raw} \sim 0.4$. This is in line with what was found for the correlation at 1.4 GHz: indeed, Cuciti et al. (2021a) showed that the scatter is, at least in part, caused by the different dynamical state of clusters, meaning that more disturbed clusters host more powerful RHs.

It is known that galaxy clusters have a bimodal behaviour in the radio power at 1.4 GHz vs host mass diagram, where disturbed clusters populate the correlation and relaxed systems appear as a separated population with upper limits to their radio power (Cassano et al. 2013; Cuciti et al. 2021a). To check whether a similar behaviour is found also at 150 MHz, we focus on clusters in the redshift range $0.06 \leq z \leq 0.4$ and on radio halos with $100 \leq r_{\rm e}/{\rm kpc} \leq 400$. The e-folding radius range is necessary for a fair comparison between RHs and upper limits, as the latter were all derived by assuming $r_{\rm e} = 200$ kpc

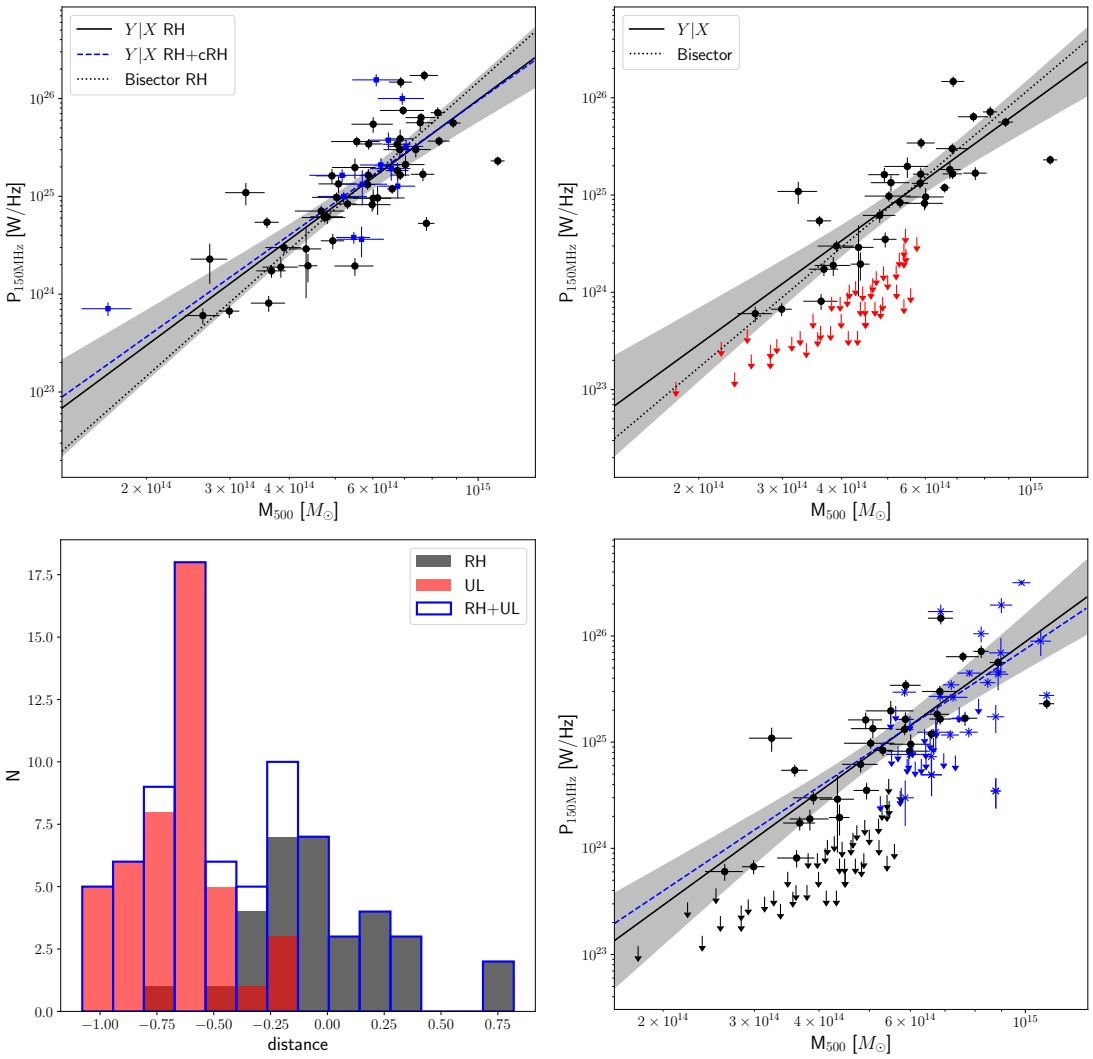

Figure 6.2: *Top left*: Radio power-mass diagram for RHs (black points) and cRHs (blue squares) in the scaling relation sample. The solid and dotted lines are obtained by fitting RHs with the BCES Y|X (the shadowed region represents the corresponding 95% confidence region) and bisector methods, respectively. The dashed line is obtained by fitting RHs plus cRHs with the BCES Y|X method. *Top right*: Radio power-mass diagram for RHs and upper limits with $0.06 < z < 0.4$ and $100 < r_e/\mathrm{kpc} < 400$. The solid and dotted lines are obtained with the BCES Y|X (the shadowed region represents the corresponding 95% confidence region) and bisector methods, respectively. *Bottom left*: Distribution of distances of RHs (black) and upper limits (red) from the correlation. *Bottom right*: Radio power-mass diagram for RHs and upper limits from our sub-sample as in the top right panel (black dots/arrows) and from Cuciti et al. (2021a) (scaled from 1.4 GHz to 150 MHz by assuming $\alpha = 1.3$; blue stars/arrows). The black solid line is the same as in the top right panel. The dashed blue line is the correlation obtained for RHs and USSRHs in Cuciti et al. (2021a).

(Chapter 5). In these ranges we have 32 radio halos and 46 upper limits, which we report in the top right panel of Fig. 6.2. We fitted the RHs in these ranges as outlined above, and found consistent slope and raw scatter with the previous cases (see Table 6.2).

Almost all of the upper limits (43 out of 46) are well below the 95% confidence region of the correlation. In the bottom left panel of Fig. 6.2 we report the distribution of the distance along the P_{150} axis of radio halos and upper limits from the correlation. The global distribution exhibits two peaks, thus indicating a bimodality; despite some overlapping, RHs are located on/above the correlation and upper limits lie below it.

6.2.3 Comparison with high frequency samples

In the bottom right panel of Fig. 6.2 we show radio halos and upper limits with $0.06 \leq z \leq 0.4$ and $100 \leq r_e/\mathrm{kpc} \leq 400$ in our LOFAR sample, and compare them with the sample analysed in Cuciti et al. (2021b) (for consistency, data points were scaled from 1.4 GHz to 150 MHz by assuming $\alpha = 1.3$). Until now, that was the largest complete sample of clusters with deep radio observations at frequencies $\nu > 600$ MHz. Both our new scaling relation and that derived in Cuciti et al. (2021b) for RHs and USSRHs at 1.4 GHz are reported. This comparison shows that we can now investigate the correlation and the position of the upper limits in a much larger mass range, that was previously inaccessible.

We notice that not only the number of radio halos, but also the number of available upper limits has dramatically increased. Furthermore, the upper limits derived with LOFAR are deeper than those derived at high frequency (see Fig. 5.13 in Chapter 5 for a comparison). For clusters with similar masses ($M_{500} \sim 6 \times 10^{14} M_\odot$) the upper limits at 150 MHz are typically a factor of $\sim 2-5$ lower than those at 1.4 GHz (scaled by assuming $\alpha = 1.3$). While at 1.4 GHz, some upper limits below $M_{500} \sim 6.5 \times 10^{14} M_\odot$ were close or consistent with the correlation, at 150 MHz this takes place only for $M_{500} < 3 \times 10^{14} M_\odot$. This suggests the existence of a correlation extending to masses of $M_{500} \sim 3 \times 10^{14} M_\odot$.

In spite of the low statistics and relatively small mass range of the high frequency sample, the correlation found at 150 MHz is well in line with the extrapolation of the one derived at 1.4 GHz also in the low mass regime.

6.3 Detecting RHs: the role of upper limits

By employing the sub-sample of RHs (Chapter 4) and upper limits (Chapter 5) that follow the selection criteria described in Sect. 6.1.2, we can predict the expected occurrence of Planck clusters hosting radio halos at the completion of LoTSS. In the next sections, we briefly introduce the theoretical background and assumptions of the turbulent re-acceleration scenario, and compare the corresponding predictions with the observed occurrence in our sample. Specifically, in this section we show the crucial role of upper limits in this analysis.

In Fig. 6.3 we show either the radio power (red points) or upper limits (green triangles) of halos as a function of redshift for clusters in our sub-sample for the occurrence. This plot allows to explore which is the minimum power of a radio halo that could be detected in LoTSS-DR2.

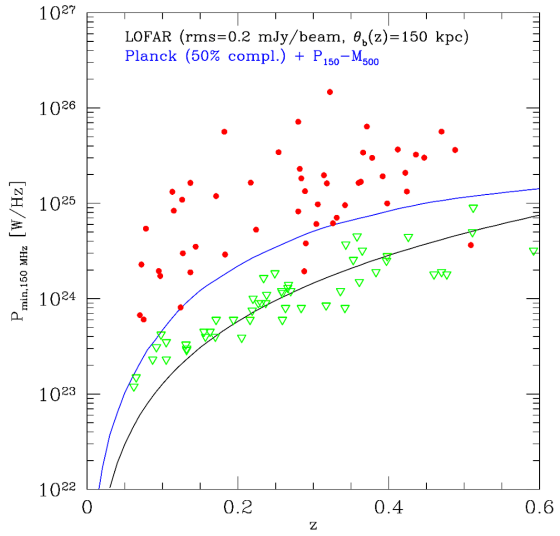

Figure 6.3: Radio power at 150 MHz of halos (red dots) and upper limits (green triangles) as a function of z. The black line represents the minimum radio power derived from Eq. 6.5 (with $\sigma_{\rm rms} = 200$ μJy beam^{-1}, $\theta_{\rm beam}(z) = 150$ kpc, $r_{\rm e}(z) = 170$ kpc, $\xi = 5$). The blue line is obtained by combining the $P_{150} - M_{500}$ best-fit correlation and the 50% Planck completeness (M, z) line.

As derived in previous papers (Cassano et al. 2010; Cassano et al. 2012), we consider the following analytical expression to estimate the minimum flux density (integrated within $3r_{\rm e}$) of a RH that can be detected in a given survey:

$$S_{\rm min}(< 3r_{\rm e}, z) \sim 4.44 \times 10^{-3}\, \xi \left(\frac{\sigma_{\rm rms}}{10\ \mu{\rm Jy\ beam^{-1}}}\right)\left(\frac{\theta_{\rm beam}}{10\ {\rm arcsec}}\right)^{-1}\left(\frac{r_{\rm e}}{\rm arcsec}\right)\ [{\rm mJy}]\ , \quad (6.5)$$

where ξ is the signal to noise ratio, $\sigma_{\rm rms}$ is the rms noise, and $\theta_{\rm beam}$ is the angular size of the beam. The corresponding minimum radio power $P_{\rm min}(z)$ is reported in Fig. 6.3 as a black line by assuming $\sigma_{\rm rms} = 200$ μJy beam^{-1}, and fixed linear values of $\theta_{\rm beam}(z) = 150$ kpc and $r_{\rm e}(z) = 170$ kpc (which is about the median $r_{\rm e}$ in our sample). With this choice of parameters, Eq. 6.5 with $\xi = 5$ roughly describes the behaviour of the upper limits as a function of redshift.

The blue line in Fig. 6.3 has been obtained by applying the reference $P_{150} - M_{500}$ best-fit relation (see Sect. 6.2.2) to the 50% Planck completeness line. It indicates the minimum power of radio halos in PSZ2 clusters under the assumption that they follow the radio power-mass correlation. The fact that this line is always above the one traced by the upper limits indicates that LOFAR would be able to detect radio halos in clusters with mass above the 50% completeness line. As a consequence, to compare model expectations with observations we will use the blue line to determine which is the minimum power of a detectable RH in PSZ2 clusters (lying above the 50% completeness line) at each redshift.

6.4 Merger-driven turbulent re-acceleration scenario

In this Section we summarise the theoretical framework and procedures that allow us to predict the occurrence of radio halos at the completion of LoTSS in the context of the turbulent re-acceleration scenario. We refer to Cassano & Brunetti (2005); Cassano et al. (2006) for a detailed description of the model.

We model the properties of the RHs and their cosmic evolution by means of a Monte-Carlo approach, which is based on the semi-analytic model of Lacey & Cole (1993, i.e. the extended Press & Schechter (1974)) to describe the hierarchical process of formation of galaxy cluster dark matter halos. The merger history of a synthetic population of galaxy clusters is followed back in time and the generation of turbulence in the ICM is estimated for each merger identified in the merger trees. The injected turbulent energy is calculated as a fraction ($\eta_t \sim 0.1 - 0.3$) of the work (PdV) done by the subclusters falling into the main cluster. In our analysis, we consider constant parameters (homogenous model; Cassano et al. 2010), namely a volume-averaged magnetic field strength $\langle B \rangle = 2\,\mu$G (in line with e.g., Bonafede et al. 2010), $\eta_t = 0.2$, and a RH size $R_{RH} = 400$ kpc (in line with the median size of the halos in our sample), which have already been used in recent works (Cassano et al. 2019; Botteon et al. 2021a; Di Gennaro et al. 2021c).

The most important expectation of turbulent re-acceleration scenarios is that the synchrotron spectrum of RHs should become gradually steeper above a frequency ν_s[1] that is determined by the competition between acceleration and energy losses, and which is connected to the energetics of the merger events that generate the halos (e.g. Fujita et al. 2003; Cassano & Brunetti 2005). As a consequence, the population of RHs is expected to be made of a complex mixture of sources with different spectra.

In a survey carried out at the observing frequency ν_o, RHs can be detectable only if $\nu_s \geq \nu_o$. The luminosity function of radio halos (RHLF) with $\nu_s \geq \nu_o$ (i.e. the expected number of halos per comoving volume and radio power 'observable' at frequency ν_o) can be estimated as:

$$\frac{dN_{RH}(z)}{dV dP(\nu_o)} = \frac{\frac{dN_{RH}(z)}{dMdV}}{\frac{dP(\nu_o)}{dM}} , \tag{6.6}$$

where $dN_{RH}(z)/dMdV$ is the theoretical mass function of RHs with $\nu_s \geq \nu_o$, that is obtained by combining Monte-Carlo calculations of the fraction of clusters with RHs and the Press & Schechter (1974) mass function of clusters (e.g. Cassano et al. 2006). We estimate $dP(\nu_o)/dM$ from the reference radio power-mass correlation obtained at 150 MHz.

By integrating the RHLF (Eq. 6.6) above a given $S_{min}(z)$, we can obtain the number $N_{RH}^{\Delta z}$ of RHs with $S \geq S_{min}(z)$ in the redshift interval $\Delta z = z_2 - z_1$ as:

$$N_{RH}^{\Delta z} = \int_{z_1}^{z_2} dz \left(\frac{dV}{dz}\right) \int_{P_{min}(S^*_{min},z)} \frac{dN_{RH}(P(\nu_o),z)}{dP(\nu_o)dV} dP(\nu_o) . \tag{6.7}$$

[1] At $\nu > \nu_s$ the synchrotron spectrum of RHs steepens. Operatively, we adopt the convention that RHs have spectral index $\alpha = 1.9$ between $\nu_s/2.5$ and ν_s, and define USSRHs as those halos having $\alpha > 1.9$ between 250-600 MHz.

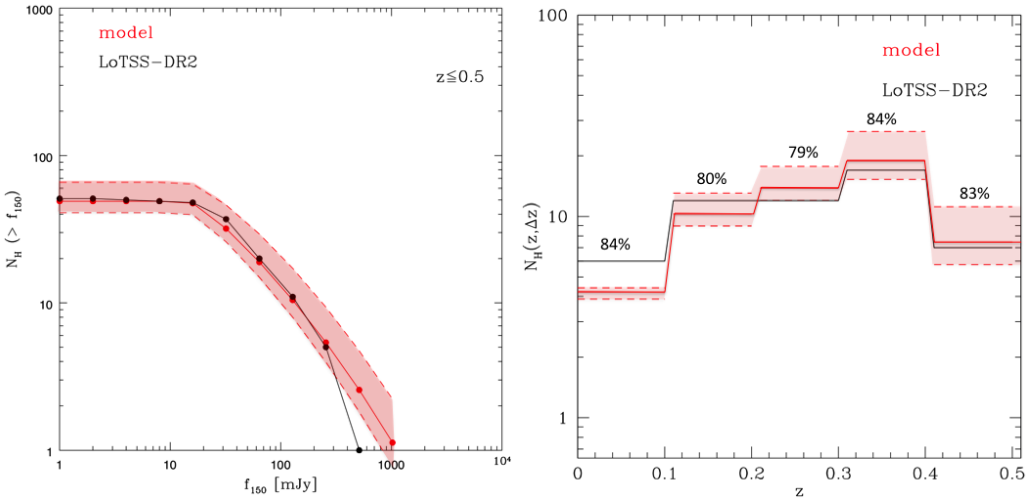

Figure 6.4: In all the panels we report the observed and expected number of RHs in black and red, respectively. *Left*: Expected and observed number of RHs in PSZ2 clusters with a flux density greater than S_{150} at $z \leq 0.5$ in the LoTSS-DR2 area. *Right*: Number of RHs in redshift bins ($N_{\rm RH}(z, \Delta z)$); the predicted percentages of USSRHs ($\nu_{\rm s} < 610$ MHz) is reported in each redshift bin.

6.5 Radio halos in LoTSS-DR2 vs model predictions

The Planck selection function implies that our measures arise from the combined effect of a simultaneous mass and redshift selection. To proceed with a comparison between observations and models, predictions must be calculated including the same selection effects we have in the observed sample.

To derive the expected number of detectable RHs in PSZ2 clusters in the LoTSS-DR2 footprint we used Eq. 6.7, and normalised the predicted number of RHs to match the number of clusters in our sample. As explained in Sect. 6.3, our deep upper limits to the flux density of NDE clusters allowed us to probe the capability of LOFAR to detect RHs in PSZ2 clusters. Therefore, we can estimate $S_{\rm min}(z)$ in Eq. 6.7 for each redshift by considering the Planck selection function combined with the $P_{150} - M_{500}$ correlation (i.e. the blue line in Fig. 6.3).

In the left panel of Fig. 6.4 we show the cumulative ($z \leq 0.5$) number of RHs expected in PSZ2 clusters in the LoTSS-DR2 area as a function of flux density (red line and region) vs the observed number of RHs (black dots and line). The error bars on the expected numbers are derived by making a Monte Carlo randomisations on the scatter of the $P_{150} - M_{500}$ correlation. We note a very good agreement between the observed and expected flux density distribution of radio halos (the deviation of the observed points at the highest flux density could be due to the insufficient statistics, just one observed RH).

The cumulative number of RHs in Fig. 6.4 is due to the contribution of RHs observed at different z. Both IC losses and the merger rate for a given mass depend on redshift, thus it is important to compare model predictions with the observed distribution of RHs with z. Therefore, we derived the redshift distribution, and show the number of RHs per

Table 6.3: Fraction of clusters with radio halos in high-mass clusters.

Instrument	observed $f_{\rm RH}$	$f_{\rm RH}$ from model
LOFAR	67-73%	67.0 ± 17.8%
GMRT	41-48%	44.6 ± 10.0%

Notes. Ranges in the observed $f_{\rm RH}$ values are obtained considering the U cases once as RH clusters and once as clusters without RH.

redshift bins $N_{\rm RH}(z, \Delta z)$ in the right panel of Fig. 6.4. Also in this case, we found very good agreement between the observed and predicted distribution of RHs.

6.5.1 The quest of very steep spectrum halos

Overall, we have shown that a simple version of the turbulent re-acceleration model, which is based on homogeneous conditions in the ICM and Monte Carlo simulations of merger-turbulence connection, and that uses reference parameters already adopted in previous works, provides an excellent description of the LOFAR observations.

In Fig. 6.4 (right), the reported values are the percentages of USSRHs ($\nu_{\rm s} \sim 150-600$ MHz) predicted by our model, being $\sim 70-80\%$ of the detected Planck radio halos in LoTSS-DR2. Unfortunately, these predictions cannot be tested with current data as many RHs discovered by LOFAR do not have follow-up observations at other frequencies.

What we can do with current data is comparing the fraction of clusters with RHs observed in our LOFAR sample with that observed with GMRT at 610 MHz in PSZ2 clusters with $M_{500} \geq 6 \times 10^{14}\, M_{\odot}$ and $z \leq 0.35$ (Cuciti et al. 2021a). In this mass and redshift range we measure a fraction of clusters with RHs $\sim 70\%$ in our LOFAR sample, compared to $\sim 45\%$ that is measured in the GMRT sample. We derive the expected fraction of clusters with RHs in the cluster population with $M_{500} \geq 6 \times 10^{14}\, M_{\odot}$ in the redshift range $z \sim 0.08-0.35$, by assuming our statistical model and requiring $\nu_{\rm s} > 610$ MHz and $\nu_{\rm s} > 150$ MHz to be compared with the GMRT and LOFAR fractions, respectively. We report all the measured and predicted fractions in Table 6.3. This can be considered an indirect proof of the presence of USSRHs in the PSZ2-DR2 sample. Indeed, we found a good agreement between the observed fractions of clusters with RHs and those derived from the model. The model predicts that the difference between the low and high-frequency fractions is caused by the intervening population of very-steep spectrum halos ($\sim 33\%$ of halos at these cluster masses and redshifts) that become visible preferentially at lower frequencies.

6.5.2 Radio halos and connection with cluster dynamics

As reported in Chapter 4, we derived the concentration c and centroid shift w parameters for the clusters with available Chandra and/or XMM-Newton X-ray observations (see also Zhang et al. 2023, for details) to characterise their dynamical state. By applying the same selection criteria of our occurrence sample (Sect. 6.1.2), we obtain a morphological sample of 93 clusters.

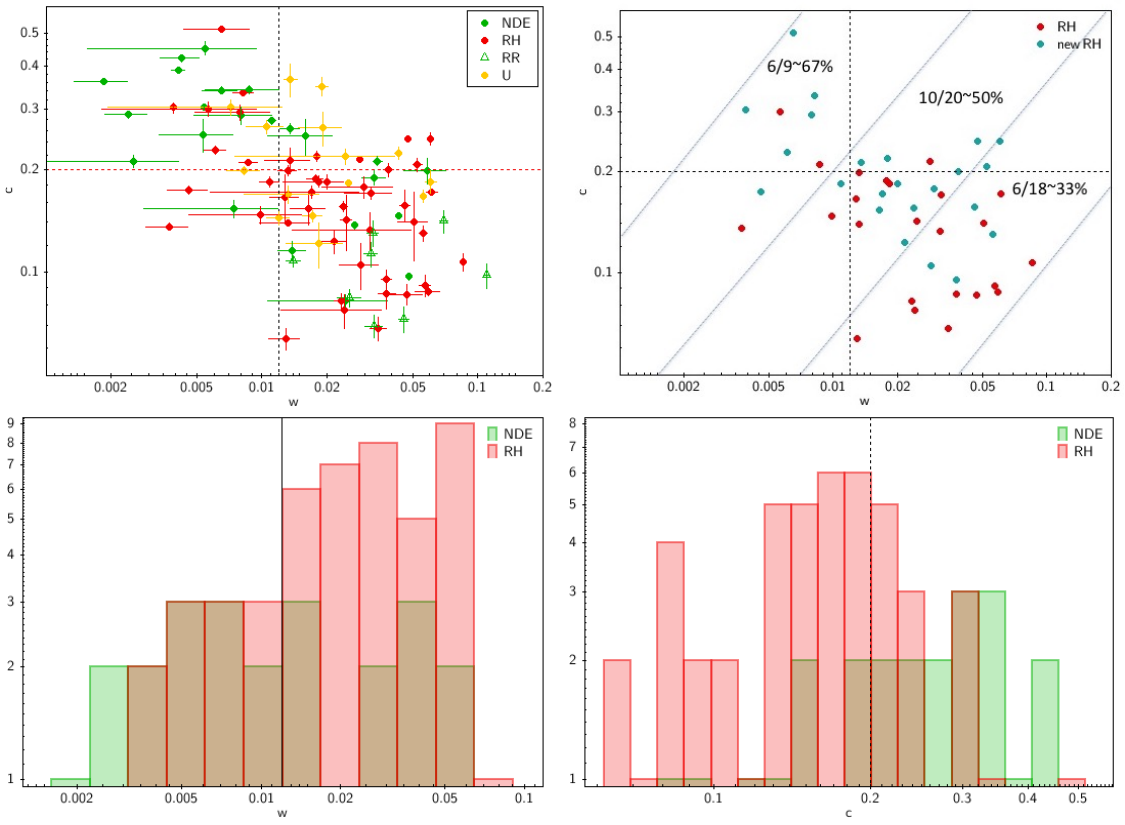

Figure 6.5: *Top left*: $c - w$ diagram for the full morphological sample. *Top right*: $c - w$ diagram for previously known (red) and newly discovered (cyan) RHs in the morphological sample. Fractions of newly RHs are reported for each $c - w$ regions. *Bottom*: Distributions of w (left panel) and c (right panel) for RH and NDE objects. In all the panels, the vertical ($w = 0.012$) and horizontal ($c = 0.2$) dashed lines are adopted from Cassano et al. (2010) as reference values to distinguish between relaxed and disturbed systems.

In the top left panel of Fig. 6.5 we report the $c - w$ distribution of these 93 clusters together with the reference dividing lines $c = 0.2$ and $w = 0.012$ (see Cassano et al. 2010, for details). We see that the fraction of clusters with RHs has a tendency to increase from more relaxed (high c, low w) to more disturbed (high w, low c) systems. In contrast, the fraction of NDE clusters tends to increase towards the more relaxed systems. Unfortunately, the information about the dynamics is incomplete, especially for NDE clusters (morphological parameters are indeed available for 32% of NDE and 85% of RH objects). This prevents us from drawing firm conclusions about the relative fraction of RHs and NDEs vs cluster dynamics. However, since the dynamical information about RHs is quite complete, we can confidently say that RHs are found preferentially in merging systems, as also suggested by histograms in Fig. 6.5 (bottom panels); indeed, $\sim 77\%$ of RHs live in clusters with $c < 0.2$ and $\sim 80\%$ of RHs live in clusters with $w > 0.012$ ($\sim 72\%$ of RH have both $c < 0.2$ and $w > 0.012$).

In addition, we notice that the fraction of newly detected RHs by LOFAR (cyan points in Fig. 6.5, top right panel) increases going from the more disturbed to the more relaxed regions of the plot. This indicates that LOFAR is able to unveil radio halos in less disturbed systems. Although we do not have spectral information about these newly detected RHs, based on our framework we speculate that the majority of them are likely characterised by very steep spectra. A possible contamination can be due to the presence of MHs (not distinguished from RHs in this work, see Chapter 4) in relaxed clusters, but to our knowledge, only one target (A1068) is a confirmed MH.

6.6 Summary and conclusions

In this work we exploited the detected RHs (Chapter 4), upper limits for non-detections (Chapter 5), and X-ray information (Chapter 4, see also Zhang et al. (2023) for details) of the Planck clusters in LoTSS-DR2 to carry out the first statistical studies of radio halos at low radio frequencies and test theoretical models. This is the largest complete sample of galaxy clusters observed at radio frequencies to date, spanning unprecedentedly wide ranges in redshift and mass. The main results that we achieved are summarised below.

- The connection existing between the radio power of RHs and the mass of the host cluster is well established at 1.4 GHz, but still fairly unexplored at low frequencies. We confirm the existence of this correlation at 150 MHz in our sample (Table 6.2 and Fig. 6.2), as well. As predicted by models and simulations, the correlation shows a relatively large scatter, likely caused by a superposition of clusters in different types and stages of mergers, and radio halos with different spectra and sizes. Furthermore, in line with finding at higher frequencies, we found evidence of a clear bimodal distribution between radio halos, which are located on or above the correlation, and upper limits, which are located well below the correlation.

- In spite of the lower statistics available at 1.4 GHz, the correlation found at 150 MHz is in agreement with that derived at 1.4 GHz (bottom right panel of Fig. 6.2) by Cuciti et al. (2021a). The number of upper limits, as well as their mass range,

has also substantially increased with respect to the past. The upper limits obtained with LOFAR are generally much deeper than those obtained with the GMRT, and this allowed us to probe mass ranges below $M_{500} \sim 6 \times 10^{14} M_{\odot}$ for the first time, and infer the presence of the correlation down to $M_{500} \sim 3 \times 10^{14} M_{\odot}$.

- We used semi-analytic models developed in the framework of the merger-driven turbulent re-acceleration scenario to derive the expected properties of the RH population in the PSZ2 clusters. Although our model is rather simplified, we have shown that it provides an excellent description of the observed properties of the RH population in our LOFAR sample, being able to reproduce the integral number of RHs, their flux density, and redshift distribution (Fig. 6.4). Using the same modelling we predict that $\sim 100 - 200$ RHs could be detected in PSZ2 clusters (above the 50% completeness line and $z \sim 0.07 - 0.5$) by the full LoTSS.

- The model predicts that a large fraction of RHs in our sample are characterised by very steep spectra. Future follow-up observations at higher frequency of all RHs in our sample will definitively test this expectation, making the golden test of the scenario. With currently available data, we compared the occurrence of RHs in our sample with that derived from a sample of PSZ2 clusters with $M \geq 6 \times 10^{14}\, M_{\odot}$ and $z \leq 0.35$ observed with GMRT at 610 MHz (Cuciti et al. 2021a). In the same mass and redshift ranges, we found an increase of the fraction of clusters with RHs that goes from $\sim 45\%$ in the GMRT sample to $\sim 70\%$ in the LOFAR sample. The observed increase is in line with the presence of a larger population of USSRHs at 150 MHz, which arise at lower frequency because of their very steep spectra.

- Observations at low radio frequency are expected to find RHs also in less disturbed systems. Although the morphological information is not complete for our sample (especially for NDE clusters), we see that the fraction of clusters with RHs has a tendency to increase towards more disturbed systems (Fig. 6.5). In addition, we see that the fraction of newly detected RHs by LOFAR increases going from merging to more relaxed systems, indicating that LOFAR starts to observe RHs in less disturbed systems, possibly unveiling RHs with very steep radio spectra.

Chapter 7

The distant steep spectrum radio halo in MACS J1149.5+2223

In the last part of this Thesis, we will present multi-frequency radio and X-ray data of two interesting galaxy clusters, both hosting a very steep spectrum radio halo. In particular, this Chapter is devoted to the study of the USSRH in the distant (redshift $z = 0.544$) galaxy cluster MACS J1149.5+2223 (hereafter MACS J1149).

Previous studies of MACS J1149 suggested the presence of two misaligned relics and a candidate USSRH (Bonafede et al. 2012). Distant radio halos with steep spectra are particularly important, since turbulent re-acceleration models predict that their number should increase at higher redshift (Cassano et al. 2006, 2010a). Indeed, the turbulent energy provided to the emitting electrons has to compete with prominent radiative losses via inverse Compton with the CMB photons ($B_{\rm CMB} \propto (1+z)^2$).

We present new LOFAR HBA and JVLA radio data, which we combined with archival GMRT data to investigate the different diffuse sources in MACS J1149. In addition to the radio data, we analysed archival Chandra X-ray observations, aiming to search for surface brightness discontinuities and possible correlations between the thermal and non-thermal emission of the cluster. Finally, the combination of high-z and steep α allowed us to perform a stringent test that rules out a pure hadronic origin for the halo. The results presented in this Chapter are based on the following paper:

- (Bruno et al. 2021) **L. Bruno**, K. Rajpurohit, G. Brunetti, F. Gastaldello, A. Botteon, A. Bonafede, D. Dallacasa, R. Cassano, R. J. van Weeren, V. Cuciti, G. Di Gennaro, T. Shimwell, M. Brüggen; *The LOFAR and JVLA view of the distant steep spectrum radio halo in MACS J1149.5+2223*. Published by A&A, 650, A44.

7.1 Galaxy cluster MACS J1149

MACS J1149 ($\rm RA_{J2000}$ $11^h49^m35^s$, $\rm Dec_{J2000}$ $22^o24'11''$) is a massive ($M_{500} = (10.4 \pm 0.5) \times 10^{14}$ $M_\odot$; Planck Collaboration et al. 2016) galaxy cluster, first discovered by the MAssive Cluster Survey (MACS; Ebeling et al. 2001) in the X-ray band.

Previous lensing and spectroscopy studies revealed the very complex structure of this cluster, which has at least three dark matter sub-halos (Smith et al. 2009; Golovich et al.

2016, 2019). The two most massive sub-clusters are located north-west and south-east, with respect to the main cluster, at a projected distance of $\sim$ 1 Mpc (Golovich et al. 2016). The third less massive sub-cluster is located $\sim$ 300 kpc north of the first sub-cluster (see Fig. 7.1).

As shown by deep Chandra X-ray observations (Ogrean et al. 2016), the ICM has a globally high temperature of $kT \sim 10$ keV and is elongated along the NW-SE axis, although the main X-ray concentration is associated with the most massive NW sub-cluster only. The presence of many massive components, the elongated morphology, and the absence of a central cool core concentration are indications of a disturbed dynamical state of the cluster. This is further confirmed by the concentration ($c = 0.120 \pm 0.003$) and centroid-shift ($w = 0.017 \pm 0.001$) parameters estimated by Yuan & Han (2020); these morphological parameters locate MACS J1149 among the disturbed clusters in the $c - w$ bimodal distribution reported by Cassano et al. (2010b). Ogrean et al. (2016) also report the presence of an X-ray surface brightness discontinuity, likely being a cold front, located in the N-NE part of the cluster.

In the radio band, by using VLA and GMRT data, Bonafede et al. (2012) found evidence of diffuse emission, with two possible misaligned relics at south-east and west, and a candidate steep spectrum halo, with $\alpha \sim 2$, in line with the complex dynamics of the system. During the preparation of this work, Giovannini et al. (2020) presented some of the new JVLA observations of the cluster that we used in our analysis (see Sect. 8.2.4 for details). These authors revise the nature of the candidate west relic, classify it as a radio galaxy, and suggest that the south-east relic might be instead a filamentary structure, whose major axis is parallel to the merger axis. In the following, we will refer to the SE source as the 'relic', following the original classification proposed by Bonafede et al. (2012).

7.2 Observations and data reduction

In this section we present the X-ray and radio data, summarised in Table 8.3 and Table 8.1, respectively, and briefly describe the reduction processes.

7.2.1 Chandra X-ray data

We analysed archival Chandra X-ray data (first presented by Ogrean et al. 2016) of MACS J1149, observed in VFAINT mode with ACIS-I. We reprocessed the six observations using `CIAO` v. 4.12, with `CALDB` v. 4.9.0. We extracted light curves from the S2 chip (when available) or from one of the I-chips (free of the target emission) in order to filter out soft proton flares with the `lc-clean` algorithm, which left 287.8 ks of total clean time.

We combined each point spread function (PSF) and the exposure maps to produce a single exposure-corrected PSF map. This map was used as input in the `wavdetect` task to find point sources, which we then inspected by eye. Spurious sources were excluded and the confirmed sources were excised.

Table 7.1: Details of the Chandra X-ray data analysed in this work (PI: C. Jones).

ObsID	CCDs	Observation date	Clean time (ks)
16238	I0,I1,I2,I3	09-Feb.-2015	30.4
16239	I0,I1,I2,I3,S2	17-Jan.-2015	48.8
16306	I0,I1,I2,I3,S2	05-Feb.-2014	68.7
16582	I0,I1,I2,I3,S2	08-Feb.-2014	17.6
17595	I0,I1,I2,I3	18-Feb.-2015	57.1
17596	I0,I1,I2,I3	10-Feb.-2015	65.2

Table 7.2: Details of the LOFAR (LoTSS, pointing name: P177+22), GMRT (PI: M. Brüggen, project code: 20_066), and JVLA (PI: A. Bonafede, project code: 13A-056; PI: R. J. van Weeren, project code: 14B-205) radio data analysed in this work.

Instrument	Configuration	Central frequency (MHz)	Frequency coverage (MHz)	Observation date	On-source time (h)
LOFAR	Dual-inner-HBA	144	120-168	04-May-2017	8.0
GMRT	-	323	305-340	27-Jun.-2011, 16-Aug.-2011	1.0+4.0
JVLA	B	1500	1000-2000	17-Nov.-2013, 7-Apr.-2015	2.0+3.5
JVLA	C	1500	1000-2000	24-Jun.-2013	2.5
JVLA	D	1500	1000-2000	14-Feb.-2013, 4-Mar.-2013	0.75+0.75

Notes. Additional archival GMRT (610 MHz) and JVLA (2.8 GHz) data are available. We only used these data to check the flux density scale of the point sources in the field. The halo is too faint and is undetected at 2.8 GHz, and it is not fully recovered at 610 MHz owing to the insufficient depth and missing short baselines of these data.

The X-ray analysis of galaxy clusters requires a careful treatment of the background, which has various origins: the local hot bubble (LHB), the galactic halo (GH), the unresolved X-ray sources (CXB), and the particle background (NXB). In particular, we modelled the LHB and the GH with a single absorbed thermal plasma (APEC model) of $kT = 0.20$ keV, and the CXB with an absorbed power-law of photon index $\Gamma = 1.45$; the NXB was obtained by fitting the single spectra extracted from the reprojected stowed background observations and combining a power-law, a decaying exponential, and a number of Gaussian profile lines (as described in Bartalucci et al. 2014). To model the sky components, we extracted the spectra from the observations in the same regions free of ICM emission and we jointly fitted these with the `XSPEC` v. 12.10.1 package (Arnaud 1996) in the 0.7-11.0 keV band. The NXB emission parameters were kept fixed as obtained by the fit of the single observations. We adopted the Cash statistics (Cstat; Cash 1979) and fixed the (atomic + molecular) hydrogen column density in the direction of the cluster to $n_{\rm H} = 2.06 \times 10^{20}$ cm^{-2} (Willingale et al. 2013). In the following, errors on fitted parameters are quoted at the 68% confidence level.

7.2.2 LOFAR radio data

MACS J1149 is located at 21 arcmin from the centre of the LoTSS pointing P177+22, which was observed for 8 h on 4 May 2017 using the HBA Dutch array operating in the 120-168 MHz frequency range. The source 3C 295 was used as flux density scale calibrator.

Data were processed by means of the LOFAR KSP pipeline v2.2 (see details in Sect. 3.3.1). Additional cycles of amplitude and phase self-calibration were performed to improve the calibration of the sources within an extraction region of sizes $27' \times 27'$ centred on the target. We then checked for possible systematics in the flux density scale[1] by comparing compact discrete sources in the field with the TIFR GMRT Sky Survey Alternative Data Release (TGSS-ADR; Intema et al. 2017), finding no significant offset; typical offsets are of the order of 3%, where only one source has a $\sim$ 10% offset.

7.2.3 GMRT radio data

We retrieved archival GMRT data (first presented by Bonafede et al. 2012) in the 305-340 MHz band, for a total bandwidth of 32 MHz, split into 256 channels. Two observations of 1 and 4 h on-source time are available, and the sources 3C286 and 3C147 were used as absolute flux density scale calibrators. We reprocessed these observations independently via the Source Peeling and Atmospheric Modeling (`SPAM`) automated pipeline (Intema et al. 2009), which corrects for ionospheric effects and removes direction-dependent gain errors, thereby improving the noise and fidelity of the images. Strong sources in the field of view were used to derive directional-dependent gains and fit a phase-screen over the entire field of view. Finally, images were corrected for the system temperature variations between the calibrator and the target.

During the imaging steps, we found that the flux density of the point sources in the field were different for the two observations, independent of the adopted primary calibrator. We measured their flux density at 144 (LOFAR), 610 (GMRT), 1500 (JVLA, L band), and 2800 (JVLA, S band) MHz (see notes in Table 8.1) to check for the spectra of the sources. The expected power-laws are well fitted in the case of the shallower GMRT data, whereas the deeper data appear to be systematically biased low. The logs of the 4 h observation report of high wind speeds, which could have affected some scans and system gains. To account for this problem, we corrected the deeper images by multiplying them for a factor of 1.23, that is the mean ratio of the source flux densities in the shallow and deep maps.

7.2.4 JVLA radio data

MACS J1149 was observed with the JVLA at 1-2 GHz (L band) in B, C, and D configurations, for 5.5, 2.5 , and 1.5 hours on-source time, respectively (see Table 8.1 for details), with 3C286 as flux density calibrator and J1150+2417 as phase calibrator. The data were recorded with 16 spectral windows, each divided into 64 channels.

[1] At the time of this work, the derivation of the factor to correct the flux density scale a posteriori (see Sect. 3.3.1) was not implemented by the reduction pipelines.

Table 7.3: Summary of the parameters adopted to produce the radio maps discussed in the paper. Columns 2, 3, and 4 indicate the minimum baseline ($B_{\rm min}$), the robust parameter of the Briggs weighting, and the tapering used, respectively. Column 5 reports the reached resolution (θ).

Dataset	$B_{\rm min}$	Robust	Taper	θ
LOFAR	80λ	-0.5	-	$10'' \times 6''$
LOFAR	80λ	0	$5''$	$19'' \times 15''$
LOFAR*	170λ	0	$10''$	$27'' \times 21''$
GMRT*	170λ	0	$10''$	$20'' \times 14''$
$\rm JVLA_{[B+C+D]}$	-	0	-	$5'' \times 4''$
$\rm JVLA^{*}_{[D]}$	170λ	0	-	$29'' \times 28''$

Notes. *These maps were smoothed with a $30'' \times 30''$ beam and used to measure the flux density of the halo.

Data reduction was carried out with the National Radio Astronomy Observatory (NRAO) Common Astronomy Software Applications (`CASA`; McMullin et al. 2007) v. 4.7. We removed radio frequency interference (RFI) by means of the `AOFlagger` software (Offringa 2010; Offringa et al. 2012). The data from B, C, and D configurations were calibrated independently, by performing the standard calibration procedure, which includes the initial phase, bandpass, and gain calibrations. In addition, we performed two rounds of phase-only self-calibration and two rounds of amplitude and phase self-calibration on the individual datasets. Finally, we combined the B, C, and D configuration data to create deep images.

7.2.5 Radio imaging and source subtraction

The imaging process was carried out for all the datasets with `WSClean` v. 2.7, which is designed for wide-field, multi-frequency, and multi-scale synthesis. All images are corrected for the primary beam attenuation. For each dataset, we produced maps with different baseline weightings to study the radio emission of the target on various spatial scales.

The weighting schemes adopted for the maps discussed in the next sections are summarised in Table 8.2. To properly image the diffuse emission and consistently compare the LOFAR, GMRT, and JVLA (D array) maps, we adopted a common minimum baseline of 170λ (which gives a maximum recoverable scale of $\sim 20'$, corresponding to ~ 8 Mpc), a Brigss (Briggs 1995) weighting with robust 0, and a tapering of the long baselines ($10''$). We then smoothed these maps with a $30'' \times 30''$ beam. In addition, we produced an intermediate resolution ($19'' \times 15''$) LOFAR map, which we used for subsequent analysis (see Sect. 7.3.4 and 7.4.1).

We have to remove the contribution of the sources embedded in the halo to measure its flux density. For LOFAR and GMRT datasets, we selected the sources by imaging the data at high resolution, excluding the shortest baselines ($< 4\rm k\lambda$; corresponding to maximum angular scales of $\sim 50''$), then we subtracted the clean components in the model

image from the *uv*-data. We tested the consistency of this process by comparing the flux density of the halo with that obtained by algebraically subtracting the flux density of the embedded sources from the total (halo plus sources) flux density, finding a good agreement (within 3% and 5% of the flux density for LOFAR and GMRT, respectively). Subtracting the clean components of the discrete sources is not sufficiently accurate with the JVLA datasets, given the very low flux density of the halo. The low sensitivity to extended sources of the B array and the insufficient depth of the C array data, do not allow us to accurately recover the halo emission. On the other hand, the low resolution of the D array makes it difficult to obtain a good model of both point and extended sources. However, we can use the sensitive high-resolution images to identify faint compact sources in the halo region, which contribute to the total flux density when measured from lower resolution images. Therefore, we accurately measured the flux density of point sources in B and C configurations at high resolution, the extended sources in D configuration at low resolution, and then we subtracted their contribution out of the total (halo plus sources) flux density obtained in D array. The model subtraction from the *uv*-data biases the net flux density of the halo at 1.5 GHz high, but the algebraic subtraction might bias the net flux density low; to take into account this effect, we safely considered the 20% of the flux density as the uncertainty on the subtraction.

The uncertainties ΔS on the reported flux densities are given by

$$\Delta S = \sqrt{\left(\sigma \cdot \sqrt{N_{\rm beam}}\right)^2 + (\xi_{\rm cal} \cdot S)^2 + (\xi_{\rm sub} \cdot S)^2}, \tag{7.1}$$

where σ is the RMS noise of the map, $N_{\rm beam}$ is the number of independent beams within the considered region, $\xi_{\rm cal}$ is the calibration error, and $\xi_{\rm sub}$ is the uncertainty of the source subtraction. As mentioned, we assumed $\xi_{\rm sub} = 3\%,\ 5\%,$ and 20% for LOFAR, GMRT, and JVLA, respectively. We adopted $\xi_{\rm cal} = 10\%$ for LOFAR (which is lower than the 20%[2] reported in Shimwell et al. 2019, given the low-significance offset found with respect to the TGSS image), $\xi_{\rm cal} = 10\%$ for GMRT (Chandra et al. 2004), and $\xi_{\rm cal} = 5\%$ for JVLA (Perley & Butler 2013).

7.3 Results

In this section we first show the results of the X-ray and radio data analysis, then we investigate the connection between the thermal and non-thermal emission.

7.3.1 Global X-ray properties

In Fig. 7.1 (left) we present the exposure-corrected map of MACS J1149 in the 0.5-3 keV band, obtained by merging the six Chandra observations listed in Table 8.3. The cyan circles indicate the locations of the three sub-clusters, as reported by Golovich et al. (2016); they have virial masses of $M_1 \sim M_2 \sim 10^{15}\ M_\odot$, $M_3 \sim 10^{14}\ M_\odot$, respectively.

[2]This value refers to LoTSS-DR1; the improved calibration of LoTSS-DR2 provides $\xi_{\rm cal} = 10\%$, in line with our findings.

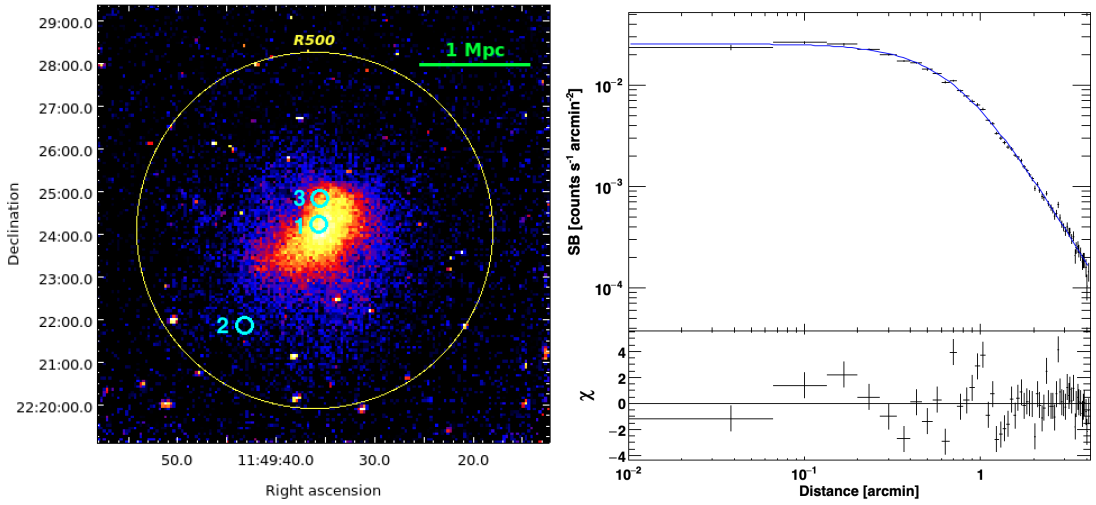

Figure 7.1: *Left:* MACS J1149 X-ray map obtained with Chandra in the 0.5-3 keV band (1 pix = 4″). The region within R_{500} is indicated in yellow and cyan circles label the location of the three sub-clusters, as reported by Golovich et al. (2016). The cluster is elongated along NW-SE. Sub-cluster 1 is associated with the main X-ray concentration, whereas no clumps associated with sub-cluster 2 are clearly visible. *Right:* X-ray surface brightness profile. Data are fitted by a β-model (blue line).

The ICM appears elongated along the NW-SE axis, where sub-clusters 1 and 2 lie. Even though sub-clusters 1 and 2 have similar masses, only the most massive sub-cluster 1 is associated with the main X-ray concentration; the depth of the data would be sufficient to detect X-ray clumps associated with sub-cluster 2, if any.

In the right panel of Fig. 7.1 we show the surface brightness profile within a circle (centred on the pixel coincident with the X-ray peak) of radius $R_{500} = 1.6$ Mpc, extracted and fitted by means of the `PROFFIT` v. 1.5 code (Eckert et al. 2011). The background was assumed to be constant. It was estimated in a source-free region and subtracted, whereas the data were fitted with a simple beta profile under the assumptions of a isothermal gas and a spherical geometry (Cavaliere & Fusco-Femiano 1976) as follows:

$$n_{\rm th}(r) = n_{\rm th,0}\left[1+\left(\frac{r}{r_{\rm c}}\right)^2\right]^{-\frac{3}{2}\beta}, \tag{7.2}$$

where $n_{\rm th}$ is the thermal particle density number, $r_{\rm c}$ is the core radius, and the index β represents the ratio of the kinetic energy of the galaxies to the thermal energy of the gas. The thermal particle distribution is related to the X-ray surface brightness profile $I_{\rm X}(r)$ as (Sarazin 1986a)

$$I_{\rm X}(r) = \sqrt{\pi} n_{\rm th,0}^2 r_{\rm c} \Lambda(T) \frac{\Gamma(3\beta-0.5)}{\Gamma(3\beta)}\left[1+\left(\frac{r}{r_{\rm c}}\right)^2\right]^{\frac{1}{2}-3\beta}, \tag{7.3}$$

where $\Lambda(T) \sim 2.5\times10^{-27}\sqrt{T}$ erg cm^3 s^{-1} is the cooling function in the case of a plasma at a temperature T emitting through thermal bremsstrahlung (e.g. Gitti et al. 2012b). We

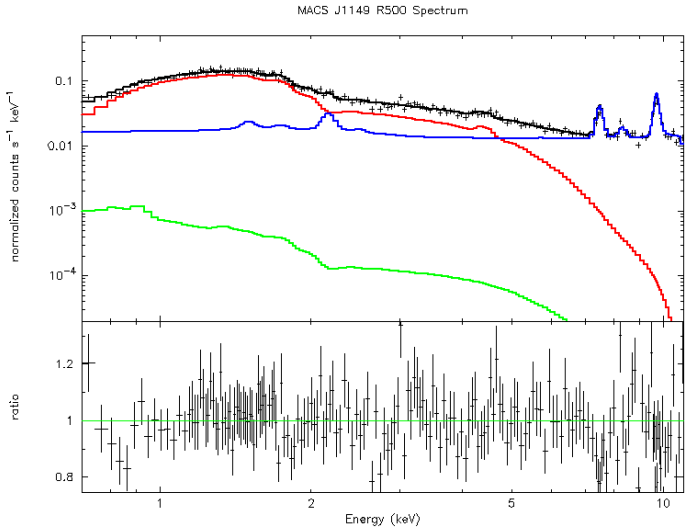

Figure 7.2: MACS J1149 X-ray spectrum within R_{500}. Data and best-fit model are shown in black. The red, green, and blue curves indicate the cluster emission, the sky background, and the NXB, respectively. The bottom panel shows the ratio of the data to the model. Fits were performed simultaneously for all the observations, but we report only one spectrum for a clearer inspection of the plot.

obtained $\beta = 0.66 \pm 0.01$ and $r_c = 288 \pm 8$ kpc, where $\chi^2/\mathrm{dof} = 2.3$, which is consistent with the typical values found for merging clusters (Forman et al. 1984).

Finally, the X-ray spectrum extracted within R_{500} is shown in Fig. 7.2; we jointly fitted all the observations, but we report only one spectrum to avoid confusion in the plot. The particle and sky background components were modelled as described in Section 7.2.1, whereas we adopted an absorbed APEC for the ICM emission. We obtained a global temperature of $kT = 10.5 \pm 0.3$ keV and a metallicity of $Z = 0.23 \pm 0.05\ Z_\odot$ (Cstat/dof = 3530/3076). The computed flux within R_{500} is $F^{500}_{[0.1-2.4\ \mathrm{keV}]} = (1.67 \pm 0.01) \times 10^{-12}$ erg s^{-1} cm^{-2}, which gives a luminosity of $L^{500}_{[0.1-2.4\ \mathrm{keV}]} = (1.35 \pm 0.01) \times 10^{45}$ erg s^{-1}, in agreement with the values reported by Ogrean et al. (2016).

7.3.2 Surface brightness edges

We searched for possible substructures in the X-ray surface brightness distribution. As a first step, we used the `CONTBIN` v. 1.6 code (Sanders 2006) to adaptively bin the surface brightness map into regions with a signal-to-noise ratio of S/N = 30, thus ensuring enough source and background counts. Then, we extracted the spectra within those regions and jointly fitted them, such that the background and metallicity were kept fixed to the previously obtained values, to produce the temperature map shown in Fig. 7.3; the error map on the right was obtained as the mean of the lower and upper errors. As a general trend, we note that the eastern regions of the cluster are colder than the western regions; this is also visible in the temperature map shown in Ogrean et al. (2016) and obtained with a lower S/N = 10. Moreover, we observe a difference in temperature northwards

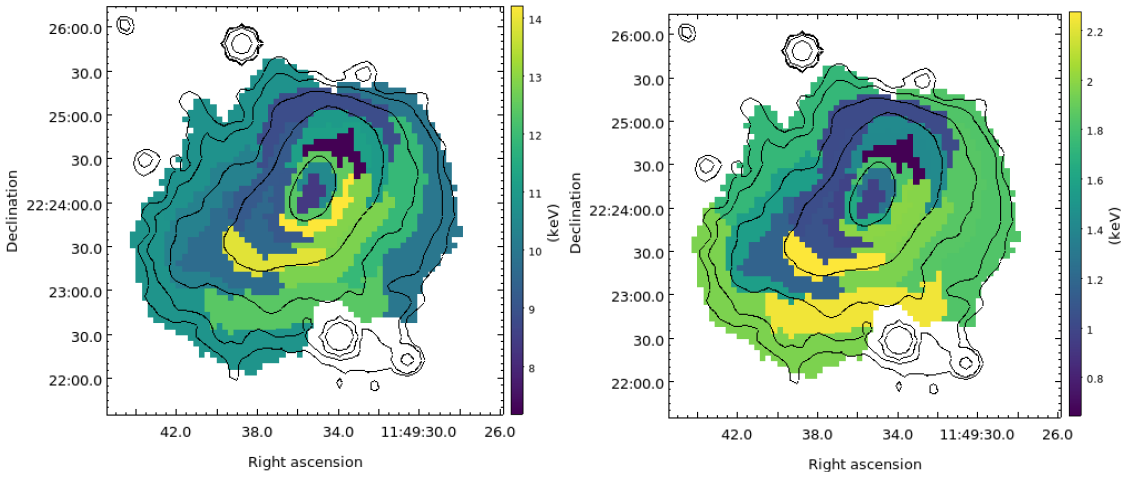

Figure 7.3: Temperature (left) and associated error (right) maps, reported in keV units. The X-ray surface brightness contours of Fig. 7.1 are reported in black. The temperature map suggests the presence of a significant lower kT region in NW.

Table 7.4: Properties of the surface brightness discontinuities in Fig. 8.10. Column 3 indicates the distance ($R_{\rm D}$) of the edge from the sector centre. Column 4 reports the density compression factor (C). Column 6 reports the total source plus background counts ($N_{\rm counts}$) in each sector. Column 7 lists the temperature in the inner and outer sub-sectors.

Edge	Centre	$R_{\rm D}$ (arcmin)	C	Region	$N_{\rm counts}$	kT (keV)
NE	11:49:33.8 +22:24:18.9	$0.90^{+0.01}_{-0.01}$	$1.38^{+0.11}_{-0.11}$	inner	2600	$9.8^{+0.9}_{-0.9}$
				outer	2300	$10.7^{+1.5}_{-1.1}$
NW	11:49:36.3 +22:24:17.9	$1.13^{+0.02}_{-0.01}$	$1.52^{+0.11}_{-0.11}$	inner	1900	$9.0^{+1.0}_{-0.8}$
				outer	1300	$11.8^{+2.3}_{-3.1}$

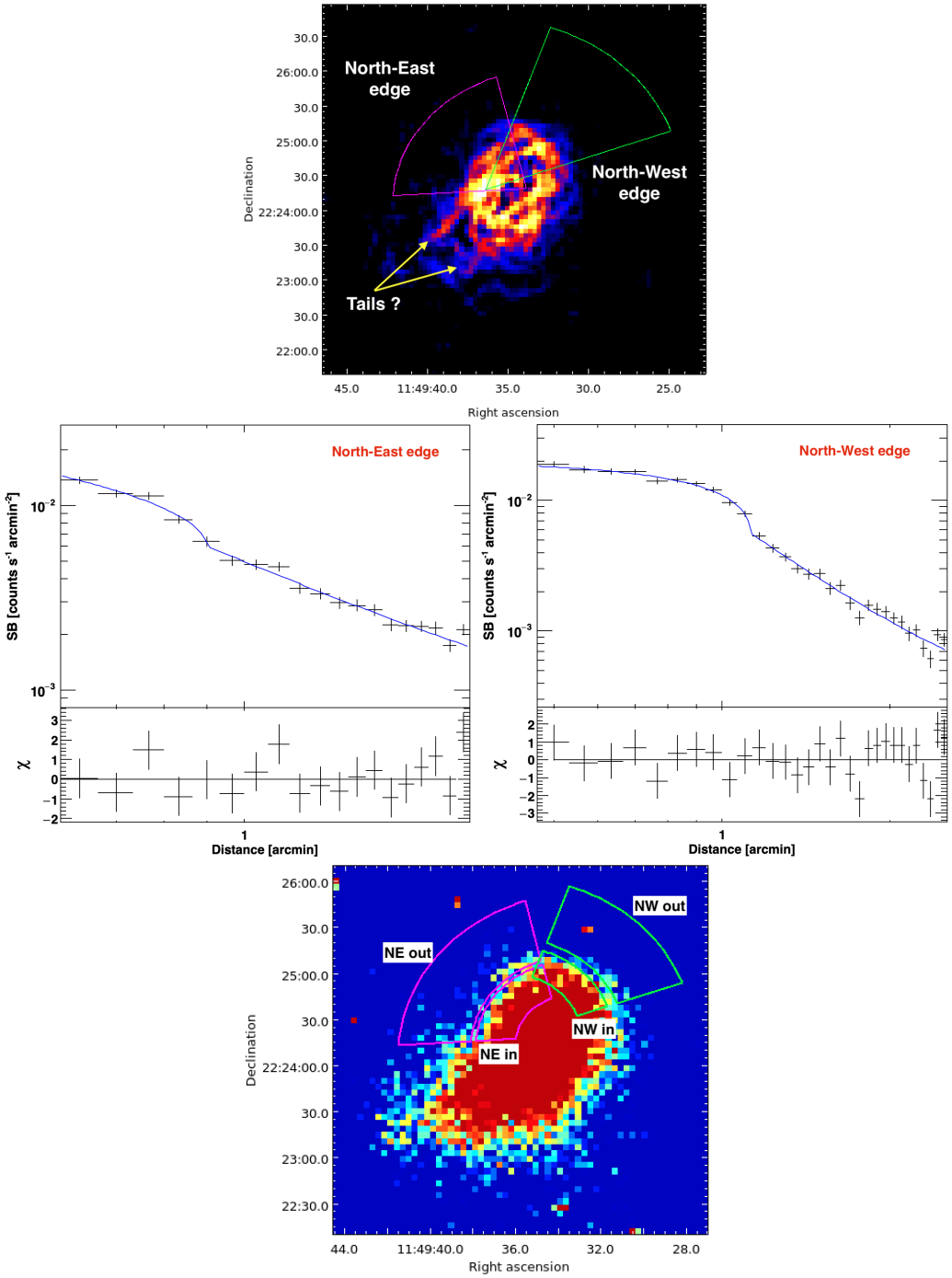

Figure 7.4: *Top:* GGM-filtered X-ray image with $\sigma_{\rm GGM} = 4'$. Two possible surface brightness edges are revealed in the NE and NW. Two filamentary structures (the 'tails') are present at south. *Middle left:* Best fit (χ^2/dof = 0.99) of the NE edge with a broken power-law. The density compression factor is $C = 1.38 \pm 0.11$. *Middle right:* Best fit (χ^2/dof = 1.12) of the NW edge with a broken power-law. The density compression factor is $C = 1.52 \pm 0.11$. A fit with a single power-law is rejected (χ^2/dof = 1.80) and thus not shown. *Bottom:* X-ray count image showing the sectors used to extract the spectra upstream and downstream the surface brightness discontinuities. There are no significant temperature jumps.

and southwards with respect to the global value, but the error map indicates that only the northern region has a temperature significantly different ($kT = 7.2 \pm 0.6$ keV) from that of the surrounding bins.

Discontinuities and substructures in the surface brightness profile can be enhanced by means of the Gaussian gradient magnitude (GGM; Sanders et al. 2016a,b) filtering. We tested different $\sigma_{\rm GGM}$ scales (i.e. the width of the derivative of the Gaussian curve): too narrow scales ($< 4''$) are usually not efficient in detecting edges in the outskirts of the cluster, owing to the low counts, whereas too large scales ($> 8''$) could give excessively smoothed images (e.g. Botteon et al. 2018). We found that possible discontinuities are better highlighted with $\sigma_{\rm GGM} = 1, 2$ pixels, where 1 pixel correspond to $4''$ in our maps.

In Fig. 8.10 (top panel) we show the GGM-filtered image with $\sigma_{\rm GGM} = 1$ pix. This map reveals two distinct possible edges in the NE and NW, instead of the single one reported by Ogrean et al. (2016), which partially covers both of the edges. In particular, the candidate NW edge is coincident with the cold region highlighted by the temperature map. We do not find discontinuities in the south, however we confirm the presence of two filamentary structures, as found with the unsharp mask analysis by Ogrean et al. (2016), who referred to these structures as the X-ray tail (SW) and peak (SE). The GGM-filtering suggests that they could both be tails, likely associated with the cluster dynamics.

We extracted the surface brightness profiles in the purple and green sectors to study the two candidate discontinuities. We fitted these discontinuities with a broken power-law model (e.g. Owers et al. 2009) as follows:

$$n(r) = \begin{cases} C n_0 \left(\frac{r}{R_{\rm D}}\right)^{-a} & \text{if r} \leq \text{R}_{\rm D} \\ \\ n_0 \left(\frac{r}{R_{\rm D}}\right)^{-b} & \text{if r} > \text{R}_{\rm D} \end{cases}, \tag{7.4}$$

where C is the density compression factor, a and b are the power-law slopes, and $R_{\rm D}$ is the radius of the edge. The fitted profiles are shown in Fig. 8.10 (middle panels) and the obtained values are summarised in Table 7.4. The two discontinuities give similar compression factors, where $C = 1.38 \pm 0.11$ for the NE, and $C = 1.52 \pm 0.11$ for the NW. The NE edge is less prominent than the NW edge and we also tested a single power-law model. The resulting χ^2/dof of the fits are 0.99 and 1.80 with the broken power-law and the single power-law, respectively, thus we rejected the latter case.

The nature of the edges can be investigated by the sign of the jump in temperature. Therefore, we extracted the spectra in inner (downstream) and outer (upstream) sectors, with respect to the radii of the jumps (see Fig. 8.10, bottom). We did not find clear indications of temperature discontinuities: we obtained $kT_{\rm in,NE} = 9.8^{+0.9}_{-0.9}$ keV and $kT_{\rm out,NE} = 10.7^{+1.5}_{-1.1}$ keV for the NE edge, and $kT_{\rm in,NW} = 9.0^{+1.0}_{-0.8}$ keV and $kT_{\rm out,NW} = 11.8^{+2.3}_{-3.1}$ keV for the NW edge (see Table 7.4).

Under the assumption of a shock moving outwards from the cluster centre, the Hugoniot-Rankine density jump condition for a mono-atomic thermal gas can be used to compute the corresponding Mach number

$$\mathcal{M} = \sqrt{\frac{3C}{4 - C}}. \tag{7.5}$$

The associated temperature jump is given by:

$$\frac{T_{\rm in}}{T_{\rm out}} = \frac{5\mathcal{M}^4 + 14\mathcal{M}^2 - 3}{16\mathcal{M}^2}. \tag{7.6}$$

Eq. 7.5 provides Mach numbers of $\mathcal{M}_{\rm NE} = 1.26 \pm 0.08$ and $\mathcal{M}_{\rm NW} = 1.36 \pm 0.08$, implying temperature jumps of $(T_{\rm in}/T_{\rm out})_{\rm NE} = 1.25 \pm 0.07$ and $(T_{\rm in}/T_{\rm out})_{\rm NW} = 1.35 \pm 0.08$. In the most favourable scenario, by assuming the upper limits for the downstream temperatures (i.e. $kT_{\rm in,NE} = 10.7$ keV and $kT_{\rm in,NW} = 10.0$ keV), the corresponding upstream temperatures from Eq. 7.6 would result in $kT_{\rm out,NE} = 8.6 \pm 0.5$ keV and $kT_{\rm out,NW} = 7.4 \pm 0.4$ keV. We fixed these temperatures and re-fitted the spectra, but the Cstat increases ($\Delta{\rm Cstat}_{\rm NE} = 1.9$, $\Delta{\rm Cstat}_{\rm NW} = 4.4$). Lower downstream temperatures would result in even worse fit, thus we conclude that the edges are unlikely to be shock fronts.

The two discontinuities may be associated with cold fronts. The N-NE edge revealed by Ogrean et al. (2016) was classified as a candidate cold front, which would be one of the most distant cold fronts to date, if confirmed. This N-NE edge is roughly located in the middle between the NE and NW edges we found and has a compression factor consistent with ours. Even though GGM filtering is efficient in separating the discontinuities, the low photon counts of the source in the upstream sectors do not allow us to confirm whether the NE and NW can be considered a single or double edge; in this regard, projection effects may play an important role. That said, we note that the temperature map in Fig. 7.3 suggests similarities with the prototypical case of Abell 3667 (Owers et al. 2009; Ichinohe et al. 2017), where the coolest gas of the system is pushed at the tip of the cold front surrounded by the hotter gas. This interpretation would be in line with the merger scenario described by Golovich et al. (2016) between sub-cluster 1 and sub-cluster 2.

7.3.3 Radio maps and properties

In the left panel of Fig. 7.5 we present our 144 MHz LOFAR map at $10'' \times 6''$ resolution, while the right panel reports the 1.5 GHz JVLA map at $5'' \times 4''$ resolution obtained by combining the data in B, C, and D arrays. These high-resolution images show the presence of several compact and extended sources.

The bright elongated sources in the south-east ('J') and west ('L') are the relic and the candidate relic, respectively, as reported by Bonafede et al. (2012); these sources are well recovered at both frequencies. As mentioned, the source 'L' has been recently reclassified as a radio galaxy (Giovannini et al. 2020). This is further confirmed by means of our deeper JVLA data: the bottom right panel of Fig. 7.5 focusses on the source 'L' and unambiguously indicates that it is a radio galaxy that has a well-resolved core and jets, no hotspots, and has a FRI (Fanaroff & Riley 1974) morphology. We measured a flux density of $S_{144} = 63.8 \pm 6.4$ mJy, $S_{323} = 39.9 \pm 4.1$ mJy, and $S_{1500} = 17.2 \pm 0.9$ mJy at 144, 323, and 1500 MHz, respectively. We fitted these values with a single power-law, obtaining a spectral index $\alpha_{144}^{1500} = 0.56 \pm 0.01$ between 144 and 1500 MHz, which is consistent with the typical spectra of radio galaxies. We note that the flux density measured by Giovannini et al. (2020) at 1.5 GHz is significantly lower (by a factor ~ 2); their maps are shallower (the RMS is ~ 2 times higher) than ours and allow these authors to recover

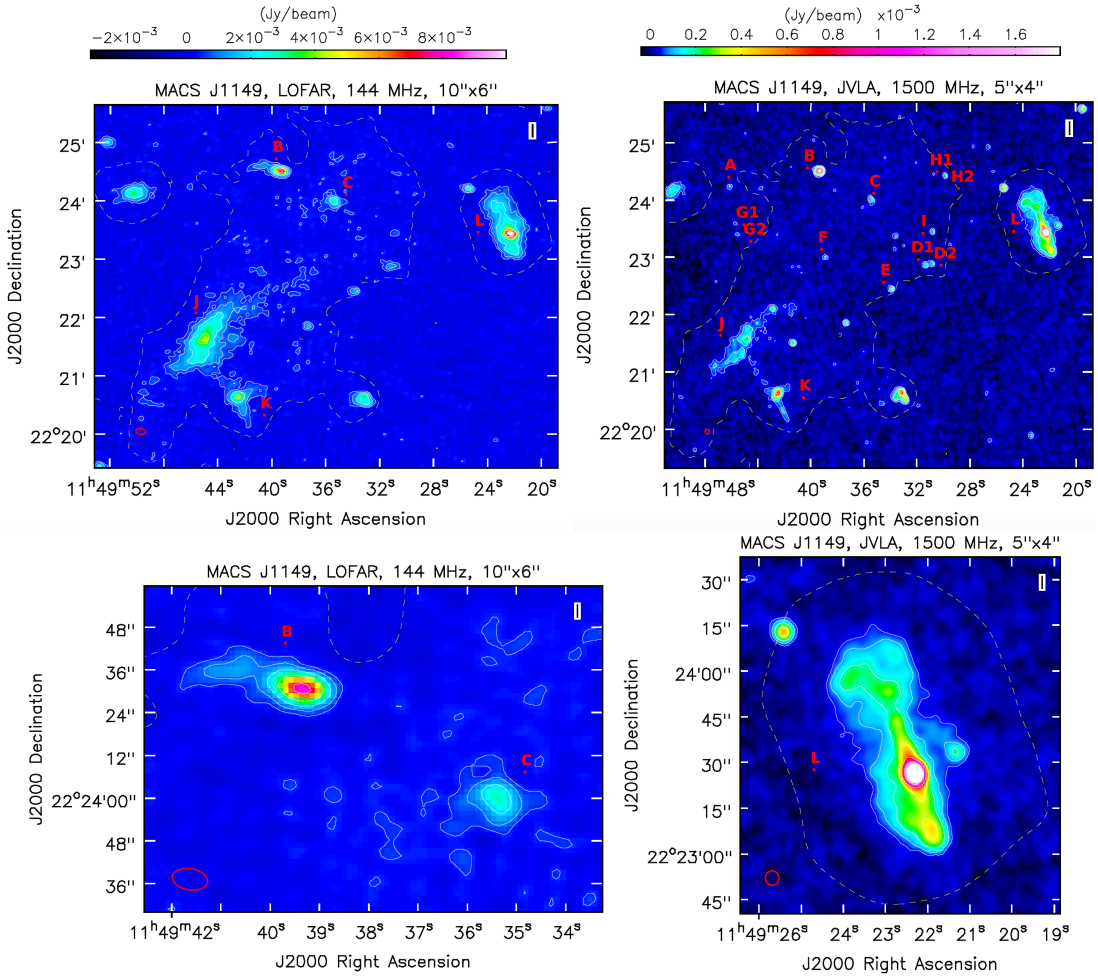

Figure 7.5: MACS J1149 radio maps at high resolution. In all the panels, the white contour levels are $[\pm 3,\ 6,\ 12, ...] \times \sigma$. The dashed yellow contour indicates the 3σ (with $\sigma \sim 0.30$ mJy beam^{-1}) level of the $30'' \times 30''$ resolution LOFAR map after the subtraction of the embedded sources (see also Fig. 7.6). *Top left*: 144 MHz LOFAR map at $10'' \times 6''$ resolution ($P.A. = 81^{o}$, $\sigma \sim 0.15$ mJy beam^{-1}). The western source 'L' has recently been reclassified as a radio galaxy. The SE relic is labelled as 'J' and a bridge-like structure links it to the source 'K'. *Top right*: 1.5 GHz JVLA (B, C, D arrays combined) map at $5'' \times 4''$ resolution ($P.A. = 16^{o}$, $\sigma \sim 18$ μJy beam^{-1}) showing the discrete sources embedded in the radio halo. *Bottom left*: Zoom of the above LOFAR image on the two extended sources 'B' (head-tail radio galaxy) and 'C'. *Bottom right*: Zoom of the above JVLA image on the radio galaxy 'L' showing its FRI morphology.

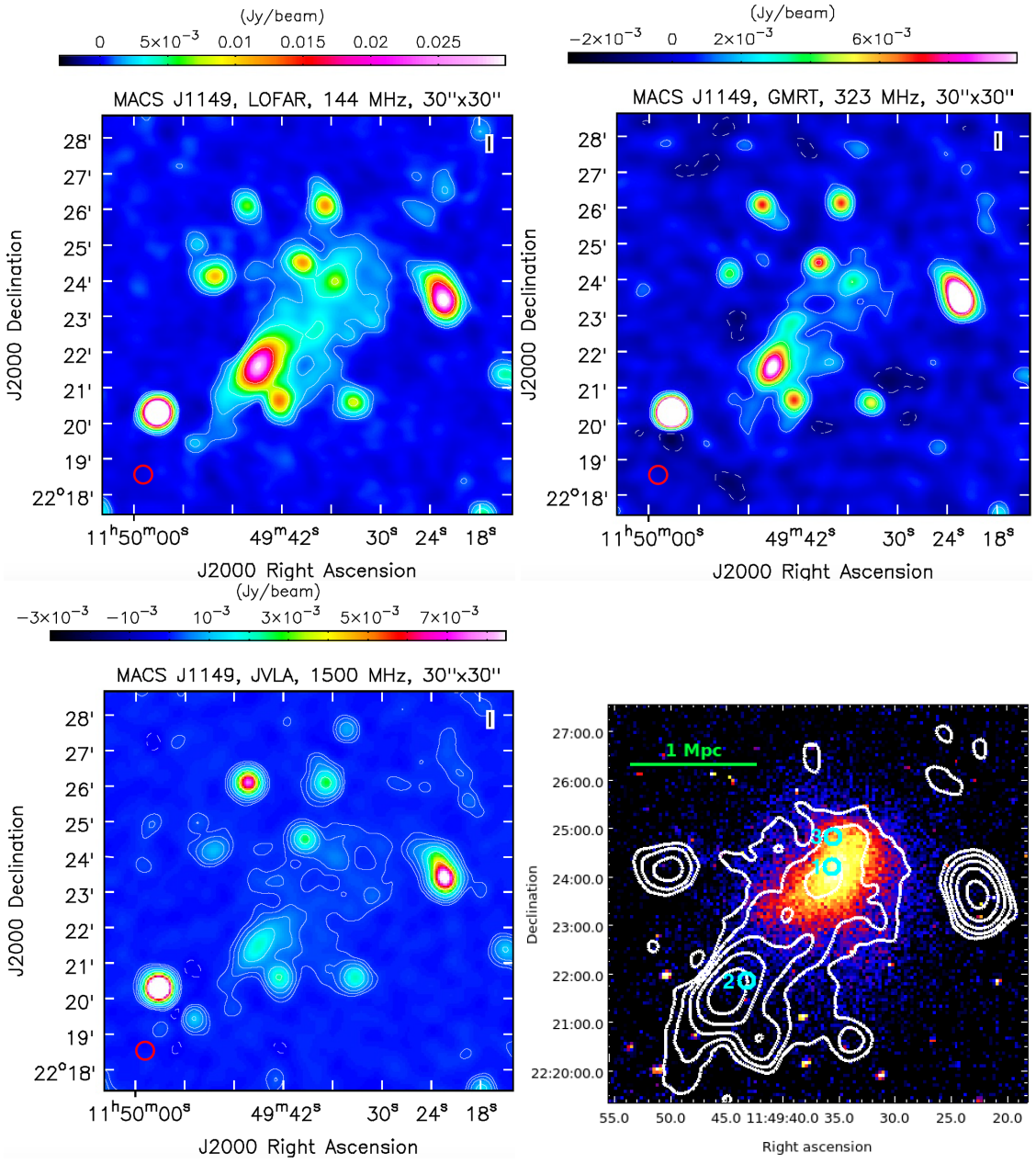

Figure 7.6: MACS J1149 radio maps at 30″×30″ resolution. In all the panels, the contour levels are $[\pm 3,\ 6,\ 12, ...] \times \sigma$. *Top left*: 144 MHz LOFAR map ($\sigma \sim 0.30$ mJy beam^{-1}). *Top right*: 323 MHz GMRT map ($\sigma \sim 0.30$ mJy beam^{-1}). *Bottom left*: 1.5 GHz JVLA (D array) map ($\sigma \sim 45$ μJy beam^{-1}). *Bottom right*: 144 MHz LOFAR contours (after the subtraction of the embedded sources) overlaid on the X-ray image of Fig. 7.1.

Table 7.5: Flux density at 144, 323, and 1500 MHz of the sources shown in Figs. 7.5 and 7.6

Source	S_{144} (mJy)	S_{323} (mJy)	S_{1500} (mJy)
Halo	65.8 ± 7.1	19.4 ± 3.1	2.0 ± 0.5
A			0.15 ± 0.01
B	16.6 ± 1.7	8.1 ± 0.8	3.1 ± 0.2
C	4.1 ± 0.4	3.2 ± 0.3	1.1 ± 0.1
D1+D2	2.9 ± 0.3	0.8 ± 0.1	0.38 ± 0.02
E		0.7 ± 0.1	0.28 ± 0.01
F			0.19 ± 0.01
G1+G2			0.52 ± 0.03
H1+H2			0.31 ± 0.02
I	0.7 ± 0.1		0.16 ± 0.01
L	63.8 ± 6.4	39.9 ± 4.1	17.1 ± 0.9

Notes. Sources D1 and D2 are unresolved at 144, 323, and 1500 (D array) MHz. Sources G1, G2, H1, and H2 are unresolved at 1500 (D array) MHz. Missing values mean that the source is undetected at 3σ level.

only the brightest inner emission of the source (roughly corresponding to the 12σ level in the bottom right panel of Fig. 7.5).

The halo emission is not clearly detected at the 3σ level, owing to its low surface brightness and the high resolution of the images. There are two extended sources, 'B' and 'C', highlighted in the bottom left panel. An accurate description of the SE relic 'J' is beyond the scope of this work, however we notice that the source 'K' at its SW appears to be partially embedded in diffuse emission and shows an interesting bridge-like structure linking 'K' with the SE relic. As a result of their shallower data, this bridge is not detected by Giovannini et al. (2020). It is not clear whether this diffuse emission belongs to the relic or the source itself. As discussed by Giovannini et al. (2020), the orientation of 'J' is expected to be perpendicular to the merger axis if it is a relic induced by the merger shock. Therefore, they proposed that 'J' might be a radio filament associated with the merger and not a relic.

Fig. 7.6 shows the $30'' \times 30''$ resolution maps at 144 MHz (top left), 323 MHz (top right), and 1.5 GHz (bottom left), which we used to consistently measure the flux density of the halo. For the first time, we have deep radio maps of the halo at high and low frequencies and a more reliable measure of the spectrum can be performed. In all these images, the diffuse emission extends up to $\sim 400''$ (~ 2.6 Mpc) along the NW-SE direction, even though it is fully recovered at 144 MHz only. The morphology of the halo emission is similar at 144 MHz, 323 MHz, and 1.5 GHz. It has a projected NW-SE length of $\sim 200''$ (~ 1.3 Mpc) and is interconnected with the relic. In the bottom right panel of Fig. 7.6 we overlay the LOFAR contours (after the subtraction of the sources embedded in the halo) on the X-ray image of Fig. 7.1. The radio emission of the halo is co-spatial with the X-ray emission of the ICM, as typically observed in galaxy clusters.

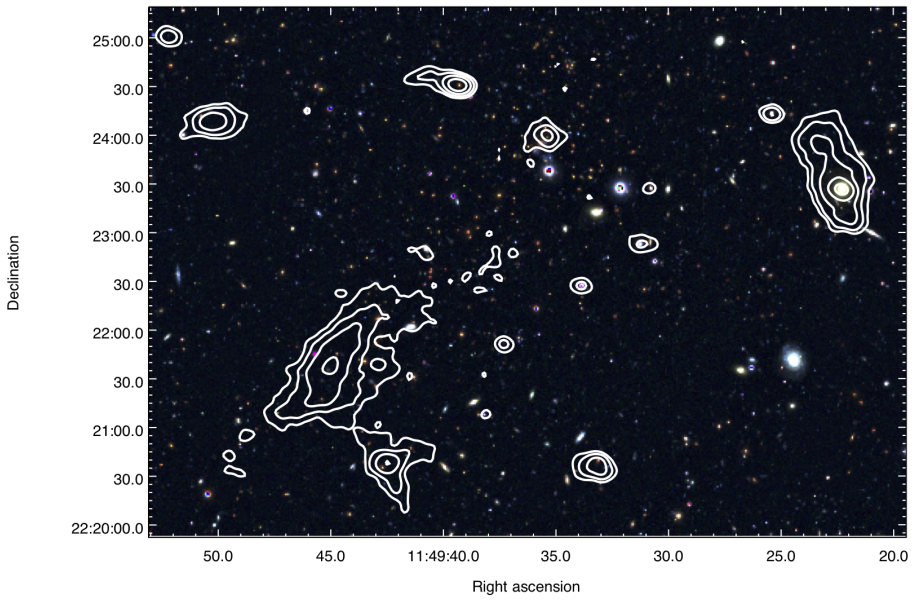

Figure 7.7: Japanese Virtual Observatory Subaru (RVB filters) image of MACS J1149. The contours of the 144 MHz LOFAR map ($10'' \times 6''$, *P.A.* = 81°) shown in Fig. 7.5 are shown in white.

A number of compact sources, labelled in Fig. 7.5, and the above-mentioned 'B' and 'C' sources are embedded within the halo. In particular, source 'B' at 144 MHz apparently has a head-tail morphology; the tail is barely visible above 323 MHz. Source 'C' lies in the centre of the halo and appears extended. In Fig. 7.7 we overlay the high-resolution LOFAR contours on the RVB-filters image of the cluster obtained with Subaru/Suprime-Cam (Miyazaki et al. 2002). This image suggests a possible association of the source 'C' with a cluster member galaxy (coordinates $\mathrm{RA_{J2000}}$ $11^h49^m35.51^s$, $\mathrm{Dec_{J2000}}$ $22^o24'03.76''$).

As discussed in Sect. 7.2.5, the approaches of subtracting the visibilities and the flux densities of the sources are consistent in the LOFAR and GMRT datasets. However, given the very low flux density of the halo at 1500 MHz, small errors in the subtraction may bias it high, and given the JVLA image properties we have more confidence in the algebraic subtraction. Table 8.4 summarises the net flux density of the halo and the embedded sources (we also report the source 'L'). The obtained values of the halo within the 3σ LOFAR contours (avoiding contamination of the regions nearby the relic[3]) are S_{144} = 65.8 ± 7.1 mJy, S_{323} = 19.4 ± 3.1 mJy, and S_{1500} = 2.0 ± 0.5 mJy, respectively. The resulting spectrum across 144 and 1500 MHz is reported in Fig. 7.8. We fitted the flux density values with a single power-law, obtaining a spectral index of $\alpha_{144}^{1500} = 1.49 \pm 0.12$. We iterated the measures in different regions of the halo (in particular, within the brightest X-ray counterpart; see Fig. 7.6, bottom right), consistently finding an average $\alpha \sim 1.5$ everywhere and thus confirming that MACS J1149 is a steep spectrum radio halo. We

[3]The flux density of the halo was measured in a region that roughly corresponds to that sampled with red boxes in Fig. 7.10, right panel.

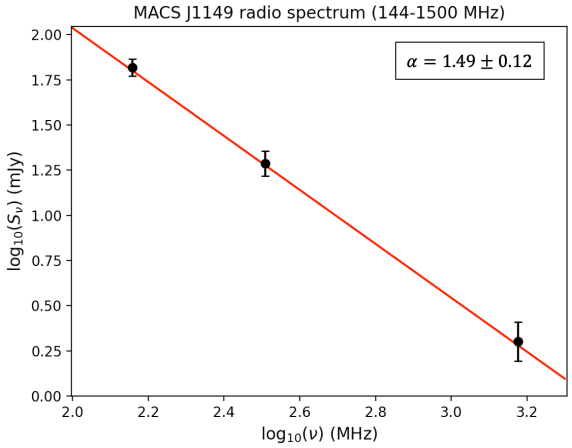

Figure 7.8: Radio spectrum of the halo between 144 and 1500 MHz (see Table 8.4). The solid line indicates the fitted power-law. The resulting spectral index is $\alpha_{144}^{1500} = 1.49 \pm 0.12$.

note that Bonafede et al. (2012) measure $S_{323} = 29 \pm 4$ mJy and $S_{1500} = 1.2 \pm 0.5$ mJy ($\alpha_{323}^{1500} = 2.1$), whereas Giovannini et al. (2020) obtained $S_{1500} = 0.9 \pm 0.1$ mJy. The inconsistency of these values with our measure at 1.5 GHz derives from the fact that our observations includes D array data that are deeper and more sensitive to the extended emission, thus allowing us to properly recover the emission of the halo at high frequency and providing a more reliable measure of the total flux density; the higher flux density at 323 MHz reported by Bonafede et al. (2012) is likely due to the different adopted weighting scheme and a larger considered area that might be contaminated by the SE relic.

By using the flux density and the fitted spectral index, we computed the corresponding radio powers as $P_\nu = 4\pi D_L^2 S_\nu (1+z)^{\alpha-1}$. We obtained $P_{144} = (9.3 \pm 1.0) \times 10^{25}$ W Hz^{-1}, $P_{323} = (2.7 \pm 0.5) \times 10^{25}$ W Hz^{-1}, and $P_{1500} = (2.8 \pm 0.7) \times 10^{24}$ W Hz^{-1}, at 144, 323, and 1500 MHz, respectively. Radio halos with steep spectrum are found to be radio underluminous with respect to the correlation reported by Cassano et al. (2013) between the 1.4 GHz radio power and mass of the host cluster. By extrapolating from the radio spectrum, the flux density at 1.4 GHz results $S_{1400} = 2.2 \pm 0.6$ mJy, and we calculated a power of $P_{1400} = (3.1 \pm 0.9) \times 10^{24}$ W Hz^{-1}. Indeed, MACS J1149 as well falls below this correlation by a factor of ~ 3, as shown with a red dot in Fig. 7.9.

7.3.4 Thermal-non-thermal correlation

As typically found in radio halos, the non-thermal emission in MACS J1149 roughly follows the thermal emission (Fig. 7.6, bottom right). The left panel of Fig. 7.10 shows the radio (I_R), and X-ray (I_X) surface brightness radial profiles, extracted in circular beam-size annuli and normalised at their respective maxima; we used the LOFAR image at $19'' \times 15''$ resolution. We note that I_R decreases with the radius slower than I_X.

A point-to-point correlation of the type of $I_R \propto I_X^k$ between the radio and X-ray surface brightness is found for a number of radio halos (e.g. Feretti et al. 2001; Govoni et al.

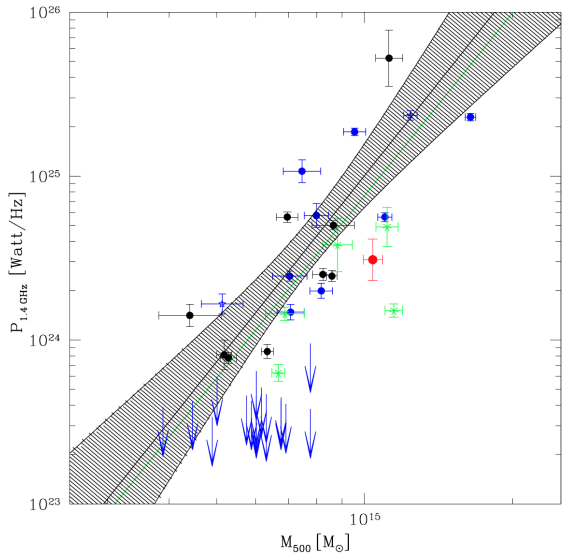

Figure 7.9: Distribution of galaxy clusters in the P_{1400}-M_{500} plane (adapted from Cassano et al. 2013, see it for details of the legend). MACS J1149 (red dot) has $M_{500} = (10.4 \pm 0.5) \times 10^{14}$ $M_\odot$ and $P_{1400} = (3.1 \pm 0.9) \times 10^{24}$ W Hz^{-1}; it is is under-luminous with respect to the correlation by a factor of ~ 3 and is located among the steep spectrum radio halos (green dots).

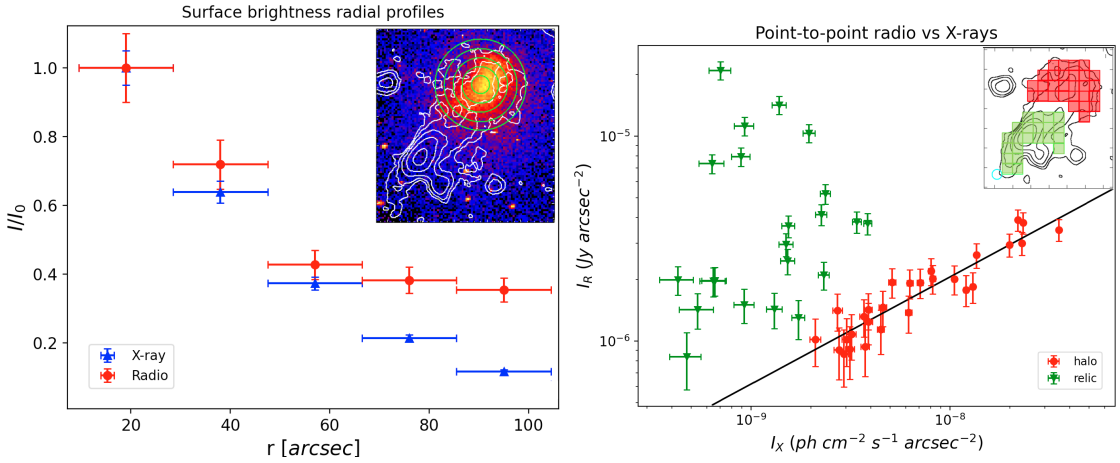

Figure 7.10: *Left*: Radio (red circles) and X-ray (blue triangles) surface brightness radial profiles within the halo region, normalised at their maximum. The source-subtracted LOFAR map at 19″ × 15″ resolution sampled with concentric annuli of 19″ width is shown in the corner. *Right*: Point-to-point analysis of the I_R-I_X relation. In the corner, we report the contours of the 30″ × 30″ source-subtracted LOFAR map, gridded with green and red 30″×30″ square boxes for the relic and halo, respectively. The halo points present a sub-linear correlation with a slope in the range [0.42-0.60]. The black line represents the best fit obtained with the BCES-orthogonal method at 3σ threshold.

Table 7.6: Results from the I_R-I_X point-to-point analysis of the halo. We tested BCES bisector, BCES orthogonal, and linmix methods with various radio thresholds. The obtained slopes k are listed in column 3.

Method	Threshold	k
Bisector	2σ	0.55 ± 0.04
	3σ	0.51 ± 0.04
	4σ	0.46 ± 0.04
Orthogonal	2σ	0.56 ± 0.04
	3σ	0.52 ± 0.04
	4σ	0.48 ± 0.04
Linmix	2σ	0.53 ± 0.05
	3σ	0.51 ± 0.05
	4σ	0.48 ± 0.05

2001; Giacintucci et al. 2005; Hoang et al. 2019; Botteon et al. 2020b; Xie et al. 2020), which have typical sub-linear slopes $k < 1$, meaning that I_R increases slower than I_X. We investigated this relation in MACS J1149 by means of the code described in Ignesti et al. (2020a). The code allows us to sample an extended radio source down to a given threshold in surface brightness by gridding it with square cells. Both I_R and I_X are measured within each cell, then the data are fitted with a power-law and the Pearson (ρ_p) and Spearman (ρ_s) ranks are computed.

The LOFAR source-subtracted map at resolution $30'' \times 30''$ was used to grid both the halo and relic with beam-size cells, as represented in the right panel of Fig. 7.10. The green and red points mark the relic and halo cells, respectively. The plot clearly shows that the halo data follow a tight ($\rho_p = 0.93$, $\rho_s = 0.91$) correlation, whereas the data extracted from the region of the relic are uncorrelated. Halos and the ICM are thought to share a similar volume, whereas the volume occupied by relics is much lower because, at a first approximation, they can be considered as bidimensional sources; therefore a physical correlation is only expected for the halos. Since no correlation seems to exist between the relic and the ICM, this allows us to better discriminate the halo region from that of the relic. Nevertheless, the transition region was excluded to avoid any possible contamination to the fit of the correlation slope.

We explored the correlation strength of the halo through various fitting methods: BCES (Bivariate Correlated Errors and intrinsic Scatter; Akritas & Bershady 1996) bisector and orthogonal, and linmix (Kelly 2007). Moreover, we checked for possible biases due to the choice of the radio brightness threshold. The results are listed in Table 7.6. There is a good agreement among the three methods, but we notice that the fit is sensitive to the adopted threshold, especially in the case of BCES bisector and orthogonal. Even though the values of k are consistent, lower thresholds give steeper indices, as recently discussed in Botteon et al. (2020b). Anyway, we find that the I_R-I_X correlation is strongly sub-linear in MACS J1149, where k is in the range [0.42-0.60].

7.4 Discussion

In this Section, we discuss the formation process of the halo and its connection with the cluster dynamics.

7.4.1 Constraining the hadronic contribution

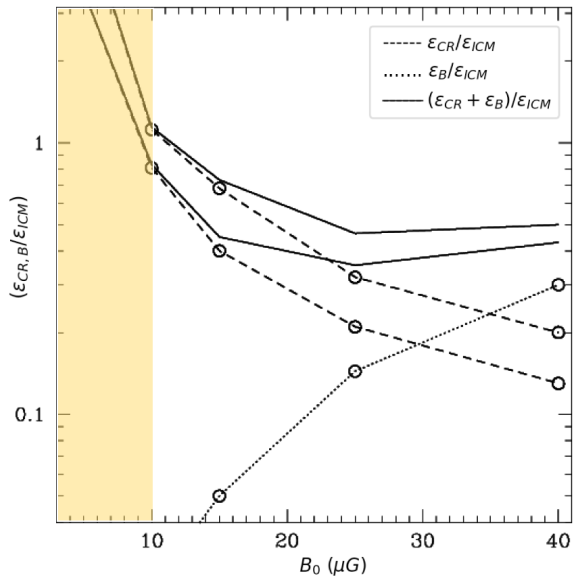

Figure 7.11: Non-thermal to thermal energy budget as a function of the central magnetic field in a pure hadronic model. The dashed, dotted, and solid lines are the CRe to ICM energy ratio, the magnetic to ICM energy ratio, and the total non-thermal to ICM energy ratio, respectively; these are required to match the observed radio emission up to radii of $2.2r_c$ (lower dashed and solid lines) and $2.5r_c$ (upper dashed and solid lines). The non-thermal energy budget for typical values of $B_0 \lesssim 10$ μG in galaxy clusters is indicated by the yellow area. A pure hadronic model would require unrealistically high values of $(\varepsilon_{CR} + \varepsilon_B)/\varepsilon_{ICM}$ and/or B_0.

In general, hadronic scenarios are disfavoured by the observed connection between radio halos and the cluster dynamics (e.g. Brunetti & Jones 2014; van Weeren et al. 2019). In a few cases, the spectral properties of the halos (e.g. Brunetti et al. 2008; Wilber et al. 2018) and the limits to the gamma-ray emission of the hosting clusters (Brunetti et al. 2012, 2017; Zandanel & Ando 2014) provide constraints that are sufficiently stringent to allow pure hadronic models to be excluded. The radio halo in MACS J1149 combines a high redshift with a steep radio spectrum (Fig. 7.8) and a flat radial profile (Fig. 7.10, left), which overall challenge a hadronic origin. In the following, we show that the properties of MACS J1149 allow us to test hadronic models without using complementary constraints from gamma-rays. The theoretical background and assumption adopted in our procedure are reported in Appendix E.

The ratio of CRp and thermal energy budget required to match the observed radio emission assuming a pure hadronic model is shown in Fig. 7.11 as a function of B_0. We also show the ratio of the thermal ($\varepsilon_{\rm ICM}$) and non-thermal ($\varepsilon_{\rm CR} + \varepsilon_{\rm B}$) energy budget, integrated within maximum radii of $2.2r_{\rm c}$ and $2.5r_{\rm c}$, where the halo is clearly visible (see Fig. 7.6). For typical values of $B_0 < 10$ μG in galaxy clusters (e.g. Bonafede et al. 2010), an untenable $\varepsilon_{\rm CR}/\varepsilon_{\rm ICM} > 1$ is required. The CRe energy budget declines with increasing B_0; however the minimum $(\varepsilon_{\rm CR} + \varepsilon_{\rm B})/\varepsilon_{\rm ICM}$ is reached for unusually high values of the magnetic field $B_0 \sim 25$ μG. Moreover, the CRe energy budget is still extremely large ($\sim 40-50\%$). In comparison, the Fermi satellite constrains the CRe energy budget to few percent in Coma and other nearby galaxy clusters (Ackermann et al. 2014; Brunetti et al. 2017).

Under the assumption of a spherical symmetry of the ICM and CRp distribution, the most important parameter is the minimum energy of CRp. If we conservatively assumed $E_{\rm min} = 300$ MeV (i.e. the minimum threshold for CRp-p collisions), $\varepsilon_{\rm CR}$ would result to be 30% smaller than in Fig. 7.11; on the other hand, extending the CRp spectrum at lower energies down to $E_{\rm min} = 20$ keV and $E_{\rm min} = 1$ MeV would boost up $\varepsilon_{\rm CR}$ by a factor of 3.4 and 2.3, respectively. For these reasons, we can rule out an hadronic origin of the halo; by considering $\varepsilon_{\rm CR}/\varepsilon_{\rm ICM}$ to be few percent, CRe would contribute to $< 10\%$ of the halo emission. Nevertheless, we cannot exclude that hadronic collisions still play a role by injecting secondary particles that are eventually re-accelerated by turbulence (Brunetti & Lazarian 2011a; Pinzke et al. 2017).

7.4.2 Merger scenario

Lensing and spectroscopy studies concluded that MACS J1149 consists of at least three main sub-clusters (Smith et al. 2009; Golovich et al. 2016), whose locations are indicated by open circles in Fig. 7.1. Sub-clusters 1 and 2 are the most massive; they have virial masses of $M_1 \sim M_2 \sim 10^{15}$ $M_\odot$, whereas sub-cluster 3 is one order of magnitude less massive $M_3 \sim 10^{14}$ $M_\odot$.

The ICM has a clearly elongated structure along the NW-SE axis and although sub-clusters 1 and 2 have similar masses, only the first is associated with the main X-ray concentration. According to the scenario proposed by Golovich et al. (2016), a major merger between sub-clusters 1 and 2 occurred ~ 1 Gyr ago along the NW-SE direction in the plane of the sky and sub-cluster 2 was stripped of its gas. The two X-ray tails of Fig. 8.10 in the south could be related to this event. Besides the major merger between sub-clusters 1 and 2, a minor merger between sub-clusters 1 and 3 has begun ~ 100 Myr ago, likely along the line of sight (Golovich et al. 2019). Given the high mass ratio, this interaction does not significantly affect the ICM and the major merger dynamics.

In proximity of the N-NE candidate cold front identified by Ogrean et al. (2016), we find instead that there may be two distinct X-ray surface brightness discontinuities in NE and NW, which are possibly cold fronts. However, by referring to the case of Abell 3667 (Owers et al. 2009; Ichinohe et al. 2017), we suggest a simpler scenario in which we are observing a single cold front, where the coolest gas was pushed towards the NW and it is surrounded by hotter gas. Under this assumption, our cold front can likely be explained

with the major merger described above, and its origin could be associated with the cool core of a sub-cluster. However, because of the low count statistics in the upstream regions, at present we cannot disentangle the nature of the discontinuities.

The major merger likely induced the formation of the relic and the halo through shocks and turbulence. Finding that the candidate misaligned W relic is a FRI radio galaxy is in line with this scenario. The steepening of the spectral index of the SE relic towards the centre of the cluster (Bonafede et al. 2012) would also be consistent with this model, however its orientation is peculiar, as it is parallel to the merger axis and not perpendicular, as observed for relic sources. The interaction of a merger shock with remnants or clouds filled by pre-existing relativistic electrons may explain this feature. On the other hand, Giovannini et al. (2020) suggested that the SE source might be a radio filament associated with the halo. Nevertheless, with our data we do not exclude the possibility that the SE source might be a radio galaxy.

Steep spectrum radio halos are predicted as a result of less efficient turbulent acceleration or stronger energy losses (e.g. Brunetti et al. 2008; Cassano et al. 2010b). The former case may result from a less energetic sequence of merger events (e.g. Cassano et al. 2006) or may mark the final evolution phase of energetic mergers where a significant fraction of the turbulence has already been dissipated (Donnert et al. 2013). In both cases, halos are predicted to be under-luminous. The old major merger in MACS J1149 may be in line with the advanced evolution phase scenario, however it is difficult to discriminate between the two possibilities.

7.5 Summary and conclusions

In this work, we constrained the spectrum of the radio halo in the high-redshift ($z = 0.544$) MACS J1149 galaxy cluster, by means of multi-frequency LOFAR, GMRT, and JVLA radio data at 144, 323, and 1500 MHz, and found it to be steep. In addition, we used Chandra X-ray data to compare the thermal and non-thermal emission of the target.

MACS J1149 is a merging system consisting of at least three sub-clusters. The X-ray data analysis showed that the ICM is characterised by a remarkably high temperature ($kT = 10.5 \pm 0.3$ keV) and luminosity ($L^{500}_{[0.1-2.4\,\mathrm{keV}]} = (1.35 \pm 0.01) \times 10^{45}$ erg s^{-1}), and is elongated along the NW-SE axis, where the two most massive sub-clusters lie. Despite its large mass, no X-ray clumps are associated with the SE sub-cluster.

We found two surface brightness discontinuities, which we interpret as evidence of a temperature gradient within a single cold front, where the coolest gas was pushed towards NW. In this case, the cold front may be explained as the cool core remnant of a sub-cluster involved in the major merger occurred ~ 1 Gyr ago. A higher S/N in the upstream regions is required to better constrain the nature of the discontinuities.

We produced radio images at different frequencies and resolutions, showing that the halo is co-spatial with the ICM. The measured flux densities provide a spectral index $\alpha^{1500}_{144} = 1.49 \pm 0.12$ between 144 and 1500 MHz. The computed radio powers of the halo are $P_{144} = (9.3 \pm 1.0) \times 10^{25}$ W Hz^{-1}, $P_{323} = (2.7 \pm 0.4) \times 10^{25}$ W Hz^{-1}, and $P_{1500} = (2.8 \pm 0.7) \times 10^{24}$ W Hz^{-1}. As typical steep spectrum halos, MACS J1149 is

under-luminous (by a factor of $\sim$ 3) with respect to the correlation found by Cassano et al. (2013) between the 1.4 GHz radio power versus the mass of the cluster.

A point-to-point comparison of the radio and X-ray surface brightness showed a tight sub-linear correlation $I_R \propto I_X^k$, which we investigated through various fitting methods and radio thresholds; we consistently found a slope k in the range [0.42-0.60].

Finally, owing to the high redshift of the cluster, the steep spectrum of the halo, and its flat spatial distribution, we were able to test hadronic models without constraints from gamma-ray observations. Our analysis demonstrated that a significant contribution to the halo from pure hadronic collisions is ruled out. In line with previous studies, the old ($\sim$ 1 Gyr ago) major merger between the two most massive sub-clusters likely induced turbulence in the ICM, which accelerated particles and formed the halo. The steep spectrum of the halo may results both from low turbulence in combination with high radiative (inverse Compton) losses or an advanced evolution phase.

In addition, we confirm the recent reclassification proposed by Giovannini et al. (2020) of the W source as a radio galaxy, and in particular we point out its FRI morphology. The peculiar orientation of the SE relic may indicate a different nature of this source and requires a more detailed analysis.

Chapter 8

The puzzling multi-component radio halo in Abell 2142

This is the second Chapter devoted to the analysis of a single target with multifrequency data. We report on our study of the galaxy cluster Abell 2142 (A2142), which is a notably puzzling target exhibiting unusual thermal and non-thermal properties. A number of previous studies at different wavelengths showed that A2142 is neither a typically disturbed major merging cluster, nor a relaxed cool core cluster; nevertheless, it is characterised by an extremely complex dynamics triggered by many minor merger events. Radio observations revealed a peculiar radio halo consisting of two well-distinct components of unclear origin.

Thanks to new deep LOFAR HBA and LOFAR LBA observations of this cluster, we detected a third radio component exhibiting a very steep spectral index. Our discovery makes A2142 a unique science case in the field of diffuse cluster sources, hosting an hybrid radio halo consisting of three components, one of which having an ultra-steep spectrum. By means of complementary radio and X-ray data, we investigate the spectral properties and connection between the thermal and non-thermal emission of each component. Furthermore, the high sensitivity of our LOFAR data allows to search for the presence of a megahalo in A2142, which is one of the most favoured candidate to host a megahalo in a non-major merging system.

This Chapter is based on the following work (in preparation):

- **L. Bruno** et al.; *The puzzling giant, multi-component, ultra-steep spectrum radio halo in Abell 2142*.

8.1 The galaxy cluster Abell 2142

A2142 ($\mathrm{RA_{J2000}} = 15^{\mathrm{h}}58^{\mathrm{m}}20^{\mathrm{s}}$, $\mathrm{Dec_{J2000}} = 27^{\mathrm{o}}14'00''$) is a nearby ($z = 0.0894$, $D_{\mathrm{L}} = 408.6$ Mpc, $1'' = 1.669$ kpc) galaxy cluster of mass $M_{500} = (8.8 \pm 0.2) \times 10^{14}\ M_{\odot}$ within a radius $R_{500} = 14.07 \pm 0.70$ arcmin, corresponding to 1408.5 ± 70.4 kpc at the cluster redshift (Planck Collaboration et al. 2016; Tchernin et al. 2016). It is located in the centre of the homonym A2142 supercluster (Einasto et al. 2015; Gramann et al. 2015), which has an

elongated shape and, in turn, is part of an interacting system with the Corona Borealis supercluster (Pillastrini 2019).

As derived from photometric and spectroscopical optical studies, A2142 consists of $\sim$ 900 confirmed member galaxies within a radius of $\sim$ 3.5 Mpc, which are hierarchically organised in many structures and sub-structures consisting of small groups (Owers et al. 2011; Einasto et al. 2018; Liu et al. 2018). The main and richest structure hosts the primary brightest cluster galaxy 'BCG1', which is located at the centre of the potential well of the cluster (Okabe & Umetsu 2008; Wang & Markevitch 2018). The dynamics of A2142 is extremely complex owing to several ongoing minor mergers, as galaxy groups of $\sim$ 10 members belonging to various sub-structures are infalling towards the cluster centre (e.g. Owers et al. 2011; Eckert et al. 2017; Liu et al. 2018). At a projected distance of $\sim$ 180 kpc from 'BCG1', the secondary brightest cluster galaxy 'BCG2' has a high peculiar velocity (e.g. Oegerle et al. 1995) and is likely the main member of another merging group. Even though the cluster is still accreting through these minor mergers, Einasto et al. (2018) compared the present mass of A2142 and the evolution of simulated cosmic large structures to infer a possible estimate of the epoch of the last major merger; based on this, these authors suggest that the last major merger should have occurred $\gtrsim$ 4 Gyr ago, thus forming the main structure of A2142.

In the X-ray band, the ICM has an elongated morphology along the NW-SE axis, and is aligned with the filamentary structure of the supercluster. The global temperature is $kT \gtrsim 9-10$ keV, but it moderately decreases towards the central regions, where $kT \lesssim 7$ keV (e.g. Henry & Briel 1996). A2142 has morphological and thermodynamical properties intermediate between those of a relaxed cool core and an unrelaxed merging cluster (e.g. Cavagnolo et al. 2009; Rossetti et al. 2013; Tchernin et al. 2016; Cuciti et al. 2021a). Even though an X-ray peak is present as in relaxed clusters, the density and temperature of the ICM derived from its spectrum are not consistent with typical values found for cool cores, therefore A2142 is considered as a rare case of a 'warm' core cluster (Wang & Markevitch 2018).

A2142 hosts the first cold fronts discovered by Chandra (Markevitch et al. 2000). In particular, A2142 exhibits a system of three roughly concentric cold fronts which follow a spiral-like path and are located close to the two BCGs (Markevitch et al. 2000; Markevitch & Vikhlinin 2007; Wang & Markevitch 2018). The X-ray peak of the warm core shows a prominent offset of 30 kpc with respect to the centre of the gravitational potential well of the cluster (Wang & Markevitch 2018). It was suggested that an intermediate mass-ratio merger did not completely disrupt the core, but displaced a large fraction of gas from the minimum of the gravitational potential; this event caused extreme sloshing motions of the cool gas, which then induced the formation of the cold fronts (Rossetti et al. 2013). In this scenario, the spiral pattern of the cold fronts is associated with the development of Kelvin-Helmoltz instabilities (Wang & Markevitch 2018). A further cold front was discovered by XMM-Newton at SE, at a distance of $\sim$ 1 Mpc from the centre (Rossetti et al. 2013). The SE cold front may result from the long-term evolution of the central sloshing, thus indicating that it is a phenomenon able to move large amount of gas from the core up to very large scales (Rossetti et al. 2013).

In the radio band, diffuse synchrotron emission was first detected with the Very Large

Table 8.1: Details of the LOFAR LBA (PI: L. Bruno, project code: LC17_012), LOFAR HBA (pointing name: P239+27 & PI: F. Vazza, project code: LC14_018), GMRT (PI: T. Venturi, project code: 23_017), and VLA (PI: D. Farnsworth, project code: 11B-156) radio data analysed in this work.

Instrument	Band name	Frequency coverage (MHz)	Observation date	On-source time (h)
LOFAR	LBA	30-78	08,17,23-Dec.-2021	16.0
LOFAR	HBA	120-168	15-Sept.-2018; 25,31-Oct.-2020; 13-Nov.-2020	32.0
GMRT	3	307-339	27-Mar.-2013	5.0
$VLA_{[C-array]}$	L	1000-2000	27-Apr.-2012	0.5
$VLA_{[D-array]}$	L	1000-2000	9-Oct.-2011	1.5

Array (VLA) in the central regions of the cluster (Giovannini & Feretti 2000), and then with the Green Bank Telescope (GBT) up to $\sim$ 2 Mpc (Farnsworth et al. 2013). Deep follow-up observations at low frequencies with the Giant Metrewave Radio Telescope (GMRT) allowed Venturi et al. (2017) to classify the diffuse emission as a giant radio halo with two components, which are characterised by different morphological and spectral properties. The most compact, roundish, and brightest component (the 'core', 'H1') is spatially confined by the inner cold fronts, and exhibits a spectral index $\alpha \sim 1.3$ between 118 and 1780 MHz (as typical for radio halos). The faintest, elongated, and largest component (the 'ridge', 'H2') extends up to the SE cold front, and exhibits a steeper $\alpha \sim 1.5$ between 118 and 1780 MHz. The outermost emission revealed by the GBT at 2 Mpc (Farnsworth et al. 2013) is not detected with the GMRT, thus its properties are poorly constrained. Venturi et al. (2017) suggested that both H1 and H2 may trace regions of turbulent particle re-acceleration. In this case, turbulence in H1 would be generated by the dissipation of the kinetic energy of gas sloshing in the core, similarly to the scenario invoked for the formation of mini-halos (e.g. Mazzotta & Giacintucci 2008; Fujita & Ohira 2013; ZuHone et al. 2013); turbulence in the ridge could have been induced by less energetic mergers (including the same intermediate mass-ratio merger likely associated with the origin of core sloshing), or trace the evolution of the central perturbations at larger scales. Alternatively, A2142 could be an hybrid hadronic-leptonic radio halo, in which secondary CRe dominate the emission in H1, whereas the turbulent re-accelerated electrons dominate the emission in H2.

8.2 Observations and data reduction

In this Section we present the data analysed in this work and the corresponding data reduction. The details of the radio data are summarised in Table 8.1, while the details of Chandra X-ray data are summarised in Table 8.3.

8.2.1 LOFAR HBA radio data

A2142 was first observed by LOFAR in September 2018 (pointing P239+27) in the context of LoTSS. Furthermore, given the interest on the target, we obtained additional 16

Table 8.2: Summary of the parameters for LOFAR images discussed in 8.3.1. Col. 1: central frequency (ν). Cols. 2, 3, 4: minimum baseline ($B_{\rm min}$), robust parameter of the Briggs weighting, and Gaussian tapering. Cols. 5, 6: restoring beam (θ), reached noise (σ).

ν (MHz)	$B_{\rm min}$ (λ)	Robust	Taper ($''$)	θ ($'' \times ''$)	σ (mJy beam^{-1})
50	30	−1.0	-	14×10	1.9
50	30	−0.5	15	22×13	1.6
50	30	−0.5	30	44×32	2.7
50	30	−0.5	60	69×63	4.4
143	80	−0.5	-	9×6	0.075
143	80	−0.5	15	21×20	0.16
143	80	−0.5	30	38×35	0.25
143	80	−0.5	60	73×66	0.40
143	50	−0.5	120	128×117	1.0

Table 8.3: Details of the Chandra X-ray data analysed in this work (PI of ObsID 5005: L. van Speybroeck; PI of ObsIDs 15186, 16564, 16565: M. Markevitch.)

ObsID	CCDs	Observation date	Clean time (ks)
5005	S2,I0,I1,I2,I3	13-Apr.-2005	41.5
15186	S1,S2,S3,I2,I3	19-Jan.-2014	82.7
16564	S1,S2,S3,I2,I3	22-Jan.-2014	43.2
16565	S1,S2,S3,I2,I3	24-Jan.-2014	19.5

hours (acquired between October and November 2020) of the KSP guaranteed time to reach a total exposure of 24 hours. The High Band Antennas (HBA) Dutch array operating in the 120-168 MHz frequency range was employed for all the observations, with 23 core stations and 14 remote stations. Data were recorded with an integration time of 1 s and 64 channels (of width 3 kHz each) per sub-band. The source 3C 295 was used as flux density scale calibrator.

All the data were processed together by means of the LOFAR Surveys Key Science Project reduction pipelines (see details in Chapter 3). Astrometric offsets were corrected by aligning the radio sources with their optical counterparts in the Pan-STARRS catalogue. We finally extracted the calibrated *uv*-data corresponding to a square region of sizes $25.8' \times 25.8'$ centred on the target, and performed 8 additional cycles of amplitude and phase self-calibration which improved the quality of our images.

As outlined in Chapter 3, uncertainties in the beam model of LOFAR HBA can introduce offsets in the flux density scale. We therefore aligned the flux density scale with the NVSS catalogue, and derived a median correcting factor of 0.8793 that need to be multiplied by each LOFAR HBA image of the A2142 field.

8.2.2 LOFAR LBA radio data

We proposed and obtained 16 hours of observation with the Low Band Antenna (LBA) in the frequency range 30-78 MHz (PI: L. Bruno, project code: LC17_012). Observations were carried out on December 2021 in `LBA Sparse Even` mode by 24 core stations and 14 remote stations, with two beams simultaneously pointing on the target and on the flux density calibrator 3C 295, respectively. Data were first acquired with an integration time of 1 s and 64 channels (of width 3 kHz each) per sub-band, and then averaged to 4 s and 8 channels per sub-band after excision of Radio Frequency Interference (RFI) and demixing (de Gasperin et al. 2020b).

Calibration was performed by means of the Library for Low-Frequencies (LiLF) pipelines (see Chapter 3). We then applied the extraction technique to our calibrated datasets. Several extraction regions have been tested to maximise the signal-to-noise ratio of our images after the full self-calibration process; the best results were obtained with a circular extraction region of diameter $23'$. We thus performed 4 rounds of amplitude and phase self-calibration.

8.2.3 GMRT radio data

We retrieved archival GMRT observations of A2142 at 305-340 MHz (band-3) for 5 hours on-source, first presented by Venturi et al. (2017). The total bandwidth is 32 MHz (split into 256 channels). The sources 3C286 and 3C48 were used as absolute flux density scale calibrators.

We reprocessed the data by means of the Source Peeling and Atmospheric Modeling (`SPAM`) automated pipeline (Intema et al. 2009), which corrects for ionospheric effects and removes direction-dependent gain errors. Bright sources in the field are used to derive direction-dependent gains and fit a phase-screen over the field of view. Finally, images

are corrected for the system temperature variations between the calibrators and the target. These procedures allowed us to reach a noise level of $\sim$ 40 μJ beam^{-1} at 9″, which is noticeably lower (by a factor $\sim$ 3) than that reached by Venturi et al. (2017), mainly due to an improved calibration of the short baselines.

Additional, yet unpublished, uGMRT band-3 observations are available in the archive: 30 min on-source (PI: D. Vir Lal, project code: 32_084) and 3 hours on-source (PI: D. T. Venturi, project code: 33_052). We split the total bandwidth of 200 MHz into 6 sub-bands, which were then processed independently with `SPAM` and combined again for imaging, as usually done with wide-band uGMRT data. Despite the larger bandwidth, the reached noise level at 11″ is $\sim$ 50 μJ beam^{-1}, and thus worse than the narrow-band data described above. For this reason, we will not employ these uGMRT data in the following analysis.

8.2.4 VLA radio data

We retrieved mosaic (three pointings) VLA observations of A2142 at 1-2 GHz (L-band) in C and D configurations, for 0.5 and 1.5 hours, respectively. The source 3C286 was used as flux density calibrator, whereas J1609+2641 was used as phase calibrator. The data were recorded with 16 spectral windows, each divided into 64 channels.

The data reduction was carried out with the National Radio Astronomy Observatory (NRAO) Common Astronomy Software Applications (`CASA`; McMullin et al. 2007) v. 5.1, by performing standard initial phase, bandpass, and gain calibrations. Due to the usual high Radio Frequency Interference (RFI) in this band, $\sim$ 50% of the bandwidth was flagged. Further rounds of self-calibration were not required. In order to obtain deeper images, we combined the C and D configuration data. We finally split the remaining bandwidth into two datasets of $\sim$ 250 MHz width each, centred on 1380 and 1810 MHz.

8.2.5 Radio imaging and source subtraction

The imaging process was carried out for GMRT and LOFAR datasets with `WSClean` v. 2.10 (Offringa et al. 2014; Offringa & Smirnov 2017), which can account for wide-field, multifrequency, and multiscale synthesis. To properly combine the VLA pointings, we imaged these datasets with `tclean` in `CASA` through mosaic, multifrequency, and multi-scale synthesis.

We produced images by varying the relative weights of baselines through the robust parameter of the Briggs weighting (Briggs 1995) and Gaussian tapering to study the radio emission on different spatial scales. The weighting schemes adopted for the images discussed in the next sections are summarised in Table 8.2.

To accurately measure the flux densities of the diffuse emission, the contribution of the embedded discrete sources needs to be removed. Following Venturi et al. (2017), we first obtained models of the discrete sources by imaging the data at high resolution, excluding baselines < 2kλ, corresponding to maximum recoverable scales of $\sim$ 100″ (i.e. $\sim$ 170 kpc at the cluster redshift). This procedure was carried out with `WSClean` for all the datasets, including the VLA observations, whose pointings were handled separately. Then, the clean components in the model images were subtracted from the *uv*-data. Even

though this process allowed us to remove the majority of the sources, residual artifacts associated with the two extended head-tail radio galaxies are still present; moreover, by decreasing the resolution, very faint residuals from compact sources can also be enhanced and severely contaminate the diffuse emission (see discussion in Chapter 5). Owing to the complexity of the involved sources, the definition of quantitative uncertainties in the flux density measurements due to the subtraction quality at each frequency is not trivial; therefore, here we assume no systematic subtraction errors, but consider regions of the target where discrete sources are absent as much as possible when measuring the flux density (see details in Sect 8.3.2).

By ignoring the subtraction error contribution, uncertainties ΔS on the flux densities are given by:

$$\Delta S = \sqrt{\left(\sigma \cdot \sqrt{N_{\rm beam}}\right)^2 + (\xi_{\rm cal} \cdot S)^2} \tag{8.1}$$

where σ is the RMS noise of the image, $N_{\rm beam}$ is the number of independent beams within the considered region, and $\xi_{\rm cal}$ is the calibration error. We adopted $\xi_{\rm cal} = 10\%$ for LOFAR HBA (Shimwell et al. 2022b) and LBA (de Gasperin et al. 2021), $\xi_{\rm cal} = 6\%$ for GMRT band-3 (Chandra et al. 2004), and $\xi_{\rm cal} = 5\%$ for VLA L-band (Perley & Butler 2013). In the following, position angles (*P.A.*) of radio beams and regions are measured north-eastwards.

8.2.6 Chandra X-ray data

We analysed the archival Chandra X-ray data of A2142 that are summarised in Table 8.3. Observations were carried out in 2005 and 2014, in VFAINT mode, with both ACIS-I and ACIS-S CCDs to recover the full extension of the target. We reprocessed the four observations using `CIAO` v. 4.13, with `CALDB` v. 4.9.4. We extracted light curves in source-free regions to filter out soft proton flares with the `lc-clean` algorithm. This procedure left a total clean time of 186.9 ks.

After correcting each pointing for the corresponding point spread function and exposure map, we combined them to produced a single flux image in the 0.5-2 keV band with the task `mergeobs`. Candidate point sources were identified through the `wavdetect` task; after visual inspection, we ignored spurious sources and subtracted the confirmed ones.

Background event files were obtained through the `blanksky` tool, which re-projects blansky pointings in the direction of our observations, and calculates normalisation factors to match the count rates in the 9-12 keV band (with the parameter `weight_method=particle-rate`). These event files were used as input for `blanksky_image` tool to produce the corresponding background images.

X-ray spectral analyses were carried out with `XSPEC` (Arnaud 1996) v. 12.10.1. It is worth to mention that present releases of `XSPEC` are not able to properly deal with spectra extracted from re-scaled background events produced by `blanksky`. To this aim, we therefore manually re-scaled the exposure time of the re-projected blansky pointings to match the count rates of our observations in the 9-12 keV band.

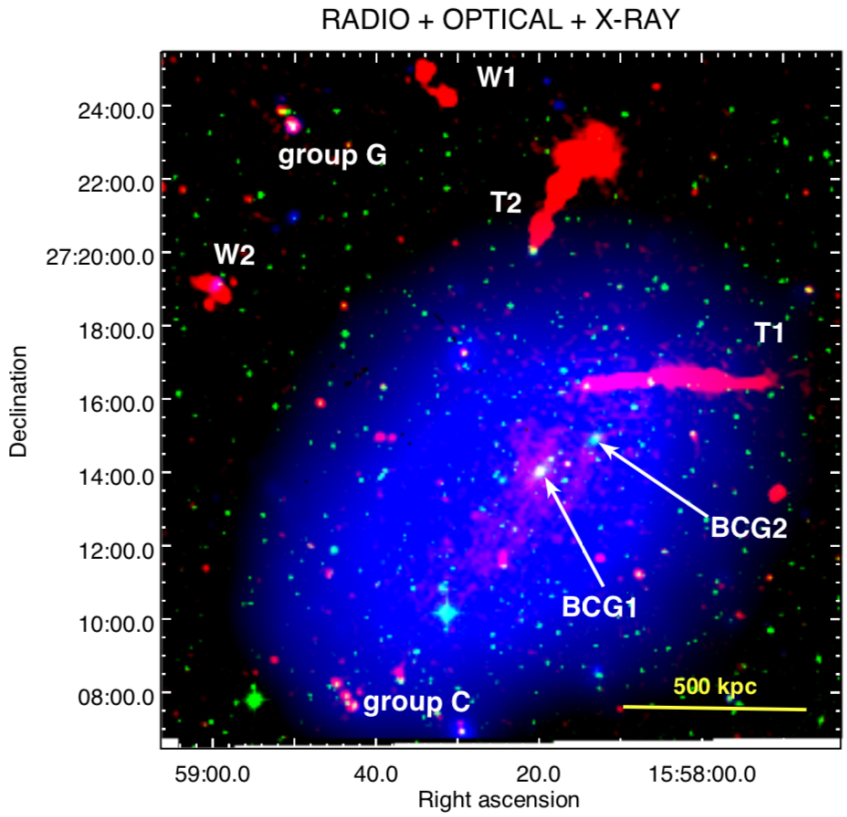

Figure 8.1: Composite RGB image of A2142: radio (GMRT, 323 MHz) in red, optical (DSS-2, red filter) in green, and X-rays (XMM-Newton) in blue. The discrete sources discussed in the text are labelled as in Venturi et al. (2017).

8.2.7 XMM-Newton X-ray data

A2142 was first observed by XMM-Newton in July 2011 (ObsID 0674560201, PI: M. Rossetti), and then followed-up in July 2012 (ObsIDs 0694440101, 0694440501, 0694440601, 0694440201, PI: D. Eckert) as part of the XMM Cluster Outskirts Project (X-COP) to map both the centre and periphery of the cluster. These data consist of a mosaic of five pointings for a total exposure time of 195 ks. We retrieved the final products of these data (count, exposure, background, and background-subtracted flux maps in the 0.7-1.2 keV band) from the public website of the project[1] (see Rossetti et al. 2013; Tchernin et al. 2016, for details on observations and data processing.)

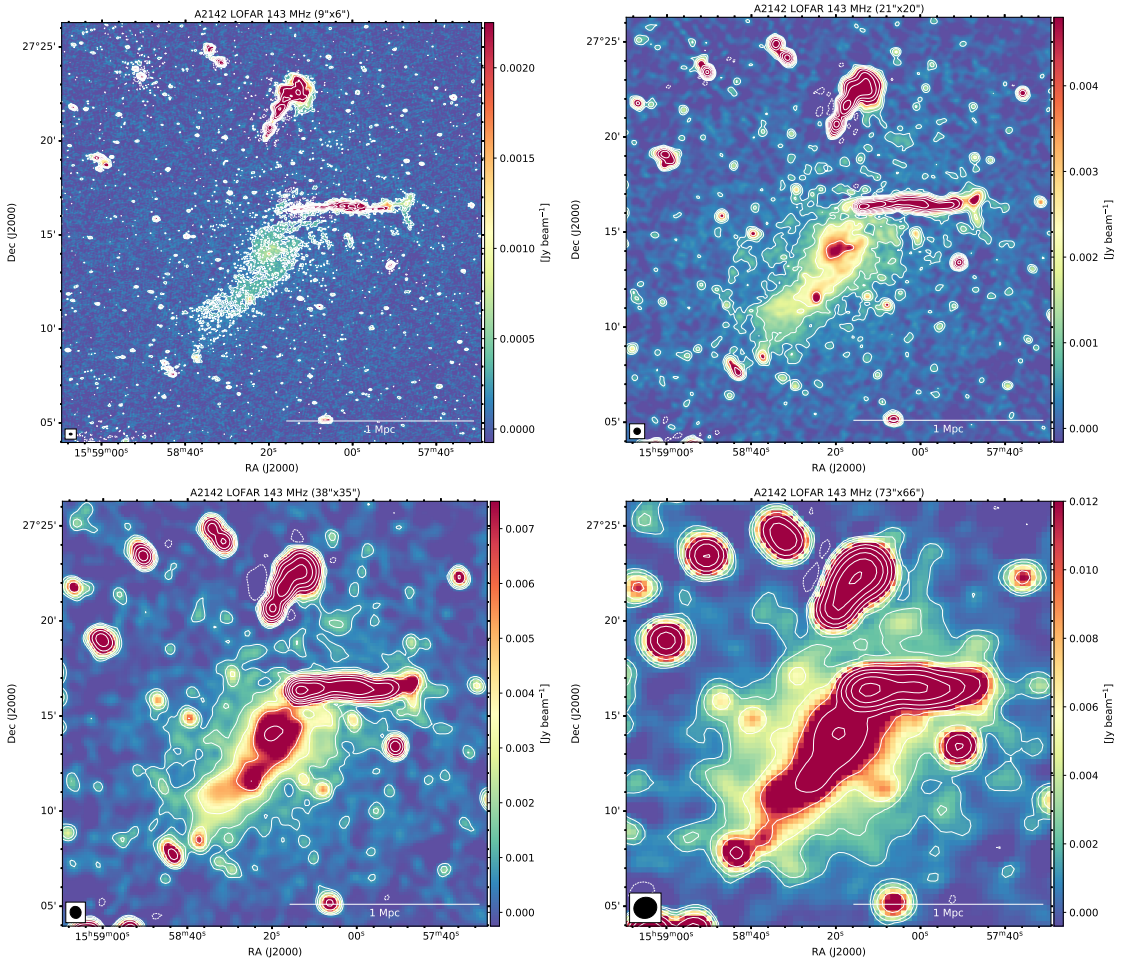

Figure 8.2: A2142 LOFAR HBA radio images at 143 MHz at different resolutions. *Top left*: $9'' \times 6''$ resolution (*P.A.* = 88°, σ = 0.075 mJy beam^{-1}). *Top right*: $21'' \times 20''$ resolution (*P.A.* = 84°, σ = 0.16 mJy beam^{-1}). *Bottom left*: $38'' \times 35''$ resolution (*P.A.* = 16°, σ = 0.25 mJy beam^{-1}). *Bottom right*: $73'' \times 66''$ resolution (*P.A.* = 288°, σ = 0.40 mJy beam^{-1}). In all the panels, the contour levels are $[\pm 3,\ 6,\ 12, ...] \times \sigma$.

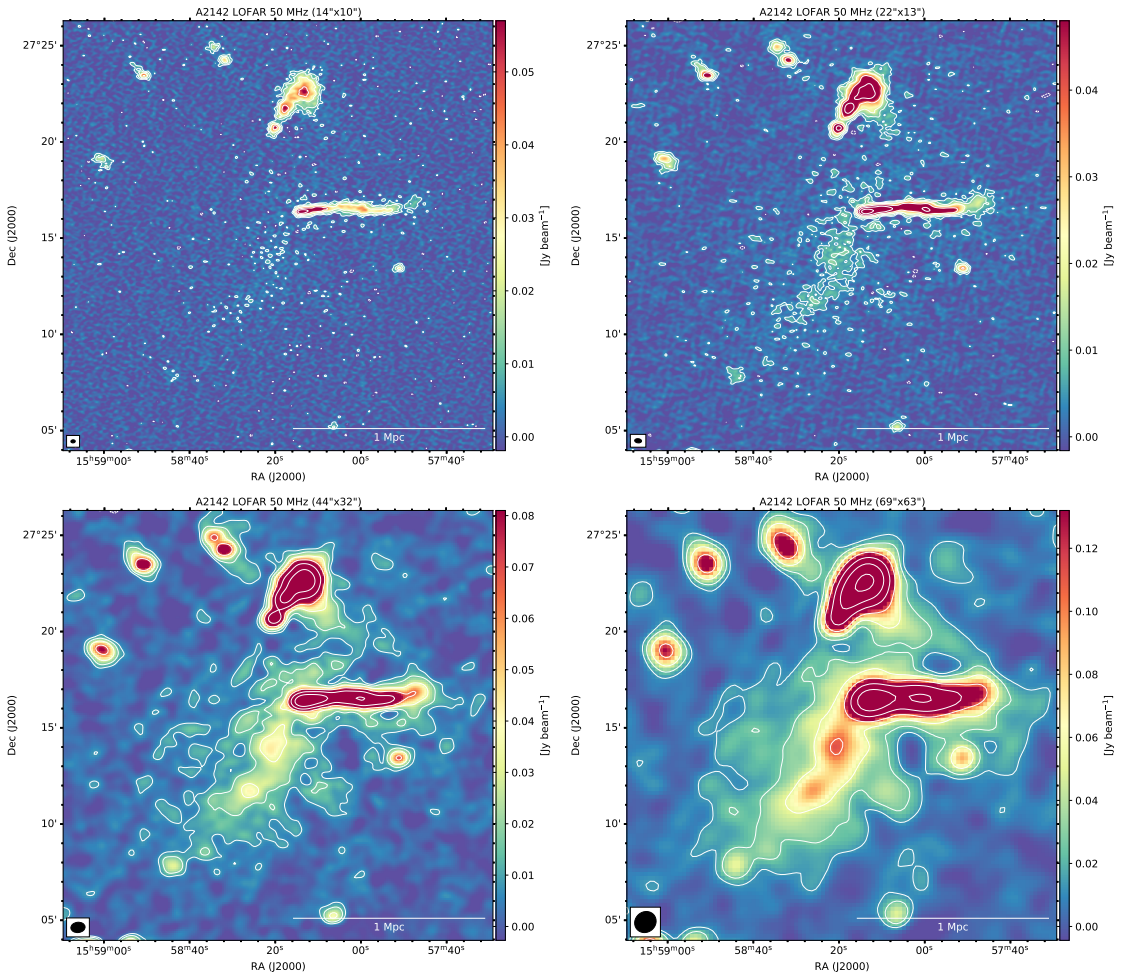

Figure 8.3: A2142 LOFAR LBA radio images at 50 MHz at different resolutions. *Top left*: $14'' \times 10''$ resolution ($P.A.$ = 86°, σ = 1.9 mJy beam^{-1}). *Top right*: $22'' \times 13''$ resolution ($P.A.$ = 84°, σ = 1.6 mJy beam^{-1}). *Bottom left*: $44'' \times 32''$ resolution ($P.A.$ = 84°, σ = 2.7 mJy beam^{-1}). *Bottom right*: $69'' \times 63''$ resolution ($P.A.$ = 50°, σ = 4.4 mJy beam^{-1}). In all the panels, the contour levels are $[\pm 3,\ 6,\ 12, ...] \times \sigma$.

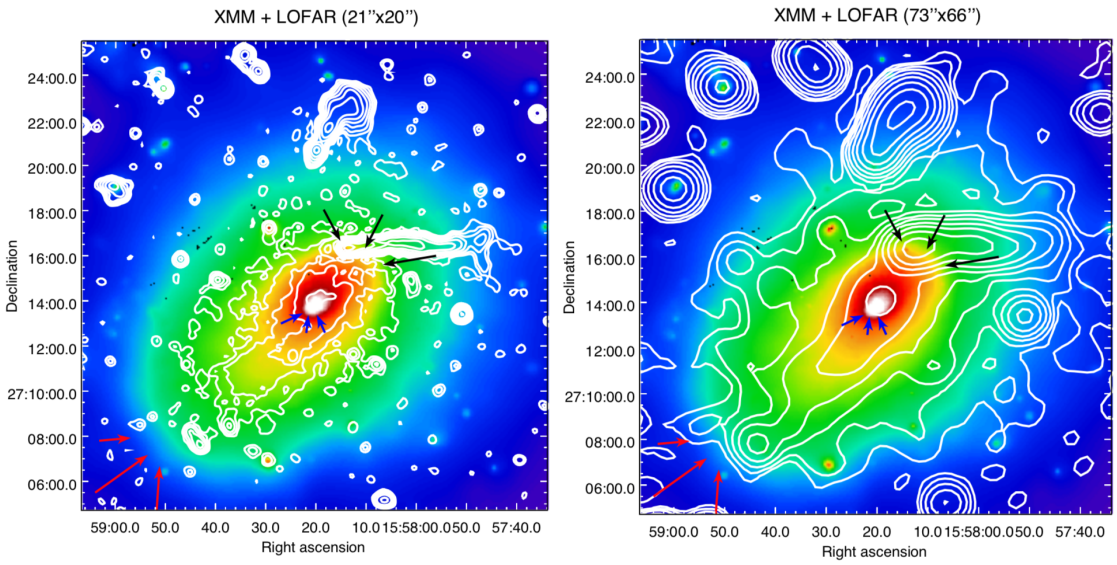

Figure 8.4: A2142 LOFAR HBA radio contours from images in Fig. 8.2 (upper right and lower right panels) overlaid on XMM-Newton X-ray image. The location of the cold fronts are indicated by arrows.

8.3 Results

8.3.1 Radio images

In this Section we present the new LOFAR images of A2142 shown in Figs. 8.2 and 8.3. A2142 hosts a number of compact and extended radio galaxies that were intensively discussed in Venturi et al. (2017). Here we summarise the most interesting sources, which are labelled in the composite radio (GMRT), X-ray (XMM-Newton), and optical (DSS-2) image reported in Fig. 8.1 as in Venturi et al. (2017).

The most spectacular extended radio galaxies are 'T1' and 'T2', two head-tail galaxies. The core (i.e. the head) of T1 is coincident with the NW cold front, and the tail has a projected length of $\sim 5.5'$, corresponding to $\sim$ 550 kpc, if measured from the LOFAR HBA image at the highest resolution ($9'' \times 6''$). The morphology of the tail is not straight and its width is not constant. Additional radio emission is detected, which shows that the tail ends with a thin filament directly connected to a perpendicular arc-shaped structure, extending for $\sim 2'$ ($\sim$ 200 kpc) in the NS direction. The head-tail galaxy T2 is located at a projected distance of $\sim$ 650 kpc from the cluster centre, and extends north-westwards for $\sim 4'$ ($\sim$ 400 kpc) in the highest resolution image. The complex morphology of T2 suggests an interplay with ICM motions. The location of the two BCGs is reported in Fig. 8.1. As mentioned, the primary BCG is coincident with the cluster centre, whereas the secondary one is likely the main member of merging group. Only BCG1 is radio active, hosting a compact radio galaxy. We refer to Venturi et al. (2017) for information on 'W1' and 'W2' (two wide-angle tails which are not cluster members), and galaxy groups 'G'

[1] https://dominiqueeckert.wixsite.com/xcop

Table 8.4: Flux densities of H1, H2, and H3 as derived from the regions shown in Fig. 8.5. Column 8 reports the fitted spectral index.

Source	Region	S_{50} (mJy)	S_{143} (mJy)	S_{323} (mJy)	S_{1380} (mJy)	S_{1810} (mJy)	α
H1	red	266.4 ± 27.6	89.1 ± 8.9	33.6 ± 2.1	7.5 ± 0.4	5.1 ± 0.4	1.09 ± 0.02
H2	blue	414.4 ± 43.0	117.8 ± 11.8	47.5 ± 2.9	-	-	1.16 ± 0.02
H3	green	360.8 ± 41.9	73.7 ± 7.6	27.0 ± 2.5	-	-	1.39 ± 0.08
H3	purple	169.3 ± 29.0	32.5 ± 3.9	-	-	-	$1.57^{+0.27}_{-0.29}$

Notes. The regions defined for H1 and H2 roughly cover their total extensions and flux densities are thus total values. Flux densities of H3 are instead local values. Uncertainties on α are fitting errors, except for the last case where we calculated the upper and lower limits from the measured flux densities.

(in the north-east, see also the X-ray counterpart in Eckert et al. 2017) and 'C' (in the south).

The diffuse components H1 and H2 are visible at 143 MHz at high resolution, whereas they are undetected at the 3σ level in the $14'' \times 10''$ LBA image. With an intermediate resolution ($22'' \times 13''$), the core and the ridge are detected at 50 MHz as well. By decreasing the resolution and increasing the sensitivity to the diffuse emission, further emission is revealed perpendicularly to the ridge, as suggested by Farnsworth et al. (2013) with GBT observations. Here we unambiguously confirm the existence of a third radio halo component, 'H3', which has an elliptical morphology elongated in the NW-SE direction, and embeds the core, the ridge, and the two head-tail galaxies T1 and T2, as shown in the $73'' \times 66''$ and $69'' \times 63''$ images at 143 and 50 MHz, respectively.

In Fig. 8.4, the radio contours of the $21'' \times 20''$ and $73'' \times 66''$ resolution images at 143 MHz are overlaid on the XMM-Newton image of the cluster, with arrows indicating the position of the cold fronts. The core is confined by the southern central cold front, whereas the northern boundary is not clear owing to the presence of T1. The ridge extends along the NW-SE axis, towards the outermost southern cold front. The region in-between the core and the ridge, at south-east of the cold front, shows a depletion of radio emission, which forms a 'bay'-like structure (see e.g. Fig. 8.2, top panels). The bulk of the volume of the ICM is occupied by H3 and its radio emission follows the spatial distribution of the thermal X-ray emission, as typical of giant radio halos, reaching the outermost cold front at south. We measured the maximum extension of H3 by considering the 2σ level of a LOFAR HBA image at resolution $128'' \times 117''$ (not shown); we can approximate its morphology as an ellipse of projected axis lengths of 2.4×2.0 Mpc.

The discovery of H3 makes A2142 a unique science case in the field of diffuse radio sources, potentially hosting a notably large radio halo with three distinct components in a massive galaxy cluster with absence of a clear major merger. In the next sections we will analyse the properties of the radio halo in detail with multi-frequency data to investigate the origins and relative connections of its components.

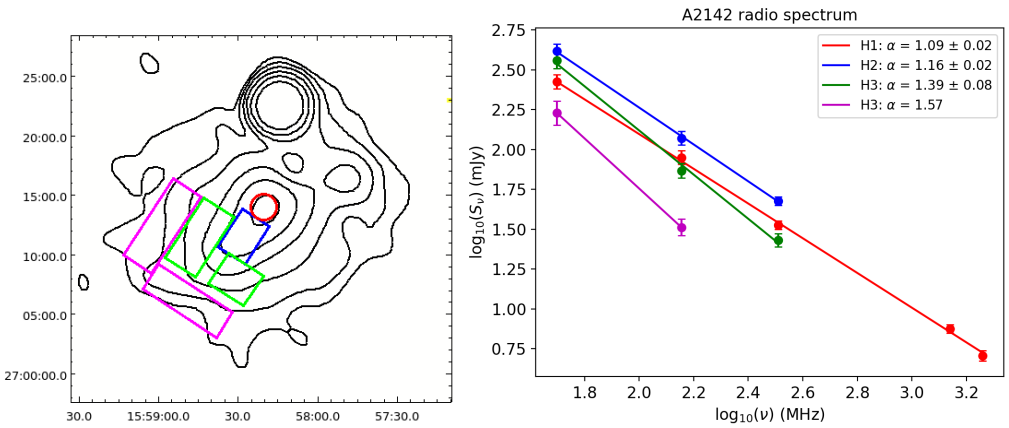

Figure 8.5: *Left*: Regions used to measure the flux densities of H1, H2, and H3 from various images overlaid on the 143 MHz contours ([2, 3, 6, 12, 24, 48]×σ) of the 136″ × 136″ image (see details in the text). *Right*: Radio spectra of H1, H2, H3 fitted with power-laws.

8.3.2 Spectral indices of H1 and H2

The spectral index is a key parameter to probe the mechanisms responsible for the origin of radio halos. Owing to the extremely complex structure of A2142, a straightforward measure of α is not trivial, thus requiring different methods to check for self-consistency of our results. First, to accurately determine the spectral index of the various components, we produced images with common *uv*-ranges that allow us to consistently measure the flux densities and minimise systematics introduced by inhomogeneous *uv*-coverage of the different instruments.

H1. We obtained images at 50, 143, 323, 1380, and 1810 MHz with an *uv*-range of [250λ-15kλ], and then convolved them at the same resolution of 25″ × 25″. This first set of images provides sufficient resolution and sensitivity to measure the flux density of H1. As the northern limit of H1 cannot be easily determined, we considered the core as a sphere centred on BCG1 and confined at south by the inner cold fronts, and thus we measured the flux density in a circle (red circle in Fig. 8.5) of radius $R_{\rm H1}$ = 1.1′ ∼ 110 kpc.

H2. The *uv*-coverage of VLA is much sparser at short spacings than those of LOFAR and GMRT. To avoid flux density losses due to missing short baselines that would bias the spectral index towards steeper values, we excluded the VLA data from the measures in H2. Therefore we produced images at 50, 143, and 323 MHz with a wider *uv*-range of [60λ-18kλ], and by tapering (`taper-gaussian`) the baselines to 15″ (corresponding to 25 kpc). Images were again convolved with a 25″ × 25″ beam as a good compromise between resolution and sensitivity. Similarly to Venturi et al. (2017), we considered a box (blue box in Fig. 8.5) of sides 3.8″ × 2.7″ (corresponding to 380 × 270 kpc) and *P.A.* = 33° that roughly follows the shape of the ridge until it is detected at the 3σ level of each image.

H3. With the same *uv*-range [60λ-18kλ] as above, we obtained images at 50, 143, and

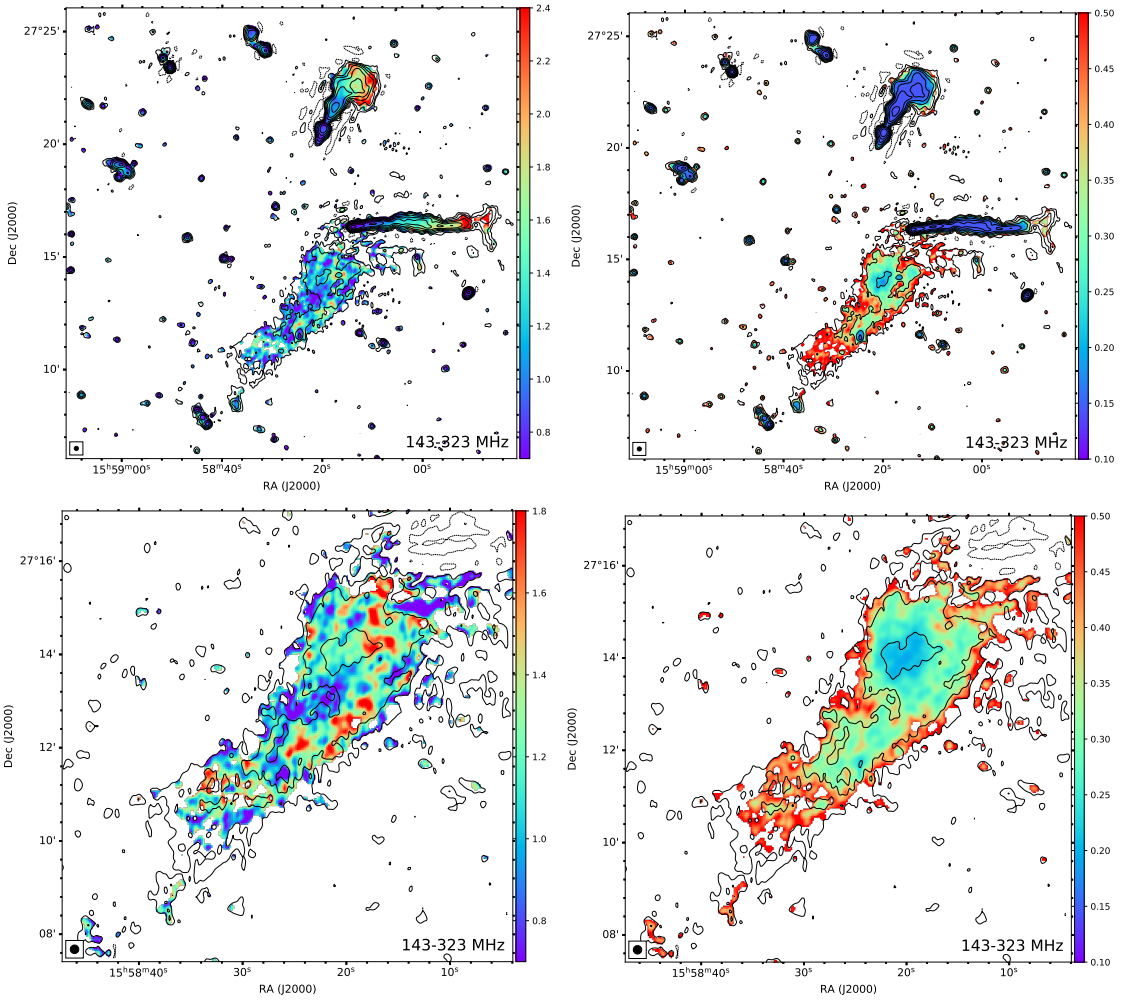

Figure 8.6: A2142 spectral index and associated error maps between 143 and 323 MHz at $11'' \times 11''$ resolution, before (upper panels) and after (lower panels) the subtraction of the discrete sources. LOFAR contours are drawn in black.

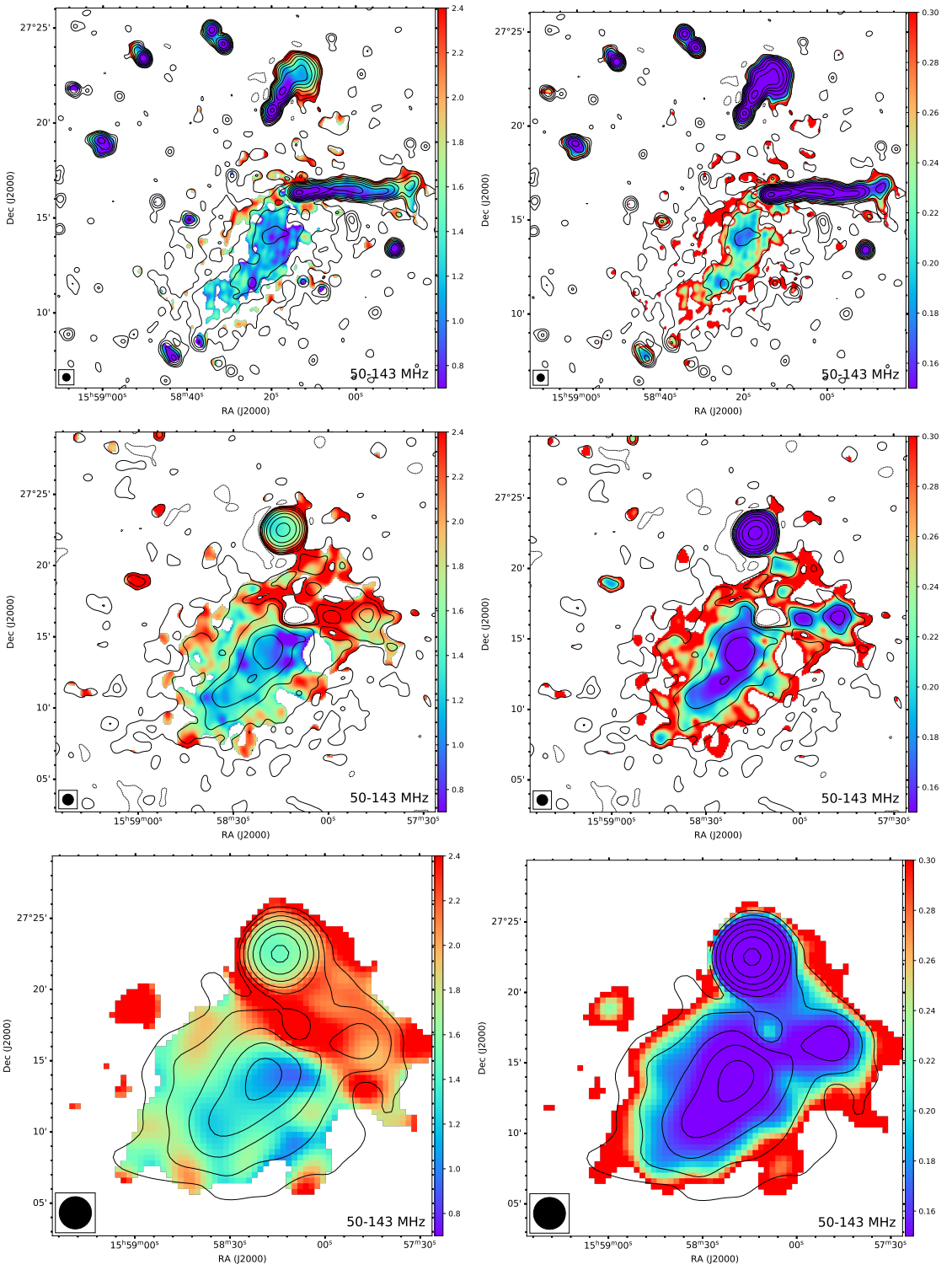

Figure 8.7: A2142 spectral index (left panels) and associated error (right panels) maps between 50 and 143 MHz at various resolutions. *Top*: maps at 24″ × 24″ resolution with discrete sources. *Middle*: maps at 45″ × 45″ resolution after the subtraction of the discrete sources. *Bottom*: maps at 136″ × 136″ resolution after the subtraction of the discrete sources. In all the panels, the corresponding contours at 143 MHz are drawn in black.

323 MHz by tapering the baselines to 60″ (100 kpc), and convolved them at 85″ × 85″. At this low resolution, residuals from the discrete source subtraction are enhanced and have a non-negligible contribution when compared with the faint diffuse emission. In our images, the quality of the subtraction at 50 and 323 is worse than that at 143 MHz, but quantitative estimates cannot be easily obtained, as explained in 8.2.5. Therefore, to avoid as much as possible the contamination from residual of discrete sources, we measured the local flux densities of H3 in two boxes (green boxes in Fig. 8.5) of sides 6′ × 3′ (600 × 300 kpc) and 3.5′ × 3′ (350 × 300 kpc), where the halo is detected at 3σ at each frequency. These images show that only the inner parts of H3 are recovered at 323 MHz due to insufficient noise sensitivity, whereas LOFAR is able to recover a larger region. We thus obtained images at 50 and 143 MHz with an uv-range of [50λ-18kλ], by tapering the baselines to 120″ (200 kpc), and convolved them at 134″ × 134″. Again, we considered two boxes (purple boxes in Fig. 8.5) of sides 7.7′ × 2.8′ (770 × 280 kpc) and 7.4′ × 2.5′ (740 × 250 kpc) free from source contamination, where the halo is detected at the 2σ level of both images.

All the regions defined as above are overlaid on the 134″ × 134″ HBA image of Fig. 8.5. We exploited the measured flux densities reported in Table 8.4 to fit the radio spectra with power-laws, as shown in Fig. 8.5. The fitted spectral indices are $\alpha_{\rm H1}^{[50-1810]} = 1.09 \pm 0.02$ for H1, $\alpha_{\rm H2}^{[50-323]} = 1.16 \pm 0.02$ for H2, $\alpha_{\rm H3}^{[50-323]} = 1.39 \pm 0.08$ in the inner parts of H3, and $\alpha_{\rm H3}^{[50-143]} = 1.57$ in the outer parts of H3. In the latter case, with only two data points, we cannot provide fitting errors; however, by considering the uncertainties ΔS, we can determine the minimum and maximum spectral index, yielding $\alpha = 1.28$ and $\alpha = 1.84$. Even though a uniform $\alpha \sim 1.3$ in H3 is still possible within the errors, it is reasonable to assume that it radially steepens outwards, reaching values $\alpha \gtrsim 1.5$ (see also the derivation of α from the total flux density in Sect. 8.3.3).

Further evidence of the spectral behaviours of H1, H2, and H3 is inferred from the spectral index maps at different spatial resolutions that we obtained with analogous imaging procedures as above. In Fig. 8.6 we reported the spectral index (and associated errors[2]) maps at 11″ × 11″ between 143 and 323 MHz (with and without discrete sources). The spectral index maps between 50 and 143 MHz, at resolutions 24″ × 24″, 46″ × 46″ (source subtracted), and 136″ × 136″ (source subtracted) are shown in Fig. 8.7. The spectral indices inferred from these maps are consistent with the fitted spectra within the errors. In H1 the spectral index is $\alpha \sim 1.1$, and a slight steepening is observed towards H2. Interestingly, the high resolution 143-323 MHz spectral index maps (Fig. 8.6) show a flattening in the region coincident with the radio bay. Outside H2, the spectrum further steepens up to ~ 1.6. In the northern part, unreliable spectral indices $\alpha \gtrsim 2$ are the result of subtraction artifacts from T1 and T2. However, it is plausible that the tails of these galaxies release very old populations of electrons that are then re-accelerated by turbulence, and contribute to the steepest regions of the halo northwards.

We point out that our integrated spectra are flatter than $\alpha \sim 1.3$ and $\alpha \sim 1.5$, as reported by Venturi et al. (2017) for H1 and H2, respectively. For H1, this can be the

[2]Errors are obtained as $\Delta\alpha = \left|\frac{1}{\ln\left(\frac{\nu_1}{\nu_2}\right)}\right| \sqrt{\left(\frac{\Delta S_1}{S_1}\right)^2 + \left(\frac{\Delta S_2}{S_2}\right)^2}$, where ΔS are computed as in Eq. 8.1.

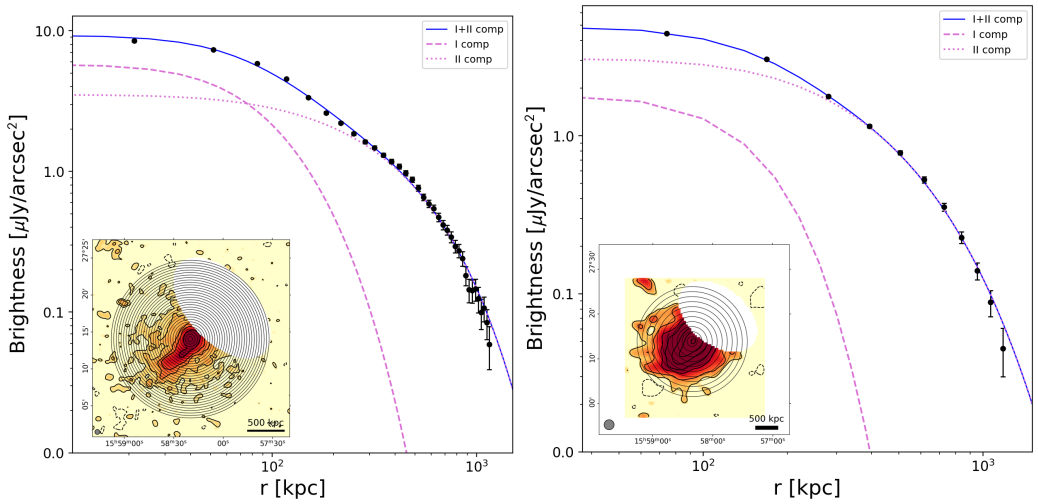

Figure 8.8: Fit of the surface brightness of LOFAR HBA images at $40'' \times 40''$ (left, see inset) and $134'' \times 134''$ (right, see inset) with a double spherically-symmetric exponential model (Eq. 8.3). In both cases, residuals from T1 and T2 were masked and the width of the sampling annuli is half of the beam FWHM.

consequence of the different regions chosen to measure the flux densities: indeed, Venturi et al. (2017) considered a larger box and their measure could have been contaminated by the outer and steeper part of the halo. On the other hand, the regions used for H2 are similar and discrepancies may be a combination of various factors; indeed, we improved the calibration of the GMRT data, have a more accurate LOFAR HBA measure (for instance, uncertainties in Venturi et al. (2017) are $\sim 35\%$ for the LOFAR measure), and considered only the datasets with the densest *uv*-coverage.

8.3.3 Spectral index of H3

In Sect. 8.3.2 we obtained accurate measures of α for H1 and H2, and we found hints about the ultra-steep spectrum of H3. Even though the spectral index maps (Fig. 8.7) confirm the local values inferred from the green and purple boxes in Fig. 8.5, we now aim to determine global flux densities and more accurate α for H3 as well.

As a first approach, we masked the regions of H1, H2, and residuals from subtraction, and then obtained an estimate of the average surface brightness of H3 over an ellipse of 2.4 Mpc $\times$ 2.0 Mpc. By assuming that H3 uniformly fills the masked regions with the same average brightness, we estimated total flux densities of $S_{50} = 3116.6$ mJy and $S_{143} = 628.3$ mJy.

More accurate values can be derived by fitting the surface brightness profile of the halo. Under simple assumptions of spherical symmetry, the surface brightness profile of both mini-halos and radio halos can be typically reproduced by an exponential law (Murgia et al. 2009) as:

$$I(r) = I_0 e^{-\frac{r}{r_e}} \tag{8.2}$$

where I_0 is the central brightness and r_e is the e-folding radius. However, Eq. 8.2 is not

Table 8.5: Results of the outer component in the double exponential fit of Eq. 8.3. Cols. 1, 2: frequency and resolution of the input image. Cols. 3, 4: fitted central surface brightness and e-folding radius. Cols. 5, 6: corresponding flux density ($S_{\rm fit} = 0.8{\times}2\pi I_0 r_{\rm e}^2$) integrated up to $3r_{\rm e,out}$ and error contribution (in percentage) from the fitting uncertainties (see details in the table notes).

ν (MHz)	θ	$I_{0,\rm out}$ (μJy arcsec^{-2})	$r_{\rm e,out}$ (kpc)	$S_{\rm out,fit}$ (mJy)	$\xi_{\rm fit}$ (%)
50	$46'' \times 46''$	19.4 ± 1.1	299.0 ± 11.8	3129.7 ± 628.6	10
50	$132'' \times 132''$	19.5 ± 1.1	304.9 ± 15.5	3271.2 ± 528.3	12
143	$40'' \times 40''$	3.9 ± 0.2	303.8 ± 7.3	649.5 ± 110.6	7
143	$134'' \times 134''$	4.7 ± 0.3	272.2 ± 8.7	628.4 ± 85.0	9

Notes. Errors on the fitted flux density are computed as $\Delta S_{\rm fit} = \sqrt{\left(\sigma \cdot \sqrt{N_{\rm beam}}\right)^2 + (\xi_{\rm cal} \cdot S_{\rm fit})^2 + (\xi_{\rm fit} \cdot S_{\rm fit})^2}$ to include the uncertainties on the fitted parameters; $\xi_{\rm fit}$ is obtained from the standard formula for the error propagation as $\xi_{\rm fit} = \sqrt{\left(\frac{\Delta I_0}{I_0}\right)^2 + 4\left(\frac{\Delta r_{\rm e}}{r_{\rm e}}\right)^2}$.

able to fit the surface brightness of A2142 owing to its complex structure. We can assume that both H1 and H3 have spherical symmetry[3], and that H3 fills a fraction of the volume of H1 and H2. We therefore considered a double exponential function as:

$$I(r) = I_{0,\rm in} e^{-\frac{r}{r_{\rm e,in}}} + I_{0,\rm out} e^{-\frac{r}{r_{\rm e,out}}} \ , \tag{8.3}$$

where the contributions of the inner and outer components are summed.

As shown in the examples in Fig. 8.8 for LOFAR HBA images at $40'' \times 40''$ and $134'' \times 134''$ resolution, the double exponential model can well reproduce the profile of A2142. In Table 8.5 we report the central brightness and e-folding radius for the outer component which we are interested in, i.e. H3. The flux density is computed by integrating the surface brightness in annuli up to a radial distance of $\hat{r} = 3r_{\rm e}$, which typically sets the finite extension of radio halos; this radial cut-off provides the 80% of the flux density obtained by integrating the surface brightness at $\hat{r} = \infty$, thus yielding $S_{\rm fit} = 0.8 \times 2\pi I_0 r_{\rm e}^2$. We found discrepancies in the fitted I_0 and $r_{\rm e}$ at 143 MHz, depending on the input image; this is likely due to the (unmodelled) ridge, which contaminates the fits with different weights. On the other hand, the corresponding flux densities are well in agreement within the errors, and with the rough estimate provided above by considering the elliptical geometry and assuming a uniform distribution of the average brightness, thus confirming the reliability of our approach.

By considering $S_{50} = 3271.2 \pm 528.3$ mJy and $S_{143} = 628.4 \pm 85.0$ mJy, we obtain a global $\alpha_{\rm H3}^{[50-143]} = 1.57 \pm 0.20$, which is perfectly consistent with local values inferred in Sect. 8.3.2. This confirms that H3 has an ultra-steep spectrum.

[3]Even though an ellipsoidal geometry would be more reliable, we do not expect that our assumption introduces significant biases in the fitted parameters, being the minor to major axis length ratio (1.2) relatively small.

Table 8.6: Radio powers of H1, H2, and H3 at 50, 143, 323, 1380, and 1810 MHz from measures reported in Sects. 8.3.2 and 8.3.3. Values marked with '**' and '***' are obtained by extrapolation with $\alpha = 1.16$ and $\alpha = 1.57$, respectively.

Source	P_{50} (10^{24} W Hz^{-1})	P_{143} (10^{24} W Hz^{-1})	P_{323} (10^{23} W Hz^{-1})	P_{1380} (10^{23} W Hz^{-1})	P_{1810} (10^{22} W Hz^{-1})
H1	5.1 ± 0.5	1.7 ± 0.2	6.4 ± 0.4	1.4 ± 0.1	9.7 ± 0.8
H2	7.9 ± 0.8	2.3 ± 0.2	9.1 ± 0.6	1.7 ± 0.2**	12.1 ± 1.4**
H3	64.8 ± 10.5	12.5 ± 1.7***	34.7 ± 7.4***	3.5 ± 1.7***	23.2 ± 12.2***

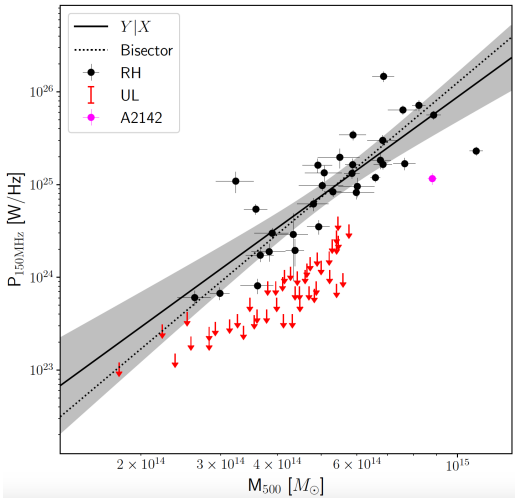

Figure 8.9: Radio power at 150 MHz vs host mass correlation (see Chapter 6). Black dots and red arrows are radio halos and upper limits, respectively, having $0.06 < z < 0.4$ and $100 < r_e < 400$ kpc. A2142 (purple dot) is under-luminous by a factor ~ 3 with respect to the scatter of the correlation, in line with the behaviour of ultra-steep spectrum radio halos.

8.3.4 Radio power

By considering the flux densities and spectral indices of H1, H2, and H3, we computed the corresponding radio powers as $P_\nu = 4\pi D_L^2 S_\nu (1+z)^{\alpha-1}$. These are reported in Table 8.6.

Fig. 8.9 shows the radio power at 150 MHz vs host mass diagram (Chapter 6, Sect. 6.2.2). We scaled P_{143} of H3 to 150 MHz ($P_{150} = (1.2 \pm 0.2) \times 10^{25}$ W Hz^{-1}) and reported it (purple dot) in the diagram. As typical of ultra-steep spectrum radio halos, A2142 is located well below (by a factor of ~ 3) the scatter of the correlation, again confirming the nature of H3 and providing tight constraints on its origin.

8.3.5 Thermal properties and non-thermal emission

In this Section we compare the thermal and non-thermal properties derived from our X-ray and radio data, respectively.

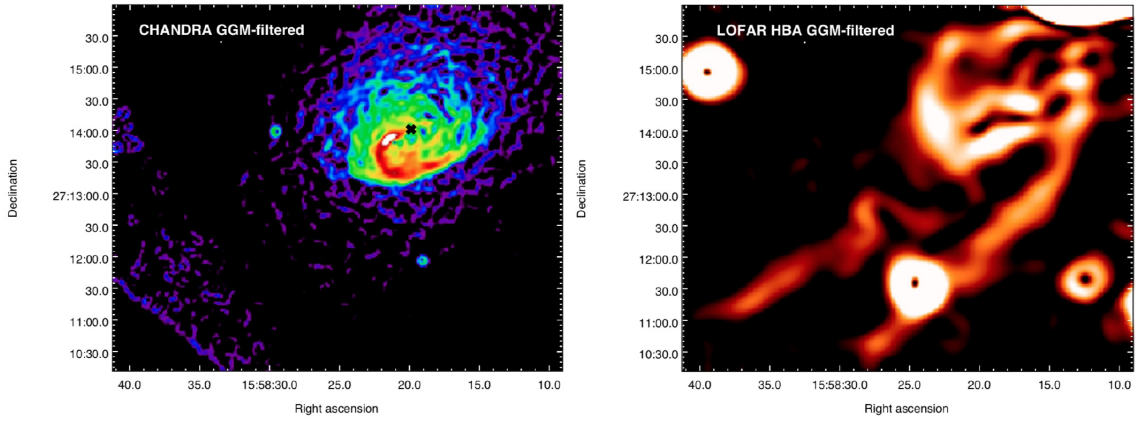

Figure 8.10: GGM-filtered images of A2142. *Left*: Chandra X-ray flux image filtered with $\sigma_{\rm GGM} = 3''$. The black cross marks the location of the BCG. *Right*: LOFAR HBA radio image filtered with $\sigma_{\rm GGM} = 12''$. The radio emission of H1 follows the spiral pattern of the X-ray cold fronts.

To enhance surface brightness discontinuities and sub-structures in the cluster, we applied the Gaussian gradient magnitude (GGM; Sanders et al. 2016b,a) filtering. We assumed $\sigma_{\rm GGM} = 2$ pix and $\sigma_{\rm GGM} = 8$ pix for our Chandra and LOFAR HBA images (where 1 pix = 1.5 arcsec in both cases) as the width of the derivative of the Gaussian filter function. Even though the usage of this technique has been commonly limited to X-ray images, interesting features are highlighted by the GGM-filtering in our radio image as well, as shown in Fig. 8.10. In the left panel, some gas departs from the BCG[4] (black cross) and originates the inner cold fronts following a clear spiral path. This spiral morphology is analogously found for the radio counterpart (right panel), where the brightest spots spatially correspond to the boundaries of the cold fronts. The GGM-filtered radio image also suggests that the ridge may be directly connected with the core, being an extended arm of the spiral, and thus hinting at a common origin of the two radio components. On the other hand, even by filtering the Chandra image with wider $\sigma_{\rm GGM}$, we do not find a corresponding X-ray filamentary emission that could confirm this hypothesis.

By using XMM-Newton X-ray images in different energy bands (see details of this procedure in Rossetti et al. 2007), Rossetti et al. (2013) produced projected entropy maps of A2142, and found that the ridge follows a trail of low-entropy ICM phase. We investigated this trend with Chandra data as well. Through `CONTBIN`[5] (Sanders 2006), we adaptively binned our 0.5-2 keV exposure-corrected image in regions with an high signal-to-noise ratio of SNR = 100. We extracted the spectra in each region of the event and blanksky files, subtracted the corresponding background contribution from the ICM emission, and simultaneously fitted the resulting spectra in `XSPEC` with an absorbed thermal plasma component (`phabs` × `apec`), by keeping fixed the hydrogen column density and

[4]The X-ray peak is found at a distance of $21''$ = 35 kpc from BCG1, in line with Wang & Markevitch (2018).

[5]https://github.com/jeremysanders/contbin

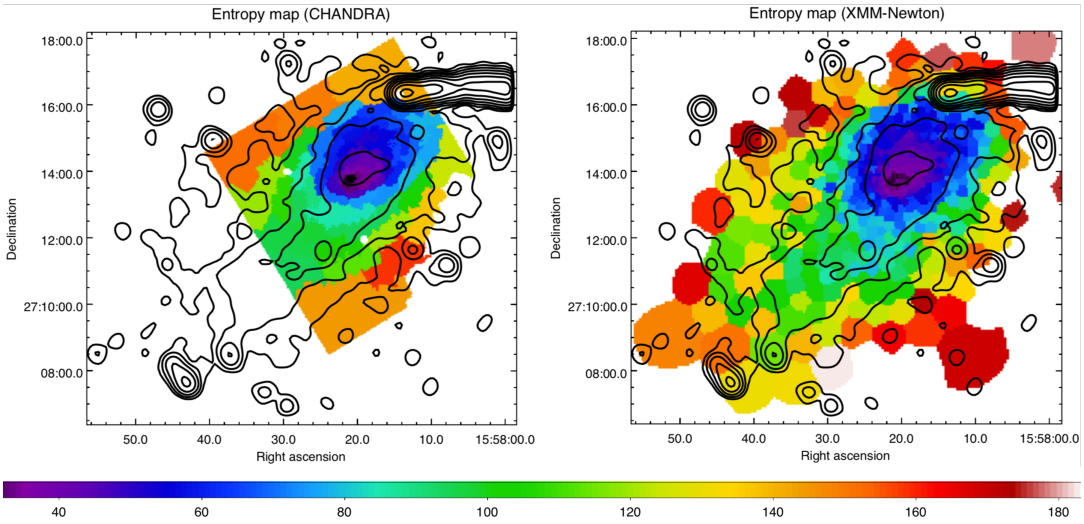

Figure 8.11: Projected entropy maps of A2142 derived from Chandra (left) and XMM-Newton (right) in units of keV cm$^{5/3}$ arcmin$^{-2/3}$. Black contours are those of Fig. 8.2, upper right panel.

metal abundance at values of $N_{\rm H} = 3.8 \times 10^{20}$ cm^{-2} and $Z = 0.28\ Z_{\odot}$ (Markevitch et al. 2000). The Cash statistics (Cstat; Cash 1979) was assumed for the fits; the chosen high SNR ensured Cstat/d.o.f in the range 0.90-1.14 for each region, thus indicating the reliability of our fits. The procedure and systematics related to the derivation of the entropy map by using the fitted temperature and `apec` normalisation are described in Appendix F. In Fig. 8.11 we both show our projected entropy map (left panel) and that produced by Rossetti et al. (2013) (multiplied by the pixel area to match our units). Despite the different procedures, resolution, and SNR, the two maps are well in agreement in the common area that covers a radius of $\sim$ 350 kpc. The LOFAR HBA contours at $21'' \times 20''$ resolution (Fig. 8.2, upper right panel) are overlaid on the maps. In the radio core, the ICM has entropy values $s \lesssim 60$ keV cm$^{5/3}$ arcmin$^{-2/3}$. As claimed by Rossetti et al. (2013), we confirm that the ridge is co-spatial with a trail of gas that extends in the NW-SE direction and is characterised by lower entropy values $s \sim 100$ keV cm$^{5/3}$ arcmin$^{-2/3}$ than those found in H3, where $s > 130$ keV cm$^{5/3}$ arcmin$^{-2/3}$ in its inner parts.

8.3.6 Point-to-point radio vs X-ray analysis

As the ICM provides particles and magnetic fields that generate the synchrotron diffuse emission, a spatial correlation between the radio and X-ray surface brightness exists for both radio halos and mini-halos as $I_{\rm R} \propto I_{\rm X}^{k}$. The slope k of this correlation indicates the relative spatial distributions of thermal and non-thermal components, and can be thus used to probe the origin of the diffuse radio emission (Brunetti & Jones 2014). Super-linear slopes $k > 1$ are associated with narrow distributions of the emitting electrons that rapidly decline with the radius, while the thermal particles occupy larger volumes. Conversely, sub-linear $k < 1$ slopes are associated with narrow thermal and broader non-thermal distributions, respectively, thus supporting a scenario where particle are accelerated and

Table 8.7: Results from the point-to-point radio vs X-ray correlation analysis. Cols. 1, 2, 3: frequency, resolution, and noise of the input radio image. Col. 4: adopted noise threshold. Col. 5: fitted slope. Cols. 6, 7: Spearman (ρ_S) and Pearson (ρ_P) ranks.

ν (MHz)	θ	σ (μJy beam^{-1})	$\sigma_{\rm thresh}$ (σ)	k	ρ_S	ρ_P
143	$9'' \times 6''$	75	3^{*}	0.47 ± 0.03	0.68	0.68
143	$9'' \times 6''$	75	3^{**}	0.24 ± 0.05	0.49	0.50
143	$21'' \times 20''$	150	8^{**}	0.66 ± 0.07	0.84	0.87
143	$21'' \times 20''$	150	4^{**}	0.75 ± 0.07	0.76	0.79
143	$21'' \times 20''$	150	3^{**}	0.84 ± 0.07	0.78	0.81
143	$21'' \times 20''$	150	2^{**}	0.91 ± 0.06	0.80	0.82
143	$38'' \times 34''$	250	16	0.34 ± 0.04	0.84	0.89
143	$38'' \times 34''$	250	8	0.49 ± 0.05	0.79	0.83
143	$38'' \times 34''$	250	4	0.67 ± 0.03	0.87	0.89
143	$38'' \times 34''$	250	2	0.74 ± 0.03	0.90	0.92
143	$128'' \times 117''$	1000	4	0.81 ± 0.04	0.98	0.97
143	$128'' \times 117''$	1000	3	0.82 ± 0.03	0.98	0.97
143	$128'' \times 117''$	1000	2	0.82 ± 0.03	0.98	0.98
143	$128'' \times 117''$	1000	2^{***}	0.75 ± 0.06	0.92	0.93
50	$22'' \times 13''$	1600	4^{*}	0.28 ± 0.07	0.66	0.68
50	$22'' \times 13''$	1600	3^{*}	0.34 ± 0.05	0.77	0.77
50	$22'' \times 13''$	1600	2^{*}	0.42 ± 0.05	0.74	0.73
50	$69'' \times 63''$	4400	8	0.49 ± 0.08	0.88	0.90
50	$69'' \times 63''$	4400	4	0.52 ± 0.03	0.90	0.94
50	$69'' \times 63''$	4400	3	0.54 ± 0.03	0.86	0.92
50	$69'' \times 63''$	4400	2	0.56 ± 0.03	0.89	0.93
50	$132'' \times 126''$	9000	3	0.63 ± 0.06	0.95	0.95
50	$132'' \times 126''$	9000	2	0.64 ± 0.05	0.94	0.94
50	$132'' \times 126''$	9000	2^{***}	0.50 ± 0.11	0.90	0.88
323	$9'' \times 8''$	45	3^{*}	0.40 ± 0.04	0.57	0.59
323	$9'' \times 8''$	45	3^{**}	0.30 ± 0.08	0.42	0.44
323	$40'' \times 34''$	170	16	0.27 ± 0.07	0.69	0.74
323	$40'' \times 34''$	170	8	0.45 ± 0.05	0.79	0.84
323	$40'' \times 34''$	170	4	0.57 ± 0.04	0.87	0.88
323	$40'' \times 34''$	170	2	0.65 ± 0.04	0.87	0.88
1380	$26'' \times 24''$	50	4^{*}	0.70 ± 0.08	0.81	0.85
1380	$26'' \times 24''$	50	3^{*}	0.75 ± 0.07	0.83	0.84
1380	$26'' \times 24''$	50	2^{*}	0.78 ± 0.07	0.83	0.84
1810	$18'' \times 17''$	35	4^{*}	0.45 ± 0.10	0.69	0.71
1810	$18'' \times 17''$	35	3^{*}	0.48 ± 0.10	0.54	0.57
1810	$18'' \times 17''$	35	2^{*}	0.54 ± 0.10	0.59	0.59

Notes. * H1 only; ** H2 only; *** H3 only.

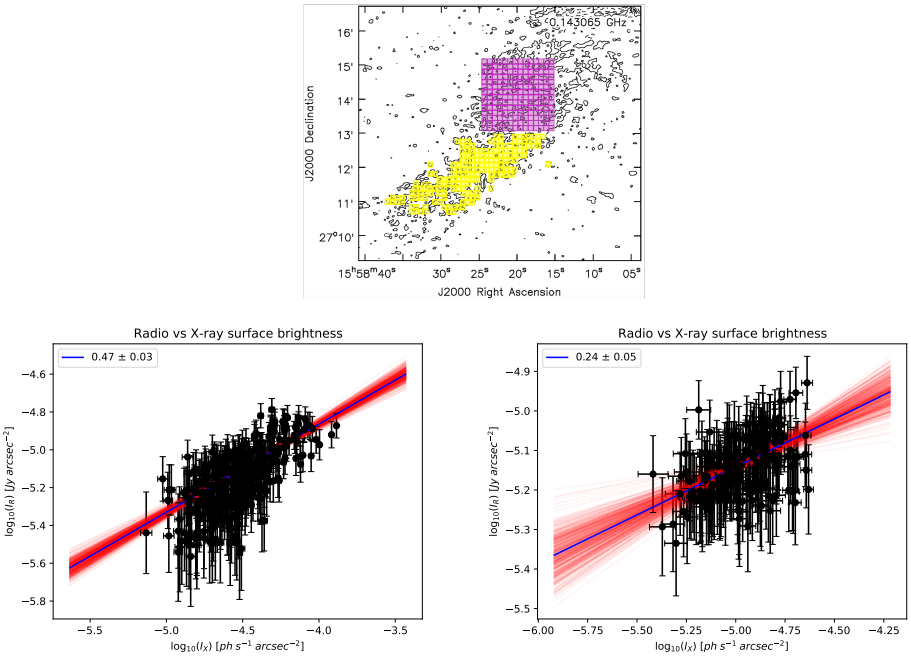

Figure 8.12: *Top*: 143 MHz, source-subtracted, A2142 image at $9'' \times 6''$ resolution used for the point-to-point radio vs X-ray analysis. The sampling square boxes have sizes of $9'' \times 9''$. Contour levels are drawn at $[\pm 3,\ 6,\ 12, ...] \times \sigma$. *Bottom left*: linear best fit for H1 (magenta area). *Bottom right*: linear best fit for H2 (yellow area).

transported by turbulence generated on large scales. Radio halos have been found to exhibit sub-linear slopes (e.g. Hoang et al. 2019; Bruno et al. 2021; Duchesne et al. 2021; Rajpurohit et al. 2021c; Pasini et al. 2022), while super-linear slopes have been found in mini-halos (e.g. Govoni et al. 2009; Ignesti et al. 2020a; Biava et al. 2021; Riseley et al. 2022).

We investigated the emission of each diffuse component in A2142 through the Point-to-point TRend EXtractor code[6] (PT-REX; Ignesti et al. 2022), by gridding the regions of interest with beam-size square boxes. The extracted surface brightness values are then fitted in a logarithmic plane as $\log_{10} I_{\rm R} = k \log_{10} I_{\rm X} + c$ (where c is the intercept) with `linmix` (Kelly 2007), which can account for the errors of the measurements and intrinsic scatter of the linear regression through a Bayesian statistical approach. We considered XMM-Newton X-ray images as input, owing to a larger field of view with respect to Chandra images, which were smoothed at the same resolution of the input radio image. A summary of the input radio images, noise threshold, fitted slope, and Spearman and Pearson ranks is reported in Table 8.7. As representative examples, we show some of the obtained results in Figs. 8.12 and 8.13, by using LOFAR HBA images at $9'' \times 6''$ and $38'' \times 34''$ resolution, respectively, as inputs.

As shown in Fig. 8.12, the slope of the correlation is sub-linear in H1, being $k \sim 0.3 - 0.5$ (see '*' cases in Table 8.7), with the exact value that depends on the input radio

[6] https://github.com/AIgnesti/PT-REX

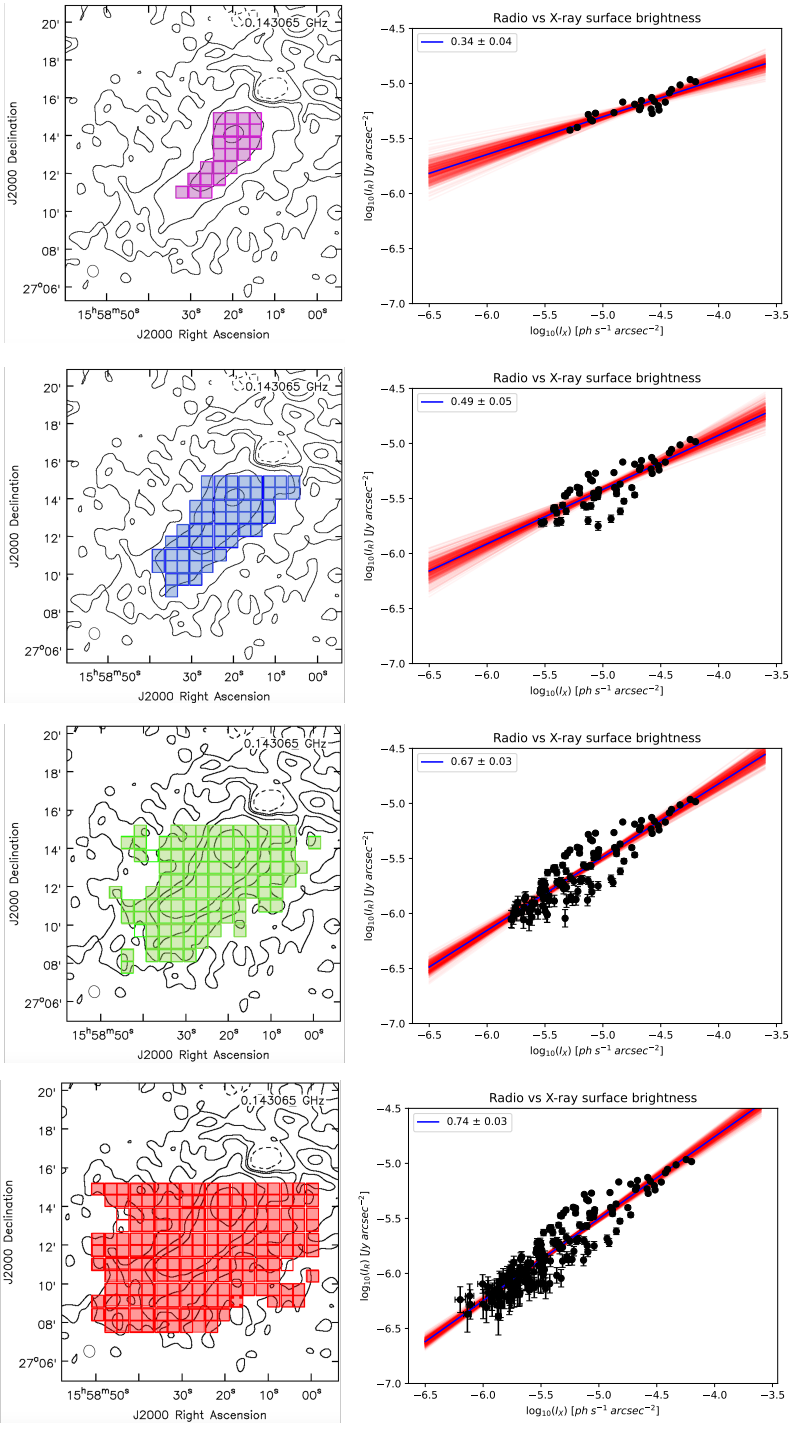

Figure 8.13: *Left panels*: 143 MHz, source-subtracted, A2142 image at $38'' \times 34''$ resolution used for the point-to-point radio vs X-ray analysis. The sampling square boxes have sizes of $38'' \times 38''$. Contour levels are drawn at $[\pm 2,\ 4,\ 8, ...] \times \sigma$. *Right panels*: corresponding linear best fits.

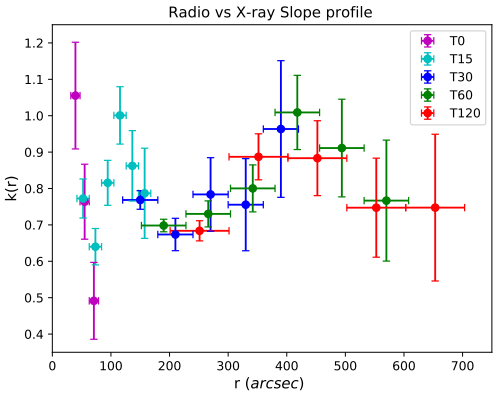

Figure 8.14: Radio vs X-ray correlation slope as a function of the radial distance from BCG1. The concentric elliptical sampling sectors have widths that depend on the beam of the radio image and the required SNR. The tapering adopted to produce each input LOFAR HBA image to study different spatial scales is reported in the legend (in units of arcsec).

image (in terms of ν, θ, and SNR). In H2 ('**' cases in Table 8.7), results are controversial. Indeed, the fitted slopes range from $k \sim 0.2 - 0.3$ to $k \sim 0.7 - 0.9$ (see also ρ_S and ρ_P in Table 8.7). The inconsistency of the slopes found for H2 is likely driven by the complex geometry of the ridge, which does not allow us to firmly constrain k in this region.

Furthermore, as in the example shown in Fig. 8.13, we used the same input images and sizes of the sampling boxes, but varying the brightness threshold. In all the cases, the radio and X-ray emission are strongly correlated, and the fitted sub-linear slopes are in the range $k \sim 0.7 - 0.8$ for H3. Interestingly, our tests suggest a radial steepening of k from the centre towards the outer regions, especially in the transition from H2 to H3. As shown in previous works (Botteon et al. 2020b; Bruno et al. 2021), it is known that lower $\sigma_{\rm thresh}$ tend to provide steeper slopes. Indeed, this is consistent with results obtained from $\sigma_{\rm thresh} = 2\sigma,\ 3\sigma,\ 4\sigma$, but discrepancies are only marginal for our target. We instead find remarkable differences when using $\sigma_{\rm thresh} = 2\sigma,\ 4\sigma,\ 8\sigma,\ 16\sigma$, which can hardly be explained as simple fitting fluctuations. These results may hint at a physical radial steepening of k; a similar trend has been recently claimed in the Coma cluster by Bonafede et al. (2022b) for the first time. These authors suggest that the radial steepening of the slope can be related to the radial profile of the magnetic field and/or the non-thermal to thermal energy ratio content, thus indicating that the observed trends of k may be a common phenomenon in radio halos, but still unexplored. If this is the case, our results may trace the same behaviour in A2142.

To investigate the radial behaviour of $k = k(r)$, we complemented the point-to-point analysis with the following procedure. We considered concentric elliptical sectors that approximately follow the distribution of the ICM to measure I_R and I_X. The slope as a function of the radial distance is thus computed as $k(r) = (\Delta(\ln I_R))/(\Delta(\ln I_X))$, being $\Delta(\ln I)$ the difference of the logarithms of the brightness evaluated in two consecutive bins. As explained above, the geometry of the ridge likely affects the derivation of k,

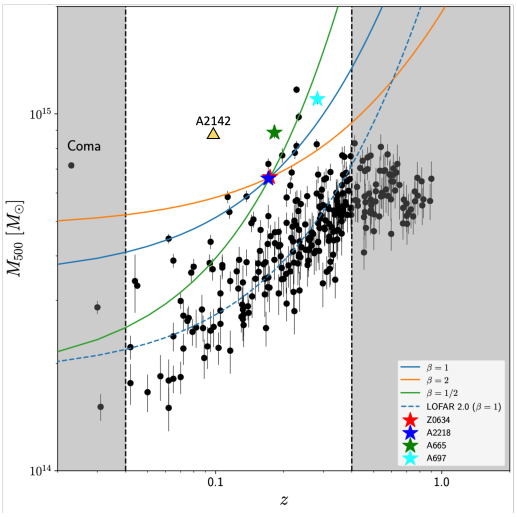

Figure 8.15: Mass-redshift plane (adapted from Cuciti et al. 2022) for the Planck clusters in LoTSS-DR2 (Botteon et al. 2022b). The combination of M_{500} and z makes A2142 to possibly host a candidate megahalo in a non-merger cluster. The other 4 known megahalos are indicated with stars.

therefore we avoided the region of H2. The width of the annuli was set depending on the resolution of the radio image and the required SNR. In Fig. 8.14 we report the derived radial profiles $k(r)$ for different resolutions and SNR. We found a possible super-linear correlation within the innermost $\sim 50 - 100$ kpc, but this is more likely caused by the off-set between the radio and X-ray peaks; indeed, (i.) the super-linearity is not supported by the point-to-point analysis in H1, which is instead much less affected by the off-set, and (ii.) the value of k rapidly drops with the distance. On average, the slope is found to be sub-linear; we observe some features at ~ 150 kpc and ~ 650 kpc that may be related to the transitions H1-H2 and H2-H3, respectively, and/or depend on geometrical effects. The radial trend of $k(r)$ that we obtained may be used to constrain the magnetic field of A2142 (similarly to Bonafede et al. (2022b) for Coma), but this is beyond the aim of this work.

8.4 Discussion

In this Section we discuss the possible existence of a megahalo in A2142 and the origin of the three components of the halo.

8.4.1 A megahalo in A2142 ?

Megahalos are diffuse sources exhibiting a radial decline of the radio brightness that is flatter than that of their embedded radio halos (Cuciti et al. 2022). In addition, the megahalos discovered so far share a large extension ($\sim R_{500}$), a highly disturbed dynamical state of the host, an ultra-steep spectrum, and are located in a well-defined region in

the mass-redshift plane reported by Cuciti et al. (2022). Numerical simulations indicate that megahalos originate from turbulence induced by large scale accretion, meaning that the merging state of the host is not a fundamental condition. The possible discovery of a megahalo in A2142, whose dynamical state appears as intermediate between a major merger and a relaxed cool core, would be a milestone confirmation of theoretical predictions. In this respect, A2142 has some properties in common with these sources, and the presence of a megahalo may be expected based on its position in the $M_{500} - z$ plane, as shown in Fig. 8.15.

To investigate the presence of a megahalo in A2142, we considered the 143 MHz, source-subtracted image (residuals from T1 and T2 were masked) at $134'' \times 134''$ resolution, which provides the largest recovered extension of H3. We extracted the surface brightness profile in annuli of width $67''$ (i.e. half FWHM of the restoring beam) up to the 2σ contour level in different directions to check for possible biases associated with geometrical effects and/or residuals from subtraction. The extraction sectors and computed profiles are reported in Fig. 8.16.

Possible emission from a megahalo may be lost due to a combination of inadequate *uv*-coverage at short spacings and noise sensitivity. The shortest baseline we assumed for imaging is 50λ, which can recover sources in the sky of size $\sim 1.15^{\circ}$, corresponding to $\sim$ 7 Mpc at the cluster redshift. Even though sources of such large scales require proper calibration processes to be recovered (e.g. Bonafede et al. 2021b), we should safely observe radio emission up to $\sim$ 4 Mpc with losses $\ll$ 20% at most (see results with standard minimum baseline of 80λ derived in Chapter 5), if it existed. This excludes that a possible megahalo on scales $\gg R_{500}$ is completely lost due to missing short spacings.

A megahalo may be not revealed by our observations due to insufficient noise sensitivity. In Cuciti et al. (2022), the surface brightness profile starts to flatten at levels of ~ 0.2 μJy arcsec^{-2} for 3 out of 4 megahalos; by converting this brightness value in units of Jy kpc^{-2}, the faintest megahalo is found to be A697 ($z = 0.28$). Our image allows us to reach brightness levels (corrected for the cosmological dimming, for a fair comparison with A697) that are at least a factor of 2 lower than A697, but we do not find any hint of radial flattening up to radii of $0.95R_{500}$ (as also confirmed by the global fit shown in Fig. 8.8), thus excluding the presence of a megahalo on these scales.

Given our findings, we conservatively consider the total radio power of H3 as an upper limit to the radio power of a possible megahalo. By scaling the radio power to 1400 MHz ($P_{1400} = (3.5 \pm 0.5) \times 10^{23}$ W Hz^{-1}) for consistency with Cuciti et al. (2022) and considering a prolate ellipsoidal geometry ($V = 5.0$ Mpc^3, by assuming semi-axes of $1.2 \times 1.0 \times 1.0$ Mpc), we obtain a corresponding (volume-averaged) emissivity of $J_{1400} = (2.4 \pm 0.3) \times 10^{-44}$ erg s^{-1} cm^{-3} Hz^{-1}, which has interestingly the same order of magnitude of the emissivity of the known megahalos. Clearly, one difference with the megahalos in Cuciti et al. (2022) is that in A2142 a large radio halo is present, and this would make more difficult the detection of additional fainter emission on large scales. In this respect, it is worth to notice that radio halos within megahalos have small radii ($\sim 400 - 600$ kpc), thus suggesting that megahalos may be unambiguously detected in proper massive and nearby clusters (see Fig. 8.15) only under favourable conditions of size of the embedded radio halo.

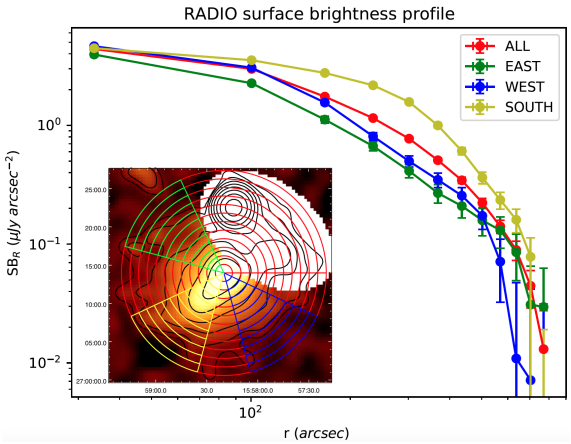

Figure 8.16: Azimuthally-averaged surface brightness profile of A2142 at 134″ × 134″ resolution, up to $0.95R_{500}$. The inset reports the four sectors considered to extract the profiles: 0° – 360° (red), 115° – 165° (green), 205° – 255° (yellow), 285° – 335° (blue). No flattening of the profile is observed, thus excluding the presence of a megahalo.

In summary, the (conservative) upper limit on the emissivity is consistent with that of the known megahalos, and the possible detection of a megahalo in A2142 might be disfavoured by the presence of the large H3 component. On the other hand, the sensitivity reached by LOFAR HBA allows to investigate deeper surface brightness thresholds than those of the faintest megahalo (A697) reported by Cuciti et al. (2022). If a megahalo existed in A2142, as expected by current models and simulations, it should be at least a factor of 2 fainter than A697, thus providing important constraints to be explored in future works.

8.4.2 Probing the hybrid halo origin

The results collected in the previous Sections can be exploited to discuss the origin and connection of each component (H1, H2, H3) of the puzzling hybrid radio source.

The core has a roundish morphology, is confined by multiple cold fronts on scales $\sim$ 200 kpc, has a moderately steep spectrum $\alpha \sim 1.1$, and the slope of the radio vs X-ray correlation is sub-linear (on scales $\sim$ 100 – 200 kpc). These properties may support the hypothesis that H1 is a mini-halo originating from turbulence induced by sloshing of cold gas. Nevertheless, the event that triggered the central sloshing is unclear. Rossetti et al. (2013) and Venturi et al. (2017) proposed the hypothesis of an intermediate mass-ratio merger with the group of BCG2. Such an event is less disruptive than major mergers and would likely not affect the global properties and morphology of the ICM. On the other hand, strong sloshing motions could be induced by this kind of merger, being able to move a large amount of cold gas away from the centre, where then mixing with the hotter gas phase is favoured (Wang & Markevitch 2018). This could lead to the formation of the prominently off-set warm core from a former cool core; moreover, BCG1 would be deprived of most of the available fuel, thus explaining the absence of a powerful central

AGN as in classical relaxed clusters.

The extreme sloshing motions in A2142 likely involve not only the inner regions of the cluster, but also larger scales, as witnessed by the presence of the southernmost cold front at $\sim$ 1 Mpc from the centre (Rossetti et al. 2013) and the trail of low-entropy gas. In this case, sloshing could be partly responsible for the formation of the ridge, which extends for $\sim$ 400 kpc along the NW-SE axis. The spectral index is similar ($\alpha \sim 1.2$) to that of the core, and the GGM filtering and the projected entropy distribution of the ICM hint at a common origin for H1 and H2. Turbulent motions induced by sloshing may trigger the radio emission of the ridge by re-accelerating particles and amplifying magnetic fields along the low-entropy trail. It is worth to notice that turbulence in the ridge might be also supplied by the infalling groups along the NW-SE axis, which is the direction of the main accretion filament of the A2142-supercluster (Einasto et al. 2015; Einasto et al. 2018; Einasto 2020); future numerical simulations are needed to investigate this scenario.

The observational evidences that we found for H3 (large size, $\alpha \sim 1.6$, exponential radial profile, co-spatial thermal and non-thermal emission, sub-linear k) allowed us to classify it as a giant ultra-steep spectrum radio halo. Concerning the origin of H3, we discuss two possible scenarios, connected to either (i.) an old major merger or (ii.) multiple minor mergers.

The first scenario for the origin of H3 is related to the last major merger. The epoch of the last major merger is estimated to be $\sim$ 4 Gyr ago (Einasto et al. 2018) based on statistical arguments on mass growth from cosmological simulations. At the present epoch, the turbulence injected by such event may have not been completely dissipated (see also Brunetti et al. 2004; Donnert et al. 2013). Therefore, the origin of H3 could be associated with this major merger, and its ultra-steep spectrum could be the consequence of particle ageing dominating over turbulent re-acceleration. Furthermore, the hypothesis of an extremely old evolutionary stage of the halo may open to the possibility of an intriguing new scenario to explain the peculiar thermal properties of A2142. We can speculate that a former cool core was first disrupted by the major merger, and over the last few Gyr after this event it has started to reform again; nevertheless, this process is hampered by the perturbing minor mergers, thus explaining the presence of a warm core rather than a classical cool core. In this case, A2142 would represent the missing evolutionary link between major merging and cool core systems.

Alternatively to the major merger scenario, the ultra-steep spectrum of H3 could be associated with minor mergers. It is unlikely that a single intermediate mass-ratio merger (as discussed for H1 and H2) is able to inject enough turbulent energy via sloshing to uniformly re-accelerate electrons on the large scales ($\gtrsim$ 2 Mpc) of H3. However, a high number of minor mergers occurring over the cluster volume may be able to continuously supply turbulence that powers the radio emission of H3, by re-accelerating electrons with a lower efficiency than turbulence induced by major mergers.

The uncommon thermal and non-thermal properties A2142 offers the possibility to discuss the hypothesis of an evolutionary connection between H1, H2, and H3. By considering the model proposed by Zandanel et al. (2014), H1 and H3 might have an hadronic and leptonic origin, respectively. Secondary CRe might significantly contribute to the

emission of H1, but, in this case, the sub-linear value of k on scales $\sim$ 100 – 200 kpc would indicate particular conditions, namely a flat CRp distribution in the core and a high ($B > B_{\rm CMB}$, being $B_{\rm CMB} \sim 4$ μG at the cluster redshift) magnetic field (Brunetti & Jones 2014; Ignesti et al. 2020a). Conversely, as already discussed, the observed properties (size, correlation slope, and spectral index) of H2 and H3 indicate that the emission in these regions is less contributed from secondary CRe, and the leptonic scenario is thus strongly favoured. In summary, at present we cannot exclude that the multi-component halo in A2142 marks an evolution from an hadronic-dominated (H1) to a leptonic-dominated (H2, H3) regime, and further investigation is required.

Finally, A2142 is an interesting target to search for the origin of seed relativistic particles. Indeed, the possibility that (aged) particles originating in the core are transported and re-accelerated by sloshing turbulence along the ridge (Brunetti & Jones 2014) is a reasonable scenario that would be also in line with thermal features, such as the low-entropy trail and the southernmost cold front. Furthermore, the seed particles to be re-accelerated in H2 and H3 may be primary CRe injected in the ICM by AGN and galaxy members of the groups infalling in A2142, as hinted by the prominent tails of T1 and T2.

8.5 Summary and conclusions

Recent discoveries achieved by means of sensitive low frequency data indicate that peculiar diffuse radio sources in galaxy clusters may be common in the Universe. These targets challenge our current knowledge, mostly limited to classical giant radio halos and mini-halos, whose formation processes are still not completely understood as well. Investigating possible scenarios on the origin of ultra-steep spectrum radio halos, hybrid diffuse sources, and radio emission extending beyond the canonical cluster outskirts is thus necessary to make a step forward in the understanding of physics of cosmic rays and cosmic magnetism.

The main member of the A2142-supercluster is the nearby and massive galaxy cluster A2142, which is characterised by a dynamical state that is intermediate between a classical major merger and relaxed cool core. This target offers a unique chance to simultaneously probe many properties of peculiar diffuse sources. It hosts a puzzling radio halo that was known to consist of two distinct components, namely the core (H1) and the ridge (H2). The core is roundish and confined by a system of multiple inner cold fronts, whereas the ridge is elongated and roughly co-spatial with a trail of low-entropy thermal gas that ends in an extremely distant cold front ($\sim$ 1 Mpc from the centre). Furthermore, the ridge is aligned with the main accretion filament of A2142.

In this work we presented new deep LOFAR HBA and LOFAR LBA observations, which allowed us to detect a new radio component, H3, whose emission follows the X-ray thermal counterpart distribution up to scales $\gtrsim$ 2 Mpc. We investigated the properties, origin, and physical connection of the three components with complementary archival GMRT, VLA, CHANDRA, and XMM-Newton data, and literature information from optical and lensing studies.

We improved the accuracy of the spectral indices of the core and the ridge first measured by Venturi et al. (2017), finding $\alpha = 1.09 \pm 0.02$ in H1 and $\alpha = 1.16 \pm 0.02$ in H2.

We measured an ultra-steep spectral index $\alpha = 1.57 \pm 0.20$ in H3. We showed that the sum of two exponential laws can well reproduce the observed global profile of an hybrid source rather than a single one, routinely used to fit the emission of classical giant and mini radio halos (e.g. Murgia et al. 2009). We performed a point-to-point comparison of the radio and X-ray surface brightness, obtaining a sub-linear correlation between these quantities for H1 and H3, whereas in H2 our analysis is inconclusive, likely due to the complex (3D) geometry of the ridge. Furthermore, we complemented this analysis by deriving the radial profile of the radio vs X-ray slope; even though the global trend of $k(r)$ is sub-linear for $r \gtrsim 150$ kpc, we found features at $\sim$ 150 kpc and $\sim$ 650 kpc, possibly marking the transitions H1-H2 and H2-H3, respectively.

As proposed in the past (Venturi et al. 2017), our findings confirm the possibility that radio emission in H1 is powered by turbulence induced by sloshing in the core, as in usual mini-halos. The hypothesis of an intermediate mass-ratio merger has been invoked to explain some peculiar thermal features, such as the presence of the warm core, the trail of low-entropy gas, and the southernmost cold front (Rossetti et al. 2013). This event could lead to strong sloshing involving scales well beyond the inner regions, without affecting the global morphology of the ICM. Extreme sloshing could be responsible for turbulent motions along the ridge, thus triggering its radio emission. Further supplies of turbulence might also come from merging groups along the main accretion filament of A2142, but numerical simulations are required to verify this complex scenario.

The properties of H3 allowed us to classify it as an ultra-steep spectrum radio halo. We investigated two different possibilities for the origin of H3. In the first case, the last major merger (estimated to took place $\sim$ 4 Gyr ago, Einasto et al. 2018) could have disrupted the former cool core and triggered the radio halo, which at present is observed in a extremely old evolutionary phase. In this scenario, minor mergers may contribute by hampering the restoring of a classical cool core, thus explaining the presence of a warm core. As an alternative possibility, turbulence is injected over the cluster volume by continuous minor mergers with small groups of galaxies. These mergers would inefficiently re-accelerate particles, thus leading to ultra-steep spectra as predicted by leptonic models.

We also discussed scenarios that suggest a physical and/or evolutionary connection between the various radio components. At present, we cannot exclude that H1 is generated by secondary electrons; in this case, the radio components would mark a transition from an hadronic-dominated (H1) to a leptonic-dominated (H2, H3) regime. On the other hand, it is likely that particles from H1 have been transported towards H2 by the strong sloshing, and then re-accelerated by turbulence. As the number of hybrid sources is rapidly increasing, alternative scenarios may be discussed and tested.

Finally, we explored the possibility that A2142 hosts a megahalo, owing to many similarities with the confirmed cases reported by Cuciti et al. (2022). Despite the high sensitivity of our data, the surface brightness profile does not provide any hint of a megahalo in A2142. Therefore we obtained upper limits to both the surface brightness and volume-averaged emissivity.

The valuable results achieved in this work are the first steps forward the understanding of hybrid and ultra-steep spectrum radio halos, but at the same time opened new questions on the relative roles of primary/secondary CRe and major/minor mergers in shaping the

thermal and non-thermal properties of galaxy clusters. The various formation scenarios that we proposed, as well as our upper limits on the presence of a megahalo, need to be further investigated and complemented by numerical simulations in the future.

Chapter 9

Conclusions and future prospects

Cluster mergers can transfer a fraction of their energy to non-thermal components in the ICM via shocks and turbulence. These events are responsible for the origin of a variety of diffuse radio sources in galaxy clusters, including radio halos (RHs), which are the main subject of this Thesis. Owing to their steep ($\alpha \sim 1.3$) synchrotron spectra, diffuse sources can be properly studied at low frequencies (hundreds of MHz). In this respect, LOFAR is a next-generation interferometer operating in the range $\sim 10 - 250$ MHz with unprecedented capabilities in this regime, which allow to enter a new parameter space to study the diffuse sources. Thanks to LOFAR, not only the number of RHs has dramatically increased in recent years, but also populations of ultra-steep ($\alpha \gtrsim 1.5$) spectrum radio halos (USSRHs), peculiar multi-component RHs, and diffuse sources extending even beyond the canonical cluster boundaries have been revealed.

In this PhD Thesis we aimed to study various diffuse radio sources observed by LOFAR. This Thesis is divided in two parts. In the first part (Chapters 4, 5, 6) we carried out a milestone project to investigate the statistical properties and occurrence of RHs in the largest-ever sample of galaxy clusters observed at radio frequencies in the context of LoTSS-DR2. I was involved in the group leading this project within the survey KSP collaboration; specifically, I led a work aimed to derive solid upper limits to the radio power in clusters that lack a detected RH. The second part of this Thesis (Chapters 7, 8) is devoted to the analysis of LOFAR observations of two single targets, making use of complementary multifrequency radio and X-ray data. I focused on two USSRHs, one of which being also a unique case of an hybrid RH consisting of three radio components. The details of these works and future prospects are summarised below.

The *Planck* clusters in the LOFAR sky

The areas covered by LoTSS-DR2 include 309 *Planck* clusters spanning wide ranges in mass ($M_{500} = [1.1 - 11.7] \times 10^{14}\ M_{\odot}$) and redshift ($z = [0.016 - 0.9]$) that have never been probed before in studies of diffuse radio sources.

In Chapter 4 we presented the full sample. We described the challenging data reduction, imaging, and analysis processes, and built a decision tree to classify the radio sources in the most objective and reproducible way. We finally classified 83 (including candidate)

RHs, 26 (including candidate) radio relics, 47 diffuse sources of uncertain origin, and 140 non-detections of diffuse emission (NDE). The detection rate of RHs in our sample is $30 \pm 11\%$, and mostly important, about half of them are new discoveries.

In Chapter 5 we presented my main contribution to the project. We dealt with the sub-sample of 140 NDE clusters, and through the injection technique of mock visibilities into the observed *uv*-datasets, we simulated RHs with varying angular size and flux density. By means of our simulations, we demonstrated that flux density losses due to insufficient number of short baselines are negligible ($\lesssim 10\%$) for generic extended targets of size up to $\sim 15'$, as a consequence of the extremely dense *uv*-coverage at short spacings of a standard (8 hour long) LoTSS pointing. We discovered a helpful scaling relation ($S_{\rm UL} \propto \sigma N_{\rm beam}^{0.8}$) to easily derive solid upper limits as a function of the noise (σ) of the image and extent (in terms of number of beams, $N_{\rm beam}$) of the mock halo, without the need of performing any injection, and thus allowing us to save a large amount of computing time. We showed that our relation can be safely adopted if residuals from discrete source subtraction are negligible, otherwise the standard injection and visual inspection of the images is recommended to determine more reliable limits. By means of these methods, we obtained 75 upper limits, which are much deeper (by a factor $\sim 2-5$) than those in the literature (re-scaled to 150 MHz) from other instruments. These limits, when compared to the radio power of detected RHs, are fundamental to investigate the statistical properties, origin, and evolution of the diffuse sources.

In Chapter 6 we presented the first statistical analysis performed at low frequencies in such a large sample of clusters, which include a notably higher number of RHs and upper limits compared to previous works. We obtained the new correlation between the radio power at 150 MHz vs host mass, finding that it extends down to masses $M_{500} \sim 3 \times 10^{14}\ M_{\odot}$. Furthermore, we confirmed the bimodal distribution of RHs and upper limits, with the former scattering around the correlation, and the latter lying below it without following specific trends. We then adopted semi-analytic models developed in the framework of the merger-driven turbulent re-acceleration scenario to infer the expected occurrence of RHs in our sample. In spite of our simplified model and assumptions, we found that predictions are almost perfectly in agreement with our observational findings.

Overall, our large program will have a fundamental legacy value for future studies of diffuse emission in galaxy clusters carried out with the next generation interferometers, not only for the achieved results, but also in terms of the methods that we developed to deal with such high number of targets.

Our data have opened to the chance of carrying out many projects for the very near future. First, the classification method based on the decision-tree may be automatised by using our sample as a reference training set for machine-learning algorithms. Second, a similar relation to derive upper limits without injection should be explored for other instruments (in Chapter 5 we discussed the cases of JVLA and uGMRT) since we showed that it is an efficient tool. It is worth to notice that for some NDE clusters the calibration and source-subtraction might be improved, thus possibly leading to deeper upper limits; to this aim, we are also testing strategies to implement the promising stacking technique to our clusters. In this respect, the depth of our upper limits might potentially allow to derive stringent constraints on the content of cosmic rays in clusters and test models of

dark matter interactions. Finally, in our statistical analysis, current data did not allow us to probe the dynamical state of the majority of NDE clusters and the spectral index of RHs, which is predicted to be very steep for $\sim 1/3$ of our detections. Therefore, we have recently started two large observing campaigns (PI: R. Cassano, Co-I: L. Bruno) with XMM-Newton and uGMRT at 700 MHz; these new X-ray and radio data will be essential to shed light on the main open questions of our work.

The ultra-steep spectrum radio halo MACS J1149

In Chapter 7 we presented new LOFAR HBA and JVLA observations of MACS J1149, a massive ($M \sim 10^{15}\ M_{\odot}$) merging system at high-redshift ($z = 0.544$). Previous works claimed the presence of an USSRH and a pair of misaligned radio relics at south-east and west.

Our high-resolution images showed that the western relic is actually a FRI-type radio galaxy. We confirmed the nature of the very-steep spectrum halo, by measuring $\alpha = 1.49 \pm 0.12$ between 144 and 1500 MHz. By means of the point-to-point analysis applied to Chandra and LOFAR data, we probed the spatial correlation between the thermal and non-thermal emission; we found a sub-linear slope ($k \sim 0.4 - 0.6$) indicative of a leptonic origin of the halo.

Thanks to the favourable combination of high-z and steep α, we were able to test a pure hadronic scenario, finding unrealistically high values of the non-thermal energy budget that rule out this origin for the halo in MACS J1149. Likely, the USSRH in MACS J1149 is in an advanced evolutionary stage, in which the bulk of turbulence has been already dissipated and radiative losses are prominent.

In this work, we were not able to firmly constrain the nature of the south-east relic because of its atypical orientation, which is parallel to the merger axis. This evidence might indicate that this target is a radio phoenix rather than a relic. Additional archival JVLA (3 GHz) and GMRT (600 MHz) data (unemployed in our work because of their insufficient sensitivity to the emission of the halo) can be used to perform a key spectral analysis of this source, which would definitely confirm its nature.

The ultra-steep spectrum, multi-component radio halo in A2142

In Chapter 8 we presented new deep LOFAR HBA and LOFAR LBA observations of A2142, a nearby ($z \sim 0.09$) and massive ($M \sim 9 \times 10^{14}\ M_{\odot}$) cluster exhibiting unique thermal and non-thermal properties. Its dynamical state appears as intermediate between that of classical major merging and relaxed cool core systems. Previous radio observations detected two well-distinct radio components; the core (H1) is similar to a mini-halo, whereas the ridge (H2) has an elongated morphology and its origin is unclear.

Our LOFAR data revealed a new radio component (H3), which is co-spatial with the thermal X-ray emission of the ICM up to scales $\gtrsim 2$ Mpc and embeds both H1 and H2.

By complementing our LOFAR observations with GMRT and VLA data, we determined the spectral index of each component; this is steep in H1 ($\alpha = 1.09 \pm 0.02$) and in H2 ($\alpha = 1.16 \pm 0.02$), whereas it is ultra-steep in H3 ($\alpha = 1.57 \pm 0.20$).

X-ray (Chandra and XMM-Newton) data provided crucial information to probe the origin of the halo components by means of thermodynamical maps and point-to-point radio vs X-ray comparisons. In line with previous works, we found that H1 is spatially confined by inner cold fronts, and that H2 follows a trail of low-entropy gas departing from the warm core in the direction of the southern cold front at $\sim$ 1 Mpc distance from the centre. Our results suggest that H1 and H2 are likely connected; their origin may be associated with an intermediate mass-ratio merger that induced turbulence via intense sloshing motions. Our findings indicate that H1 is a mini-halo powered by sloshing-induced turbulence, but we cannot exclude an hadronic contribution from secondary CRe within the inner $\sim$ 100 kpc; furthermore, more complex dynamical processes could also inject turbulence in H2, and its origin cannot be firmly claimed.

H3 fills the bulk of the volume of the cluster. The radio and X-ray emission are sub-linearly ($k \sim 0.7 - 0.8$) correlated, similarly to a giant radio halo powered by turbulence. Its ultra-steep spectrum suggests two possible formation scenarios. In the first case, H3 would be an extremely old radio halo tracing turbulence induced by the last ($\sim$ 4 Gyr ago) major merger; perturbations from more recent minor and intermediate mergers with groups infalling to the cluster prevent the complete restoring of a typical cool core. As an alternative possibility, H3 may trace inefficient turbulent re-acceleration on large scales triggered by the continuous minor mergers occurring over the cluster volume.

Finally, A2142 is a favoured candidate to host a megahalo given its mass, redshift, size, and ultra-steep spectral index. We investigated the presence of a megahalo with our deep LOFAR HBA data by computing the surface brightness radial profile, but we did not found evidences supporting this hypothesis. We therefore determined upper limits to the surface brightness and volume-averaged emissivity of a possible megahalo in A2142.

Our work allowed us important steps forward a better understanding of the thermal and non-thermal emission of A2142, but many questions are still open. We need to further constrain the possible contribution of secondary CRe in the core. Numerical simulations are required to test the relative roles of large-scale sloshing and infall of groups in the injection of turbulence along the ridge. Furthermore, by estimating the average amount of turbulent energy provided by merging groups in A2142, we might constrain the two scenarios proposed for the origin of H3. Finally, our deep upper limits on the presence of a megahalo need to be compared with current simulations.

The complex environment of A2142 hosts peculiar radio galaxies, such as the prominent head-tail galaxies T1 and T2. We have in plan to study in details some of them to investigate (i.) the origin of the seed CRe that are then re-accelerated by turbulence and (ii.) the interaction between radio galaxies and the ICM. To this aim, we will include the international baselines in our datasets to reach sub-arcsec resolution.

To conclude, we point out that the deep LOFAR LBA observations (PI: L. Bruno) presented in this work include additional mosaic pointings on the Corona Borealis field, which is interacting with the A2142-supercluster, and the space in-between the two targets. In the next future we will analyse these pointings to lead a pioneering search for

diffuse radio emission between these superclusters from cosmic chains of clusters.

Appendix A

X-ray data reduction

In this Appendix we summarise the Chandra and XMM-Newton X-ray data reduction for the *Planck* clusters in LoTSS-DR2 (Chapter 4).

A.0.1 Chandra data reduction and analysis

We analysed Chandra data with the *Chandra* Interactive Analysis of Observations (CIAO) software v4.13 using CALDB v4.9.4 (Fruscione et al. 2006), reprocessing data from the level 1 event files and following the standard data reduction threads[1]. We reprocessed event files using the `chandra_repro` tool and soft proton flares were excluded with the `deflare` task with the `lc_clean` routine analysing the light curves extracted from the S2 chip when in ACIS-I configuration and from the S3 chip when in ACIS-S configuration. We used the `fluximage` tool to produce images in the 0.5−7.0 keV bands and the appropriate exposure and point spread function maps. For the purpose of background subtraction we used the `blanksky` and `blankskyimage` tools to provide a corresponding background image to be subtracted. We detected the point sources using the `wavdetect` tool, and by means of `dmfilth` we replaced their emission with the mean count rate in a surrounding annulus. Images were smoothed to a resolution of 30 kpc at the cluster redshift to minimize the effect of having different physical sizes for the same pixel scale given the broad redshift range of our sample (see the discussion in Yuan & Han 2020). The peak of the X-ray image used as the centre of the cluster has been selected as the brightest pixels in the smoothed image after masking the point sources. When multiple observations were available for the same object, we used the observation with the longest available exposure time. For all cases, our single ObsID images have at least 500 counts, which is a safe limit to have a robust measurement of the X-ray morphological parameters (e.g. Nurgaliev et al. 2013).

A.0.2 XMM-Newton data reduction and analysis

We used XMM-Newton Science Analysis System (SAS) v18.0.0 for XMM-Newton European Photon Imaging Camera (EPIC) data reduction (Gabriel et al. 2004). MOS and pn

[1] http://cxc.harvard.edu/ciao/threads/index.html

event files are obtained from the observation data files with the tasks `emproc` and `epproc`. The out-of-time (OoT) event files of pn are produced by `epproc` as well. We extracted count images in the 0.5−2.0 keV band. OoT count maps are directly subtracted from each pn count image following the user guide[2]. The corresponding exposure maps were generated using task `eexpmap` with parameter `withvignetting=yes`. Each exposure map was then multiplied by the on-axis effective area calculated by `arfgen`.

We used stacked filter wheel closed (FWC) event files as non X-ray backgrounds (NXB). For each ObsID, the FWC event files were reprojected using task `evproject` to match the observation. For the two MOS detectors, the NXB count maps were scaled using the blank regions out-of-FoV. For the pn detector, because of the contamination in out-of-FoV regions, we estimated the scaling factor based on the long term NXB variation due to solar activities, which is described in Zhang et al. (2023).

Point source detection and removal procedures are the same as the Chandra data analysis. For each object, we stacked the point-source-removed NXB subtracted count images and exposure maps, respectively. The stacked net count image was then divided by the stacked exposure map to obtain the final point source free flux map for morphological analysis. The X-ray peak of each object is determined from the 30 kpc Gaussian smoothed flux map.

[2] http://xmm-tools.cosmos.esa.int/external/xmm_user_support/documentation/sas_usg/USG/removingOoTimg.html

Appendix B

Image gallery and tables

In this Appendix we collect the images and tables for our *Planck* clusters in LoTSS-DR2 sample (Chapter 4), which are also available on the project website https://lofar-surveys.org/planck_dr2.html. The tables report: the main properties of the targets in the full PSZ2/LoTSS-DR2 sample (Table B.1), the X-ray morphological parameters for the clusters observed with Chandra/XMM-Newton (Table B.2), and the quantities derived for radio halos (Table B.3).

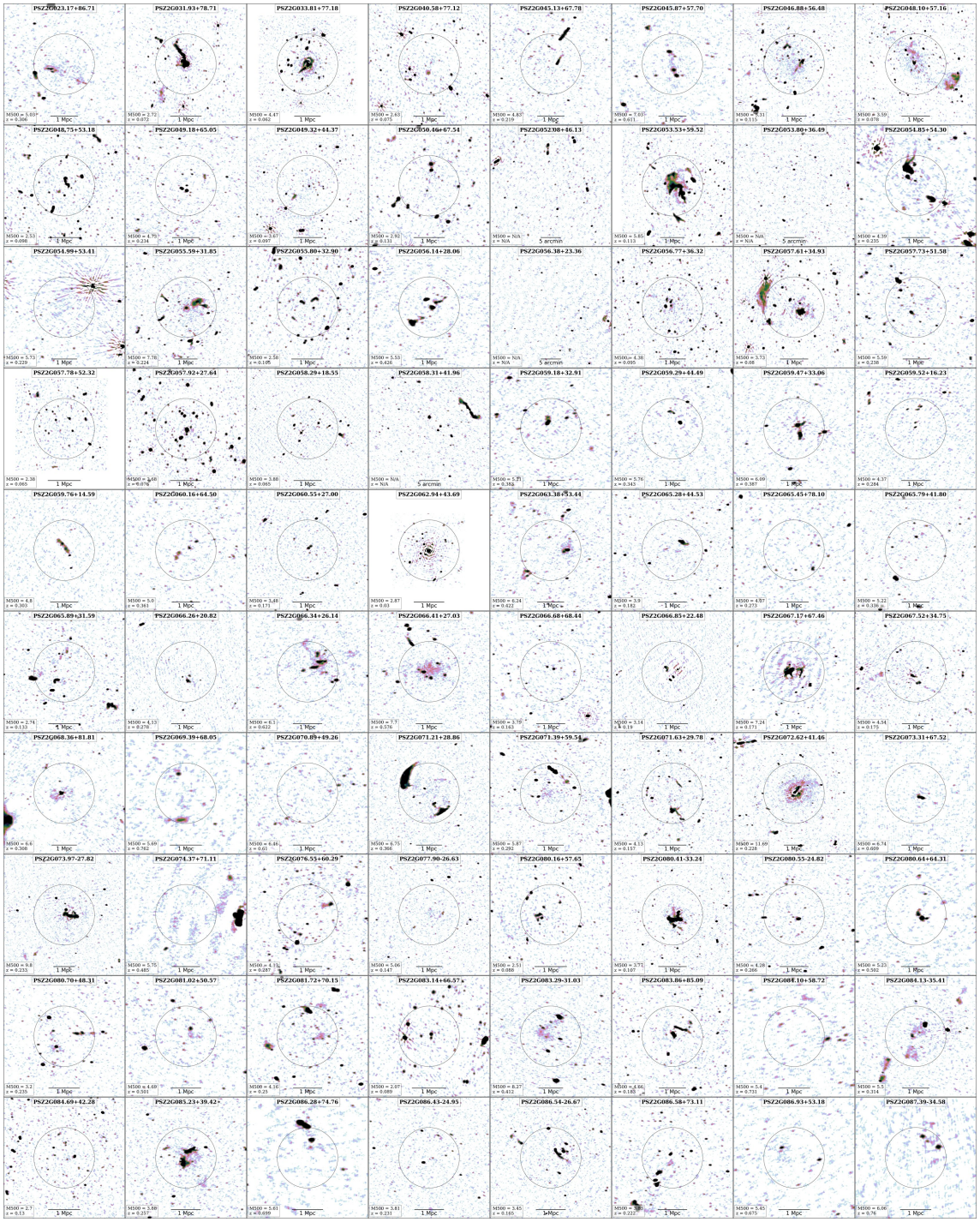

Figure B.1: LOFAR image gallery of the targets in our sample.

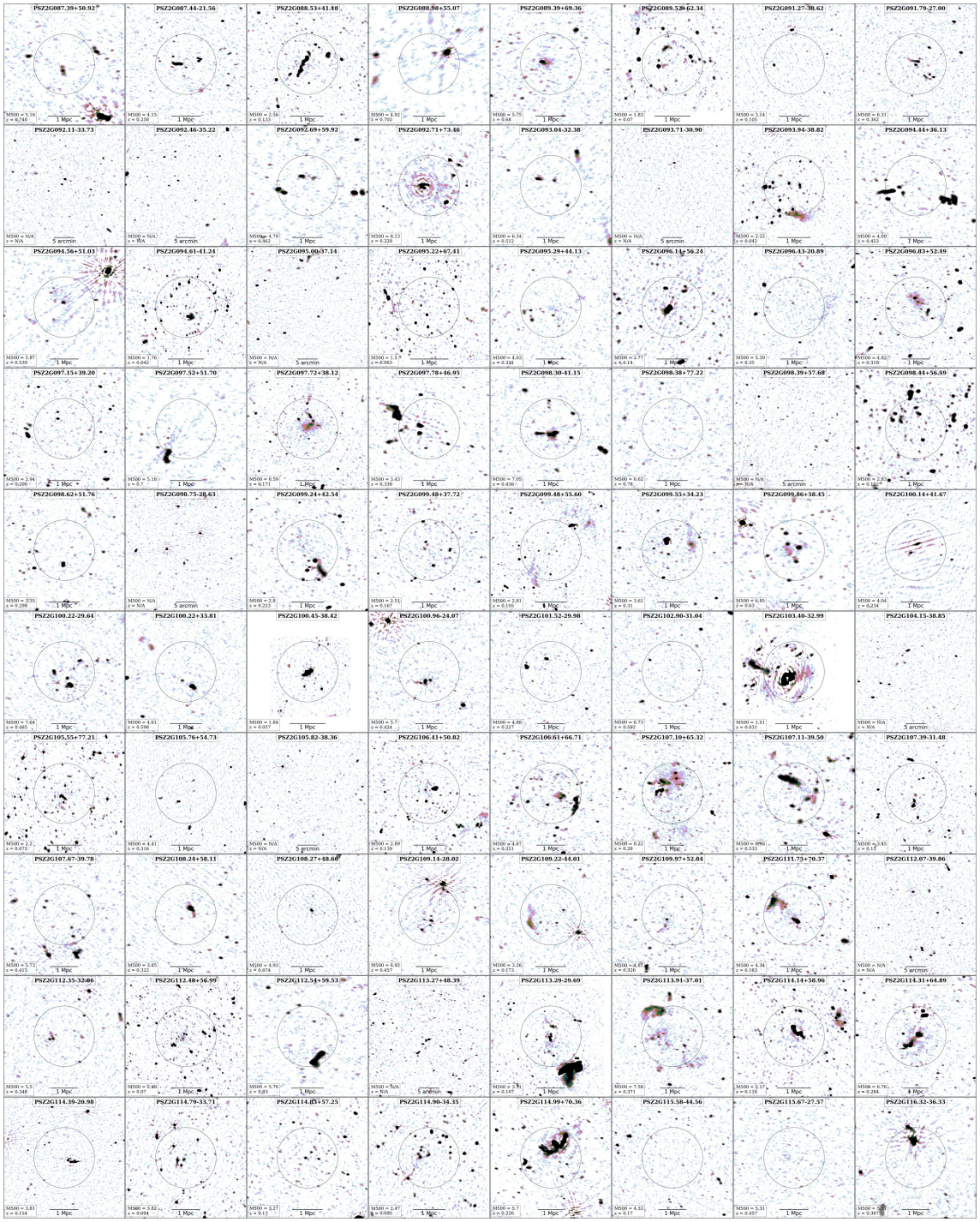

Figure B.1: continued.

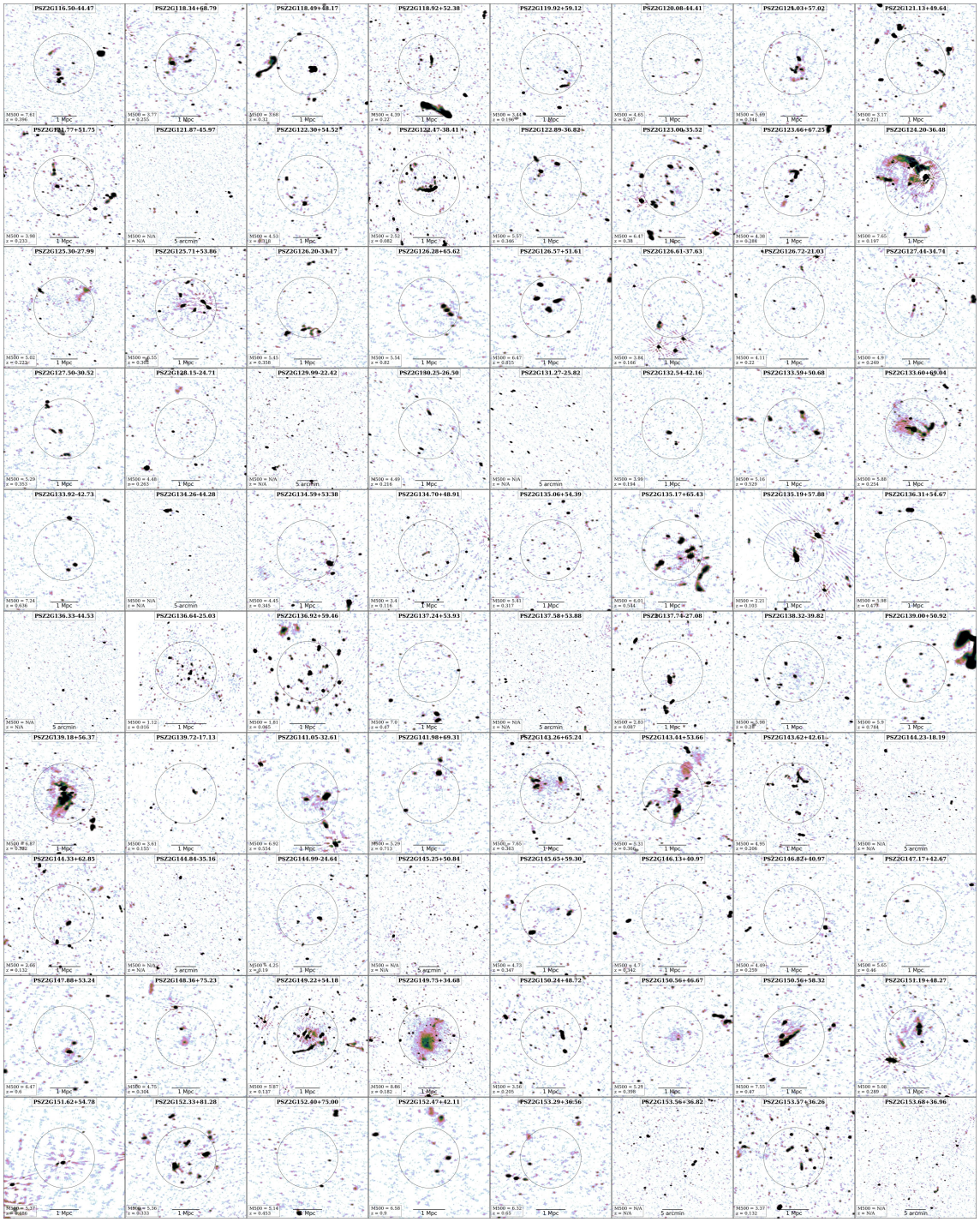

Figure B.1: continued.

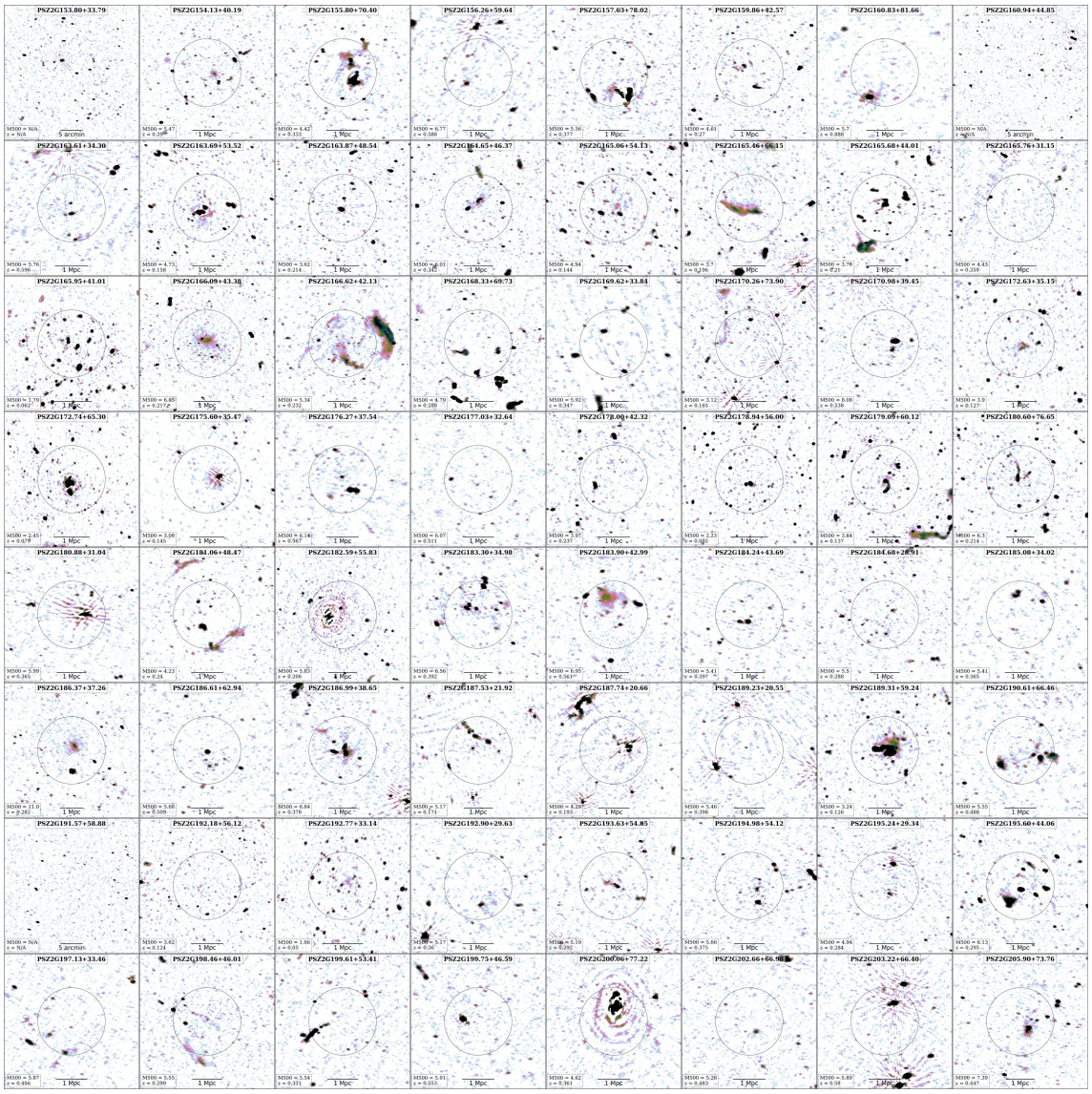

Figure B.1: continued.

Table B.1: The full sample of PSZ2 clusters in LoTSS-DR2.

Name	RA [deg]	DEC [deg]	z	M_{500} [$\times 10^{14}\ M_{\odot}$]	$M_{500\mathrm{err}}$ [$\times 10^{14}\ M_{\odot}$]	r_{500} [kpc]	$r_{500\mathrm{err}}$ [kpc]	IQ	rms [mJy beam^{-1}]	Classification	X-ray	Comment
PSZ2 G023.17+86.71	196.4731	26.5262	0.306	5.03	0.56	1093	41	1	0.093	RH	C/X	New RH
PSZ2 G031.93+78.71	205.4709	26.3684	0.072	2.72	0.24	966	28	2	0.099	RH, U	C/X	U emission on the SE, outside R500
PSZ2 G033.81+77.18	207.2221	26.5946	0.062	4.47	0.14	1144	12	3	0.102	N/A	C/X	—
PSZ2 G040.58+77.12	207.3622	28.0946	0.075	2.63	0.22	955	26	2	0.112	RH	C/X	New RH
PSZ2 G045.13+67.78	217.9958	29.5567	0.219	4.83	0.45	1113	35	1	0.105	NDE	—	—
PSZ2 G045.87+57.70	229.5874	29.4696	0.611	7.03	0.68	1085	35	1	0.110	RH	X	—
PSZ2 G046.88+56.48	231.0469	29.9129	0.115	5.31	0.23	1191	17	1	0.124	RH	C/X	—
PSZ2 G048.10+57.16	230.3161	30.6278	0.078	3.59	0.21	1058	21	1	0.101	RH, RR	C/X	—
PSZ2 G048.75+53.18	234.9669	30.6960	0.098	2.53	0.31	935	39	1	0.124	NDE	C	—
PSZ2 G049.18+65.05	221.1194	31.2334	0.234	4.73	0.49	1099	38	1	0.096	NDE	C	—
PSZ2 G049.32+44.37	245.1404	29.8941	0.097	3.67	0.26	1059	25	2	0.116	RH	C/X	New RH
PSZ2 G050.46+67.54	218.1680	31.5879	0.131	2.92	0.34	971	38	1	0.098	NDE	C	—
PSZ2 G052.08+46.13	243.4439	32.0814						1	0.093	NDE	—	—
PSZ2 G053.53+59.52	227.5546	33.4915	0.113	5.85	0.23	1231	16	1	0.093	RH, U	C/X	U emissions in the outskirts
PSZ2 G053.80+36.49	254.9008	31.7432						1	0.115	NDE	—	—
PSZ2 G054.85+54.30	233.8283	34.3446	0.235	4.39	0.46	1072	38	2	0.099	NDE	—	—
PSZ2 G054.99+53.41	234.9018	34.4313	0.229	5.73	0.38	1174	26	3	0.122	N/A	C/X	—
PSZ2 G055.59+31.85	260.6150	32.1354	0.224	7.78	0.31	1302	17	1	0.106	RH	C/X	—
PSZ2 G055.80+32.90	259.4624	32.5608	0.105	2.58	0.31	939	37	1	0.124	NDE	—	—
PSZ2 G056.14+28.06	265.0748	31.6030	0.426	5.53	0.57	1077	37	1	0.133	NDE	—	—
PSZ2 G056.38+23.36	270.3845	30.3962						2	0.226	NDE	—	—
PSZ2 G056.62+88.42	194.4923	27.7528	0.045	3.30	0.07	1039	7	-1	-1.000	—	—	Toward the direction of the Coma cluster
PSZ2 G056.77+36.32	255.6663	34.0511	0.095	4.38	0.20	1124	17	1	0.123	RH	C/X	New RH
PSZ2 G057.61+34.93	257.4672	34.4613	0.080	3.73	0.19	1071	18	2	0.140	RR, U	C/X	U emission in the center
PSZ2 G057.73+51.58	237.1413	36.1034	0.238	5.59	0.51	1160	36	1	0.113	NDE	—	—
PSZ2 G057.78+52.32	236.2149	36.1219	0.065	2.38	0.22	926	28	1	0.124	NDE	C/X	—
PSZ2 G057.80+88.00	194.9118	27.9537	0.023	7.17	0.09	1356	6	-1	-1.000	—	—	Coma cluster
PSZ2 G057.92+27.64	266.0678	32.9986	0.076	2.68	0.21	961	25	2	0.118	NDE	C/X	—
PSZ2 G058.29+18.55	276.3360	30.4320	0.065	3.88	0.17	1091	16	3	0.555	N/A	C/X	—
PSZ2 G058.31+41.96	249.0508	36.0554						1	0.095	NDE	—	—
PSZ2 G059.18+32.91	260.2029	35.3248	0.383	5.21	0.56	1074	39	1	0.145	NDE	—	—
PSZ2 G059.29+44.49	245.9901	36.9729	0.343	5.76	0.69	1128	45	1	0.123	NDE	—	—
PSZ2 G059.47+33.06	260.0786	35.6002	0.387	6.09	0.58	1129	36	2	0.170	U	C/X	—
PSZ2 G059.52+16.23	279.3393	30.6642	0.284	4.37	0.55	1052	45	3	2.503	N/A	—	Redshift updated from Streblyanska et al. (2019)
PSZ2 G059.76+14.59	281.1949	30.2468	0.303	4.80	0.51	1077	38	3	0.457	N/A	—	Redshift updated from Streblyanska et al. (2019)
PSZ2 G060.10+15.59	280.2784	30.9322	0.190	4.67	0.47	1112	37	-1	-1.000	—	—	—
PSZ2 G060.16+64.50	221.0737	35.9376	0.361	5.00	0.63	1068	45	1	0.088	NDE	—	—
PSZ2 G060.55+27.00	267.5745	35.0761	0.171	3.48	0.41	1015	40	2	0.147	NDE	C/X	—
PSZ2 G061.75+88.11	194.7270	28.0231	0.044	3.40	0.63	1051	66	-1	-1.000	—	—	Toward the direction of the Coma cluster
PSZ2 G062.94+43.69	247.1565	39.5602	0.030	2.87	0.12	997	14	3	0.123	N/A	C/X	—
PSZ2 G063.38+53.44	234.5073	39.4147	0.422	6.24	0.60	1123	36	1	0.111	cRH	—	New cRH
PSZ2 G065.28+44.53	246.0751	41.2470	0.182	3.90	0.48	1050	44	1	0.099	NDE	C	—
PSZ2 G065.45+78.10	204.8180	33.0102	0.273	4.07	0.53	1031	46	1	0.111	NDE	—	—
PSZ2 G065.79+41.80	249.7168	41.5990	0.336	5.22	0.59	1094	42	1	0.094	NDE	—	—
PSZ2 G065.89+31.59	263.2231	40.6419	0.133	2.74	0.36	949	42	1	0.119	NDE	—	—
PSZ2 G066.26+20.82	276.8511	38.2587	0.278	4.13	0.50	1034	42	2	0.194	NDE	—	—
PSZ2 G066.34+26.14	270.3078	39.8546	0.622	6.10	0.67	1031	38	2	0.110	cRH	—	New cRH. Redshift updated from Aguado-Barahona et al. (2019)
PSZ2 G066.41+27.03	269.2019	40.1327	0.576	7.70	0.53	1134	26	1	0.118	RH	C/X	New RH
PSZ2 G066.68+68.44	215.4320	37.2821	0.163	3.79	0.34	1047	32	1	0.083	NDE	C/X	—
PSZ2 G066.85+22.48	275.0416	39.2985	0.190	3.14	0.41	974	43	3	0.354	N/A	—	Redshift updated from Aguado-Barahona et al. (2019)
PSZ2 G067.17+67.46	216.5032	37.8160	0.171	7.24	0.26	1295	16	2	0.192	U	C/X	—
PSZ2 G067.52+34.75	259.3134	42.4618	0.175	4.54	0.34	1107	28	2	0.112	NDE	C/X	—
PSZ2 G068.36+81.81	200.6946	31.6565	0.308	6.60	0.43	1195	26	2	0.163	NDE	X	—
PSZ2 G069.39+68.05	215.4044	38.3613	0.762	5.69	0.77	952	43	2	0.183	cRH, cRR	—	New cRH and cRR. Redshift updated from Buddendiek et al. (2015)
PSZ2 G070.89+49.26	239.1791	44.6533	0.610	6.46	0.69	1055	38	1	0.087	NDE	X	—
PSZ2 G071.21+28.86	268.0130	44.6695	0.366	6.75	0.45	1178	26	1	0.101	RH, RR	X	Double RR
PSZ2 G071.39+59.54	225.3359	42.3464	0.292	5.87	0.42	1157	27	2	0.084	RH*	C/X	New RH*
PSZ2 G071.63+29.78	266.8257	45.1899	0.157	4.13	0.29	1080	25	1	0.101	NDE	C/X	Possible revived fossil plasma in the S
PSZ2 G072.62+41.46	250.0941	46.7103	0.228	11.69	0.26	1490	11	3	0.111	N/A	C/X	—
PSZ2 G073.31+67.52	215.1737	39.9245	0.609	6.74	0.59	1071	31	3	0.475	N/A	C/X	—
PSZ2 G073.97-27.82	328.4233	17.6986	0.233	9.80	0.28	1402	13	2	0.216	NDE	C/X	—
PSZ2 G074.37+71.11	210.9114	38.4697	0.485	5.75	0.58	1067	36	3	0.169	N/A	C	—
PSZ2 G075.08+19.83	281.6991	45.7759	0.200	3.45	0.38	1002	37	-1	-1.000	—	—	Redshift updated from Streblyanska et al. (2019)
PSZ2 G076.55+60.29	223.0302	44.4554	0.287	4.13	0.48	1031	40	1	0.067	RH*	C	New RH*. Redshift updated from Streblyanska et al. (2018)
PSZ2 G077.90-26.63	330.2281	20.9701	0.147	5.06	0.26	1160	20	2	0.216	RH*	C/X	New RH*
PSZ2 G080.16+57.65	225.2369	47.2874	0.088	2.51	0.21	937	26	1	0.127	RR	C/X	—
PSZ2 G080.41-33.24	336.5396	17.3767	0.107	3.77	0.27	1066	26	1	0.139	NDE	C/X	Revived fossil plasma
PSZ2 G080.55-24.82	330.8550	23.9105	0.266	4.28	0.53	1051	43	1	0.135	NDE	—	—
PSZ2 G080.64+64.31	216.8313	44.1308	0.502	5.23	0.59	1026	39	1	0.133	NDE	C	—
PSZ2 G080.70+48.31	238.2988	51.1483	0.235	3.20	0.41	965	41	1	0.068	cRH	—	New cRH
PSZ2 G081.02+50.57	234.8082	50.6137	0.501	4.69	0.54	991	38	1	0.061	RH	X	New RH

Table B.1: continued.

Name	RA [deg]	DEC [deg]	z	M_{500} [$\times 10^{14}\ M_{\odot}$]	$M_{500\,\mathrm{err}}$ [$\times 10^{14}\ M_{\odot}$]	r_{500} [kpc]	$r_{500\,\mathrm{err}}$ [kpc]	IQ	rms [mJy beam^{-1}]	Classification	X-ray	Comment
PSZ2 G081.72+70.15	210.0995	41.0129	0.250	4.16	0.44	1047	37	1	0.097	U	C	Two uncertain sources located to the W with respect to the bulk of the X-ray emission
PSZ2 G083.14+66.57	213.4445	43.6523	0.089	2.07	0.26	878	36	2	0.077	NDE	—	—
PSZ2 G083.29-31.03	337.1296	20.6221	0.412	8.27	0.44	1239	22	1	0.118	RH	C/X	New RH
PSZ2 G083.86+85.09	196.4623	30.8931	0.183	4.66	0.33	1114	27	1	0.079	NDE	C/X	—
PSZ2 G084.10+58.72	222.3158	48.5589	0.731	5.40	0.62	947	36	1	0.073	RH	C/X	—
PSZ2 G084.13-35.41	340.4853	17.5233	0.314	5.50	0.58	1122	40	2	0.127	RH, U	X	New RH. U emission to the S of the RH
PSZ2 G084.69+42.28	246.7659	55.4802	0.130	2.70	0.26	946	31	1	0.068	NDE	X	—
PSZ2 G085.23+39.42	251.6292	56.4674	0.257	3.88	0.39	1021	35	1	0.083	cRH	—	New cRH
PSZ2 G086.28+74.76	204.4773	38.8708	0.699	5.61	0.71	972	41	3	0.091	N/A	—	Redshift updated from Streblyanska et al. (2018)
PSZ2 G086.43-24.95	335.5578	27.1430	0.231	3.81	0.50	1024	46	1	0.127	NDE	—	—
PSZ2 G086.54-26.67	336.7802	25.8145	0.165	3.45	0.39	1015	39	1	0.120	NDE	C	—
PSZ2 G086.58+73.11	205.8750	40.1328	0.222	3.83	0.50	1029	45	1	0.073	cRR, U	—	New cRR. U emission in the center
PSZ2 G086.93+53.18	228.4787	52.7984	0.675	5.45	0.51	971	30	1	0.101	RH	C/X	—
PSZ2 G087.39-34.58	342.3068	19.7139	0.760	6.06	0.63	973	34	2	0.184	NDE	—	Redshift updated from Streblyanska et al. (2018)
PSZ2 G087.39+50.92	231.5690	54.1431	0.748	5.16	0.57	927	34	3	0.098	N/A	X	—
PSZ2 G087.44-21.56	334.0988	30.4251	0.258	4.15	0.51	1043	43	1	0.120	NDE	—	—
PSZ2 G088.53+41.18	247.3887	58.5338	0.133	2.56	0.34	929	42	1	0.076	NDE	—	Complex radio emission associated to the brightest optical galaxy
PSZ2 G088.98+55.07	224.7806	52.8020	0.702	4.92	0.62	929	39	3	0.105	N/A	C/X	—
PSZ2 G089.39+69.36	208.4259	43.4835	0.680	5.75	0.72	987	41	1	0.067	cRH	—	—
PSZ2 G089.52+62.34	215.5299	48.4769	0.070	1.83	0.19	847	30	2	0.078	RR	C	Two RR located in the N
PSZ2 G091.27-38.62	347.3346	17.8953	0.105	3.14	0.39	1003	42	2	0.146	NDE	—	Redshift updated from Barrena et al. (2018)
PSZ2 G091.79-27.00	341.3603	28.1444	0.362	6.31	0.48	1154	29	1	0.104	RR	X	New RR
PSZ2 G092.11-33.73	345.4059	22.4833						2	0.161	NDE	—	—
PSZ2 G092.46-35.22	346.4589	21.3244						1	0.141	NDE	—	—
PSZ2 G092.69+59.92	216.6347	51.2521	0.462	4.79	0.60	1013	43	1	0.078	NDE	C/X	Redshift updated from Aguado-Barahona et al. (2019)
PSZ2 G092.71+73.46	203.8014	41.0004	0.228	8.13	0.27	1320	14	3	0.075	N/A	C/X	—
PSZ2 G093.04-32.38	345.4276	24.0403	0.512	6.34	0.72	1090	42	2	0.200	NDE	—	Redshift updated from Barrena et al. (2018)
PSZ2 G093.71-30.90	345.1839	25.6114						3	0.350	N/A	—	—
PSZ2 G093.94-38.82	349.3656	18.7010	0.042	2.22	0.17	912	23	1	0.192	U	C/X	—
PSZ2 G094.44+36.13	255.2898	64.2391	0.453	4.09	0.43	964	34	1	0.078	NDE	C/X	—
PSZ2 G094.56+51.03	227.0614	57.8918	0.539	5.87	0.44	1051	26	3	0.086	N/A	X	—
PSZ2 G094.61-41.24	350.9896	16.7655	0.042	1.76	0.23	845	37	2	0.128	U	C/X	—
PSZ2 G095.00-37.14	349.3564	20.5736						1	0.144	NDE	—	—
PSZ2 G095.22+67.41	207.8526	46.3557	0.062	1.50	0.21	795	38	1	0.084	U	X	—
PSZ2 G095.29+44.13	238.1346	62.0545	0.331	4.03	0.35	1006	29	2	0.103	cRH*	—	New cRH*
PSZ2 G096.14+56.24	218.8388	55.1414	0.140	2.77	0.25	951	28	2	0.086	NDE	—	—
PSZ2 G096.43-20.89	342.0362	35.5560	0.350	5.39	0.51	1100	34	2	0.122	cRR	—	New cRR. Redshift updated from Boada et al. (2019)
PSZ2 G096.83+52.49	223.2488	58.0366	0.318	4.92	0.37	1080	27	1	0.073	RH	C	—
PSZ2 G097.15+39.20	246.9034	65.3963	0.206	2.94	0.32	948	34	1	0.088	NDE	—	—
PSZ2 G097.52+51.70	223.8162	58.8752	0.700	5.18	0.51	946	31	2	0.105	U	X	—
PSZ2 G097.72+38.12	248.9776	66.2023	0.171	6.59	0.16	1255	10	1	0.076	RH	C/X	—
PSZ2 G097.78+46.95	231.0525	62.0227	0.338	3.43	0.39	950	36	2	0.104	NDE	—	—
PSZ2 G098.30-41.15	353.5972	18.0003	0.436	7.05	0.61	1164	34	1	0.100	cRH	—	New cRH
PSZ2 G098.38+77.22	199.6059	38.5853	0.780	6.62	0.71	994	36	1	0.102	NDE	—	Redshift updated from Boada et al. (2019)
PSZ2 G098.39+57.68	215.5698	54.9011						1	0.091	NDE	—	—
PSZ2 G098.44+56.59	216.7791	55.7497	0.132	2.83	0.27	960	30	1	0.090	NDE	—	—
PSZ2 G098.62+51.76	222.8271	59.3306	0.298	3.35	0.48	958	47	2	0.075	NDE	—	Redshift updated from Streblyanska et al. (2018)
PSZ2 G098.75-28.63	348.4410	29.6117						2	0.113	NDE	—	—
PSZ2 G099.24+42.54	238.0378	65.3405	0.223	2.80	0.39	927	43	1	0.104	U	—	U emissions in the center and outskirts
PSZ2 G099.48+37.72	248.6714	67.6423	0.167	2.51	0.28	911	34	1	0.104	U	—	—
PSZ2 G099.48+55.60	217.1485	56.8766	0.105	2.81	0.21	967	25	1	0.098	RR	C/X	New RR. Double RR
PSZ2 G099.55+34.23	257.6109	68.7321	0.310	3.61	0.38	977	34	1	0.112	cRH*, U	—	New cRH*. U emission in the W. Redshift updated from Aguado-Barahona et al. (2019)
PSZ2 G099.86+58.45	213.6782	54.7836	0.630	6.85	0.49	1067	25	2	0.075	RH	C/X	—
PSZ2 G100.14+41.67	239.0257	66.3545	0.234	4.04	0.28	1044	24	3	0.315	N/A	C	—
PSZ2 G100.22-29.64	350.2543	29.2136	0.485	7.64	0.59	1173	30	2	0.135	NDE	—	—
PSZ2 G100.22+33.81	258.4193	69.3734	0.598	4.61	0.47	947	33	2	0.169	NDE	—	Redshift updated from Streblyanska et al. (2019)
PSZ2 G100.45-38.42	354.1311	21.1519	0.057	1.84	0.27	853	42	1	0.143	NDE	C/X	Revived fossil plasma
PSZ2 G100.96-24.07	348.3483	34.5796	0.424	5.70	0.73	1089	47	2	0.119	cRH	—	—
PSZ2 G101.52-29.98	351.5963	29.3258	0.227	4.88	0.52	1114	39	1	0.114	NDE	—	—
PSZ2 G102.90-31.04	353.3020	28.7678	0.592	6.73	0.72	1078	39	2	0.111	NDE	—	—
PSZ2 G103.40-32.99	354.5043	27.0818	0.031	1.51	0.13	805	23	3	0.164	N/A	X	—
PSZ2 G104.15-38.85	357.2018	21.7235						1	0.095	NDE	—	—
PSZ2 G105.55+77.21	197.7544	39.2463	0.072	2.20	0.22	900	30	1	0.140	U	X	—
PSZ2 G105.76+54.73	212.5897	59.6801	0.316	4.41	0.45	1042	36	1	0.149	NDE	—	—
PSZ2 G105.82-38.36	358.3931	22.5789						1	0.098	NDE	—	—
PSZ2 G106.41+50.82	216.3149	63.1860	0.139	2.89	0.25	964	27	1	0.073	U	C/X	—
PSZ2 G106.61+66.71	202.6355	49.1529	0.331	4.67	0.56	1056	42	1	0.055	RH	C	—
PSZ2 G107.10+65.32	203.1777	50.5183	0.280	8.22	0.28	1300	15	1	0.075	RH, RR	C/X	Double RH. Radio bridge. RR in A1758S. Revived fossil plasma
PSZ2 G107.11-39.50	359.7704	21.7518	0.533	6.93	0.67	1114	36	1	0.102	U	—	—
PSZ2 G107.39-31.48	357.6390	29.5399	0.150	3.45	0.45	1019	45	1	0.104	NDE	—	—
PSZ2 G107.67-39.78	0.3019	21.5932	0.415	5.73	0.75	1095	48	2	0.101	U	—	—

Table B.1: continued.

Name	RA [deg]	DEC [deg]	z	M_{500} [$\times 10^{14}\ M_{\odot}$]	$M_{500\,\mathrm{err}}$ [$\times 10^{14}\ M_{\odot}$]	r_{500} [kpc]	$r_{500\,\mathrm{err}}$ [kpc]	IQ	rms [mJy beam^{-1}]	Classification	X-ray	Comment
PSZ2 G108.24+58.11	207.2301	57.3469	0.322	3.85	0.53	994	46	1	0.183	U	—	—
PSZ2 G108.27+48.66	216.7773	65.6528	0.674	4.93	0.49	940	32	1	0.134	cRH	—	New cRH
PSZ2 G109.14-28.02	358.2865	33.2800	0.457	6.92	0.62	1147	34	3	0.096	N/A	—	—
PSZ2 G109.22-44.01	2.5556	17.7559	0.173	3.26	0.48	993	49	2	0.190	cRR	—	New cRR
PSZ2 G109.97+52.84	209.9356	62.5279	0.326	4.81	0.38	1069	28	1	0.067	RH	C	New RH
PSZ2 G111.75+70.37	198.2642	46.2812	0.183	4.34	0.33	1088	27	1	0.076	RH, RR	C/X	RR in the NE
PSZ2 G112.07-39.86	3.8730	22.2454						2	0.135	NDE	—	—
PSZ2 G112.35-32.86	2.6884	29.1673	0.348	5.50	0.68	1108	46	2	0.166	NDE	X	—
PSZ2 G112.48+56.99	203.9932	59.2210	0.070	2.99	0.15	998	17	1	0.058	RH	C	New RH
PSZ2 G112.54+59.53	202.4759	56.8123	0.830	5.76	0.66	930	36	1	0.071	NDE	—	Redshift updated from Zohren et al. (2019)
PSZ2 G113.27+48.39	209.7444	67.4431						1	0.072	NDE	—	—
PSZ2 G113.29-29.69	2.9363	32.4325	0.107	3.71	0.27	1060	25	2	0.114	U	C/X	—
PSZ2 G113.91-37.01	4.9004	25.2965	0.371	7.58	0.55	1223	30	1	0.122	RH, RR	C/X	New RH and RR. Double RR
PSZ2 G114.14+58.96	201.3065	57.5834	0.116	2.17	0.30	884	41	2	0.069	NDE	—	Possible revived fossil plasma
PSZ2 G114.31+64.89	198.7658	51.8329	0.284	6.76	0.37	1216	22	1	0.071	RH	C/X	—
PSZ2 G114.39-20.98	2.2522	41.1782	0.154	3.81	0.35	1053	32	1	0.187	NDE	—	—
PSZ2 G114.79-33.71	5.1456	28.6657	0.094	3.82	0.22	1075	21	2	0.133	NDE	C/X	—
PSZ2 G114.83+57.25	201.4457	59.3305	0.170	3.27	0.30	995	31	1	0.076	NDE	—	—
PSZ2 G114.90-34.35	5.3526	28.0504	0.095	2.47	0.32	929	41	2	0.140	U	—	—
PSZ2 G114.99+70.36	196.7286	46.5257	0.226	5.70	0.35	1174	24	2	0.086	U	C	Complex radio emission
PSZ2 G115.58-44.56	7.3620	17.9947	0.170	4.32	0.40	1091	34	1	0.100	NDE	—	—
PSZ2 G115.67-27.57	5.0172	34.8529	0.457	5.31	0.75	1050	50	1	0.100	cRH	—	—
PSZ2 G116.32-36.33	6.9294	26.2373	0.367	5.31	0.63	1087	43	3	0.128	N/A	C/X	—
PSZ2 G116.50-44.47	8.0345	18.1536	0.396	7.61	0.60	1213	32	1	0.111	RH*, RR	X	New RH* and RR
PSZ2 G118.34+68.79	195.3484	48.2419	0.255	3.77	0.49	1012	44	1	0.071	cRH*	—	—
PSZ2 G118.49+48.17	201.0202	68.6690	0.320	3.68	0.41	980	37	1	0.077	NDE	—	Redshift updated from Aguado-Barahona et al. (2019)
PSZ2 G118.92+52.38	198.5514	64.5643	0.220	4.39	0.29	1078	24	1	0.059	U	—	—
PSZ2 G119.92+59.12	195.7642	57.9334	0.196	3.44	0.33	1002	32	1	0.072	U	—	—
PSZ2 G120.08-44.41	10.7148	18.4071	0.267	4.65	0.64	1080	49	2	0.218	NDE	—	—
PSZ2 G121.03+57.02	194.9266	60.0741	0.344	5.69	0.43	1123	28	1	0.089	RR, U	C	New RR. U emission in the center
PSZ2 G121.13+49.64	195.8869	67.4415	0.221	3.17	0.36	967	37	1	0.091	NDE	X	—
PSZ2 G121.77+51.75	194.5723	65.3600	0.233	3.98	0.41	1038	35	1	0.056	NDE	—	—
PSZ2 G121.87-45.97	12.0892	16.8876						2	0.237	NDE	—	—
PSZ2 G122.30+54.52	193.6463	62.5963	0.318	4.53	0.45	1050	35	1	0.094	NDE	—	—
PSZ2 G122.47-38.41	12.4689	24.4527	0.082	2.52	0.31	939	38	2	0.115	U	—	—
PSZ2 G122.89-36.82	12.8246	26.0510	0.346	5.57	0.73	1114	49	1	0.083	NDE	—	—
PSZ2 G123.00-35.52	12.9231	27.3461	0.380	6.47	0.65	1156	39	2	0.077	RH*	X	New RH*
PSZ2 G123.66+67.25	192.4223	49.8718	0.284	4.38	0.51	1053	41	1	0.064	NDE	C	—
PSZ2 G124.20-36.48	14.0018	26.3784	0.197	7.65	0.36	1308	20	3	0.113	N/A	C/X	—
PSZ2 G125.30-27.99	15.4081	34.8346	0.223	5.02	0.55	1126	41	1	0.111	U	—	—
PSZ2 G125.71+53.86	189.2251	63.1843	0.302	6.55	0.33	1195	20	3	0.072	N/A	C/X	—
PSZ2 G126.20-33.17	16.0136	29.6172	0.358	5.45	0.74	1101	50	1	0.123	NDE	—	—
PSZ2 G126.28+65.62	190.6409	51.4447	0.820	5.54	0.66	922	37	1	0.055	U	—	Redshift updated from Burenin et al. (2018)
PSZ2 G126.57+51.61	187.4359	65.3561	0.815	6.47	0.61	973	31	1	0.066	NDE	C	Redshift updated from Burenin et al. (2018)
PSZ2 G126.61-37.63	16.0784	25.1450	0.166	3.84	0.50	1050	46	3	0.169	N/A	X	—
PSZ2 G126.72-21.03	17.6030	41.6924	0.220	4.11	0.57	1055	49	1	0.110	NDE	—	Redshift updated from Burenin et al. (2018)
PSZ2 G127.44-34.74	17.0569	27.9786	0.249	4.90	0.71	1106	54	2	0.131	NDE	—	—
PSZ2 G127.50-30.52	17.5164	32.1829	0.353	5.29	0.67	1092	46	1	0.107	NDE	X	—
PSZ2 G128.15-24.71	18.8768	37.9135	0.263	4.48	0.60	1068	48	1	0.069	NDE	—	Redshift updated from Streblyanska et al. (2019)
PSZ2 G129.99-22.42	21.3891	39.9803						1	0.081	NDE	—	—
PSZ2 G130.25-26.50	20.9524	35.9025	0.216	4.49	0.50	1088	40	2	0.102	NDE	—	—
PSZ2 G131.27-25.82	22.2049	36.4447						1	0.141	NDE	—	—
PSZ2 G132.54-42.16	20.4346	20.1398	0.194	3.99	0.51	1054	45	1	0.152	NDE	X	—
PSZ2 G133.59+50.68	176.7040	65.0891	0.529	5.16	0.57	1011	37	1	0.076	RH*	X	New RH*
PSZ2 G133.60+69.04	187.2235	47.6123	0.254	5.88	0.40	1173	27	1	0.069	RH	C	Possible revived fossil plasma
PSZ2 G133.92-42.73	21.4010	19.4054	0.636	7.24	0.96	1085	48	1	0.116	NDE	—	Redshift updated from Burenin (2017)
PSZ2 G134.26-44.28	21.3587	17.8353						1	0.152	NDE	—	—
PSZ2 G134.59+53.38	177.7969	62.3578	0.345	4.45	0.54	1034	42	2	0.080	NDE	—	—
PSZ2 G134.70+48.91	173.3085	66.3869	0.116	3.40	0.22	1027	22	2	0.107	NDE	C/X	—
PSZ2 G135.06+54.39	178.0903	61.3191	0.317	5.41	0.42	1115	29	1	0.065	NDE	—	—
PSZ2 G135.17+65.43	184.8205	50.9217	0.544	6.01	0.60	1057	35	2	0.071	RH, RR	C	—
PSZ2 G135.19+57.88	180.5387	58.0593	0.103	2.21	0.23	893	31	3	0.133	N/A	C	—
PSZ2 G136.31+54.67	176.9598	60.7656	0.477	5.98	0.51	1084	31	1	0.069	NDE	—	Redshift updated from Streblyanska et al. (2019)
PSZ2 G136.33-44.53	22.8257	17.3003						1	0.197	NDE	—	—
PSZ2 G136.64-25.03	28.2988	36.1888	0.016	1.12	0.11	732	24	2	0.125	NDE	C/X	—
PSZ2 G136.92+59.46	180.0852	56.2524	0.065	1.81	0.16	846	25	2	0.103	U	X	—
PSZ2 G137.24+53.93	175.2772	61.1942	0.470	7.00	0.48	1146	26	1	0.063	NDE	—	Redshift updated from Boada et al. (2019)
PSZ2 G137.58+53.88	174.8622	61.1503						1	0.084	NDE	—	—
PSZ2 G137.74-27.08	28.7835	33.9443	0.087	2.83	0.28	975	32	2	0.123	NDE	X	Possible revived fossil plasma
PSZ2 G138.32-39.82	25.5157	21.5330	0.280	5.98	0.56	1169	37	1	0.138	RH	C	—
PSZ2 G139.00+50.92	170.0451	63.2596	0.784	5.90	0.70	955	38	1	0.077	NDE	—	Redshift updated from Aguado-Barahona et al. (2019)

Table B.1: continued.

Name	RA [deg]	DEC [deg]	z	M_{500} [$\times 10^{14}\ M_{\odot}$]	$M_{500\,\mathrm{err}}$ [$\times 10^{14}\ M_{\odot}$]	r_{500} [kpc]	$r_{500\,\mathrm{err}}$ [kpc]	IQ	rms [mJy beam^{-1}]	Classification	X-ray	Comment
PSZ2 G139.18+56.37	175.5928	58.5227	0.322	6.87	0.38	1205	22	1	0.068	RH	C/X	—
PSZ2 G139.72-17.13	34.9806	42.8317	0.155	3.61	0.44	1033	42	1	0.153	NDE	—	Redshift updated from Streblyanska et al. (2019)
PSZ2 G141.05-32.61	30.0905	27.8208	0.554	6.92	0.77	1104	41	2	0.124	cRH	—	New cRH
PSZ2 G141.98+69.31	183.2387	46.3648	0.713	5.29	0.68	948	40	1	0.087	NDE	—	Redshift updated from Aguado-Barahona et al. (2019)
PSZ2 G143.26+65.24	179.8427	49.7742	0.363	7.65	0.43	1230	23	1	0.061	RH	C/X	—
PSZ2 G143.44+53.66	168.7489	59.4513	0.366	5.31	0.57	1088	39	2	0.067	U	—	Possible revived fossil plasma
PSZ2 G143.62+42.61	150.8432	67.1371	0.206	4.95	0.34	1127	26	1	0.087	NDE	—	—
PSZ2 G144.23-18.19	39.7214	40.1886						1	0.096	cRH	—	New cRH
PSZ2 G144.33+62.85	177.3062	51.6086	0.132	2.66	0.35	940	42	1	0.063	NDE	—	—
PSZ2 G144.84-35.16	32.4230	24.3554						1	0.092	NDE	—	—
PSZ2 G144.99-24.64	37.1891	34.0270	0.190	4.25	0.50	1077	42	2	0.097	cRR, U	—	New cRR. U emission located in the center of the images
PSZ2 G145.25+50.84	163.3572	60.8620						1	0.073	NDE	—	—
PSZ2 G145.65+59.30	173.1514	54.2102	0.347	4.73	0.61	1054	46	2	0.076	U	X	—
PSZ2 G146.13+40.97	144.7845	66.4371	0.342	4.70	0.65	1054	49	1	0.076	NDE	—	Redshift updated from Aguado-Barahona et al. (2019)
PSZ2 G146.82+40.97	144.1849	65.9752	0.259	4.49	0.27	1071	21	1	0.070	NDE	—	—
PSZ2 G147.17+42.67	147.4525	64.9221	0.460	5.65	0.72	1071	46	1	0.078	NDE	—	Redshift updated from Aguado-Barahona et al. (2019)
PSZ2 G147.88+53.24	164.3924	58.0187	0.600	6.47	0.60	1060	33	1	0.065	cRH	—	—
PSZ2 G148.36+75.23	184.6185	40.2211	0.304	4.75	0.50	1073	38	1	0.075	RH	C	New RH
PSZ2 G149.22+54.18	164.6039	56.7926	0.137	5.87	0.22	1222	15	2	0.083	RH	C	—
PSZ2 G149.75+34.68	127.7147	65.8623	0.182	8.86	0.32	1381	17	1	0.069	RH	C/X	—
PSZ2 G150.24+48.72	155.8514	59.8085	0.205	3.56	0.42	1010	40	1	0.066	NDE	—	—
PSZ2 G150.56+46.67	152.1830	60.7778	0.398	5.21	0.62	1068	42	1	0.061	cRH	—	—
PSZ2 G150.56+58.32	168.7952	53.3275	0.470	7.55	0.51	1175	26	2	0.075	RH	C/X	—
PSZ2 G151.19+48.27	154.4084	59.5510	0.289	5.08	0.47	1103	34	2	0.059	RH, RR	C/X	—
PSZ2 G151.62+54.78	163.7128	55.3610	0.486	5.37	0.72	1042	47	3	0.155	N/A	—	—
PSZ2 G152.33+81.28	187.6699	34.6290	0.333	5.36	0.55	1105	38	2	0.084	NDE	—	Possible revived fossil plasma
PSZ2 G152.40+75.00	183.3147	39.8577	0.453	5.14	0.70	1040	47	1	0.074	NDE	—	Redshift updated from Streblyanska et al. (2018)
PSZ2 G152.47+42.11	142.4647	61.6579	0.900	6.58	0.77	946	37	1	0.096	NDE	—	Redshift updated from Aguado-Barahona et al. (2019)
PSZ2 G153.29+36.56	130.6776	62.6758	0.650	6.32	1.27	1031	68	1	0.077	NDE	—	—
PSZ2 G153.56+36.82	131.1332	62.4117						1	0.068	NDE	—	—
PSZ2 G153.57+36.26	129.9422	62.5148	0.132	3.37	0.39	1018	39	1	0.077	NDE	—	—
PSZ2 G153.68+36.96	131.3866	62.2867						1	0.070	NDE	—	—
PSZ2 G153.80+33.79	124.5597	62.6820						1	0.070	NDE	—	—
PSZ2 G154.13+40.19	137.8076	61.1324	0.290	5.47	0.45	1131	31	1	0.087	cRH	—	New cRH
PSZ2 G155.80+70.40	178.4833	42.8600	0.333	4.42	0.56	1036	44	1	0.071	NDE	—	Possible revived fossil plasma
PSZ2 G156.26+59.64	167.1024	50.2811	0.588	6.77	0.60	1081	32	2	0.096	cRH	—	—
PSZ2 G157.63+78.02	184.3872	36.7167	0.377	5.56	0.57	1100	38	2	0.072	U	—	—
PSZ2 G159.86+42.57	139.8791	56.3460	0.270	4.61	0.57	1076	44	1	0.080	NDE	—	—
PSZ2 G160.83+81.66	186.7250	33.5703	0.888	5.70	0.66	906	35	1	0.087	RH	C/X	—
PSZ2 G160.94+44.85	143.3681	54.9523						1	0.082	NDE	—	—
PSZ2 G163.61+34.30	124.7099	54.5333	0.596	5.76	0.74	1021	44	2	0.079	cRH*	—	New cRH*
PSZ2 G163.69+53.52	155.5975	50.1197	0.158	4.73	0.31	1130	24	2	0.090	U	C	—
PSZ2 G163.87+48.54	148.2005	51.8883	0.214	3.62	0.43	1013	41	1	0.059	NDE	C	—
PSZ2 G164.65+46.37	144.5898	52.0336	0.342	6.01	0.55	1144	35	1	0.070	RH	C	New RH
PSZ2 G165.06+54.13	155.9404	49.1327	0.144	4.94	0.28	1152	22	1	0.078	RH	C	—
PSZ2 G165.46+66.15	170.9186	43.0135	0.196	3.70	0.42	1027	39	1	0.108	RR	C	Double RR
PSZ2 G165.68+44.01	140.5859	51.8876	0.210	3.76	0.50	1027	46	1	0.072	NDE	—	—
PSZ2 G165.76+31.15	119.5415	52.5986	0.259	4.43	0.66	1066	54	2	0.131	NDE	—	—
PSZ2 G165.95+41.01	135.7227	52.2021	0.062	1.79	0.26	843	40	1	0.079	NDE	C/X	—
PSZ2 G166.09+43.38	139.4836	51.7221	0.217	6.85	0.32	1251	20	1	0.074	RH	C/X	—
PSZ2 G166.62+42.13	137.3948	51.5489	0.232	5.34	0.40	1145	28	1	0.081	RH, RR	C	RH contaminated by RR emission. Multiple RR
PSZ2 G168.33+69.73	174.0505	40.1032	0.288	4.79	0.50	1083	37	1	0.102	U	C	Possible revived fossil plasma
PSZ2 G169.62+33.84	124.1776	49.5502	0.347	5.92	0.63	1136	40	3	0.125	N/A	—	—
PSZ2 G170.26+73.90	178.0167	37.2537	0.165	3.12	0.42	981	45	2	0.094	U	—	—
PSZ2 G170.98+39.45	132.7602	48.5104	0.538	8.08	0.68	1170	33	2	0.092	U	C	—
PSZ2 G172.63+35.15	126.3699	47.1532	0.127	3.90	0.34	1071	31	1	0.180	RH	C	New RH
PSZ2 G172.74+65.30	167.9029	40.8574	0.079	2.45	0.21	932	27	2	0.105	U	C/X	Possible revived fossil plasma
PSZ2 G175.60+35.47	127.0828	44.7549	0.145	3.08	0.40	983	43	2	0.109	U	C	—
PSZ2 G176.27+37.54	130.0378	44.3618	0.567	6.14	0.86	1056	50	2	0.091	RH	C	—
PSZ2 G177.03+32.64	123.3526	43.2651	0.511	6.07	0.76	1075	45	1	0.120	NDE	—	Redshift updated from Aguado-Barahona et al. (2019)
PSZ2 G178.00+42.32	136.6840	43.1361	0.237	3.97	0.54	1036	47	1	0.073	NDE	—	—
PSZ2 G178.94+56.00	154.9481	41.0098	0.092	2.23	0.30	899	40	1	0.074	NDE	—	—
PSZ2 G179.09+60.12	160.1864	39.9592	0.137	3.84	0.33	1061	30	1	0.093	RH	C/X	New RH
PSZ2 G180.60+76.65	179.3110	33.6110	0.214	6.30	0.34	1218	22	2	0.094	NDE	C	—
PSZ2 G180.88+31.04	121.9739	39.7755	0.365	5.99	0.70	1133	44	3	0.112	N/A	X	—
PSZ2 G181.06+48.47	144.8501	40.7576	0.240	4.23	0.49	1057	41	1	0.066	RR	C	New RR. Double RR
PSZ2 G182.59+55.83	154.2574	39.0280	0.206	5.83	0.34	1191	23	3	0.095	N/A	C/X	—
PSZ2 G183.30+34.98	127.4335	38.4548	0.392	6.56	0.64	1156	38	2	0.097	cRH, U	—	New cRH. U emisssion located in the E
PSZ2 G183.90+42.99	137.6963	38.8112	0.561	6.95	0.74	1102	39	1	0.096	RH	X	—
PSZ2 G184.24+43.69	138.6019	38.6019	0.397	5.41	0.63	1082	42	1	0.077	NDE	—	—
PSZ2 G184.68+28.91	120.2399	36.0972	0.288	5.50	0.52	1134	36	1	0.088	RH	C/X	New RH

Table B.1: continued.

Name	RA [deg]	DEC [deg]	z	M_{500} [$\times 10^{14}\ M_{\odot}$]	$M_{500\,\mathrm{err}}$ [$\times 10^{14}\ M_{\odot}$]	r_{500} [kpc]	$r_{500\,\mathrm{err}}$ [kpc]	IQ	rms [mJy beam^{-1}]	Classification	X-ray	Comment
PSZ2 G185.08+34.02	126.5397	36.8505	0.365	5.41	0.66	1095	44	1	0.111	NDE	—	—
PSZ2 G186.37+37.26	130.7485	36.3528	0.282	11.00	0.37	1431	16	1	0.107	RH	C/X	—
PSZ2 G186.61+62.94	162.6646	35.8429	0.509	5.68	0.65	1052	40	1	0.067	cRH	—	New cRH
PSZ2 G186.99+38.65	132.5385	36.0766	0.378	6.84	0.52	1178	30	2	0.092	RH, RR	C	New RH and RR
PSZ2 G187.53+21.92	113.0646	31.6261	0.171	5.17	0.39	1158	29	2	0.160	U	C/X	—
PSZ2 G187.74+20.66	111.7531	31.0220	0.193	4.29	0.50	1080	42	3	0.218	N/A	—	—
PSZ2 G189.23+20.55	112.1961	29.6730	0.398	5.46	0.74	1085	50	2	0.147	NDE	—	—
PSZ2 G189.31+59.24	157.9544	35.0406	0.126	3.24	0.31	1007	32	1	0.103	RH	C	New RH. Revived fossil plasma
PSZ2 G190.61+66.46	166.5376	33.5720	0.488	5.55	0.65	1053	41	1	0.077	RH, RR	C	New RH and RR
PSZ2 G191.57+58.88	157.4152	33.9099						1	0.107	NDE	—	—
PSZ2 G192.18+56.12	154.0911	33.6604	0.124	3.62	0.30	1045	29	1	0.089	RH	C/X	New RH
PSZ2 G192.77+33.14	127.1718	30.4022	0.050	1.66	0.20	825	34	2	0.116	cRH	—	New cRH
PSZ2 G192.90+29.63	123.3039	29.3652	0.360	5.17	0.76	1080	53	1	0.119	cRH	—	New cRH
PSZ2 G193.63+54.85	152.5729	32.8307	0.292	5.19	0.52	1110	37	2	0.134	U	X	—
PSZ2 G194.98+54.12	151.7502	32.0212	0.375	5.66	0.66	1108	43	2	0.120	U	C	—
PSZ2 G195.24+29.34	123.6579	27.3366	0.284	4.94	0.62	1095	46	2	0.113	U	—	—
PSZ2 G195.60+44.06	140.0993	30.5038	0.295	6.13	0.48	1172	31	2	0.105	NDE	C/X	—
PSZ2 G197.13+33.46	128.6143	26.9731	0.456	5.87	0.69	1086	43	1	0.109	U	—	—
PSZ2 G198.46+46.01	142.7118	28.8476	0.299	5.55	0.54	1132	37	1	0.088	cRR, U	—	New cRR
PSZ2 G199.61+53.41	151.2012	29.2311	0.371	5.54	0.59	1101	39	1	0.095	NDE	—	—
PSZ2 G199.75+46.59	143.5387	28.0764	0.553	5.91	0.76	1048	45	2	0.098	NDE	—	—
PSZ2 G200.06+77.22	178.5581	29.2431	0.361	4.62	0.61	1041	46	3	0.130	N/A	—	—
PSZ2 G202.66+66.98	166.8142	28.7965	0.483	5.28	0.70	1038	46	1	0.115	NDE	—	Redshift updated from Streblyanska et al. (2018)
PSZ2 G203.22+66.40	166.1721	28.5492	0.580	5.89	0.71	1036	42	3	0.130	N/A	—	—
PSZ2 G205.90+73.76	174.5534	27.9203	0.447	7.39	0.55	1177	29	1	0.101	RH, RR	C	New RH and RR. Double RR

Col. 1: PSZ2 name; Cols. 2 and 3: coordinates; Col. 4: redshift; Cols. 5 and 6: mass and its error; Cols. 7 and 8: radius and its error; Cols. 9 and 10: image quality and rms noise of the reference LOFAR image (-1 denotes the targets that were not extracted and self-calibrated); Col. 11: classification of the radio emission (see Section 4.3); Col. 12: presence of archival X-ray observations (C=Chandra, X=XMM-Newton); Col. 13: comments. Cols. 1-6 are provided by the PSZ2 catalogue (Planck Collaboration XXVII 2016).

Table B.2: The subsample of galaxy clusters with Chandra/XMM-Newton data available for which we computed the X-ray morphological parameters.

Name	Subcluster	c	$c_{\rm err}$	w	$w_{\rm err}$	X-ray
PSZ2 G023.17+86.71		1.23e-01	1.00e-02	2.17e-02	2.65e-03	C+X
PSZ2 G031.93+78.71		2.14e-01	1.53e-03	2.83e-02	2.39e-04	X
PSZ2 G033.81+77.18		4.26e-01	1.77e-03	8.67e-03	2.43e-03	C+X
PSZ2 G040.58+77.12		2.27e-01	6.40e-03	6.11e-03	6.80e-04	C+X
PSZ2 G045.87+57.70		2.54e-01	5.10e-03	2.18e-02	7.02e-04	X
PSZ2 G046.88+56.48		8.24e-02	4.15e-03	2.34e-02	1.75e-03	C+X
PSZ2 G048.10+57.16		8.80e-02	2.87e-03	5.91e-02	7.59e-03	C+X
PSZ2 G048.75+53.18		3.40e-01	8.41e-03	6.49e-03	1.22e-03	C
PSZ2 G049.18+65.05		2.87e-01	1.71e-02	7.97e-03	3.10e-03	C
PSZ2 G049.32+44.37		1.84e-01	6.00e-03	1.09e-02	1.10e-03	C+X
PSZ2 G050.46+67.54		3.61e-01	5.14e-03	1.86e-03	5.16e-04	C
PSZ2 G053.53+59.52		1.39e-01	2.72e-03	1.32e-02	3.49e-03	C+X
PSZ2 G054.99+53.41		1.44e-01	1.09e-02	1.65e-02	3.19e-03	C+X
PSZ2 G055.59+31.85		3.00e-01	1.49e-02	5.65e-03	3.84e-03	C+X
PSZ2 G056.77+36.32		3.03e-01	1.05e-02	3.88e-03	1.78e-03	C+X
PSZ2 G057.61+34.93		1.08e-01	4.11e-03	1.40e-02	1.02e-03	C+X
PSZ2 G057.78+52.32	E	2.26e-01	1.83e-03	6.11e-03	4.55e-04	X
PSZ2 G057.78+52.32	W	2.25e-01	5.74e-03	1.61e-02	1.44e-03	X
PSZ2 G057.92+27.64		4.52e-01	1.96e-02	5.48e-03	3.93e-03	C+X
PSZ2 G058.29+18.55	E	1.25e-01	1.53e-02	3.63e-02	2.22e-02	C+X
PSZ2 G058.29+18.55	W	4.22e-01	3.26e-03	1.34e-02	5.43e-04	X
PSZ2 G059.47+33.06		3.66e-01	3.98e-02	1.36e-02	9.59e-04	C+X
PSZ2 G060.55+27.00		4.22e-01	1.05e-02	4.26e-03	8.72e-04	C+X
PSZ2 G062.94+43.69		4.36e-01	3.40e-04	3.00e-03	1.95e-05	X
PSZ2 G065.28+44.53		2.11e-01	6.56e-03	3.44e-02	1.78e-03	C
PSZ2 G066.41+27.03		8.83e-02	8.98e-03	2.75e-02	2.28e-02	C+X
PSZ2 G066.68+68.44		3.42e-01	8.91e-03	8.70e-03	3.25e-03	C+X
PSZ2 G067.17+67.46		2.23e-01	8.98e-03	4.29e-02	1.61e-03	C+X
PSZ2 G067.52+34.75		3.89e-01	2.42e-03	4.10e-03	2.71e-04	X
PSZ2 G068.36+81.81		1.37e-01	3.05e-03	2.69e-02	8.34e-04	X
PSZ2 G070.89+49.26		1.36e-01	4.25e-03	2.06e-02	1.20e-03	X
PSZ2 G071.21+28.86		6.38e-02	4.45e-03	1.29e-02	2.08e-03	X
PSZ2 G071.39+59.54		1.53e-01	1.51e-02	1.65e-02	3.03e-03	C+X
PSZ2 G071.63+29.78		8.24e-02	3.34e-03	2.45e-02	1.38e-02	C+X
PSZ2 G072.62+41.46		1.30e-01	7.29e-03	2.68e-02	5.08e-03	C+X
PSZ2 G073.31+67.52		1.56e-01	1.42e-02	1.58e-02	2.81e-03	C+X
PSZ2 G073.97-27.82		2.77e-01	5.97e-03	1.11e-02	5.59e-04	C+X
PSZ2 G074.37+71.11		1.43e-01	2.00e-02	2.82e-02	6.10e-03	C
PSZ2 G076.55+60.29		2.38e-01	1.70e-02	2.87e-02	3.84e-03	C
PSZ2 G077.90-26.63		2.19e-01	7.61e-03	1.80e-02	1.05e-03	C+X
PSZ2 G080.16+57.65		1.30e-01	1.12e-02	3.27e-02	2.05e-03	C+X
PSZ2 G080.41-33.24		1.98e-01	1.72e-02	5.85e-02	1.31e-02	C+X
PSZ2 G080.64+64.31		4.53e-01	1.24e-02	6.22e-03	1.50e-03	C
PSZ2 G081.02+50.57		1.49e-01	5.22e-03	3.77e-02	1.37e-03	X
PSZ2 G081.72+70.15		1.21e-01	1.80e-02	1.83e-02	5.38e-03	C
PSZ2 G083.29-31.03		1.77e-01	1.27e-02	2.97e-02	1.07e-02	C+X
PSZ2 G083.86+85.09		1.89e-01	9.11e-03	3.33e-02	4.09e-03	C+X
PSZ2 G084.10+58.72		1.77e-01	2.79e-02	2.04e-02	9.05e-03	C+X
PSZ2 G084.13-35.41		9.53e-02	5.82e-03	3.79e-02	2.14e-03	X
PSZ2 G084.69+42.28		2.70e-01	4.30e-03	1.29e-02	5.93e-04	X
PSZ2 G086.54-26.67		3.04e-01	6.40e-03	5.42e-03	8.78e-04	C
PSZ2 G086.93+53.18		1.26e-01	1.86e-02	1.86e-02	3.51e-03	C+X
PSZ2 G087.39+50.92		2.13e-01	1.16e-02	2.34e-02	2.13e-03	X
PSZ2 G088.98+55.07		2.94e-01	1.20e-01	6.44e-02	1.62e-02	C+X
PSZ2 G089.52+62.34		1.13e-01	9.41e-03	3.20e-02	2.26e-03	C
PSZ2 G091.79-27.00		7.29e-02	6.16e-03	4.54e-02	2.52e-03	X
PSZ2 G092.69+59.92		1.29e-01	4.45e-02	6.63e-02	4.53e-02	C+X
PSZ2 G092.71+73.46		1.54e-01	5.69e-03	1.44e-02	2.21e-03	C+X
PSZ2 G093.94-38.82	EN	2.14e-01	2.36e-03	4.07e-02	5.69e-04	X
PSZ2 G093.94-38.82	ES	1.93e-01	2.30e-03	3.18e-02	5.75e-04	X
PSZ2 G093.94-38.82	W	3.29e-01	3.09e-03	1.68e-02	5.35e-04	X
PSZ2 G094.44+36.13		2.83e-01	2.85e-02	1.33e-02	4.92e-03	C+X
PSZ2 G094.56+51.03		1.02e-01	4.14e-03	5.69e-02	1.67e-03	X
PSZ2 G094.61-41.24		3.23e-01	1.26e-03	7.82e-03	2.16e-04	X
PSZ2 G095.22+67.41		1.25e-01	2.28e-03	2.06e-02	8.51e-04	X
PSZ2 G096.83+52.49		2.09e-01	3.63e-03	8.69e-03	8.71e-04	C
PSZ2 G097.52+51.70		2.17e-01	8.06e-03	1.92e-02	1.10e-03	X
PSZ2 G097.72+38.12		1.70e-01	6.56e-03	3.21e-02	7.91e-03	C+X
PSZ2 G099.48+55.60		8.41e-02	4.91e-03	2.55e-02	3.21e-03	C+X
PSZ2 G099.86+58.45		1.33e-01	1.04e-02	2.15e-02	5.58e-03	C+X
PSZ2 G100.14+41.67		2.50e-01	3.02e-03	5.67e-02	5.84e-04	C
PSZ2 G100.45-38.42		4.11e-01	1.50e-03	2.64e-03	1.35e-04	X
PSZ2 G103.40-32.99		1.08e-01	1.21e-03	5.21e-03	5.06e-04	X
PSZ2 G105.55+77.21		1.82e-01	2.31e-03	2.52e-02	6.40e-04	X
PSZ2 G106.41+50.82		3.49e-01	2.12e-02	1.90e-02	1.22e-03	C+X
PSZ2 G106.61+66.71		1.40e-01	3.20e-02	5.08e-02	7.99e-03	C
PSZ2 G107.10+65.32	N	1.07e-01	5.96e-03	8.61e-02	1.15e-03	C+X
PSZ2 G107.10+65.32	S	1.42e-01	6.93e-03	3.60e-02	2.18e-03	C+X
PSZ2 G109.97+52.84		3.34e-01	5.04e-03	8.21e-03	8.83e-04	C
PSZ2 G111.75+70.37		9.16e-02	6.56e-03	5.71e-02	3.19e-03	C+X
PSZ2 G112.35-32.86		2.63e-01	9.71e-03	1.35e-02	1.41e-03	X
PSZ2 G112.48+56.99		1.74e-01	4.69e-03	4.60e-03	9.61e-04	C
PSZ2 G113.29-29.69		1.69e-01	1.02e-02	1.33e-02	5.02e-03	C+X
PSZ2 G113.91-37.01		1.57e-01	1.65e-02	4.60e-02	2.54e-03	C+X
PSZ2 G114.31+64.89		1.66e-01	2.70e-02	1.28e-02	1.92e-03	C+X
PSZ2 G114.79-33.71		1.53e-01	9.18e-03	7.39e-03	4.54e-03	C+X
PSZ2 G114.99+70.36		1.46e-01	5.90e-03	1.72e-02	1.80e-03	C
PSZ2 G116.32-36.33	N	1.50e-01	1.70e-02	1.24e-02	4.73e-03	C+X
PSZ2 G116.32-36.33	S	2.97e-01	1.26e-02	9.13e-03	1.50e-03	X
PSZ2 G116.50-44.47		1.30e-01	6.75e-03	5.60e-02	2.37e-03	X
PSZ2 G121.03+57.02		9.77e-02	7.83e-03	1.10e-01	3.74e-03	C
PSZ2 G121.13+49.64		9.88e-02	5.27e-03	3.28e-02	1.94e-03	X
PSZ2 G123.00-35.52		1.56e-01	5.28e-03	2.39e-02	1.08e-03	X
PSZ2 G123.66+67.25		2.50e-01	3.05e-02	1.59e-02	5.27e-03	C
PSZ2 G124.20-36.48	N	3.06e-01	3.56e-03	5.41e-02	8.91e-04	C+X
PSZ2 G124.20-36.48	S	1.01e-01	1.04e-02	1.90e-02	6.16e-03	C+X
PSZ2 G125.71+53.86		1.96e-01	1.68e-02	1.04e-02	3.56e-03	C+X
PSZ2 G126.61-37.63		1.70e-01	5.69e-03	8.77e-03	1.09e-03	X
PSZ2 G127.50-30.52		1.16e-01	7.32e-03	1.39e-02	2.04e-03	X
PSZ2 G132.54-42.16		2.11e-01	8.94e-03	2.55e-03	1.58e-03	X
PSZ2 G133.59+50.68		9.27e-02	5.08e-03	1.94e-02	2.18e-03	X
PSZ2 G133.60+69.04		8.67e-02	8.92e-03	3.80e-02	3.49e-03	C
PSZ2 G134.70+48.91		2.52e-01	2.79e-02	5.34e-03	1.98e-03	C+X
PSZ2 G135.17+65.43		1.05e-01	1.87e-02	4.72e-02	7.64e-03	C
PSZ2 G135.19+57.88		1.66e-01	9.31e-03	1.33e-02	2.56e-03	C
PSZ2 G136.92+59.46		9.37e-02	2.33e-03	8.87e-02	1.22e-03	X
PSZ2 G137.74-27.08		1.46e-01	2.35e-03	4.31e-02	6.91e-04	X
PSZ2 G138.32-39.82		1.98e-01	6.58e-03	1.32e-02	1.33e-03	C
PSZ2 G139.18+56.37		8.60e-02	5.90e-03	4.70e-02	8.49e-03	C+X
PSZ2 G143.26+65.24		1.42e-01	2.62e-02	2.46e-02	1.49e-03	C+X

Table B.2: continued.

Name	Subcluster	c	$c_{\rm err}$	w	$w_{\rm err}$	X-ray
PSZ2 G145.65+59.30		1.44e-01	6.56e-03	1.20e-02	1.45e-03	X
PSZ2 G148.36+75.23		2.06e-01	9.02e-03	5.27e-02	2.43e-03	C
PSZ2 G149.22+54.18		1.36e-01	3.42e-03	3.72e-03	8.17e-04	C
PSZ2 G149.75+34.68		1.72e-01	3.39e-03	6.13e-02	3.66e-03	C+X
PSZ2 G150.56+58.32		1.33e-01	1.62e-02	3.16e-02	1.77e-02	C+X
PSZ2 G151.19+48.27		7.73e-02	8.77e-03	2.41e-02	1.18e-02	C+X
PSZ2 G160.83+81.66		2.78e-01	3.08e-02	1.72e-02	3.92e-03	C+X
PSZ2 G163.69+53.52		1.98e-01	5.88e-03	8.31e-03	1.41e-03	C
PSZ2 G163.87+48.54		4.61e-01	3.51e-03	1.61e-03	3.40e-04	C
PSZ2 G164.65+46.37		2.46e-01	1.00e-02	6.05e-02	2.10e-03	C
PSZ2 G165.06+54.13		1.88e-01	5.22e-03	1.77e-02	1.53e-03	C
PSZ2 G165.46+66.15		6.96e-02	5.22e-03	3.31e-02	3.13e-03	C
PSZ2 G166.09+43.38		1.84e-01	6.80e-03	1.83e-02	5.71e-03	C+X
PSZ2 G166.62+42.13		6.85e-02	5.52e-03	3.48e-02	3.03e-03	C
PSZ2 G168.33+69.73		2.64e-01	3.00e-02	1.91e-02	4.29e-03	C
PSZ2 G170.98+39.45		1.14e-01	1.61e-02	2.69e-02	6.51e-03	C
PSZ2 G172.63+35.15		1.84e-01	8.75e-03	2.01e-02	2.14e-03	C
PSZ2 G172.74+65.30		2.18e-01	1.10e-02	2.44e-02	1.69e-02	C+X
PSZ2 G175.60+35.47		2.66e-01	1.13e-02	1.05e-02	2.00e-03	C
PSZ2 G176.27+37.54		2.43e-01	1.69e-02	1.90e-02	3.87e-03	C
PSZ2 G179.09+60.12		5.15e-01	6.11e-03	6.54e-03	2.17e-03	C+X
PSZ2 G180.60+76.65		2.89e-01	6.39e-03	2.41e-03	5.32e-04	C
PSZ2 G180.88+31.04		1.01e-01	1.15e-02	1.83e-02	4.22e-03	X
PSZ2 G181.06+48.47		1.41e-01	1.05e-02	6.95e-02	3.04e-03	C
PSZ2 G182.59+55.83		2.86e-01	1.26e-02	5.95e-03	9.26e-04	C+X
PSZ2 G183.90+42.99		1.56e-01	4.77e-03	1.82e-02	1.13e-03	X
PSZ2 G184.68+28.91		2.93e-01	1.47e-02	7.89e-03	2.99e-03	C+X
PSZ2 G186.37+37.26		1.47e-01	8.43e-03	9.89e-03	5.32e-03	C+X
PSZ2 G186.99+38.65		1.99e-01	8.38e-03	3.85e-02	2.11e-03	C
PSZ2 G187.53+21.92		3.04e-01	1.59e-02	7.20e-03	5.27e-03	C+X
PSZ2 G189.31+59.24		2.45e-01	3.64e-03	4.76e-02	7.56e-04	C
PSZ2 G190.61+66.46		1.05e-01	1.61e-02	2.87e-02	5.77e-03	C
PSZ2 G192.18+56.12		1.72e-01	7.12e-03	1.70e-02	1.12e-02	C+X
PSZ2 G193.63+54.85		1.67e-01	7.38e-03	5.62e-02	1.86e-03	X
PSZ2 G194.98+54.12		1.84e-01	1.37e-02	6.07e-02	3.54e-03	C
PSZ2 G195.60+44.06	E1	9.39e-02	5.86e-03	1.94e-02	2.35e-03	X
PSZ2 G195.60+44.06	E2	1.23e-01	7.51e-03	4.63e-02	1.97e-02	C+X
PSZ2 G195.60+44.06	W1	2.83e-01	7.56e-03	8.57e-03	9.76e-04	X
PSZ2 G195.60+44.06	W2	9.70e-02	2.07e-03	4.79e-02	7.30e-04	X
PSZ2 G205.90+73.76		2.12e-01	1.79e-02	1.35e-02	3.23e-03	C

Col. 1: PSZ2 name; Col. 2: position of the subcluster; Cols. 3 and 4: concentration parameter and its error; Cols. 5 and 6: centroid shift and its error; Col. 7: instrument used (C=Chandra, X=XMM-Newton).

Table B.3: The sample of radio halos and candidate radio halos found in this work.

Name	S_{150} (2σ) [mJy]	$S_{150_{err}}$ (2σ) [mJy]	S_{150} (fit) [mJy]	$S_{150_{err}}$ (fit) [mJy]	P_{150} [W Hz^{-1}]	$P_{150_{err}}$ [W Hz^{-1}]	I_0 [μJy arcsec^{-2}]	$I_{0_{err}}$ [μJy arcsec^{-2}]	r_1 [kpc]	$r_{1_{err}}$ [kpc]	r_2 [kpc]	$r_{2_{err}}$ [kpc]	Model	SNR	rms [mJy beam^{-1}]	χ^2_{red}	Comment
PSZ2 G023.17+86.71	25.73	3.12	29.84	3.62	9.76e+24	1.18e+24	5.79	0.34	232.8	11.7	95.1	6.4	rotated_ellipse	19.81	0.347	1.18	—
PSZ2 G031.93+78.71	189.84	78.34	176.45	78.03	2.28e+24	1.01e+24	11.39	0.20	78.7	1.1			circle	66.26	0.168	3.27	—
PSZ2 G040.58+77.12	50.33	6.76	42.92	7.82	6.04e+23	1.10e+23	0.67	0.10	165.3	21.0			circle	7.01	0.082	2.46	—
PSZ2 G045.87+57.70	10.78	2.59	11.75	2.79	2.11e+25	5.03e+24	14.18	1.90	89.0	9.6			circle	9.66	0.877	1.11	—
PSZ2 G046.88+56.48	177.19	20.99	236.45	27.77	8.36e+24	9.81e+23	1.57	0.07	369.9	13.6			circle	22.46	0.131	0.70	—
PSZ2 G048.10+57.16	300.00	39.36	354.88	44.67	5.43e+24	6.84e+23	1.58	0.05	463.4	15.6	220.7	6.3	rotated_ellipse	32.61	0.160	0.87	—
PSZ2 G049.32+44.37	45.87	7.71	70.64	10.61	1.73e+24	2.59e+23	0.61	0.05	281.2	19.7			circle	12.13	0.099	0.79	—
PSZ2 G053.53+59.52	519.08	57.38	387.17	45.84	1.32e+25	1.56e+24	11.66	0.11	171.5	1.4			circle	104.71	0.141	13.68	—
PSZ2 G055.59+31.85	30.25	5.21	33.57	5.46	5.29e+24	8.60e+23	17.48	0.71	72.3	2.3			circle	30.72	0.433	1.26	—
PSZ2 G056.77+36.32	79.79	26.53	83.39	26.97	1.95e+24	6.30e+23	1.10	0.10	223.3	15.5			circle	14.15	0.099	0.79	—
PSZ2 G063.38+53.44	27.53	5.02	29.40	5.19	2.09e+25	3.70e+24	10.76	0.58	133.0	5.8			circle	20.38	0.713	1.08	—
PSZ2 G066.34+26.14	98.35	12.89	82.29	11.71	1.55e+26	2.20e+25	22.02	0.70	190.5	5.1			circle	32.77	1.304	1.60	—
PSZ2 G066.41+27.03	89.88	10.47	111.34	12.61	1.72e+26	1.95e+25	15.50	0.42	374.5	11.0	173.6	5.1	rotated_ellipse	36.36	1.096	1.05	—
PSZ2 G069.39+68.05	14.60	2.46	18.49	4.42	5.86e+25	1.40e+25	4.73	1.01	211.9	38.5			circle	4.64	0.826	0.71	—
PSZ2 G071.21+28.86	45.99	7.74	67.70	10.82	3.41e+25	5.44e+24	1.53	0.13	490.3	35.6			circle	11.08	0.260	1.32	—
PSZ2 G080.70+48.31	8.18	2.89	6.39	2.86	1.12e+24	5.03e+23	4.58	0.65	64.1	6.5			circle	8.75	0.324	0.96	—
PSZ2 G081.02+50.57	5.39	1.08	10.59	2.09	1.15e+25	2.28e+24	1.45	0.33	238.3	36.7			circle	6.46	0.175	0.87	—
PSZ2 G083.29-31.03	53.22	5.88	54.71	6.00	3.67e+25	4.03e+24	6.71	0.28	226.5	7.8			circle	26.25	0.341	1.65	—
PSZ2 G084.10+58.72	3.80	0.85	3.97	0.96	1.13e+25	2.74e+24	6.03	1.79	85.5	17.5			circle	6.49	0.320	1.05	—
PSZ2 G084.13-35.41	51.57	13.14	56.55	13.48	1.97e+25	4.69e+24	6.16	0.31	201.8	8.4			circle	20.03	0.565	1.17	—
PSZ2 G085.23+39.42	55.35	7.81	68.62	8.84	1.49e+25	1.92e+24	5.12	0.18	211.5	4.8			circle	40.12	0.262	1.80	—
PSZ2 G086.93+53.18	8.91	1.69	11.50	2.20	2.67e+25	5.09e+24	3.29	0.54	190.7	25.2			circle	7.29	0.486	1.02	—
PSZ2 G089.39+69.36	11.77	2.17	10.93	2.14	2.58e+25	5.05e+24	10.47	0.79	104.6	6.2			circle	16.23	0.532	0.83	—
PSZ2 G096.83+52.49	39.63	7.45	45.21	7.80	1.62e+25	2.80e+24	7.92	0.23	211.0	5.9	122.2	3.9	rotated_ellipse	36.70	0.417	1.53	—
PSZ2 G097.72+38.12	152.51	16.07	140.24	14.94	1.19e+25	1.27e+24	7.44	0.14	183.2	2.9			circle	55.12	0.276	1.26	—
PSZ2 G098.30-41.15	46.52	7.17	42.00	6.87	3.24e+25	5.31e+24	40.22	1.10	83.8	1.7			circle	44.54	0.746	2.24	—
PSZ2 G099.86+58.45	21.92	4.82	19.92	4.74	3.87e+25	9.21e+24	7.36	0.49	163.2	8.6			circle	15.69	0.687	1.10	—
PSZ2 G100.96-24.07	17.18	7.03	18.45	7.24	1.33e+25	5.21e+24	5.82	0.75	143.7	14.6			circle	8.78	0.544	0.95	—
PSZ2 G106.61+66.71	19.45	2.41	17.91	2.27	7.07e+24	8.98e+23	12.82	0.52	81.7	2.5			circle	32.54	0.257	1.97	—
PSZ2 G107.10+65.32	270.18	36.21	154.77	29.94	7.16e+25	9.60e+24	22.66	1.44	251.1	16.0	102.9	7.0	rotated_ellipse	17.21	0.253	2.87	P_{150} derived from S_{150} (2σ)
PSZ2 G108.27+48.66	10.26	3.30	9.39	3.23	2.17e+25	7.47e+24	6.42	0.84	123.3	12.0			circle	9.63	0.563	0.94	—
PSZ2 G109.97+52.84	13.61	1.91	16.25	2.58	6.18e+24	9.80e+23	1.39	0.16	233.5	25.0			circle	9.07	0.127	1.95	—
PSZ2 G111.75+70.37	28.12	20.02	29.28	20.05	2.90e+24	1.99e+24	2.53	0.14	218.1	12.9	105.7	6.5	rotated_ellipse	20.34	0.149	1.49	—
PSZ2 G112.48+56.99	41.72	7.00	55.16	8.36	6.71e+23	1.02e+23	0.80	0.05	160.7	9.3			circle	16.05	0.071	1.00	—
PSZ2 G113.91-37.01	78.03	8.22	122.78	13.64	6.38e+25	7.09e+24	5.09	0.23	365.3	15.0			circle	20.92	0.786	1.47	—
PSZ2 G114.31+64.89	41.10	11.72	66.61	13.27	1.83e+25	3.64e+24	12.40	0.59	143.9	6.6			circle	19.50	0.369	1.67	—
PSZ2 G115.67-27.57	4.61	0.84	4.53	0.74	3.93e+24	6.39e+23	5.00	1.33	80.3	14.0			circle	7.86	0.287	0.93	—
PSZ2 G133.60+69.04	145.00	18.87	162.80	20.30	3.43e+25	4.28e+24	7.07	0.17	377.1	5.2	200.9	4.3	rotated_ellipse	74.85	0.248	3.13	—
PSZ2 G135.17+65.43	35.76	6.89	40.76	7.35	5.46e+25	9.84e+24	6.43	0.50	232.7	12.1			circle	19.65	0.576	1.24	—
PSZ2 G138.32-39.82	28.07	4.29	31.00	4.80	8.22e+24	1.27e+24	2.89	0.24	201.7	14.3			circle	12.23	0.419	1.07	—
PSZ2 G139.18+56.37	398.78	49.86	288.44	41.53	1.47e+26	1.84e+25	45.75	0.25	170.2	0.8			circle	195.52	0.369	20.10	P_{150} derived from S_{150} (2σ)
PSZ2 G141.05-32.61	66.30	8.94	71.57	9.78	1.00e+26	1.37e+25	6.30	0.32	314.6	12.8			circle	19.40	0.525	1.68	—
PSZ2 G143.26+65.24	33.72	4.79	34.02	5.12	1.68e+25	2.53e+24	4.30	0.27	206.5	11.7			circle	16.23	0.389	1.07	—
PSZ2 G144.23-18.19	17.33	3.12	23.80	3.96	2.10e+24	3.79e+23	1.80	0.18	174.2	15.0			circle	11.02	0.214	1.05	P_{150} and r_1 computed assuming $z = 0.2$
PSZ2 G147.88+53.24	12.90	3.63	21.86	4.27	3.75e+25	7.33e+24	5.87	0.38	187.0	10.9			circle	14.18	0.595	1.03	—
PSZ2 G148.36+75.23	20.97	2.33	18.86	2.16	6.07e+24	6.95e+23	8.57	0.58	96.6	5.1			circle	18.46	0.343	1.00	—
PSZ2 G149.22+54.18	332.74	52.81	315.77	51.81	1.64e+25	2.69e+24	6.42	0.11	246.1	3.6			circle	56.88	0.234	2.07	—
PSZ2 G149.75+34.68	711.34	74.64	574.12	61.67	5.62e+25	6.04e+24	12.23	0.08	303.9	1.6			circle	157.82	0.184	7.23	—
PSZ2 G150.56+46.67	13.87	1.58	16.18	1.88	9.98e+24	1.16e+24	4.17	0.26	153.0	7.6			circle	17.50	0.388	0.96	—
PSZ2 G150.56+58.32	54.22	11.09	60.83	11.53	5.65e+25	1.07e+25	10.66	0.37	315.3	11.2	132.6	4.8	rotated_ellipse	29.55	0.607	1.22	—
PSZ2 G151.19+48.27	38.62	7.69	47.05	9.01	1.34e+25	2.57e+24	1.66	0.13	335.5	23.7			circle	11.15	0.202	0.95	—
PSZ2 G154.13+40.19	13.50	1.82	13.20	1.83	3.80e+24	5.26e+23	9.04	0.64	76.2	4.1			circle	17.60	0.422	0.89	—
PSZ2 G156.26+59.64	6.59	1.65	7.81	1.97	1.27e+25	3.22e+24	9.74	1.90	85.9	13.7			circle	6.48	0.948	0.94	—
PSZ2 G160.83+81.66	11.67	2.70	10.56	2.67	4.98e+25	1.26e+25	15.90	1.26	91.7	5.5			circle	16.69	0.647	1.21	—
PSZ2 G164.65+46.37	23.52	5.28	22.40	5.29	9.56e+24	2.26e+24	5.87	0.33	217.1	12.0	87.5	5.4	rotated_ellipse	18.86	0.413	0.89	—
PSZ2 G165.06+54.13	43.38	9.18	60.61	10.76	3.51e+24	6.23e+23	0.88	0.06	305.0	18.4			circle	14.18	0.108	0.76	—
PSZ2 G166.09+43.38	142.10	15.44	112.78	12.81	1.65e+25	1.87e+24	7.19	0.16	202.0	3.9			circle	46.32	0.210	1.39	—
PSZ2 G166.62+42.13													—				Cannot be disentangled from RR emission
PSZ2 G172.63+35.15	56.64	7.29	68.09	9.27	2.99e+24	4.07e+23	1.79	0.16	202.5	15.1			circle	12.26	0.172	1.02	—
PSZ2 G176.27+37.54	4.73	1.11	6.47	2.12	9.62e+24	3.16e+24	2.96	1.05	139.6	40.7			circle	3.47	0.375	1.10	—
PSZ2 G179.09+60.12	25.21	6.99	36.51	8.04	1.89e+24	4.17e+23	2.55	0.22	133.0	10.4			circle	11.31	0.293	1.27	—
PSZ2 G183.30+34.98	24.35	7.35	32.35	8.01	1.92e+25	4.76e+24	5.65	0.49	184.1	13.8			circle	11.63	0.761	0.92	—
PSZ2 G183.90+42.99	57.09	5.92	52.12	5.40	7.55e+25	7.81e+24	16.35	0.39	167.6	3.1			circle	45.83	0.606	1.48	—
PSZ2 G184.68+28.91	7.03	1.23	6.86	1.41	1.94e+24	3.98e+23	5.40	0.93	70.7	9.8			circle	7.17	0.473	0.64	—
PSZ2 G186.37+37.26	88.01	9.11	85.31	9.04	2.30e+25	2.44e+24	12.40	0.43	162.2	4.8			circle	30.41	0.533	1.10	—
PSZ2 G186.61+62.94	3.10	1.10	3.21	1.11	3.64e+24	1.26e+24	2.85	0.82	94.9	18.6			circle	6.61	0.191	0.53	—
PSZ2 G186.99+38.65	54.29	7.14	55.06	7.28	3.00e+25	3.96e+24	27.68	0.90	106.1	2.8			circle	35.46	0.625	1.30	—
PSZ2 G189.31+59.24	334.87	68.03	252.77	64.40	1.09e+25	2.78e+24	25.80	0.39	102.3	1.2			circle	78.08	0.189	4.63	—
PSZ2 G190.61+66.46	17.61	2.44	35.59	4.35	3.63e+25	4.44e+24	3.22	0.23	290.5	15.0			circle	16.68	0.252	1.85	—
PSZ2 G192.18+56.12	14.92	2.52	19.45	3.59	8.10e+23	1.50e+23	0.66	0.10	174.9	22.1			circle	7.24	0.102	1.01	—
PSZ2 G192.77+33.14	108.18	14.63	118.30	18.72	7.10e+23	1.12e+23	0.54	0.06	211.7	20.8			circle	9.37	0.062	0.75	—
PSZ2 G192.90+29.63	21.71	3.05	33.96	5.14	1.64e+25	2.48e+24	2.91	0.29	249.5	21.1			circle	9.53	0.412	0.88	—
PSZ2 G205.90+73.76	45.01	6.79	36.67	6.28	3.01e+25	5.15e+24	34.30	1.53	103.3	4.7	71.7	3.1	rotated_ellipse	27.79	0.763	0.72	—

Col. 1: PSZ2 name; Cols. 2 and 3: flux density integrated within the 2σ region and its error; Cols. 4 and 5: flux density obtained from the surface brightness profile fitting and its error; Cols. 6 and 7: radio power and its error; Cols. 8 and 9: best-fit central brightness and its error; Cols. 10-13: best-fit first and second *e*-folding radii and their errors; Col. 14: model adopted for the fitting; Col. 15: SNR of the radio halo; Col. 16: rms noise of the image used to fit the surface brightness profile; Col. 17: $\chi^2_{\rm red}$ of the fit; Col. 18: comments.

Table B.4: The sample of radio halos and candidate radio halos that were classified with an asterisk (the RH* and cRH* in Table B.1) because of their low-significance. The integrated flux density of these sources cannot be determined accurately with current data.

Name	S_{150} (2σ) [mJy]	$S_{150\mathrm{err}}$ (2σ) [mJy]	S_{150} (fit) [mJy]	$S_{150\mathrm{err}}$ (fit) [mJy]	P_{150} [W Hz^{-1}]	$P_{150\mathrm{err}}$ [W Hz^{-1}]	I_0 [μJy arcsec^{-2}]	$I_{0\mathrm{err}}$ [μJy arcsec^{-2}]	r_1 [kpc]	$r_{1\mathrm{err}}$ [kpc]	Model	SNR	rms [mJy beam^{-1}]	χ^2_{red}
PSZ2 G071.39+59.54	20.01	2.30	88.87	11.90	2.60e+25	3.48e+24	1.27	0.08	529.2	36.0	circle	11.25	0.319	1.15
PSZ2 G076.55+60.29	8.14	1.67	22.52	5.72	6.33e+24	1.61e+24	0.43	0.07	453.8	82.3	circle	4.40	0.118	0.76
PSZ2 G077.90-26.63	28.02	4.04	64.10	10.75	3.89e+24	6.52e+23	1.88	0.24	218.1	26.5	circle	7.53	0.439	1.03
PSZ2 G095.29+44.13	13.82	2.08	27.38	4.36	1.08e+25	1.72e+24	1.21	0.13	328.7	32.8	circle	8.48	0.266	0.89
PSZ2 G099.55+34.23	13.48	5.97	93.17	19.09	3.14e+25	6.44e+24	0.56	0.07	851.0	112.6	circle	5.95	0.237	0.84
PSZ2 G116.50-44.47	12.62	6.73	23.23	8.29	1.42e+25	5.05e+24	3.94	0.78	187.8	36.0	circle	5.11	0.680	1.08
PSZ2 G118.34+68.79	7.31	2.48	25.05	4.47	5.33e+24	9.52e+23	0.80	0.09	321.5	32.4	circle	8.58	0.208	1.34
PSZ2 G123.00-35.52	8.28	1.86	20.43	4.27	1.13e+25	2.35e+24	2.23	0.35	228.4	34.4	circle	5.93	0.578	1.08
PSZ2 G133.59+50.68	10.19	1.45	18.96	3.35	2.37e+25	4.18e+24	1.20	0.15	362.8	43.6	circle	7.07	0.257	0.92
PSZ2 G163.61+34.30	8.50	2.19	17.02	3.71	2.87e+25	6.25e+24	1.50	0.24	324.7	44.9	circle	6.21	0.379	0.79

Col. 1: PSZ2 name; Cols. 2 and 3: flux density integrated within the 2σ region and its error; Cols. 4 and 5: flux density obtained from the surface brightness profile fitting and its error; Cols. 6 and 7: radio power and its error; Cols. 8 and 9: best-fit central brightness and its error; Cols. 10 and 11: best-fit *e*-folding radius and its error; Col. 12: model adopted for the fitting; Col. 13: SNR of the radio halo; Col. 14: rms noise of the image used to fit the surface brightness profile; Col. 15: χ^2_{red} of the fit.

Appendix C

Injections in PSZ2 G098.62+51.76

As a representative example of the various injections that we obtained in different NDE clusters, in this Appendix we report some of the images of PSZ2 G098.62+51.76, which were used to produce and discuss the plots shown in Sect. 5.3 in Chapter 5.

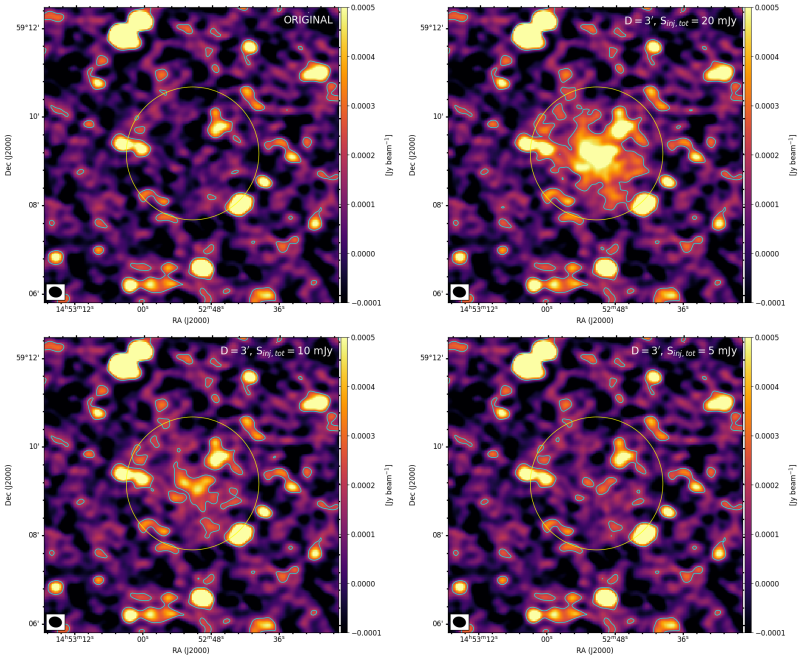

Figure C.1: Injection of mock halos with $D = 3'$ (corresponding to the diameter of the yellow circle). The 2σ contour level is reported, where σ is the noise of the pre-injection map. The upper limit is obtained with $S_{\mathrm{inj,tot}} = 5$ mJy.

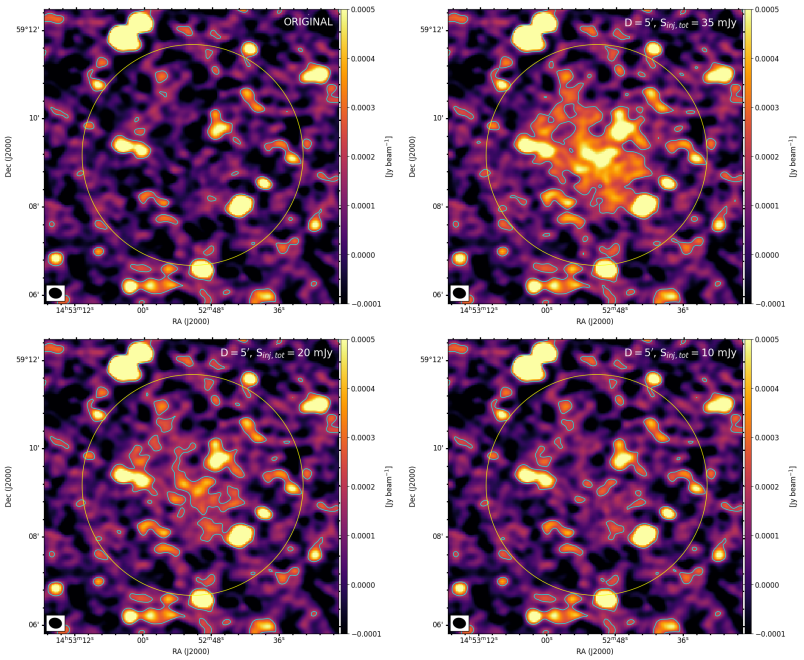

Figure C.2: Injection of mock halos with $D = 5'$ (corresponding to the diameter of the yellow circle). The 2σ contour level is reported, where σ is the noise of the pre-injection map. The upper limit is obtained with $S_{\mathrm{inj,tot}} = 10$ mJy.

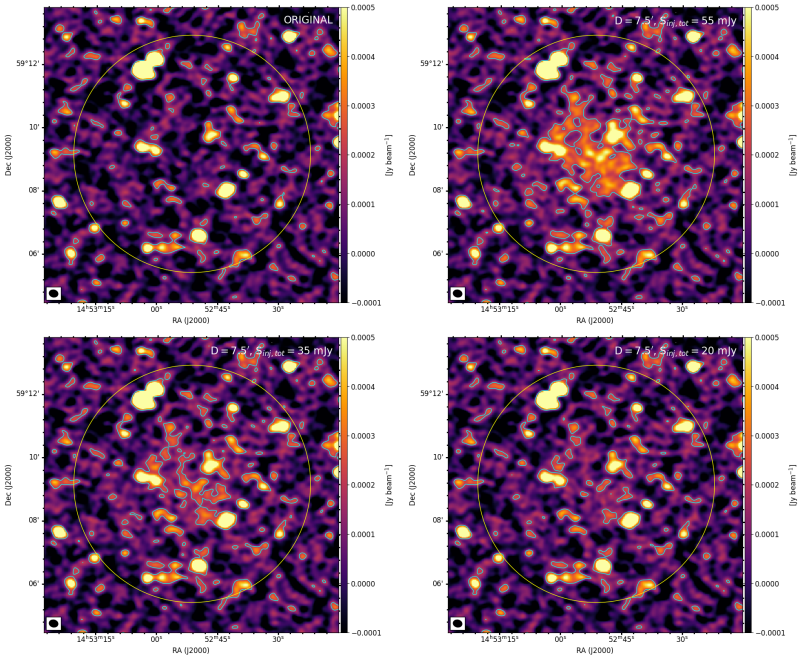

Figure C.3: Injection of mock halos with $D = 7.5'$ (corresponding to the diameter of the yellow circle). The 2σ contour level is reported, where σ is the noise of the pre-injection map. The upper limit is obtained with $S_{\mathrm{inj,tot}} = 20$ mJy.

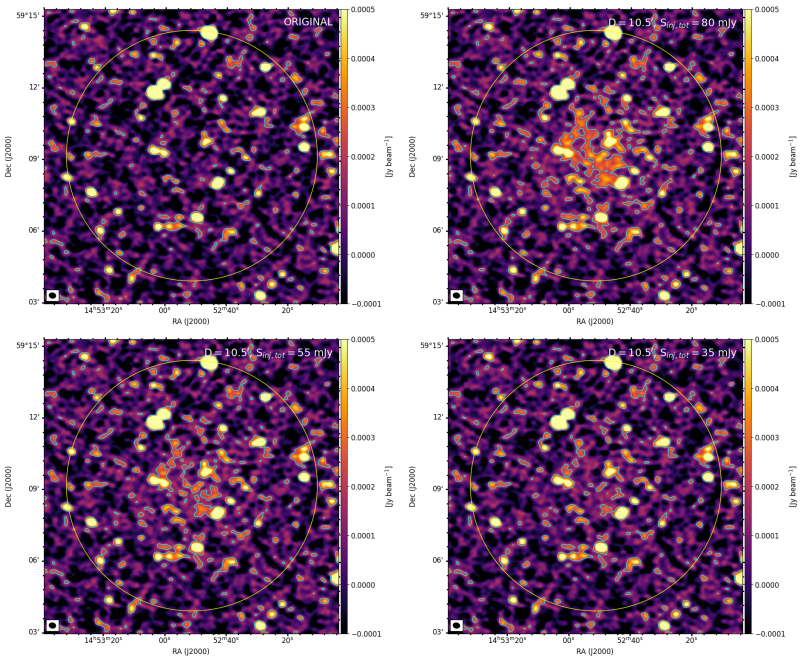

Figure C.4: Injection of mock halos with $D = 10.5'$ (corresponding to the diameter of the yellow circle). The 2σ contour level is reported, where σ is the noise of the pre-injection map. The upper limit is obtained with $S_{\mathrm{inj,tot}} = 35$ mJy.

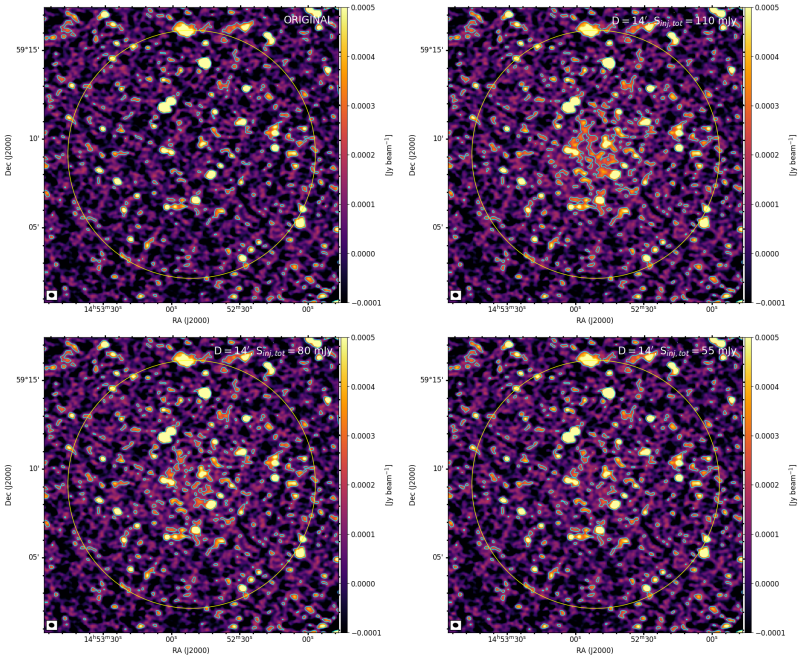

Figure C.5: Injection of mock halos with $D = 14'$ (corresponding to the diameter of the yellow circle). The 2σ contour level is reported, where σ is the noise of the pre-injection map. The upper limit is obtained with $S_{\mathrm{inj,tot}} = 55$ mJy.

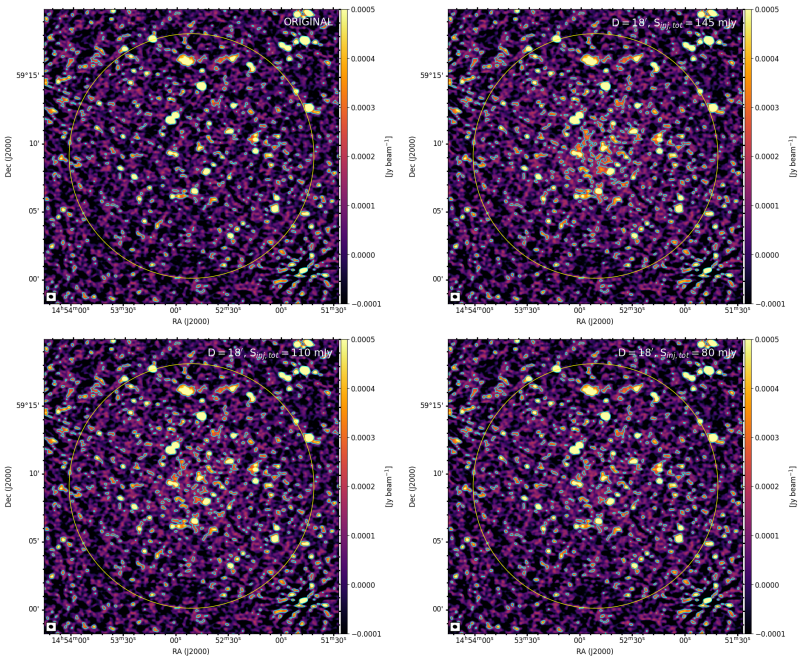

Figure C.6: Injection of mock halos with $D = 18'$ (corresponding to the diameter of the yellow circle). The 2σ contour level is reported, where σ is the noise of the pre-injection map. The upper limit is obtained with $S_{\mathrm{inj,tot}} = 80$ mJy.

Appendix D

Upper limits: table

In Table D.1 of this Appendix we summarise the main properties of the host cluster and the injected parameters used to obtain the upper limits in Chapter 5.

Table D.1: Summary of the host cluster properties and upper limit parameters for the 75 considered targets. Columns from 1 to 5 report the *Planck* pointing name, coordinates (RA, DEC), redshift (z), and mass (M_{500}) of the host. Columns 6 and 7 report the injection centre (RA_{inj}, DEC_{inj}). Column 8 reports the subtraction quality parameter (SQ) close to the injection centre. Columns 9 and 10 report the injected central brightness ($I_{0,inj}$) and e-folding radius ($r_{e,inj}$). Columns 11 and 12 report the level of the upper limit at 150 MHz in terms of flux density ($S_{150,UL}$) and radio power ($P_{150,UL}$)

Name	RA (deg)	DEC (deg)	z	M_{500} (10^{14} $M_\odot$)	RA_{inj} (deg)	DEC_{inj} (deg)	SQ	$I_{0,inj}$ (μJy arcsec^2)	$r_{e,inj}$ (arcsec)	$S_{150,UL}$ (mJy)	$P_{150,UL}$ (10^{23} W Hz^{-1})
PSZ2 G045.13+67.78	217.996	29.557	0.219	4.83 ± 0.45	217.996	29.557	2	0.323	56.5	5.0	7.5
PSZ2 G048.75+53.18	234.967	30.696	0.098	2.53 ± 0.31	234.962	30.718	2	0.289	110.4	16.8	4.2
PSZ2 G049.18+65.05	221.119	31.233	0.234	4.73 ± 0.49	221.133	31.227	2	0.688	53.73	9.5	16.5
PSZ2 G050.46+67.54	218.168	31.588	0.131	2.92 ± 0.34	218.158	31.658	2	0.2	85.75	7.0	3.3
PSZ2 G055.80+32.90	259.462	32.561	0.105	2.58 ± 0.31	259.481	32.578	2	0.154	103.87	7.9	2.3
PSZ2 G056.14+28.06	265.075	31.603	0.426	5.53 ± 0.57	265.069	31.611	2	0.997	35.85	6.1	44.5
PSZ2 G057.73+51.58	237.141	36.103	0.238	5.59 ± 0.51	237.144	36.096	2	0.452	53.05	6.1	11.0
PSZ2 G057.78+52.32	236.215	36.122	0.065	2.38 ± 0.22	236.246	36.11	2	0.118	160.2	14.4	1.5
PSZ2 G059.18+32.91	260.203	35.325	0.383	5.21 ± 0.56	260.195	35.324	2	0.485	38.23	3.4	19.0
PSZ2 G059.29+44.49	245.99	36.973	0.343	5.76 ± 0.69	245.959	37.007	2	1.072	41.02	8.6	37.0
PSZ2 G060.16+64.50	221.074	35.938	0.361	5.0 ± 0.63	221.065	35.957	2	0.411	39.69	3.1	15.0
PSZ2 G060.55+27.00	267.574	35.076	0.171	3.48 ± 0.41	267.574	35.076	2	0.313	68.68	7.0	6.0
PSZ2 G065.45+78.10	204.818	33.01	0.273	4.07 ± 0.53	204.766	32.966	1	0.347	47.98	3.8	9.5
PSZ2 G065.79+41.80	249.717	41.599	0.336	5.22 ± 0.59	249.748	41.616	2	0.356	41.59	2.9	12.0
PSZ2 G066.26+20.82	276.851	38.259	0.278	4.13 ± 0.5	276.846	38.238	2	1.614	47.37	17.3	45.0
PSZ2 G066.68+68.44	215.432	37.282	0.163	3.79 ± 0.34	215.419	37.292	1	0.242	71.42	5.9	4.5
PSZ2 G070.89+49.26	239.179	44.653	0.61	6.46 ± 0.69	239.212	44.621	2	0.89	29.69	3.7	67.0
PSZ2 G071.63+29.78	266.826	45.19	0.157	4.13 ± 0.29	266.818	45.2	2	0.22	73.66	5.7	4.0
PSZ2 G080.55-24.82	330.855	23.91	0.266	4.28 ± 0.53	330.844	23.901	2	0.486	48.89	5.5	13.0
PSZ2 G083.14+66.57	213.445	43.652	0.089	2.07 ± 0.26	213.431	43.654	2	0.157	120.31	10.8	2.2
PSZ2 G084.69+42.28	246.766	55.48	0.13	2.7 ± 0.26	246.746	55.474	2	0.164	86.31	5.8	2.7
PSZ2 G086.43-24.95	335.558	27.143	0.231	3.81 ± 0.5	335.572	27.134	2	0.379	54.25	5.3	9.0
PSZ2 G087.44-21.56	334.099	30.425	0.258	4.15 ± 0.51	334.099	30.425	2	0.461	49.98	5.5	12.0
PSZ2 G091.27-38.62	347.335	17.895	0.105	3.14 ± 0.39	347.339	17.868	1	0.235	103.87	12.1	3.5
PSZ2 G092.69+59.92	216.635	51.252	0.462	4.79 ± 0.6	216.634	51.266	2	0.533	34.21	3.0	26.5
PSZ2 G093.04-32.38	345.428	24.04	0.512	6.34 ± 0.72	345.519	24.062	2	1.567	32.36	7.8	90.0
PSZ2 G097.15+39.20	246.903	65.396	0.206	2.94 ± 0.32	246.944	65.421	2	0.212	59.23	3.5	4.6
PSZ2 G098.38+77.22	199.606	38.585	0.78	6.62 ± 0.71	199.606	38.585	1	0.69	26.87	2.4	80.0
PSZ2 G098.44+56.59	216.779	55.75	0.132	2.83 ± 0.27	216.844	55.749	2	0.175	85.2	6.1	2.9
PSZ2 G098.62+51.76	222.827	59.331	0.298	3.35 ± 0.48	222.603	59.325	2	0.403	45.11	3.9	12.0
PSZ2 G100.22+33.81	258.419	69.373	0.598	4.61 ± 0.47	258.414	69.358	2	1.029	29.96	4.4	75.0
PSZ2 G101.52-29.98	351.596	29.326	0.227	4.88 ± 0.52	351.617	29.367	2	0.385	54.98	5.5	9.0
PSZ2 G102.90-31.04	353.302	28.768	0.592	6.73 ± 0.72	353.302	28.768	1	0.446	30.1	1.9	32.0
PSZ2 G105.76+54.73	212.59	59.68	0.316	4.41 ± 0.45	212.573	59.711	2	0.648	43.33	5.8	20.5
PSZ2 G112.54+59.53	202.476	56.812	0.83	5.76 ± 0.66	202.476	56.812	1	0.456	26.31	1.5	60.0
PSZ2 G114.83+57.25	201.446	59.33	0.17	3.27 ± 0.3	201.446	59.33	2	0.21	69.01	4.8	4.0
PSZ2 G115.58-44.56	7.362	17.995	0.17	4.32 ± 0.4	7.362	17.995	1	0.21	69.01	4.8	4.0
PSZ2 G120.08-44.41	10.715	18.407	0.267	4.65 ± 0.64	10.696	18.433	2	0.521	48.75	5.9	14.0

Continued on next page

Table D.1: *Continued from previous page.*

Name	RA (deg)	DEC (deg)	z	M_{500} (10^{14} $M_{\odot}$)	RA_{inj} (deg)	DEC_{inj} (deg)	SQ	$I_{0,inj}$ (μJy arcsec^2)	$r_{e,inj}$ (arcsec)	$S_{150,UL}$ (mJy)	$P_{150,UL}$ (10^{23} W Hz^{-1})
PSZ2 G122.30+54.52	193.646	62.596	0.318	4.53 ± 0.45	193.689	62.566	2	0.628	43.15	5.6	20.0
PSZ2 G123.66+67.25	192.422	49.872	0.284	4.38 ± 0.51	192.422	49.872	2	0.281	46.65	2.9	8.0
PSZ2 G126.20-33.17	16.014	29.617	0.358	5.45 ± 0.74	16.062	29.564	2	1.243	39.9	9.4	45.0
PSZ2 G126.72-21.03	17.603	41.692	0.22	4.11 ± 0.57	17.603	41.692	2	0.438	56.3	6.6	10.0
PSZ2 G127.44-34.74	17.057	27.979	0.249	4.9 ± 0.71	17.057	27.979	2	0.733	51.3	9.2	18.5
PSZ2 G127.50-30.52	17.516	32.183	0.353	5.29 ± 0.67	17.533	32.181	2	0.716	40.26	5.5	25.5
PSZ2 G128.15-24.71	18.877	37.913	0.263	4.48 ± 0.6	18.877	37.914	1	0.302	49.29	3.5	8.0
PSZ2 G130.25-26.50	20.952	35.903	0.216	4.49 ± 0.5	20.914	35.907	2	0.267	57.1	4.1	6.0
PSZ2 G132.54-42.16	20.435	20.14	0.194	3.99 ± 0.51	20.422	20.094	1	0.288	62.08	5.3	6.0
PSZ2 G133.92-42.73	21.401	19.405	0.636	7.24 ± 0.96	21.435	19.401	2	0.93	29.14	3.8	75.0
PSZ2 G135.06+54.39	178.09	61.319	0.317	5.41 ± 0.42	178.058	61.334	1	0.268	43.24	2.4	8.5
PSZ2 G136.31+54.67	176.96	60.766	0.477	5.98 ± 0.51	176.96	60.766	1	0.347	33.61	1.9	18.0
PSZ2 G137.24+53.93	175.277	61.194	0.47	7.0 ± 0.48	175.277	61.194	1	0.373	33.89	2	19.0
PSZ2 G137.74-27.08	28.784	33.944	0.087	2.83 ± 0.28	28.784	33.944	2	0.166	122.79	11.9	2.3
PSZ2 G139.00+50.92	170.045	63.26	0.784	5.9 ± 0.7	170.065	63.242	2	1.282	26.82	4.4	150.0
PSZ2 G139.72-17.13	34.981	42.832	0.155	3.61 ± 0.44	34.926	42.849	2	0.249	74.44	6.6	4.5
PSZ2 G141.98+69.31	183.239	46.365	0.713	5.29 ± 0.68	183.169	46.356	2	0.519	27.79	1.9	51.0
PSZ2 G144.33+62.85	177.306	51.609	0.132	2.66 ± 0.35	177.26	51.591	2	0.103	85.2	3.6	1.7
PSZ2 G146.13+40.97	144.785	66.437	0.342	4.7 ± 0.65	144.792	66.417	2	0.233	41.1	1.9	8.0
PSZ2 G146.82+40.97	144.185	65.975	0.259	4.49 ± 0.27	144.185	65.975	1	0.223	49.84	2.7	6.0
PSZ2 G147.17+42.67	147.452	64.922	0.46	5.65 ± 0.72	147.504	64.925	2	0.364	34.3	2	18.0
PSZ2 G150.24+48.72	155.851	59.808	0.205	3.56 ± 0.42	155.84	59.81	2	0.18	59.45	3.0	3.9
PSZ2 G152.40+75.00	183.315	39.858	0.453	5.14 ± 0.7	183.315	39.858	1	0.372	34.59	2.1	18.0
PSZ2 G152.47+42.11	142.465	61.658	0.9	6.58 ± 0.77	142.465	61.658	2	0.945	25.67	3.0	145.0
PSZ2 G153.29+36.56	130.678	62.676	0.65	6.32 ± 1.27	130.678	62.676	2	0.574	28.86	2.3	48.0
PSZ2 G153.57+36.26	129.942	62.515	0.132	3.37 ± 0.39	129.855	62.522	2	0.181	85.2	6.3	3.0
PSZ2 G159.86+42.57	139.879	56.346	0.27	4.61 ± 0.57	139.917	56.366	2	0.442	48.36	4.9	12.0
PSZ2 G163.87+48.54	148.201	51.888	0.214	3.62 ± 0.43	148.2	51.888	2	0.215	57.51	3.4	4.8
PSZ2 G165.76+31.15	119.542	52.599	0.259	4.43 ± 0.66	119.496	52.638	2	0.44	49.84	5.2	11.5
PSZ2 G165.95+41.01	135.723	52.202	0.062	1.79 ± 0.26	135.756	52.219	2	0.095	167.36	12.7	1.2
PSZ2 G177.03+32.64	123.353	43.265	0.511	6.07 ± 0.76	123.336	43.226	2	0.873	32.39	4.4	50.0
PSZ2 G178.00+42.32	136.684	43.136	0.237	3.97 ± 0.54	136.74	43.084	2	0.371	53.22	5.0	9.0
PSZ2 G178.94+56.00	154.948	41.01	0.092	2.23 ± 0.3	154.954	40.976	2	0.219	116.79	14.2	3.1
PSZ2 G184.24+43.69	138.602	38.602	0.397	5.41 ± 0.63	138.604	38.59	2	0.612	37.39	4.1	25.0
PSZ2 G185.08+34.02	126.54	36.85	0.365	5.41 ± 0.66	126.492	36.874	2	0.865	39.41	6.4	32.0
PSZ2 G189.23+20.55	112.196	29.673	0.398	5.46 ± 0.74	112.196	29.673	2	0.683	37.34	4.5	28.0
PSZ2 G202.66+66.98	166.814	28.796	0.483	5.28 ± 0.7	166.814	28.796	1	0.549	33.38	2.9	29.0

We derived RA_{inj}, DEC_{inj} based on optical and X-ray images; when the cluster centre was ambiguous, we assumed the coordinates from *Planck*. Flux densities and radio powers are integrated up to $3r_{e,inj}$.

Appendix E

Modelling the hadronic scenario

In this Appendix we show the theoretical background considered to model a pure hadronic origin for the radio halo in MACS J1149 (Chapter 7). In particular, we aim to estimate the non-thermal energy in the cluster required to reproduce the observed radio emission in a pure hadronic scenario.

The stationary spectrum of electrons and positrons produced by hadronic collisions in the ICM is (Dolag & Enßlin 2000) given by

$$N_{\rm e}^{\pm}(p,t) = \frac{1}{\sum_{\rm rad,i}\left|\frac{{\rm d}p}{{\rm d}t}\right|}\int_{p} Q_{\rm e}^{\pm}(p,t)p{\rm d}t, \tag{E.1}$$

where p is the momentum of the particles, $\left|\frac{{\rm d}p}{{\rm d}t}\right|_{\rm rad,i}$ are the radiative and Coulomb losses, and $Q_{\rm e}^{\pm}(p,t)$ is the injection rate of electrons and positrons defined as (Brunetti & Jones 2014, and references therein)

$$\begin{aligned} Q_{\rm e}^{\pm}(p,t) = 2.1712\frac{m_\pi^2 n_{\rm th} c^2}{m_\pi^2 - m_\mu^2}\int_{E_{\rm min}}\int_{p_*}\frac{{\rm d}E_\pi {\rm d}p}{E_\pi \bar{\beta}_\mu}\beta_{\rm p} N_{\rm p}(p,t)\times \\ \times\ \frac{{\rm d}\sigma^{\pm,0}}{{\rm d}E}(E_\pi, E_{\rm p})F_{\rm e}(E_{\rm e}, E_\pi) \end{aligned}, \tag{E.2}$$

where the pedices 'π', 'μ', and 'p' refer to pions, muons, and protons, respectively, $\bar{\beta}_\mu = \sqrt{1-\left(\frac{m_\mu}{\bar{E}_\mu}\right)^2}$, $\bar{E}_\mu = \frac{E_\pi}{0.5428}\left[1-\left(\frac{m_\mu}{m_\pi}\right)^2\right]$, and $\frac{{\rm d}\sigma^{\pm,0}}{{\rm d}E}(E_\pi, E_{\rm p})$ is the differential inclusive cross-section for the production of π^+, π^-, and π^0 (we assume the cross-section as in Brunetti et al. 2017), and $F_{\rm e}(E_{\rm e}, E_\pi)$ is defined as in Brunetti & Blasi (2005) (Eqs. 36 and 37).

We derived the distribution of the thermal protons, $n_{\rm th}(r)$, from the X-ray surface brightness profile $I_{\rm X}(r)$ (index $\beta = 0.66$, core radius $r_{\rm c} = 288$ kpc, and central proton density number $n_{\rm th,0} = 3.6\times10^{-3}$ cm^{-3}; see Eqs. 7.2 and 7.3). We also assume that the magnetic field scales with the thermal proton density as

$$B(r) = B_0\left[\frac{n_{\rm th}(r)}{n_{\rm th,0}}\right]^\eta, \tag{E.3}$$

where we fixed $\eta = 0.5$, which is the value that gives the equilibrium between the thermal and magnetic energy densities (e.g. Bonafede et al. 2010).

The secondary CRe injected in the ICM magnetic field produce synchrotron radio emission with an emissivity given by (Dolag & Enßlin 2000)

$$j_{\rm R}(\nu, r) = \sqrt{3}\frac{e^3}{m_{\rm e}c^2}\int_0^{\frac{\pi}{2}} \sin^2\theta {\rm d}\theta \int N_{\rm e}^{\pm}(p) F\left(\frac{\nu}{\nu_{\rm c}}\right){\rm d}p \propto \\ \propto N_{\rm p}(p, r) n_{\rm th}(r)\frac{B(r)^{1+\alpha}}{B(r)^2 + B_{\rm CMB}^2}\nu^{-\alpha} \quad , \tag{E.4}$$

where θ is the pitch angle between B and p, $F\left(\frac{\nu}{\nu_{\rm c}}\right)$ is the synchrotron kernel (Rybicki & Lightman 1979), and $B_{\rm CMB} = 3.25(1+z)^2$ μG is the CMB equivalent magnetic field. Under the assumption of a spherical geometry, the integral of $j_{\rm R}(\nu, r)$ along the line of sight provides the surface brightness profile at a projected distance b as follows:

$$I_{\rm R}(b) = \frac{1}{4\pi(1+z)^4}\int_b^{+\infty}\frac{2r j_{\rm R}(r)}{\sqrt{r^2 - b^2}}{\rm d}r, \tag{E.5}$$

By assuming a value of the central field B_0 and taking into account the effects of the k-correction, we matched the radio profile from Eq. E.5 with the observed profile to derive the momentum distribution of CRp in the form (Brunetti & Jones 2014)

$$N_{\rm p}(p, r) = K_{\rm p}(r) p^{-s}, \tag{E.6}$$

where $K_{\rm p}(r)$ is the normalisation and $s = 2\alpha$ (where $\alpha = 1.5$, inferred from the radio spectrum of the halo). Thus, the energy budget of the CRp is obtained as

$$\varepsilon_{\rm p} = \int {\rm d}^3 r \int_{p_{\rm min}} E N_{\rm p}(p, r) {\rm d}p, \tag{E.7}$$

where we consider a minimum momentum of the CRp spectrum of $p_{\rm min} = 0.5 m_{\rm p} c$, corresponding to a kinetic energy of $E_{\rm min} \sim 110$ MeV.

Appendix F

Thermodynamical maps of A2142

In this Appendix we present and discuss the procedure employed to derive the entropy map of A2142 (Fig. 8.11 in Chapter 8).

The fit of each spectrum provides a value of temperature kT (in units of keV) and normalisation $\mathcal{N}$, where the latter is a proxy for the density. Indeed, the normalisation of the `apec` model is defined as the integral of the squared numerical density ($n_e \times n_H$) over the volume:

$$\mathcal{N} = \frac{10^{-14}}{4\pi D_A^2 (1+z)^2} \int n_e n_H dV \quad [\mathrm{cm}^{-5}] \quad , \tag{F.1}$$

where D_A is the angular distance at the cluster redshift. We define the entropy[1] as:

$$s = kT \left(\frac{\mathcal{N}}{A}\right)^{-\frac{1}{3}} \quad [\mathrm{keV\ cm}^{5/3}\ \mathrm{arcmin}^{-2/3}] \quad , \tag{F.2}$$

where A is the area of each extracting region (in units of arcmin^2). As both the temperature and density are projected (or 'pseudo') quantities, the entropy has to be considered as a projected quantity as well.

As shown in Fig. F.1, we produced (pseudo-) temperature, normalisation, and entropy maps for both single and combined ACIS-I and ACIS-S chips to check for possible biases. The associated errors maps (not shown) are computed directly from the fitting errors for kT and $\mathcal{N}$, whereas uncertainties on s are derived by assuming the standard error propagation formula as:

$$\Delta s = s \sqrt{\left(\frac{k\Delta T}{kT}\right)^2 + \frac{1}{9}\left(\frac{\Delta \mathcal{N}}{\mathcal{N}}\right)^2} \quad . \tag{F.3}$$

In Fig. F.2 we compare the values of the fitted temperature (upper panels) and normalisation (lower panels) obtained separately from ACIS-I and ACIS-S. The fitted normalisations are well in agreement within the $\sim 5\%$; on the other hand, the fitted temperatures show a larger scatter, with typical differences of $\sim 10 - 20\%$, up to $\sim 30\%$. Some intrinsic scatter is expected due to the different levels of degradation of the CHANDRA

[1] Astronomers derive the entropy as $s \propto T n_e^{-2/3}$, but many different definitions are found in the literature, lacking a universal convention.

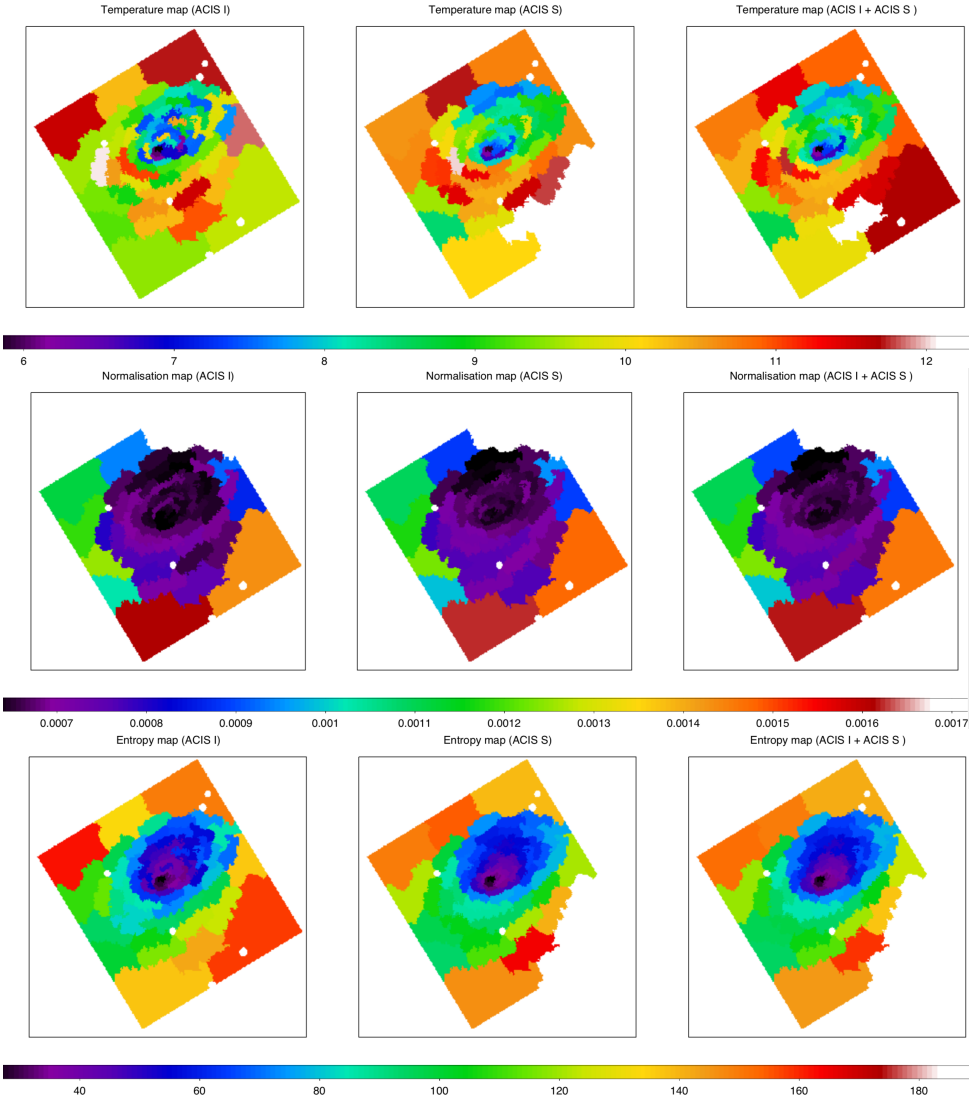

Figure F.1: Projected thermodynamical maps of A2142 obtained with Chandra ACIS-I only (left columns), ACIS-S only (middle columns), and combined ACIS-I plus ACIS-S (right columns): temperature (top panels, in units of keV), `apec` normalisation (middle panels, in units of cm^{-5}), and entropy (bottom panels, in units of keV $cm^{5/3}$ $arcmin^{-2/3}$).

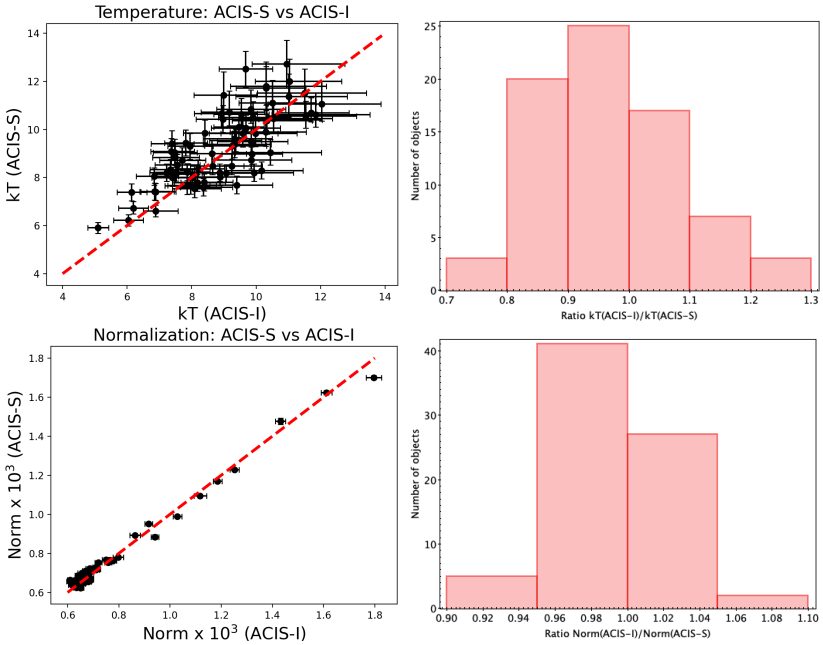

Figure F.2: Comparison of fitted temperatures (upper panels) and normalisations (lower panels) derived from ACIS-I and ACIS-S separately. Left panels report the values, and the bisector line is plotted in red. Right panels report the distribution of the ratios of ACIS-I to ACIS-S values.

chips as a function of time. In principle, spectra from the earlier ACIS-I observation are expected to provide more accurate fitted temperatures than spectra from the more recent ACIS-S observations; nevertheless, the ACIS-S observations are deeper than the ACIS-I observation by a factor 3.5. Therefore, when the spectra of all the chips are fitted simultaneously, the temperatures are primarily driven by the ACIS-S observations, and statistical errors reduce. Despite this bias unavoidably affects the entropy, we recover consistent trends for both single and combined cases in the inner regions of interest, where $s \lesssim 120$ keV cm$^{5/3}$ arcmin$^{-2/3}$; fitting errors for the combined case are $\Delta s \lesssim 5$ keV cm$^{5/3}$ arcmin$^{-2/3}$ and $\Delta s \lesssim 10$ keV cm$^{5/3}$ arcmin$^{-2/3}$ in the inner and outer regions, respectively. Therefore, we can genuinely rely on our results, which moreover are supported by the agreement with those of Rossetti et al. (2013) derived from XMM-Newton data.

Bibliography

Abell, G. O. 1958, Astrophysical Journal Supplement, 3, 211

Ackermann, M., Ajello, M., Albert, A., et al. 2014, APJ, 787, 18

Ackermann, M., Ajello, M., Albert, A., et al. 2016, APJ, 819, 149

Ackermann, M., Ajello, M., Allafort, A., et al. 2010, APJL, 717, L71

Aghanim, N., Majumdar, S., & Silk, J. 2008, Reports on Progress in Physics, 71, 066902

Akamatsu, H., Mizuno, M., Ota, N., et al. 2017, A&A, 600, A100

Akritas, M. G. & Bershady, M. A. 1996, APJ, 470, 706

Akritas, M. G. & Bershady, M. A. 1996, ApJ, 470, 706

Aleksić, J., Alvarez, E. A., Antonelli, L. A., et al. 2012, A&A, 541, A99

Alhassan, W., Taylor, A., & Vaccari, M. 2018, MNRAS, 480, 2085

Allen, S. W., Evrard, A. E., & Mantz, A. B. 2011, , 49, 409

Angelinelli, M., Vazza, F., Giocoli, C., et al. 2020, MNRAS, 495, 864

Aniyan, A. & Thorat, K. 2017, ApJS, 230, 20

Arnaud, K. A. 1996, in Astronomical Society of the Pacific Conference Series, Vol. 101, Astronomical Data Analysis Software and Systems V, ed. G. H. Jacoby & J. Barnes, 17

Arnaud, M. 2009, A&A, 500, 103

Arnaud, M., Aghanim, N., & Neumann, D. M. 2002, A&A, 389, 1

Barrena, R., Boschin, W., Girardi, M., & Spolaor, M. 2007, A&A, 469, 861

Bartalucci, I., Mazzotta, P., Bourdin, H., & Vikhlinin, A. 2014, A&A, 566, A25

Bartelmann, M., Meneghetti, M., Perrotta, F., Baccigalupi, C., & Moscardini, L. 2003, A&A, 409, 449

Basu, K. 2012, MNRAS, 421, L112

Beck, A. M., Dolag, K., Lesch, H., & Kronberg, P. P. 2013, MNRAS, 435, 3575

Bell, A. R. 1978a, MNRAS, 182, 147

Bell, A. R. 1978b, MNRAS, 182, 443

Bennett, C. L., Banday, A. J., Gorski, K. M., et al. 1996, APJL, 464, L1

Beresnyak, A., Xu, H., Li, H., & Schlickeiser, R. 2013, APJ, 771, 131

Bertone, S., Vogt, C., & Enßlin, T. 2006, MNRAS, 370, 319

Biava, N., de Gasperin, F., Bonafede, A., et al. 2021, MNRAS, 508, 3995

Bîrzan, L., Rafferty, D. A., Brüggen, M., et al. 2020, MNRAS, 496, 2613

Bîrzan, L., Rafferty, D. A., Cassano, R., et al. 2019, MNRAS, 487, 4775

Bîrzan, L., Rafferty, D. A., McNamara, B. R., Wise, M. W., & Nulsen, P. E. J. 2004, APJ, 607, 800

Blanton, E. L., Sarazin, C. L., McNamara, B. R., & Wise, M. W. 2001, APJL, 558, L15

Blasi, P. & Colafrancesco, S. 1999, Astroparticle Physics, 12, 169

Blasi, P., Gabici, S., & Brunetti, G. 2007, International Journal of Modern Physics A, 22, 681

Bonafede, A., Brüggen, M., van Weeren, R., et al. 2012, MNRAS, 426, 40

Bonafede, A., Brunetti, G., Rudnick, L., et al. 2022a, APJ, 933, 218

Bonafede, A., Brunetti, G., Rudnick, L., et al. 2022b, APJ, 933, 218

Bonafede, A., Brunetti, G., Vazza, F., et al. 2021a, APJ, 907, 32

Bonafede, A., Brunetti, G., Vazza, F., et al. 2021b, APJ, 907, 32

Bonafede, A., Cassano, R., Brüggen, M., et al. 2017, MNRAS, 470, 3465

Bonafede, A., Feretti, L., Giovannini, G., et al. 2009, A&A, 503, 707

Bonafede, A., Feretti, L., Murgia, M., et al. 2010, A&A, 513, A30

Bonafede, A., Intema, H. T., Brüggen, M., et al. 2014a, APJ, 785, 1

Bonafede, A., Intema, H. T., Bruggen, M., et al. 2014b, MNRAS, 444, L44

Boschin, W., Girardi, M., & Barrena, R. 2013, MNRAS, 434, 772

Botteon, A., Brunetti, G., Ryu, D., & Roh, S. 2020a, A&A, 634

Botteon, A., Brunetti, G., van Weeren, R. J., et al. 2020b, APJ, 897, 93

Botteon, A., Cassano, R., Eckert, D., et al. 2019, A&A, 630, A77

Botteon, A., Cassano, R., van Weeren, R. J., et al. 2021a, ApJ, 914, L29

Botteon, A., Gastaldello, F., & Brunetti, G. 2018, MNRAS, 476, 5591

Botteon, A., Gastaldello, F., Brunetti, G., & Dallacasa, D. 2016a, MNRAS, 460, L84

Botteon, A., Gastaldello, F., Brunetti, G., & Kale, R. 2016b, MNRAS, 463, 1534

Botteon, A., Giacintucci, S., Gastaldello, F., et al. 2021b, A&A, 649, A37

Botteon, A., Shimwell, T. W., Cassano, R., et al. 2022a, A&A, 660, A78

Botteon, A., Shimwell, T. W., Cassano, R., et al. 2022b, A&A, 660, A78

Botteon, A., van Weeren, R. J., Brunetti, G., et al. 2020c, MNRAS, 499, L11

Botteon, A., van Weeren, R. J., Brunetti, G., et al. 2022c, Science Advances, 8, eabq7623

Bourdin, H., Mazzotta, P., Markevitch, M., Giacintucci, S., & Brunetti, G. 2013, APJ, 764, 82

Boxelaar, J. M., van Weeren, R. J., & Botteon, A. 2021, A&C, 35, 100464

Briggs, D. S. 1995, in American Astronomical Society Meeting Abstracts, Vol. 187, American Astronomical Society Meeting Abstracts, 112.02

Brown, S. & Rudnick, L. 2011, MNRAS, 412, 2

Brunetti, G. 2009, A&A, 508, 599

Brunetti, G. & Blasi, P. 2005, MNRAS, 363, 1173

Brunetti, G., Blasi, P., Cassano, R., & Gabici, S. 2004, MNRAS, 350, 1174

Brunetti, G., Blasi, P., Reimer, O., et al. 2012, MNRAS, 426, 956

Brunetti, G., Giacintucci, S., Cassano, R., et al. 2008, , 455, 944

Brunetti, G. & Jones, T. W. 2014, International Journal of Modern Physics D, 23, 1430007

Brunetti, G. & Lazarian, A. 2007, MNRAS, 378, 245

Brunetti, G. & Lazarian, A. 2011a, MNRAS, 410, 127

Brunetti, G. & Lazarian, A. 2011b, MNRAS, 412, 817

Brunetti, G. & Lazarian, A. 2016, MNRAS, 458, 2584

Brunetti, G., Setti, G., Feretti, L., & Giovannini, G. 2001, MNRAS, 320, 365

Brunetti, G. & Vazza, F. 2020, PRL, 124, 051101

Brunetti, G., Venturi, T., Dallacasa, D., et al. 2007, APJL, 670, L5

Brunetti, G., Zimmer, S., & Zandanel, F. 2017, MNRAS, 472, 1506

Bruno, L., Brunetti, G., Botteon, A., et al. 2023, A&A, 672, A41

Bruno, L., Gitti, M., Zanichelli, A., & Gregorini, L. 2019, A&A, 631, A173

Bruno, L., Rajpurohit, K., Brunetti, G., et al. 2021, A&A, 650, A44

Buote, D. A. 2001, ApJ, 553, L15

Burns, J. O., Sulkanen, M. E., Gisler, G. R., & Perley, R. A. 1992, APJL, 388, L49

Carlstrom, J. E., Holder, G. P., & Reese, E. D. 2002, , 40, 643

Casey, C. M., Kartaltepe, J. S., Drakos, N. E., et al. 2022, arXiv e-prints, arXiv:2211.07865

Cash, W. 1979, APJ, 228, 939

Cassano, R., Botteon, A., Di Gennaro, G., et al. 2019, ApJ, 881, L18

Cassano, R. & Brunetti, G. 2005, MNRAS, 357, 1313

Cassano, R., Brunetti, G., Norris, R. P., et al. 2012, A&A, 548, A100

Cassano, R., Brunetti, G., Röttgering, H. J., & Brüggen, M. 2010, A&A, 509, A68

Cassano, R., Brunetti, G., Röttgering, H. J. A., & Brüggen, M. 2010a, A&A, 509, A68

Cassano, R., Brunetti, G., & Setti, G. 2006, MNRAS, 369, 1577

Cassano, R., Cuciti, V., Brunetti, G., et al. 2023, A&A, 672, A43

Cassano, R., Ettori, S., Brunetti, G., et al. 2013, APJ, 777, 141

Cassano, R., Ettori, S., Giacintucci, S., et al. 2010b, APJL, 721, L82

Cassano, R., Ettori, S., Giacintucci, S., et al. 2010, ApJ, 721, L82

Cava, A., Biviano, A., Mamon, G. A., et al. 2017, A&A, 606, A108

Cavagnolo, K. W., Donahue, M., Voit, G. M., & Sun, M. 2009, , 182, 12

Cavaliere, A. & Fusco-Femiano, R. 1976, A&A, 500, 95

Chambers, K. C., Magnier, E., Metcalfe, N., et al. 2016, arXiv e-prints, arXiv:1612.05560

Chandra, P., Ray, A., & Bhatnagar, S. 2004, APJ, 612, 974

Churazov, E., Vikhlinin, A., Zhuravleva, I., et al. 2012, MNRAS, 421, 1123

Clarke, T. E., Blanton, E. L., & Sarazin, C. L. 2004, APJ, 616, 178

Coe, D., Zitrin, A., Carrasco, M., et al. 2013, APJ, 762, 32

Cohen, A. S. & Clarke, T. E. 2011, , 141, 149

Coles, P. & Lucchin, F. 2002, Cosmology: The Origin and Evolution of Cosmic Structure, Second Edition

Condon, J. J., Cotton, W. D., Greisen, E. W., et al. 1998, , 115, 1693

Cuciti, V., Brunetti, G., van Weeren, R., et al. 2018, A&A, 609, A61

Cuciti, V., Cassano, R., Brunetti, G., et al. 2021a, A&A, 647, A51

Cuciti, V., Cassano, R., Brunetti, G., et al. 2015, A&A, 580, A97

Cuciti, V., Cassano, R., Brunetti, G., et al. 2021b, A&A, 647, A50

Cuciti, V., de Gasperin, F., Brüggen, M., et al. 2022, , 609, 911

Dallacasa, D., Brunetti, G., Giacintucci, S., et al. 2009, APJ, 699, 1288

de Gasperin, F., Brunetti, G., Brüggen, M., et al. 2020a, A&A, 642, A85

de Gasperin, F., Dijkema, T. J., Drabent, A., et al. 2019, A&A, 622, A5

de Gasperin, F., Intema, H. T., Shimwell, T. W., et al. 2017, Science Advances, 3, e1701634

de Gasperin, F., Rudnick, L., Finoguenov, A., et al. 2022, A&A, 659, A146

de Gasperin, F., Vink, J., McKean, J. P., et al. 2020b, A&A, 635, A150

de Gasperin, F., Williams, W. L., Best, P., et al. 2021, A&A, 648, A104

de Jong, J. M. G. H. J., van Weeren, R. J., Botteon, A., et al. 2022, arXiv e-prints, arXiv:2209.13930

De Lucia, G. & Blaizot, J. 2007, MNRAS, 375, 2

Dennison, B. 1980, APJL, 239, L93

Deo, D. K. & Kale, R. 2017, Experimental Astronomy, 44, 165

Dermer, C. D. 1986, APJ, 307, 47

Di Gennaro, G., van Weeren, R. J., Brunetti, G., et al. 2021a, Nature Astron., 5, 268

Di Gennaro, G., van Weeren, R. J., Cassano, R., et al. 2021b, A&A, 654, A166

Di Gennaro, G., van Weeren, R. J., Cassano, R., et al. 2021c, , 654, A166

Di Gennaro, G., van Weeren, R. J., Hoeft, M., et al. 2018, APJ, 865, 24

Dolag, K., Bykov, A. M., & Diaferio, A. 2008, , 134, 311

Dolag, K. & Enßlin, T. A. 2000, A&A, 362, 151

Dolag, K., Schindler, S., Govoni, F., & Feretti, L. 2001, A&A, 378, 777

Dolag, K., Vazza, F., Brunetti, G., & Tormen, G. 2005, MNRAS, 364, 753

Domínguez Sánchez, H., Huertas-Company, M., Bernardi, M., Tuccillo, D., & Fischer, J. 2018, MNRAS, 476, 3661

Donnert, J., Dolag, K., Brunetti, G., & Cassano, R. 2013, MNRAS, 429, 3564

Donnert, J., Dolag, K., Lesch, H., & Müller, E. 2009, MNRAS, 392, 1008

Donnert, J., Vazza, F., Brüggen, M., & ZuHone, J. 2018, , 214, 122

Dressler, A. 1980, APJ, 236, 351

Drury, L. O. 1983, Reports on Progress in Physics, 46, 973

Duchesne, S. W., Johnston-Hollitt, M., & Bartalucci, I. 2021, PASA, 38, e053

Duchesne, S. W., Johnston-Hollitt, M., Riseley, C. J., Bartalucci, I., & Keel, S. R. 2022, MNRAS, 511, 3525

Duchesne, S. W., Johnston-Hollitt, M., & Wilber, A. G. 2021, , 38, e031

Ebeling, H., Edge, A. C., & Henry, J. P. 2001, APJ, 553, 668

Eckert, D., Gaspari, M., Vazza, F., et al. 2017, APJL, 843, L29

Eckert, D., Gaspari, M., Vazza, F., et al. 2017, ApJ, 843, L29

Eckert, D., Jauzac, M., Vazza, F., et al. 2016, MNRAS, 461, 1302

Eckert, D., Molendi, S., & Paltani, S. 2011, A&A, 526, A79

Edler, H. W., de Gasperin, F., Brunetti, G., et al. 2022, A&A, 666, A3

Ehlert, S., McDonald, M., David, L. P., Miller, E. D., & Bautz, M. W. 2015, APJ, 799, 174

Einasto, M. 2020, arXiv e-prints, arXiv:2012.05843

Einasto, M., Deshev, B., Lietzen, H., et al. 2018, A&A, 610, A82

Einasto, M., Gramann, M., Saar, E., et al. 2015, A&A, 580, A69

Ensslin, T. A., Biermann, P. L., Klein, U., & Kohle, S. 1998, A&A, 332, 395

Enßlin, T. A. & Brüggen, M. 2002, MNRAS, 331, 1011

Enßlin, T. A. & Gopal-Krishna. 2001, A&A, 366, 26

Ettori, S., Donnarumma, A., Pointecouteau, E., et al. 2013, , 177, 119

Fabian, A. C. 2012, , 50, 455

Fabian, A. C., Crawford, C. S., Edge, A. C., & Mushotzky, R. F. 1994, MNRAS, 267, 779

Fabian, A. C., Sanders, J. S., Taylor, G. B., et al. 2006, MNRAS, 366, 417

Fanaroff, B. L. & Riley, J. M. 1974, MNRAS, 167, 31P

Farnsworth, D., Rudnick, L., Brown, S., & Brunetti, G. 2013, APJ, 779, 189

Fasano, G., Marmo, C., Varela, J., et al. 2006, A&A, 445, 805

Fasano, G., Poggianti, B. M., Bettoni, D., et al. 2015, MNRAS, 449, 3927

Feretti, L., Fusco-Femiano, R., Giovannini, G., & Govoni, F. 2001, A&A, 373, 106

Feretti, L., Giovannini, G., Govoni, F., & Murgia, M. 2012, A&Ar, 20, 54

Ferrari, C., Govoni, F., Schindler, S., Bykov, A. M., & Rephaeli, Y. 2008, , 134, 93

Flewelling, H. A., Magnier, E. A., Chambers, K. C., et al. 2020, , 251, 7

Foreman-Mackey, D., Hogg, D. W., Lang, D., & Goodman, J. 2013, PASP, 125, 306

Forman, W., Jones, C., Churazov, E., et al. 2007, APJ, 665, 1057

Forman, W., Jones, C., & Tucker, W. 1984, APJ, 277, 19

Fruscione, A., McDowell, J. C., Allen, G. E., et al. 2006, Society of Photo-Optical Instrumentation Engineers (SPIE) Conference Series, Vol. 6270, CIAO: Chandra's data analysis system, 62701V

Fujita, Y., Kohri, K., Yamazaki, R., & Kino, M. 2007, APJL, 663, L61

Fujita, Y. & Ohira, Y. 2013, MNRAS, 428, 599

Fujita, Y., Takizawa, M., & Sarazin, C. L. 2003, APJ, 584, 190

Gabici, S. & Blasi, P. 2003, APJ, 583, 695

Gabriel, C., Denby, M., Fyfe, D., et al. 2004, in Astronomical Society of the Pacific Conference Series, Vol. 314, Astron. Data Anal. Softw. Syst. XIII, ed. F. Ochsenbein, M. G. Allen, & D. Egret, 759

Gaspari, M., Churazov, E., Nagai, D., Lau, E. T., & Zhuravleva, I. 2014, A&A, 569, A67

Gendron-Marsolais, M., Hlavacek-Larrondo, J., van Weeren, R. J., et al. 2017, MNRAS, 469, 3872

Gendron-Marsolais, M. L., Hull, C. L. H., Perley, R., et al. 2021, APJ, 911, 56

George, L. T., Kale, R., & Wadadekar, Y. 2021a, MNRAS, 507, 4487

George, L. T., Kale, R., & Wadadekar, Y. 2021b, MNRAS, 507, 4487

Giacintucci, S., Markevitch, M., Brunetti, G., et al. 2014, APJ, 795, 73

Giacintucci, S., Markevitch, M., Cassano, R., et al. 2017, APJ, 841, 71

Giacintucci, S., Venturi, T., Brunetti, G., et al. 2005, A&A, 440, 867

Giovannini, G., Cau, M., Bonafede, A., et al. 2020, A&A, 640, A108

Giovannini, G. & Feretti, L. 2000, , 5, 335

Giovannini, G., Feretti, L., Govoni, F., Murgia, M., & Pizzo, R. 2006, Astronomische Nachrichten, 327, 563

Giovannini, G., Feretti, L., Venturi, T., Kim, K. T., & Kronberg, P. P. 1993, APJ, 406, 399

Giovannini, G., Tordi, M., & Feretti, L. 1999, , 4, 141

Girardi, M., Boschin, W., Gastaldello, F., et al. 2016, MNRAS, 456, 2829

Gitti, M., Brighenti, F., & McNamara, B. R. 2012a, Advances in Astronomy, 2012, 950641

Gitti, M., Brighenti, F., & McNamara, B. R. 2012b, Advances in Astronomy, 2012, 950641

Golovich, N., Dawson, W. A., Wittman, D., et al. 2016, APJ, 831

Golovich, N., Dawson, W. A., Wittman, D. M., et al. 2017, arXiv e-prints, arXiv:1711.01347

Golovich, N., Dawson, W. A., Wittman, D. M., et al. 2019, APJ, 882, 69

Gopal-Krishna, Biermann, P. L., Gergely, L. Á., & Wiita, P. J. 2012, Research in Astronomy and Astrophysics, 12, 127

Govoni, F., Enßlin, T. A., Feretti, L., & Giovannini, G. 2001, A&A, 369, 441

Govoni, F. & Feretti, L. 2004, International Journal of Modern Physics D, 13, 1549

Govoni, F., Murgia, M., Feretti, L., et al. 2005, A&A, 430, L5

Govoni, F., Murgia, M., Markevitch, M., et al. 2009, A&A, 499, 371

Govoni, F., Orrù, E., Bonafede, A., et al. 2019, Science, 364, 981

Gramann, M., Einasto, M., Heinämäki, P., et al. 2015, A&A, 581, A135

Hales, S. E. G., Baldwin, J. E., & Warner, P. J. 1988, MNRAS, 234, 919

Hales, S. E. G., Masson, C. R., Warner, P. J., & Baldwin, J. E. 1990, MNRAS, 246, 256

Hardcastle, M. J. & Croston, J. H. 2020, , 88, 101539

Hardcastle, M. J., Croston, J. H., Shimwell, T. W., et al. 2019, MNRAS, 488, 3416

Hardcastle, M. J., Gürkan, G., van Weeren, R. J., et al. 2016, MNRAS, 462, 1910

Hasselfield, M., Hilton, M., Marriage, T. A., et al. 2013, , 2013, 008

Henry, J. P. & Briel, U. G. 1996, APJ, 472, 137

Hill, G. J., Gebhardt, K., Komatsu, E., et al. 2008, in Astronomical Society of the Pacific Conference Series, Vol. 399, Panoramic Views of Galaxy Formation and Evolution, ed. T. Kodama, T. Yamada, & K. Aoki, 115

Hindson, L., Johnston-Hollitt, M., Hurley-Walker, N., et al. 2014, MNRAS, 445, 330

Hitomi Collaboration, Aharonian, F., Akamatsu, H., et al. 2016, , 535, 117

Hlavacek-Larrondo, J., Gendron-Marsolais, M.-L., Fecteau-Beaucage, D., et al. 2018, MNRAS, 475, 2743

Hoang, D. N., Brüggen, M., Botteon, A., et al. 2022, A&A, 665, A60

Hoang, D. N., Shimwell, T. W., Stroe, A., et al. 2017, MNRAS, 471, 1107

Hoang, D. N., Shimwell, T. W., van Weeren, R. J., et al. 2019, A&A, 622, A20

Hoang, D. N., Shimwell, T. W., van Weeren, R. J., et al. 2018, MNRAS, 478, 2218

Hoang, D. N., Shimwell, T. W., van Weeren, R. J., et al. 2019, A&A, 622, A21

Hoekstra, H., Bartelmann, M., Dahle, H., et al. 2013, , 177, 75

Houghton, R. C. W. 2015, MNRAS, 451, 3427

Hudson, D. S., Mittal, R., Reiprich, T. H., et al. 2010, A&A, 513, A37

Iapichino, L., Schmidt, W., Niemeyer, J. C., & Merklein, J. 2011, MNRAS, 414, 2297

Ichinohe, Y., Simionescu, A., Werner, N., & Takahashi, T. 2017, MNRAS, 467, 3662

Ignesti, A., Brunetti, G., Gitti, M., & Giacintucci, S. 2020a, A&A, 640, A37

Ignesti, A., Brunetti, G., Shimwell, T., et al. 2022, A&A, 659, A20

Ignesti, A., Shimwell, T., Brunetti, G., et al. 2020b, A&A, 643, A172

Intema, H. T., Jagannathan, P., Mooley, K. P., & Frail, D. A. 2017, A&A, 598, A78

Intema, H. T., van der Tol, S., Cotton, W. D., et al. 2009, A&A, 501, 1185

Johnston-Hollitt, M. & Pratley, L. 2017, arXiv e-prints, arXiv:1706.04930

Kaastra, J. S., Tamura, T., Peterson, J. R., et al. 2004, A&A, 413, 415

Kale, R., Parekh, V., & Dwarakanath, K. S. 2018, MNRAS, 480, 5352

Kale, R., Shende, K. M., & Parekh, V. 2019, MNRAS, 486, L80

Kale, R., Venturi, T., Giacintucci, S., et al. 2015, A&A, 579, A92

Kale, R., Venturi, T., Giacintucci, S., et al. 2013, A&A, 557, A99

Kang, H., Ryu, D., & Jones, T. W. 2012, APJ, 756, 97

Katz, N., Weinberg, D. H., & Hernquist, L. 1996, , 105, 19

Kelly, B. C. 2007, APJ, 665, 1489

Kempner, J. C., Blanton, E. L., Clarke, T. E., et al. 2004, in The Riddle of Cooling Flows in Galaxies and Clusters of galaxies, ed. T. Reiprich, J. Kempner, & N. Soker, 335

Kempner, J. C. & Sarazin, C. L. 2001, APJ, 548, 639

King, I. 1962, , 67, 471

Kravtsov, A. V. & Borgani, S. 2012, , 50, 353

Krymskii, G. F. 1977, Akademiia Nauk SSSR Doklady, 234, 1306

Lacey, C. & Cole, S. 1993, MNRAS, 262, 627

Landau, L. D. & Lifshitz, E. M. 1959, Fluid mechanics

Lane, W. M., Cotton, W. D., van Velzen, S., et al. 2014, MNRAS, 440, 327

Large, M. I., Mathewson, D. S., & Haslam, C. G. T. 1959, , 183, 1663

Lauer, T. R., Postman, M., Strauss, M. A., Graves, G. J., & Chisari, N. E. 2014, APJ, 797, 82

Limousin, M., Morandi, A., Sereno, M., et al. 2013, , 177, 155

Lindner, R. R., Baker, A. J., Hughes, J. P., et al. 2014, APJ, 786, 49

Liu, A., Yu, H., Diaferio, A., et al. 2018, APJ, 863, 102

Loi, F., Murgia, M., Govoni, F., et al. 2017, MNRAS, 472, 3605

Lovisari, L., Forman, W. R., Jones, C., et al. 2017, ApJ, 846, 51

Lukic, V., Brüggen, M., Banfield, J., et al. 2018, MNRAS, 476, 246

Lukic, V., Brüggen, M., Mingo, B., et al. 2019, MNRAS, 487, 1729

Lynden-Bell, D. 1967, MNRAS, 136, 101

Macario, G., Venturi, T., Brunetti, G., et al. 2010, A&A, 517, A43

Mandal, S., Intema, H. T., Shimwell, T. W., et al. 2019, A&A, 622, A22

Mandal, S., Intema, H. T., van Weeren, R. J., et al. 2020, A&A, 634, A4

Markevitch, M., Gonzalez, A. H., David, L., et al. 2002, APJL, 567, L27

Markevitch, M., Govoni, F., Brunetti, G., & Jerius, D. 2005, APJ, 627, 733

Markevitch, M., Ponman, T. J., Nulsen, P. E. J., et al. 2000, APJ, 541, 542

Markevitch, M. & Vikhlinin, A. 2007, , 443, 1

Matsushita, K., Belsole, E., Finoguenov, A., & Böhringer, H. 2002, A&A, 386, 77

Matthews, T. A., Morgan, W. W., & Schmidt, M. 1964, APJ, 140, 35

Mazzotta, P. & Giacintucci, S. 2008, APJL, 675, L9

McDonald, M., McNamara, B. R., van Weeren, R. J., et al. 2015, APJ, 811, 111

McMullin, J. P., Waters, B., Schiebel, D., Young, W., & Golap, K. 2007, in Astronomical Society of the Pacific Conference Series, Vol. 376, Astronomical Data Analysis Software and Systems XVI, ed. R. A. Shaw, F. Hill, & D. J. Bell, 127

McNamara, B. R. & Nulsen, P. E. J. 2012, New Journal of Physics, 14, 055023

McNamara, B. R., Nulsen, P. E. J., Wise, M. W., et al. 2005, , 433, 45

Mernier, F., Biffi, V., Yamaguchi, H., et al. 2018, , 214, 129

Metzler, C. A. 1998, arXiv e-prints, astro

Miley, G. K. & Perola, G. C. 1975, A&A, 45, 223

Miley, G. K., Perola, G. C., van der Kruit, P. C., & van der Laan, H. 1972, , 237, 269

Million, E. T. & Allen, S. W. 2009, MNRAS, 399, 1307

Mingo, B., Croston, J. H., Hardcastle, M. J., et al. 2019, MNRAS, 488, 2701

Miniati, F. 2014, APJ, 782, 21

Miniati, F. 2015, APJ, 800, 60

Miniati, F., Ryu, D., Kang, H., & Jones, T. W. 2001, APJ, 559, 59

Miyazaki, S., Komiyama, Y., Sekiguchi, M., et al. 2002, , 54, 833

Mohr, J. J., Fabricant, D. G., & Geller, M. J. 1993, ApJ, 413, 492

Molendi, S. & Pizzolato, F. 2001, APJ, 560, 194

Murgia, M., Eckert, D., Govoni, F., et al. 2010, A&A, 514, A76

Murgia, M., Fanti, C., Fanti, R., et al. 1999, A&A, 345, 769

Murgia, M., Govoni, F., Feretti, L., et al. 2004, A&A, 424, 429

Murgia, M., Govoni, F., Markevitch, M., et al. 2009, A&A, 499, 679

Nolting, C., Jones, T. W., O'Neill, B. J., & Mendygral, P. J. 2019, APJ, 885, 80

Nurgaliev, D., McDonald, M., Benson, B., et al. 2013, ApJ, 779, 112

O'Dea, C. P. & Owen, F. N. 1985, , 90, 927

Oegerle, W. R., Hill, J. M., & Fitchett, M. J. 1995, , 110, 32

Offringa, A. R. 2010, AOFlagger: RFI Software

Offringa, A. R., McKinley, B., Hurley-Walker, N., et al. 2014, MNRAS, 444, 606

Offringa, A. R. & Smirnov, O. 2017, MNRAS, 471, 301

Offringa, A. R., van de Gronde, J. J., & Roerdink, J. B. T. M. 2012, A&A, 539, A95

Ogrean, G. A., van Weeren, R. J., Jones, C., et al. 2016, APJ, 819, 113

Okabe, N. & Umetsu, K. 2008, , 60, 345

Osinga, E., van Weeren, R. J., Boxelaar, J. M., et al. 2021, A&A, 648, A11

O'Sullivan, E., Giacintucci, S., David, L. P., et al. 2011, APJ, 735, 11

Owen, F. N., Burns, J. O., & Rudnick, L. 1978, APJL, 226, L119

Owers, M. S., Nulsen, P. E. J., & Couch, W. J. 2011, APJ, 741, 122

Owers, M. S., Nulsen, P. E. J., Couch, W. J., & Markevitch, M. 2009, APJ, 704, 1349

Paolillo, M., Andreon, S., Longo, G., et al. 2001, A&A, 367, 59

Parekh, V., van der Heyden, K., Ferrari, C., Angus, G., & Holwerda, B. 2015, A&A, 575, A127

Pasini, T., Edler, H. W., Brüggen, M., et al. 2022, A&A, 663, A105

Pearce, C. J. J., van Weeren, R. J., Andrade-Santos, F., et al. 2017, APJ, 845, 81

Pedlar, A., Ghataure, H. S., Davies, R. D., et al. 1990, MNRAS, 246, 477

Perkins, J. S., Badran, H. M., Blaylock, G., et al. 2006, APJ, 644, 148

Perley, R. A. & Butler, B. J. 2013, , 204, 19

Peterson, J. R. & Fabian, A. C. 2006, , 427, 1

Peterson, J. R., Paerels, F. B. S., Kaastra, J. S., et al. 2001, A&A, 365, L104

Petrosian, V. 2001, APJ, 557, 560

Pfrommer, C. & Enßlin, T. A. 2004, A&A, 413, 17

Pfrommer, C., Enßlin, T. A., & Springel, V. 2008, MNRAS, 385, 1211

Pillastrini, G. C. B. 2019, NA, 69, 1

Pinkney, J., Rhee, G., Burns, J. O., et al. 1993, APJ, 416, 36

Pinzke, A., Oh, S. P., & Pfrommer, C. 2013, MNRAS, 435, 1061

Pinzke, A., Oh, S. P., & Pfrommer, C. 2017, MNRAS, 465, 4800

Pizzo, R. F. 2011, Journal of Astrophysics and Astronomy, 32, 567

Pizzo, R. F., de Bruyn, A. G., Bernardi, G., & Brentjens, M. A. 2011, A&A, 525, A104

Planck Collaboration, Ade, P. A. R., Aghanim, N., et al. 2014, A&A, 571, A29

Planck Collaboration, Ade, P. A. R., Aghanim, N., et al. 2011, A&A, 536, A1

Planck Collaboration, Ade, P. A. R., Aghanim, N., et al. 2016, A&A, 594, A24

Planck Collaboration XXII. 2016, A&A, 594, A22

Planck Collaboration XXVII. 2016, A&A, 594, A27

Poole, G., Fardal, M., Babul, A., et al. 2006, MNRAS, 373, 881

Pratt, G. W. & Arnaud, M. 2002, A&A, 394, 375

Press, W. & Schechter, P. 1974, ApJ, 187, 425

Rahaman, M., Raja, R., Datta, A., Burns, J. O., & Rapetti, D. 2022, MNRAS, 515, 2245

Raja, R., Rahaman, M., Datta, A., et al. 2020, MNRAS, 493, L28

Rajpurohit, K., Brunetti, G., Bonafede, A., et al. 2021a, A&A, 646, A135

Rajpurohit, K., Hoeft, M., van Weeren, R. J., et al. 2018, APJ, 852, 65

Rajpurohit, K., Hoeft, M., Vazza, F., et al. 2020, A&A, 636, A30

Rajpurohit, K., Hoeft, M., Wittor, D., et al. 2022a, A&A, 657, A2

Rajpurohit, K., Osinga, E., Brienza, M., et al. 2022b, arXiv e-prints, arXiv:2209.03288

Rajpurohit, K., van Weeren, R. J., Hoeft, M., et al. 2022c, APJ, 927, 80

Rajpurohit, K., Vazza, F., van Weeren, R. J., et al. 2021b, A&A, 654, A41

Rajpurohit, K., Wittor, D., van Weeren, R. J., et al. 2021c, A&A, 646, A56

Rasia, E., Meneghetti, M., & Ettori, S. 2013, Astron. Rev., 8, 40

Reichardt, C. L., Stalder, B., Bleem, L. E., et al. 2013, APJ, 763, 127

Ricker, P. M. & Sarazin, C. L. 2001, APJ, 561, 621

Riseley, C. J., Rajpurohit, K., Loi, F., et al. 2022, MNRAS, 512, 4210

Roger, R., Costain, C., & Bridle, A. 1973, AJ, 78, 1030

Rossetti, M., Eckert, D., De Grandi, S., et al. 2013, A&A, 556, A44

Rossetti, M., Gastaldello, F., Eckert, D., et al. 2017, MNRAS, 468, 1917

Rossetti, M., Ghizzardi, S., Molendi, S., & Finoguenov, A. 2007, A&A, 463, 839

Rudnick, L. & Lemmerman, J. A. 2009, APJ, 697, 1341

Rybicki, G. B. & Lightman, A. P. 1979, Radiative processes in astrophysics

Ryu, D., Kang, H., Hallman, E., & Jones, T. W. 2003, APJ, 593, 599

Ryu, D., Schleicher, D. R. G., Treumann, R. A., Tsagas, C. G., & Widrow, L. M. 2012, , 166, 1

Sabater, J., Best, P. N., Tasse, C., et al. 2021, A&A, 648, A2

Sadeghi, M., Javaherian, M., & Miraghaei, H. 2021, AJ, 161, 94

Sampaio, V. M., de Carvalho, R. R., Ferreras, I., Aragón-Salamanca, A., & Parker, L. C. 2022, MNRAS, 509, 567

Samui, S., Subramanian, K., & Srianand, R. 2018, MNRAS, 476, 1680

Sanders, J. S. 2006, MNRAS, 371, 829

Sanders, J. S., Fabian, A. C., Russell, H. R., Walker, S. A., & Blundell, K. M. 2016a, MNRAS, 460, 1898

Sanders, J. S., Fabian, A. C., Taylor, G. B., et al. 2016b, MNRAS, 457, 82

Santos, J., Rosati, P., Tozzi, P., et al. 2008, A&A, 483, 35

Santos-Lima, R., de Gouveia Dal Pino, E. M., Kowal, G., et al. 2014, APJ, 781, 84

Sarazin, C. L. 1986a, Reviews of Modern Physics, 58, 1

Sarazin, C. L. 1986b, Reviews of Modern Physics, 58, 1

Sarazin, C. L. 2002, in Astrophysics and Space Science Library, Vol. 272, Merging Processes in Galaxy Clusters, ed. L. Feretti, I. M. Gioia, & G. Giovannini, 1–38

Saripalli, L. 2012, , 144, 85

Savini, F., Bonafede, A., Brüggen, M., et al. 2019, A&A, 622, A24

Savini, F., Bonafede, A., Brüggen, M., et al. 2018, MNRAS, 478, 2234

Scaife, A. M. M. & Heald, G. H. 2012, MNRAS, 423, L30

Schawinski, K., Urry, C. M., Simmons, B. D., et al. 2014, MNRAS, 440, 889

Schechter, P. 1976, APJ, 203, 297

Schindler, S. & Muller, E. 1993, A&A, 272, 137

Schuecker, P., Finoguenov, A., Miniati, F., Böhringer, H., & Briel, U. G. 2004, A&A, 426, 387

Sereno, M., Ettori, S., Meneghetti, M., et al. 2017, MNRAS, 467, 3801

Shimwell, T. W., Hardcastle, M. J., Tasse, C., et al. 2022a, A&A, 659, A1

Shimwell, T. W., Hardcastle, M. J., Tasse, C., et al. 2022b, A&A, 659, A1

Shimwell, T. W., Markevitch, M., Brown, S., et al. 2015, MNRAS, 449, 1486

Shimwell, T. W., Röttgering, H. J. A., Best, P. N., et al. 2017, A&A, 598, A104

Shimwell, T. W., Tasse, C., Hardcastle, M. J., et al. 2019, A&A, 622, A1

Simionescu, A., Werner, N., Forman, W. R., et al. 2010, MNRAS, 405, 91

Skillman, S. W., Xu, H., Hallman, E. J., et al. 2013, APJ, 765, 21

Skrutskie, M. F., Cutri, R. M., Stiening, R., et al. 2006, , 131, 1163

Smirnov, O. M. & Tasse, C. 2015, MNRAS, 449, 2668

Smith, G. P., Ebeling, H., Limousin, M., et al. 2009, APJL, 707

Sommer, M. W., Basu, K., Intema, H., et al. 2017, MNRAS, 466, 996

Spergel, D. N., Bean, R., Doré, O., et al. 2007, , 170, 377

Springel, V. 2005, MNRAS, 364, 1105

Storm, E., Jeltema, T. E., Splettstoesser, M., & Profumo, S. 2017, ApJ, 839, 33

Stroe, A., van Weeren, R. J., Intema, H. T., et al. 2013, A&A, 555, A110

Subramanian, K. 2016, Reports on Progress in Physics, 79, 076901

Sunyaev, R. A. & Zeldovich, Y. B. 1972, Comments on Astrophysics and Space Physics, 4, 173

Sutherland, R. S. & Dopita, M. A. 1993, , 88, 253

Tasse, C. 2014a, arXiv e-prints, arXiv:1410.8706

Tasse, C. 2014b, A&A, 566, A127

Tasse, C., Hugo, B., Mirmont, M., et al. 2018, A&A, 611, A87

Tasse, C., Shimwell, T., Hardcastle, M. J., et al. 2021, A&A, 648, A1

Tchernin, C., Eckert, D., Ettori, S., et al. 2016, A&A, 595, A42

Thierbach, M., Klein, U., & Wielebinski, R. 2003, A&A, 397, 53

Urdampilleta, I., Akamatsu, H., Mernier, F., et al. 2018, A&A, 618, A74

Vallés-Pérez, D., Planelles, S., & Quilis, V. 2021, MNRAS, 504, 510

van de Voort, F., Bahé, Y. M., Bower, R. G., et al. 2017, MNRAS, 466, 3460

van Haarlem, M. P., Wise, M. W., Gunst, A. W., et al. 2013, A&A, 556, A2

van Weeren, R. J., Andrade-Santos, F., Dawson, W. A., et al. 2017, Nature Astronomy, 1, 0005

van Weeren, R. J., de Gasperin, F., Akamatsu, H., et al. 2019, SSR, 215, 16

van Weeren, R. J., de Gasperin, F., Akamatsu, H., et al. 2019, Space Sci. Rev., 215, 16

van Weeren, R. J., Röttgering, H. J. A., & Brüggen, M. 2011, A&A, 527, A114

van Weeren, R. J., Röttgering, H. J. A., Brüggen, M., & Cohen, A. 2009, A&A, 508, 75

van Weeren, R. J., Röttgering, H. J. A., Brüggen, M., & Hoeft, M. 2010, Science, 330, 347

van Weeren, R. J., Röttgering, H. J. A., Intema, H. T., et al. 2012a, A&A, 546, A124

van Weeren, R. J., Röttgering, H. J. A., Rafferty, D. A., et al. 2012b, A&A, 543, A43

van Weeren, R. J., Shimwell, T. W., Botteon, A., et al. 2020, arXiv e-prints, arXiv:2011.02387

van Weeren, R. J., Shimwell, T. W., Botteon, A., et al. 2021, A&A, 651, A115

van Weeren, R. J., Williams, W. L., Hardcastle, M. J., et al. 2016, , 223, 2

Vavilova, I., Dobrycheva, D., Vasylenko, M. Y., et al. 2021, A&A, 648, A122

Vazza, F., Angelinelli, M., Jones, T. W., et al. 2018, MNRAS, 481, L120

Vazza, F. & Brüggen, M. 2014, MNRAS, 437, 2291

Vazza, F., Brunetti, G., Kritsuk, A., et al. 2009, A&A, 504, 33

Venturi, T., Giacintucci, S., Brunetti, G., et al. 2007, A&A, 463, 937

Venturi, T., Giacintucci, S., Dallacasa, D., et al. 2008, A&A, 484, 327

Venturi, T., Rossetti, M., Brunetti, G., et al. 2017, A&A, 603, A125

Vikhlinin, A., Kravtsov, A., Forman, W., et al. 2006, APJ, 640, 691

Vikhlinin, A., Markevitch, M., & Murray, S. S. 2001, APJ, 551, 160

Vogelsberger, M., Genel, S., Springel, V., et al. 2014, MNRAS, 444, 1518

Vogt, C. & Enßlin, T. A. 2005, A&A, 434, 67

Voit, G. M. 2005, Reviews of Modern Physics, 77, 207

Walker, S., Simionescu, A., Nagai, D., et al. 2019, , 215, 7

Wang, Q. H. S. & Markevitch, M. 2018, APJ, 868, 45

White, M., Hernquist, L., & Springel, V. 2002, APJ, 579, 16

Wilber, A., Brüggen, M., Bonafede, A., et al. 2018, MNRAS, 473, 3536

Williams, W. L., de Gasperin, F., Hardcastle, M. J. H., et al. 2021, A&A, 655, A40

Williams, W. L., van Weeren, R. J., Röttgering, H. J. A., et al. 2016, MNRAS, 460, 2385

Willingale, R., Starling, R. L. C., Beardmore, A. P., Tanvir, N. R., & O'Brien, P. T. 2013, MNRAS, 431, 394

Wilner, D. J. & Welch, W. J. 1994, APJ, 427, 898

Wirth, A., Smarr, L., & Gallagher, J. S. 1982, , 87, 401

Wittor, D., Ettori, S., Vazza, F., et al. 2021, MNRAS, 506, 396

Wittor, D., Jones, T., Vazza, F., & Brüggen, M. 2017, MNRAS, 471, 3212

Xie, C., van Weeren, R. J., Lovisari, L., et al. 2020, A&A, 636, A3

Xu, H., Li, H., Collins, D. C., Li, S., & Norman, M. L. 2009, APJL, 698, L14

York, D. G., Adelman, J., Anderson, John E., J., et al. 2000, , 120, 1579

Yuan, Z. & Han, J. 2020, MNRAS, 497, 5485

Yuan, Z. S. & Han, J. L. 2020, MNRAS, 497, 5485

Zandanel, F. & Ando, S. 2014, MNRAS, 440, 663

Zandanel, F., Pfrommer, C., & Prada, F. 2014, MNRAS, 438, 124

Zhang, X., Simionescu, A., Gastaldello, F., et al. 2023, A&A, 672, A42

Zhuravleva, I., Churazov, E., Arévalo, P., et al. 2015, MNRAS, 450, 4184

Zhuravleva, I., Churazov, E. M., Schekochihin, A. A., et al. 2014, APJL, 788, L13

ZuHone, J. A., Markevitch, M., & Lee, D. 2011, APJ, 743, 16

ZuHone, J. A., Markevitch, M., Ruszkowski, M., & Lee, D. 2013, APJ, 762, 69

Zuhone, J. A. & Roediger, E. 2016, Journal of Plasma Physics, 82, 535820301

Zwicky, F., Herzog, E., Wild, P., Karpowicz, M., & Kowal, C. T. 1961, Catalogue of galaxies and of clusters of galaxies, Vol. I